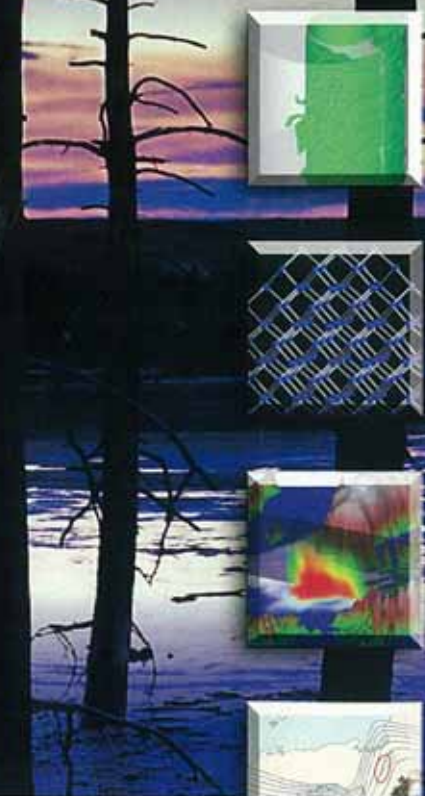


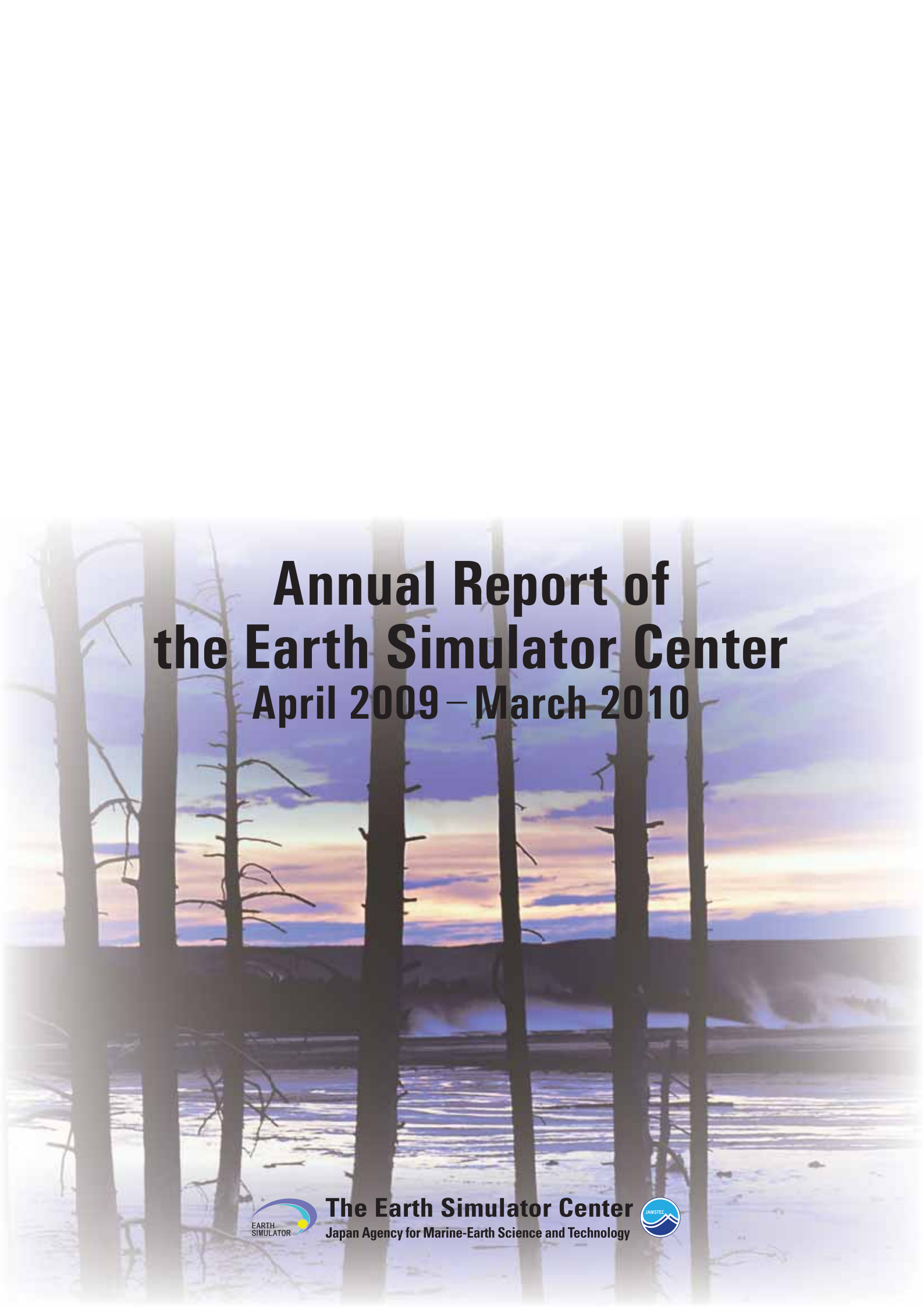
Annual Report of the Earth Simulator Center

April 2009 – March 2010



The Earth Simulator Center
Japan Agency for Marine-Earth Science and Technology





Annual Report of the Earth Simulator Center

April 2009 – March 2010



The Earth Simulator Center
Japan Agency for Marine-Earth Science and Technology



CONTENTS

Outline of the Earth Simulator Project

1. Mission and Basic Principles of the Earth Simulator	1
2. Earth Simulator Research Project	1
3. Collaboration Projects	4
4. System Configuration of the Earth Simulator	5

Earth Simulator Research Projects

Chapter 1 Earth Science

Understanding Roles of Oceanic Fine Structures in Climate and Its Variability	11
Wataru Ohfuchi Earth Simulator Center, Japan Agency for Marine-Earth Science and Technology 海洋微細構造が生み出す気候形成・変動メカニズムの解明 海洋研究開発機構 地球シミュレータセンター 大淵 済	
Simulations of Adaptation-Oriented Strategy for Climate Variability	19
Keiko Takahashi Earth Simulator Center, Japan Agency for Marine-Earth Science and Technology 気候変動に適応可能な環境探索のためのマルチスケールシミュレーション 海洋研究開発機構 地球シミュレータセンター 高橋 桂子	
Development of a High-Resolution Coupled Climate Model for Global Warming Studies	27
Akira Noda Research Institute for Global Change, Japan Agency for Marine-Earth Science and Technology 地球温暖化予測研究のための高精度気候モデルの開発研究 海洋研究開発機構 地球環境変動領域 野田 彰	
Simulations of Atmospheric General Circulations of Earth-like Planets by AFES	33
Yoshi-Yuki Hayashi Department of Earth and Planetary Sciences, Kobe University AFES を用いた地球型惑星の大気大循環シミュレーション 神戸大学大学院 理学研究科 林 祥介	
Study on the Diagnostics and Projection of Ecosystem Change Associated with Global Change	39
Michio J. Kishi Research Institute for Global Change, Japan Agency for Marine-Earth Science and Technology 地球環境変化に伴う生態系変動の診断と予測に関する研究 海洋研究開発機構 地球環境変動領域 岸 道郎	
Computational Fluid Dynamics Simulation of Daytime and Nighttime Summer Temperatures in 23 Special Wards of Tokyo	43
Yasunobu Ashie National Institute for Land and Infrastructure Management 東京 23 区の夏期昼夜間における熱環境の数値シミュレーション 国土技術政策総合研究所 足永 靖信	
Study of Cloud and Precipitation Processes Using a Global Cloud-system Resolving Model	49
Masaki Satoh Atmosphere and Ocean Research Institute, University of Tokyo Research Institute for Global Change, Japan Agency for Marine-Earth Science and Technology 全球雲解像モデルを用いた雲降水プロセス研究 東京大学 大気海洋研究所 海洋研究開発機構 地球環境変動領域 佐藤 正樹	

Observing System Research Using Ensemble-based Data Assimilation Methods	55
Takeshi Enomoto Earth Simulator Center, Japan Agency for Marine-Earth Science and Technology	
アンサンブル同化手法を用いた観測システムの最適化に関する研究	
海洋研究開発機構 地球シミュレータセンター 榎本 剛	
Process Studies and Seasonal Prediction Experiment Using Coupled General Circulation Model	63
Yukio Masumoto Research Institute for Global Change, Japan Agency for Marine-Earth Science and Technology	
大気海洋結合モデルを用いたプロセス研究と季節予測実験	
海洋研究開発機構 地球環境変動領域 升本 順夫	
Global Elastic Response Simulation	69
Seiji Tsuboi Institute for Research on Earth Evolution, Japan Agency for Marine-Earth Science and Technology	
全地球弾性応答シミュレーション	
海洋研究開発機構 地球内部ダイナミクス領域 坪井 誠司	
Simulation Study on the Dynamics of the Mantle and Core in Earth-like Conditions	75
Yozo Hamano Institute for Research on Earth Evolution, Japan Agency for Marine-Earth Science and Technology	
実地球環境でのマントル・コア活動の数値シミュレーション	
海洋研究開発機構 地球内部ダイナミクス領域 浜野 洋三	
Development of a Predictive Simulation System for Crustal Activities in and around Japan - VII	81
Chihiro Hashimoto Graduate School of Environmental Studies, Nagoya University	
日本列島域の地殻活動予測シミュレーション・システムの開発 -	
名古屋大学大学院 環境学研究所 橋本 千尋	
Numerical Simulation of Seismic Wave Propagation and Strong Motions in 3D Heterogeneous Structure	87
Takashi Furumura Center for Integrated Disaster Information Research, The University of Tokyo	
Earthquake Research Institute, The University of Tokyo	
3次元不均質場での波動伝播と強震動シミュレーション	
東京大学大学院 情報学環総合防災情報研究センター	
東京大学 地震研究所 古村 孝志	
Development of Advanced Simulation Methods for Solid Earth Simulations	95
Akira Kageyama Graduate School of System Informatics, Kobe University	
先端的固体地球科学シミュレーションコードの開発	
神戸大学大学院 システム情報学研究科 陰山 聡	
Numerical Determination of the Efficiency of Entrainment in Volcanic Eruption Columns	99
Takehiro Koyaguchi Earthquake Research Institute, University of Tokyo	
爆発的火山噴火における噴煙内部の乱流混合効率	
東京大学 地震研究所 小屋口 剛博	
Space and Earth System Modeling	105
Kanya Kusano Institute for Research on Earth Evolution, Japan Agency for Marine-Earth Science and Technology	
宇宙・地球表層・地球内部の相関モデリング	
海洋研究開発機構 地球内部ダイナミクス領域 草野 完也	

Chapter 2 Epoch-Making Simulation

Development of General Purpose Numerical Software Infrastructure for Large Scale Scientific Computing	113
Akira Nishida Research Institute for Information Technology, Kyushu University 大規模科学計算向け汎用数値ソフトウェア基盤の開発 九州大学 情報基盤研究開発センター 西田 晃	
Large Scale Simulations for Carbon Nanotubes	119
Syogo Tejima Research Organization for Information Science & Technology カーボンナノチューブの特性に関する大規模シミュレーション 高度情報科学技術研究機構 手島 正吾	
Development of the Next-generation Computational Fracture Mechanics Simulator for Constructing Safe and Sustainable Society	127
Ryuji Shioya Faculty of Information Sciences and Arts, Toyo University 安全・安心な持続可能社会のための次世代計算破壊力学シミュレータの開発 東洋大学 総合情報学部 塩谷 隆二	
Large-scale Simulation for a Terahertz Resonance Superconductor Device	133
Mikio Iizuka Research Organization for Information Science and Technology テラヘルツ発振超伝導素子に関する大規模シミュレーション 高度情報科学技術研究機構 飯塚 幹夫	
Direct Numerical Simulations of Fundamental Turbulent Flows with the World's Largest Number of Grid-points and Application to Modeling of Engineering Turbulent Flows	139
Yukio Kaneda Graduate School of Engineering, Nagoya University 乱流の世界最大規模直接数値計算とモデリングによる応用計算 名古屋大学大学院 工学研究科 金田 行雄	
A Large-scale Genomics and Proteomics Analyses Conducted by the Earth Simulator	145
Toshimichi Ikemura Nagahama Institute of Bio-Science and Technology 地球シミュレータで可能になる大規模なゲノミクスとプロテオミクス研究 長浜バイオ大学 バイオサイエンス学部 池村 淑道	
First-principles Calculation on the Diffusion of Hydrogen along a Screw Dislocation Core in BCC Iron	151
Hideo Kaburaki Japan Atomic Energy Agency 第一原理計算による BCC 鉄中らせん転位芯への水素拡散経路 日本原子力研究開発機構 蕪木 英雄	
Numerical Simulation of Turbulent Sodium Flows in Subchannels of an LMFBR Fuel Subassembly	157
Hisashi Ninokata Research Laboratory for Nuclear Reactors, Tokyo Institute of Technology 高速増殖炉燃料集合体サブチャンネル内ナトリウム冷却材の乱流シミュレーション 東京工業大学 原子炉工学研究所 二ノ方 寿	
Analysis of Mutation Mechanisms of Influenza Virus Based on the Fragment Molecular Orbital Method	163
Shigenori Tanaka Graduate School of System Informatics, Kobe University フラグメント分子軌道法によるインフルエンザウイルスの変異機構の解析 神戸大学大学院 システム情報学研究科 田中 成典	

Chapter 3 Visualization

Studies of Large-Scale Data Visualization, GPGPU Application and Visual Data Mining	171
Fumiaki Araki Earth Simulator Center, Japan Agency for Marine-Earth Science and Technology	
大規模データ可視化, GPGPU およびビジュアルデータマイニングの研究	
海洋研究開発機構 地球シミュレータセンター 荒木 文明	

Outline of the Earth Simulator Project

1. Mission and Basic Principles of the Earth Simulator

The Earth Simulator was developed for the following aims. The first aim is to ensure a bright future for human beings by accurately predicting variable global environment. The second is to contribute to the development of science and technology in the 21st century. Based on these aims, four principles are established for the projects of the Earth Simulator.

- 1) Each project should be open to researches in each research field and to the public, rather than it is confined within the limited research society.
- 2) In principle, the research achievements obtained by using the Earth Simulator should be promptly published and returned to the public.
- 3) Each project should be carried out for peaceful purposes only.

2. Earth Simulator Research Project

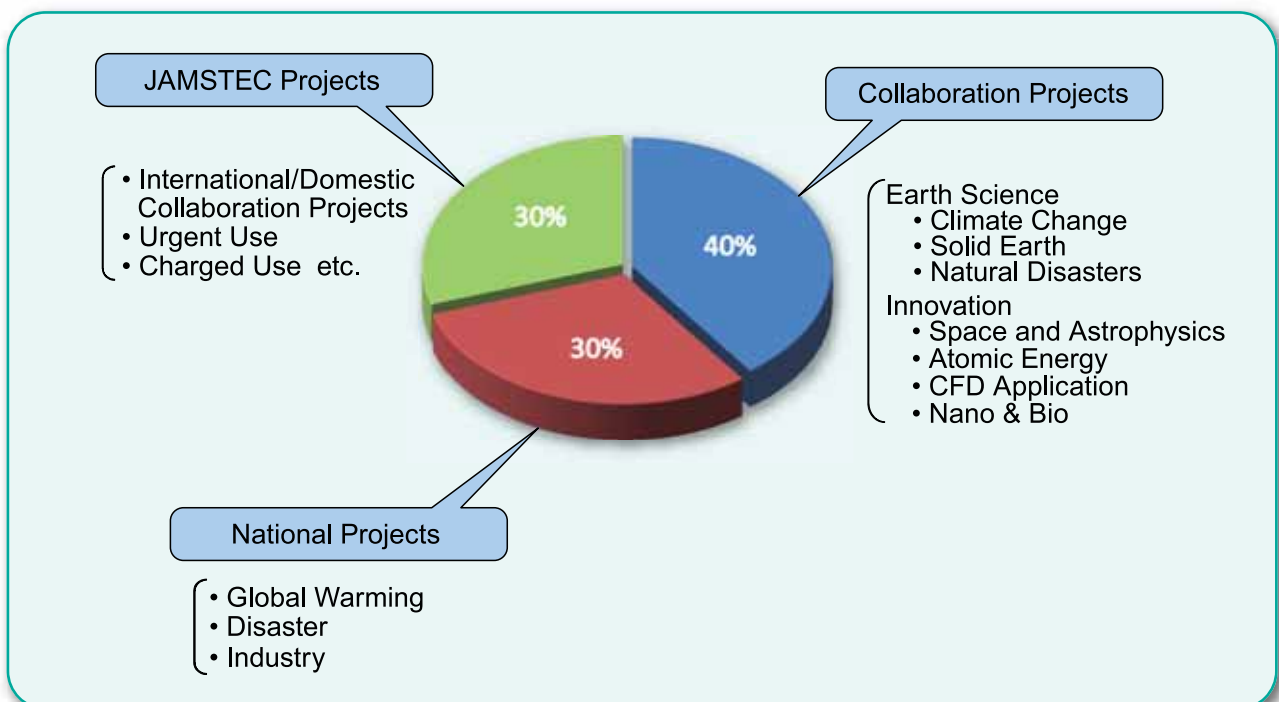
There are two fields of Earth Simulator Research Projects, as follows:

- Earth Science
- Epoch-making Simulation

Allocation of the Earth Simulator resources is planned by the Mission Definition Committee each fiscal year. The allocation of resources for each research field in FY2009 was decided to be as shown in following graph.

Public project recruitment for Earth Simulator Research Projects in FY2009 was held in February 2009, and 25 research projects were selected by the Selection Committee. The allocation of resources for each project was also decided by the Selection Committee.

The Allocation of Resources of the Earth Simulator in FY2009



Authorized Projects in FY2009

Earth Science (16 projects)

	Title	Project leader	Affiliation of project leader
1	Understanding Roles of Oceanic Fine Structures in Climate and its Variability	Wataru Ofuchi	ESC, JAMSTEC
2	Simulations of Adaptation-Oriented Strategy for Climate Variability	Keiko Takahashi	ESC, JAMSTEC
3	Development of a High-quality Climate Model for Global Warming Projection Study	Akira Noda	Research Institute for Global Change, JAMSTEC
4	Simulations of Atmospheric General Circulations of Earth-like Planets by AFES	Yoshiyuki Hayashi	Graduate School of Science, Kobe University
5	Study on the Diagnostics and Projection of Ecosystem Change Associated with Global Change	Michio Kishi	Research Institute for Global Change, JAMSTEC
6	Development of a Numerical Model of Urban Heat Island	Yasunobu Ashie	National Institute for Land and Infrastructure Management
7	Study of Cloud and Precipitation Processes using a Global Cloud-system Resolving Model	Masaki Sato	Research Institute for Global Change, JAMSTEC
8	Observing System Research using Ensemble-based Data Assimilation Methods	Takeshi Enomoto	ESC, JAMSTEC
9	Study on Predictability of Climate Variations and Their Mechanisms	Yukio Masumoto	Research Institute for Global Change, JAMSTEC
10	Global Elastic Response Simulation	Seiji Tsuboi	IFREE, JAMSTEC
11	Simulation Study on the Dynamics of the Mantle and Core in Earth-like Conditions	Yozo Hamano	IFREE, JAMSTEC
12	Predictive Simulation for Crustal Activity in and around Japan	Chihiro Hashimoto	Graduate School of Environmental Studies, Nagoya University
13	Numerical Simulation of Seismic Wave Propagation and Strong Ground Motions in 3-D Heterogeneous Media	Takashi Furumura	Center for Integrated Disaster Information Research, Interfaculty Initiative in Information Studies, The University of Tokyo/Earthquake Research Institute, The University of Tokyo
14	Development of Advanced Simulation Tools for Solid Earth Sciences	Akira Kageyama	Kobe University
15	Numerical Simulations of the Dynamics of Volcanic Phenomena	Takehiro Koyaguchi	Earthquake Research Institute, University of Tokyo
16	Space and Earth System Modeling	Kanya Kusano	IFREE, JAMSTEC

Epoch-making Simulation (9 projects)

	Title	Project leader	Affiliation of project leader
17	Development of General Purpose Numerical Software Infrastructure for Large Scale Scientific Computing	Akira Nishida	Research Institute for Information Technology, Kyushu University
18	Large-scale Simulation on the Properties of Carbon-nanotube	Syogo Tejima	Research Organization for Information Science & Technology
19	Development of the Next-generation Computational Fracture Mechanics Simulator for Constructing Safe and Sustainable Society	Ryuji Shioya	Faculty of Information Sciences and Arts, Toyo University
20	Large-scale Simulation for a Terahertz Resonance Superconductors Device	Mikio Iizuka	Research Organization for Information Science & Technology
21	Direct Numerical Simulations of Fundamental Turbulent Flows with the World's Largest Number of Grid-points and Application to Modeling of Engineering Turbulent Flows	Yukio Kaneda	Graduate School of Engineering, Nagoya University
22	A Large-scale Post-genome Analysis using Self-Organizing Map for All Genome and Protein Sequences	Toshimichi Ikemura	Nagahama Institute of Bio-Science and Technology
23	First Principles Calculation on Hydrogen Diffusion Behavior in Iron with a Dislocation and Grain Boundary	Hideo Kaburaki	Japan Atomic Energy Agency
24	Numerical Simulation of Turbulent Sodium Flows in Subchannels of an LMFBR Fuel Subassembly	Hisashi Ninokata	Graduate School of Engineering, Tokyo Institute of Technology
25	Theoretical Study of Drug Resistance Mechanism Based on the Fragment Molecular Orbital Method	Shigenori Tanaka	Graduate School of Human Development and Environment, Kobe University

JAMSTEC : Japan Agency for Marine-Earth Science and Technology

IFREE : Institute for Research on Earth Evolution

ESC : Earth Simulator Center

3. Collaboration Projects

Collaboration Projects in FY 2009

<ul style="list-style-type: none">• Institut Français de Recherche pour l'Exploitation de la Mer, France
<ul style="list-style-type: none">• Département d'Océanographie Physique et Spatiale, France
<ul style="list-style-type: none">• Ernest Orlando Lawrence Berkeley National Laboratory, USA
<ul style="list-style-type: none">• Korean Ocean Research & Development Institute, Korea
<ul style="list-style-type: none">• The National Oceanography Centre, Southampton, UK
<ul style="list-style-type: none">• The large-scale numerical simulation of the weather/oceanographic phenomena for international maritime transportation : Kobe University
<ul style="list-style-type: none">• Research and development for MSSG calculation performance optimization in the next-generation supercomputer system : RIKEN
<ul style="list-style-type: none">• Simulation of urban climate change : Building Research Institute
<ul style="list-style-type: none">• Collaborative research on the sophistication of the computational simulation software toward constructing the platform for the leading industrial research and development : Institute of Industrial Science, the University of Tokyo
<ul style="list-style-type: none">• Numerical study on rheophysical behavior of viscoelastic fluids and their mechanisms using Digital Ink Laboratory (DIL) System : DNP Fine Chemicals Fukushima Co., Ltd

4. System Configuration of the Earth Simulator

The Earth Simulator

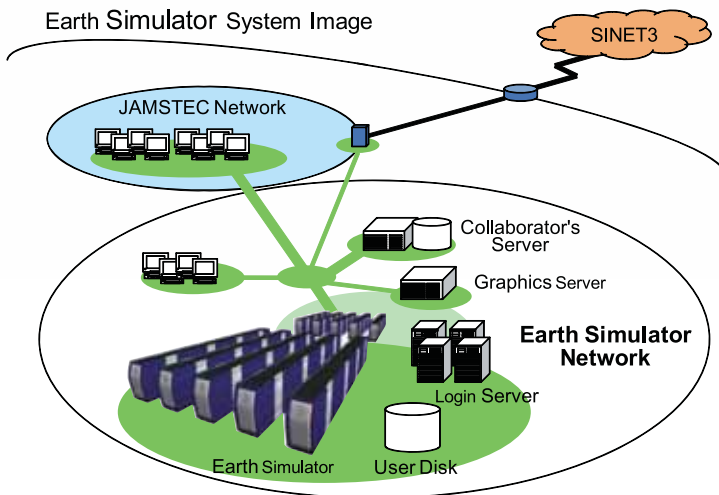
- New Earth Simulator System of Ultra High-speed Vector Parallel Super Computer -

The Earth Simulator is the upgraded system of the previous Earth Simulator, which has significantly contributed to the development of a simulation culture in the area of earth science and related technical fields, and introduces new features to bring accurate and high-speed analysis and

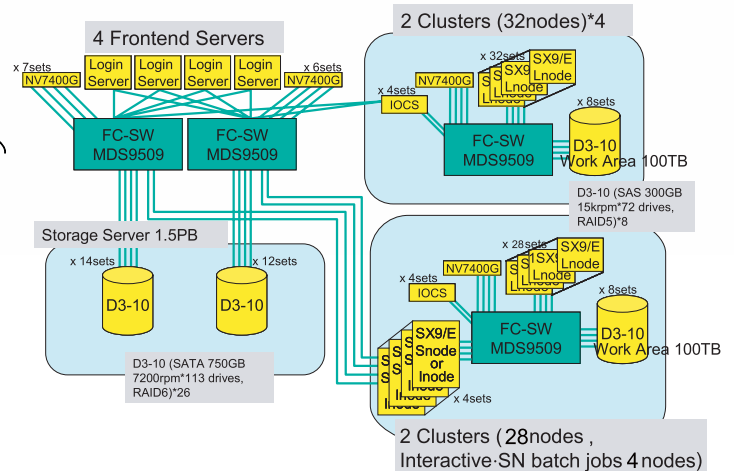
projections of global-scale environmental phenomena. The ES is also used to produce numerical simulations for advanced research fields that are beyond the scope of other computing systems.



ES System Outline



Storage System



Features of the Earth Simulator for operation and control

- (1) Clustering of nodes to control the system (transparent for users) .
A cluster consists of 32 nodes.
Most of them are for batch jobs (batch clusters).
- (2) Providing special nodes for TSS and small batch jobs.
- (3) Configuration of the TSS cluster.
 1. TSS nodes [2 nodes],
 2. Nodes for SN (Single Node) batch jobs [2 nodes],
- (4) Configuration of the batch cluster.
 1. Nodes for MN (Multi-Nodes) batch jobs,
 2. System disks for user-file staging,
- (5) Storage of user files for batch jobs on a mass-storage system.
Automated file recall (Stage-In) and migration (Stage-Out).
- (6) Connection of all the clusters to a mass-storage system

Real Applications Benchmark Performance

Application	ES (# of CPUs)	New ES (# of CPUs)	Speed up
PHASE	135.3 sec (4096)	62.2 sec (1024)	2.18
NICAM-K	214.7 sec (2560)	109.3 sec (640)	1.97
MSSG	173.9 sec (4096)	86.5 sec (1024)	2.01
SpecFEM3D	96.3 sec (4056)	45.5 sec (1014)	2.12
Seism3D	48.8 sec (4096)	15.6 sec (1024)	3.13

Harmonic Mean of Speed up Ratio : 2.22

 **Earth Simulator Research Projects** 

Chapter 1

■ Earth Science ■

Understanding Roles of Oceanic Fine Structures in Climate and Its Variability

Project Representative

Wataru Ohfuchi

Earth Simulator Center, Japan Agency for Marine-Earth Science and Technology

Authors

Wataru Ohfuchi^{*1}, Nobumasa Komori^{*1}, Bunmei Taguchi^{*1}, Akira Kuwano-Yoshida^{*1},
Masami Nonaka^{*2}, Mayumi K. Yoshioka^{*3} and Hidenori Aiki^{*2}

*1 Earth Simulator Center, Japan Agency for Marine-Earth Science and Technology

*2 Research Institute for Global Change, Japan Agency for Marine-Earth Science and Technology

*3 Hydrospheric Atmospheric Research Center, Nagoya University

We have conducted high-resolution simulations with primitive equation or non-hydrostatic atmospheric, oceanic and coupled models in order to understand mechanisms of variations of the atmosphere–ocean system with relatively small spatial scales in the oceanic part. We report in this paper decadal variations in the North Pacific, Kuroshio Extension Current fluctuations, sea-ice variations in the Arctic Sea, and typhoon development.

Keywords: atmosphere–ocean interaction, sea surface temperature front, oceanic Rossby wave, sea ice variability, typhoon development

1. Introduction

In this project, high-resolution simulations are conducted using primitive equation or non-hydrostatic models of atmosphere, ocean and coupled atmosphere–ocean systems to investigate roles of oceanic fine structures in climate and its variability. This project is mainly composed of four topics: 1. Effects of oceanic fine structures to global circulations; 2. Scale interactions in the ocean; 3. Responses of large-scale atmospheric circulation to ocean and sea-ice variability; 4. Mechanisms of typhoon genesis and development under interactions with the ocean. This report summarizes the achievements made in the fiscal year 2009.

2. Effects of oceanic fine structures to global atmospheric and oceanic circulations

We conducted relatively long-term simulations with two different horizontal resolutions using the latest version of CFES (Coupled model for the Earth Simulator) [1], which has many improvements from the previous one [2, 3] such as a new large-scale condensation scheme in AFES (Atmospheric model for the Earth Simulator) for better representation of low-level clouds [4]. The higher resolution version, called “CFES standard,” has the resolutions of T239 (about 50 km) and L48 for the atmosphere and 0.25° (about 25 km) and 54 levels for the ocean. The lower resolution version, called “CFES mini,” has half the horizontal resolution of CFES standard and will be used for centennial-

scale and ensemble simulations.

By the end of FY2008, 23-years of integration with CFES standard was completed. With its high-resolution that permits eddies in the oceanic component, CFES standard simulates frontal structures and their variability in the mid-latitude western boundary currents in a realistic manner. In addition, since its atmospheric component is fine enough to resolve local orography and boundary-layer response to ocean surface structures including meandering fronts and mesoscale eddies, these oceanic fine-scale signatures are clearly reflected in the surface atmospheric fields as revealed by high-resolution satellite observations.

Evidence emerges that sea surface temperature (SST) gradients associated with the mid-latitude western boundary currents exert deep and large-scale influences on the mean state of the atmosphere beyond local responses in the marine atmospheric boundary layer [3, 5, 6, 7]. However, it remains to be investigated whether slow oceanic frontal variability may affect time-varying atmospheric state and contribute to enhance the low-frequency variance in the mid-latitude climate.

To investigate North Pacific decadal SST anomalies and their atmospheric influence as well as other climate variability, CFES mini has been integrated for 120 years. This century-long coupled simulation represents a sharp mean SST front in the North Pacific subarctic frontal zone (SAFZ; Fig. 1b). Pronounced decadal SST variations are confined within SAFZ

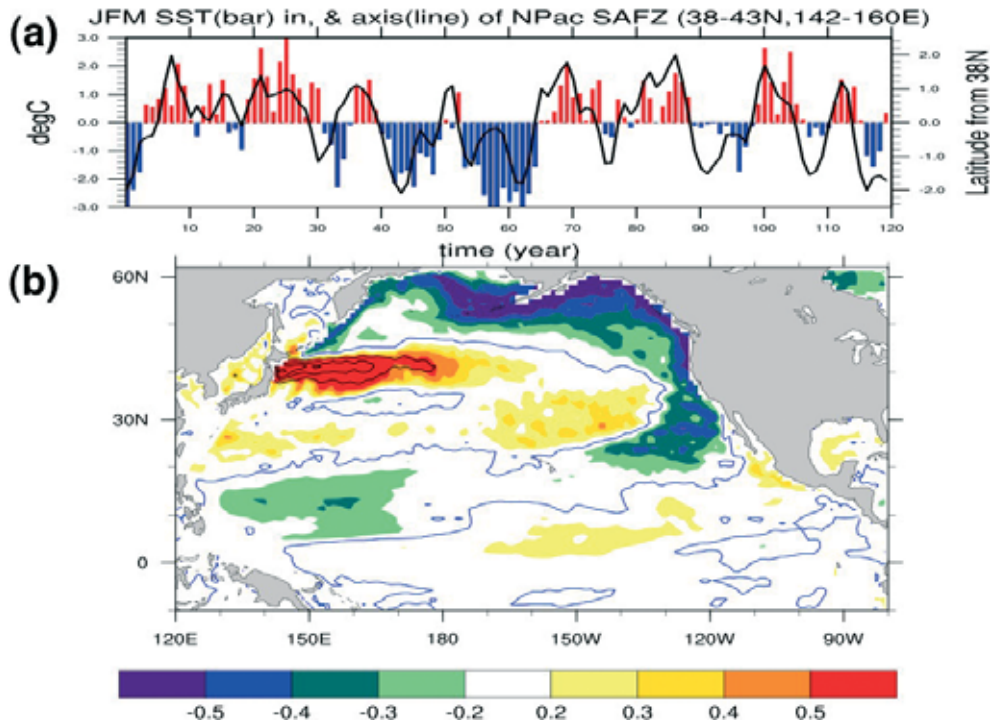


Fig. 1 Wintertime North Pacific decadal SST variability simulated in CFES mini. (a) Time series of wintertime SST anomalies averaged over the subarctic frontal zone (SAFZ; color bar) and meridional migration of the axis of the subarctic front (black line). (b) Correlation (color) and regression (contour; interval is 0.5K per one standard deviation of the reference time series) map of SST field associated with the decadal-scale SST anomalies latitudinally confined to SAFZ.

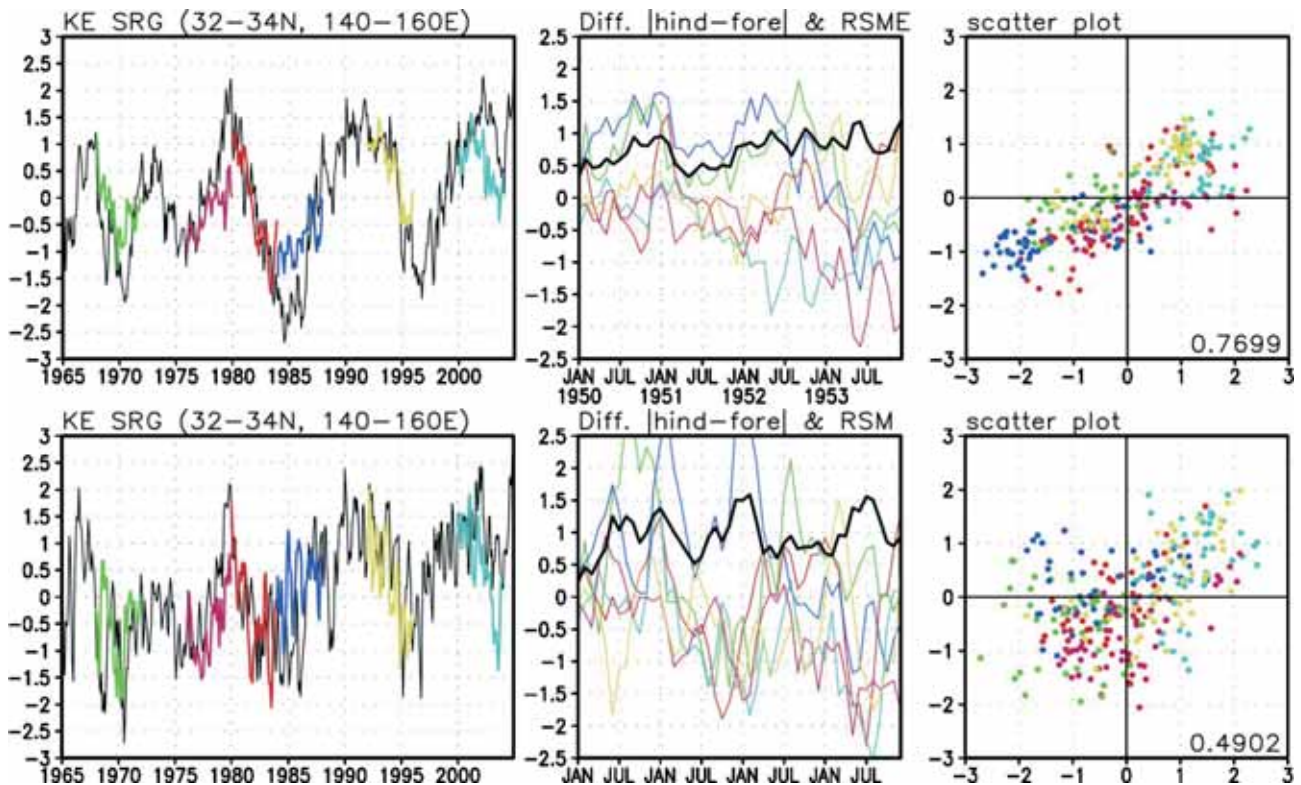


Fig. 2 (Left) Time series of area mean sea surface height anomalies (SSHAs) in (32–34N, 140–160E) in the OFES hindcast (black) and forecast (colors) integrations, (middle) their differences, and (right) their scatter plot in the overlapping periods. In the middle panel, thick black curve indicates root-mean-square of the differences. Number in the right panel shows the corresponding correlation coefficient. Upper panels are for broad-scale SSHAs applied 5-degree longitude and latitude running mean, and lower panels are for unfiltered SSHAs. SSHAs are standardized by their standard deviations in the hindcast integration.

and are well correlated with meridional migration of the front (Fig. 1a), a feature consistent with recent high-resolution OGCM studies that highlight the importance of oceanic frontal variability in generating decadal SST anomalies. Associated with the latitudinally confined SST anomalies, simulated atmospheric storm track in the North Pacific is systematically modulated as it is anchored by near-surface baroclinicity that changes in accordance with the SAFZ variations (not shown). When the SST anomalies are positive, the storm track is shifted northward, which induces anti-cyclonic surface mean flow feedback in subpolar central Pacific. The weakened Aleutian low suppresses southward-flowing Oyashio current off Japan coast, and causes northward migration of SAFZ, which in turn reinforces the initial SST anomalies. These results suggest a positive feedback between the SST anomalies and the associated atmospheric response, which could contribute to persistence of the Pacific decadal SST anomalies.

3. Scale interactions in the ocean

Previous studies have suggested importance of Rossby wave propagation for Kuroshio Extension (KE) Current variations. Then, to investigate if KE Current decadal variations

are predictable through Rossby wave propagation, we have conducted six four-year forecast experiments with OFES (Ocean model for the Earth Simulator) driven by long-year mean atmospheric field that does not include information of the ‘future’. In each case, the corresponding field in the OFES hindcast integration is given as initial condition, and anomalies in the initial condition propagate westward as Rossby waves, providing predictability for several years. Note that the hindcast integration is driven by atmospheric forcing which includes information of the ‘future’.

In Fig. 2, we examined predictability of sea surface height (SSH) variations to the south of the KE region, which is important to induce variations in the KE Current. In the region, time series of the broad-scale SSH anomalies (SSHAs) in the hindcast is well followed by those in the forecast integrations and their correlation is 0.77 (upper panels), consistent with Schneider and Millers' results [8]. Also, their root mean square difference is almost less than one standard deviation for four years. In the lower panels, it is found that unfiltered SSHAs including frontal-scale variations also follow the hindcast and their correlation is about 0.5, implying some predictability for frontal-scale KE Current variations. Indeed, in some forecast

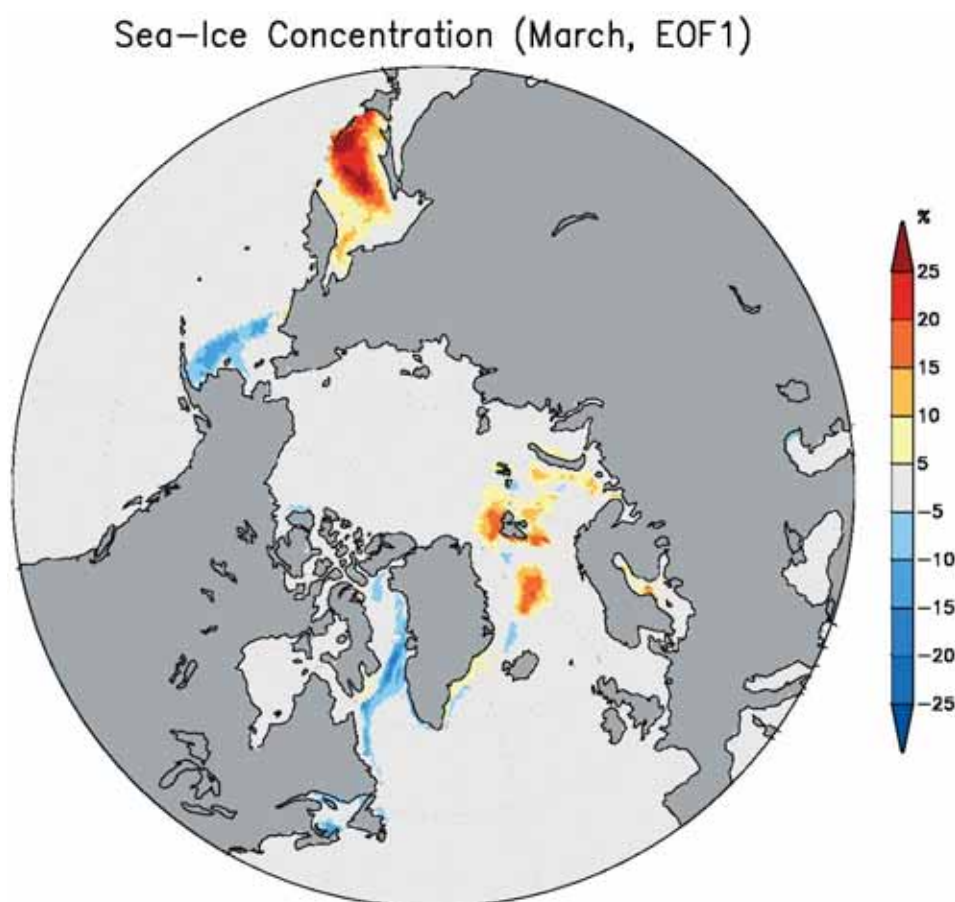


Fig. 3 First EOF of March sea-ice concentration over the Northern Hemisphere for the first through 23rd model year of a coupled atmosphere–ocean simulation with a high-resolution version of CFES (“CFES standard”).

integrations, variations in the KE Current jet found in the hindcast are fairly reproduced (not shown).

4. Responses of large-scale atmospheric circulation to ocean and sea-ice variability

Kuwano-Yoshida *et al.* [7] investigate the precipitation response to the SST front associated with the Gulf Stream using AFES simulations forced by observed and smoothed SST data. A convective rain band over the Gulf Stream in the observed SST run disappears in the smooth SST run, and the heights of cumulus convection and updrafts depend on seasonality of atmospheric vertical stability. Sampe *et al.* [6] conduct idealized “aquaplanet” experiments using AFES with zonally uniform SST. The transient eddy activity in each of the winter and summer hemispheres is organized into a deep storm track along the SST front with an enhanced low-level baroclinic growth of eddies. It is suggested that the potential importance of midlatitude atmosphere–ocean interaction in shaping the tropospheric general circulation.

Previous studies [e.g., 9, 10] identified a double-dipole pattern of wintertime sea-ice variability over the Northern Hemisphere from satellite observations, which is composed of one dipole between the Labrador Sea and the Nordic (Greenland, Barents, and Kara) Seas and the other between the Bering Sea and the Okhotsk Sea, and revealed its close link to anomalous

atmospheric circulation such as North Atlantic Oscillation. Figure 3 shows the first EOF of March sea-ice concentration over the Northern Hemisphere in CFES standard for the first through 23rd model year, and the double-dipole pattern is realistically reproduced. Detailed analysis of this phenomenon as simulated in CFES standard is under way, and a working hypothesis on its mechanism will be verified through some numerical experiments with AFES.

5. Mechanisms of typhoon genesis and development under interactions with the ocean

A three-dimensional atmosphere–ocean regional coupled model has been developed to simulate non-hydrostatic meteorological and oceanic phenomena. Two well-developed parallel models on the Earth Simulator are employed: CReSS [Cloud Resolving Storm Simulator, 11] is for the atmosphere part and NHOES [Non-Hydrostatic Ocean model for the Earth Simulator, 12] is for the ocean part. MPI decomposition of CReSS–NHOES is utilized for inter-node communications. One MPI sub-domain of a process is applied for one horizontal region of CReSS and NHOES. Intra-node parallelization is also employed with OpenMP for CReSS and microtask for NHOES.

Three experiments are conducted. Two experiments are CReSS-only simulations and the other is a CReSS–NHOES coupled simulation of T0505 (HAITANG) that landed on China

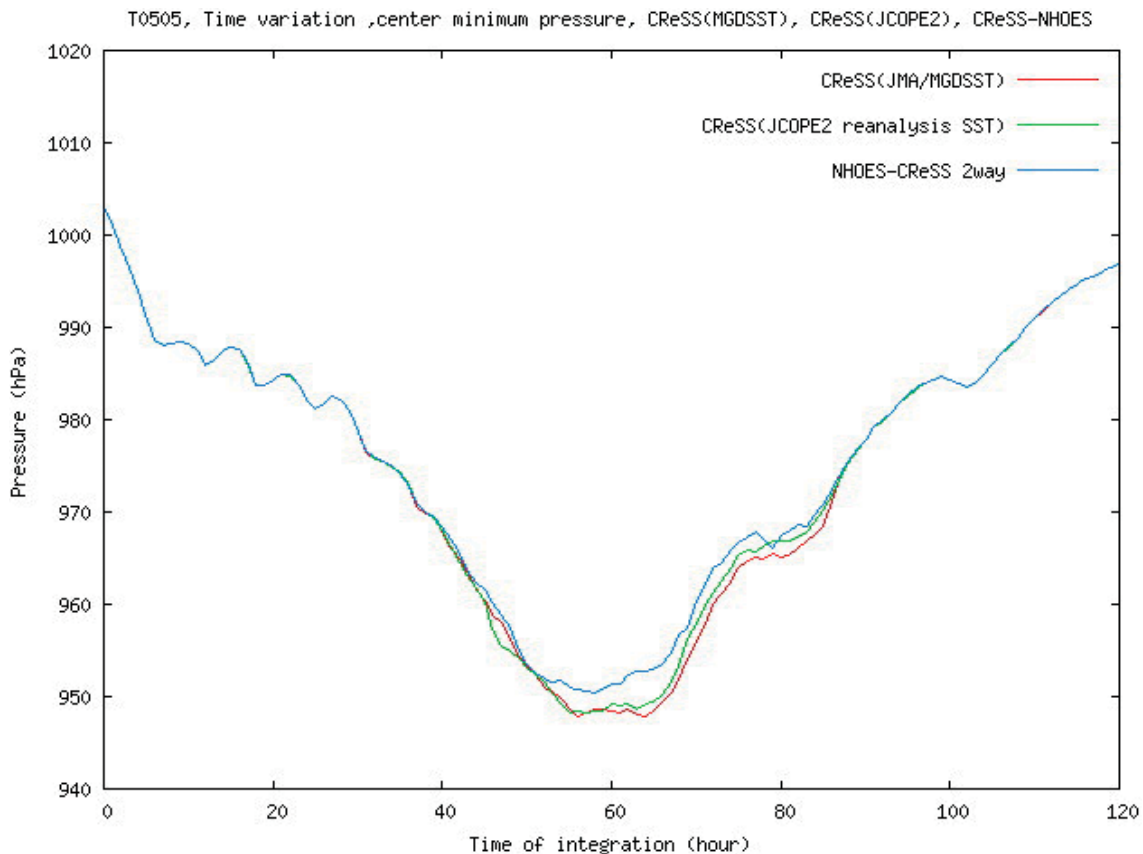


Fig. 4 Time variation of the central minimum pressure in T0505 on the sea level, during the first 5 days. The calculation was started from 00Z, on September 15, in 2005.

coast after passing the Taiwan Island during the active period as a typhoon. The CReSS-only model system has a vertically one-dimensional slab-ocean model. The JMA/RANAL dataset is utilized for the initial and lateral conditions for the atmosphere in the three experiments. The CReSS-NHOES coupled simulation utilizes the JCOPE2 reanalysis for the initial and lateral conditions of the ocean. The two CReSS-

only experiments use JCOPE2 or JMA/MGDSST for the initial condition. The horizontal resolutions were 4 km in CReSS and 1 km in NHOES. The vertical resolution of the ocean was from 2 m near the surface. The numerical simulations were performed for 15 days with 4 nodes on the Earth Simulator.

Remarkable differences resulting from air-sea interaction are shown in the comparison of the experiments with successfully

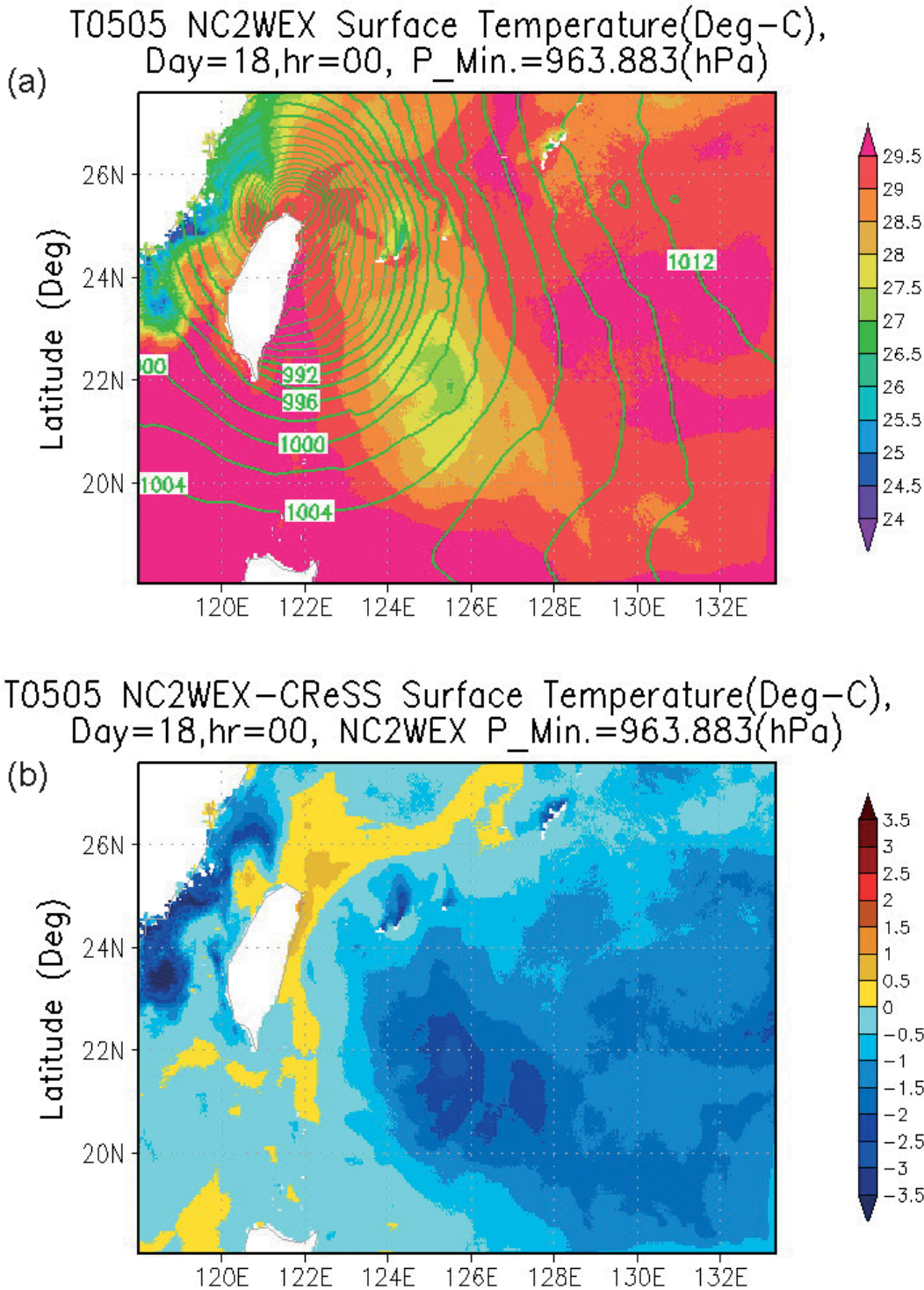


Fig. 5 SST distribution and the anomaly after 72 hours integration. (a) SST distribution (colors) and the sea level pressure (contours) in the CReSS-NHOES experiment, (b) SST anomalies of the coupled experiment to the non-coupling experiment.

simulating typical structures of T0505. In the mature stage of T0505, the central minimum pressure of the typhoon is suppressed by 5 hPa in the CReSS–NHOES coupled simulation, compared to that in the non-coupled experiments (Fig. 4). It is found in the coupled experiment that cooler SST region appeared and lasted in the southeast of T0505 after passing over the Philippine Sea (Fig. 5).

6. Concluding remarks

We briefly reported simulation results of primitive equation or non-hydrostatic atmosphere, ocean and coupled models to investigate roles of oceanic fine structures in climate and its variability. Long-term integrations using CFES at two resolutions reveals pronounced decadal variations of atmosphere and ocean in the North Pacific and sea ice in the Arctic Sea. OFES experiments are conducted to investigate predictability of Kuroshio Extension Current variations through Rossby wave propagation. Roles of atmosphere–ocean interaction in typhoon development are investigated by CReSS–NHOES simulations.

References

- [1] Komori, N., B. Taguchi, A. Kuwano-Yoshida, H. Sasaki, T. Enomoto, M. Nonaka, Y. Sasai, M. Honda, K. Takaya, A. Ishida, Y. Masumoto, W. Ohfuchi, and H. Nakamura, “A high-resolution simulation of the global coupled atmosphere–ocean system using CFES: 23-year surface climatology”, *Ocean Dyn.*, under revision.
- [2] Komori, N., A. Kuwano-Yoshida, T. Enomoto, H. Sasaki, and W. Ohfuchi, “High-resolution simulation of the global coupled atmosphere–ocean system: Description and preliminary outcomes of CFES (CGCM for the Earth Simulator)”, in *High Resolution Numerical Modelling of the Atmosphere and Ocean*, K. Hamilton and W. Ohfuchi (eds.), chap. 14, pp. 241–260, Springer, 2008.
- [3] Nonaka, M., H. Nakamura, B. Taguchi, N. Komori, A. Kuwano-Yoshida, and K. Takaya, “Air–sea heat exchanges characteristic of a prominent midlatitude oceanic front in the South Indian Ocean as simulated in a high-resolution coupled GCM”, *J. Climate*, **22** (24), 6515–6535, 2009.
- [4] Kuwano-Yoshida, A., T. Enomoto, and W. Ohfuchi, “An improved PDF cloud scheme for climate simulations”, *Quart. J. Roy. Meteor. Soc.*, accepted.
- [5] Taguchi, B., H. Nakamura, M. Nonaka, and S.-P. Xie, “Influences of the Kuroshio/Oyashio Extensions on air–sea heat exchanges and storm-track activity as revealed in regional atmospheric model simulations for the 2003/4 cold season”, *J. Climate*, **22** (24), 6536–6560, 2009.
- [6] Sampe, T., H. Nakamura, A. Goto, and W. Ohfuchi, “Significance of a midlatitude SST frontal zone in the formation of a storm track and an eddy-driven westerly jet”, *J. Climate*, **23** (7), 1793–1814, 2010.
- [7] Kuwano-Yoshida, A., S. Minobe, and S.-P. Xie, “Precipitation response to the Gulf Stream in an atmospheric GCM”, *J. Climate*, **23** (13), 3676–3698, 2010.
- [8] Schneider, N., and A. J. Miller, “Predicting western North Pacific Ocean climate”, *J. Climate*, **14** (20), 3997–4002, 2001.
- [9] Yamamoto, K., Y. Tachibana, M. Honda, and J. Ukita, “Intra-seasonal relationship between the Northern Hemisphere sea ice variability and the North Atlantic Oscillation”, *Geophys. Res. Lett.*, **33**, L14711, 2006.
- [10] Ukita, J., M. Honda, H. Nakamura, Y. Tachibana, D. J. Cavalieri, C. L. Parkinson, H. Koide, and K. Yamamoto, “Northern Hemisphere sea ice variability: lag structure and its implications”, *Tellus*, **59A**, 261–272, 2007.
- [11] Tsuboki, K., and A. Sakakibara, “Large-scale parallel computing of Cloud Resolving Storm Simulator”, in *High Performance Computing*, H. P. Zima, K. Joe, M. Sato, Y. Seo and M. Shimasaki (eds), Springer, 243–259, 2002.
- [12] Aiki, H., K. Takahashi, and T. Yamagata, “The Red Sea outflow regulated by the Indian monsoon”, *Cont. Shelf Res.*, **26** (12-13), 1448–1468, 2006.

海洋微細構造が生み出す気候形成・変動メカニズムの解明

プロジェクト責任者

大淵 濟 海洋研究開発機構 地球シミュレータセンター

著者

大淵 濟^{*1}, 小守 信正^{*1}, 田口 文明^{*1}, 吉田 聡^{*1}, 野中 正見^{*2}, 吉岡真由美^{*3}, 相木 秀則^{*2}

*1 海洋研究開発機構 地球シミュレータセンター

*2 海洋研究開発機構 地球環境変動領域

*3 名古屋大学 地球水循環研究センター

非静水圧と静水圧の大気、海洋、結合モデルを用いて高解像度シミュレーションを行い、比較的細かい空間スケールの海洋変動を伴う大気海洋システムの変動のメカニズムの解明を試みた。この論文では、北太平洋の十年スケール変動、黒潮続流域変動、北極海の海水変動、台風の発達について報告を行う。

キーワード: 大気海洋相互作用, 海面水温前線, 海洋ロスビー波, 海水変動, 台風の発達

Simulations of Adaptation-Oriented Strategy for Climate Variability

Project Representative

Keiko Takahashi

Earth Simulator Center, Japan Agency for Marine-Earth Science and Technology

Authors

Keiko Takahashi^{*1}, Ryo Ohnishi^{*1}, Takeshi Sugimura^{*1}, Yuya Baba^{*1}, Shinichiro Kida^{*1}, Koji Goto^{*2} and Hiromitsu Fuchigami^{*3}

*1 Earth Simulator Center, Japan Agency for Marine-Earth Science and Technology

*2 NEC Corporation

*3 NEC Informatec Systems LTD

A coupled atmosphere-ocean-land model MSSG has been developed in the Earth Simulator Center, which is designed to model multi-scale interactions among the atmosphere, the ocean and the coupled system. In this project of this fiscal year, we focused on introducing computational optimization architecture to the MSSG to be run with maximizing the computational power of the Earth Simulator 2. As the results, the computational performance of MSSG attained about 20% of the theoretical peak of ES2. Characteristics of cloud micro-physics with turbulence effects and heat transfer in urban area are presented and non-hydrostatic physical performance for the oceanic component of MSSG are validated in this report.

Keywords: Coupled atmosphere-ocean model, multi-scale, multi-physics, high performance computing, the Earth Simulator

1. Introduction

Multi-Scale Simulator for the Geoenvironment (MSSG), which is a coupled atmosphere-ocean-land global circulation model, has been developed for the purposed of promoting multi-scale multi-physics simulations for predicting weather or climate variabilities. Furthermore, MSSG is optimized to be run on the Earth Simulator with high computational performance and it is designed to be flexibility for different space and time scales. MSSG can simulate various scales phenomena with several different optional versions such as global/regional MSSG-A, global/regional MSSG-O, or global/regional MSSG, where MSSG-A and MSSG-O are atmospheric and oceanic components of MSSG, respectively.

In the development of MSSG of this fiscal year, we focus on the following issues,

- Improvement of MSSG computational performance on the Earth Simulator 2 (ES2) to be fit the discretization schemes for ultra high resolution simulation to the architecture of ES2,
- Improvement of physical performance of atmospheric boundary layer and cloud micro physics with turbulent scale effects, and
- Improvement of forecasting schemes and validate results of multi-scale simulations.

This report summarizes results of our project in FY2009.

2. MSSG model configuration

An atmospheric component of MSSG, which we call it MSSG-A, is a non-hydrostatic global/regional atmosphere circulation model. MSSG-A is compromised of fully compressive flux form of Satomura (2003)^[1], Smagorinsky-Lilly type parameterizations by Lilly (1962)^[2] and Smagorinsky (1965)^[3] for sub-grid scale mixing, surface fluxes by Zhang

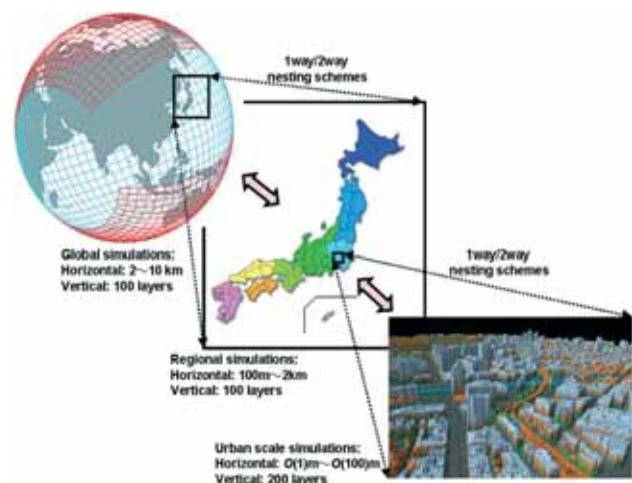


Fig. 1 Scales of MSSG for global/regional models with nesting schemes and resolution.

(1982)^[4] and Blackadar (1979)^[21], cloud microphysics with mixed phases by Reisner (1998)^[5] and cumulus convective processes by Kain (1993)^[6] and Fritsch (1980)^[7]. Cloud-radiation scheme for long wave and shortwave interactions with both explicit cloud and clear-air are adopted which is based on the scheme in MM5. Over land, the ground temperature and ground moisture are computed by using a bucket model. As upper boundary condition, Rayleigh friction layer is set.

In the ocean component, which we call it MSSG-O, incompressible and hydrostatic /nonhydrostatic equations with the Boussinesq approximation are introduced based on describing in Marshall (1997a) and Marshall (1997b). Smagorinsky type scheme by Lilly (1962) and Smagorinsky (1965) is used for the sub-grid scale mixing. Algebraic Multi-Grid (AMG) method in Stuben (1999) is used in order to solve a Poisson equation in MSSG-O. In MSSG, we used the AMG library based on aggregation-type AMG in Davies (1976), which has been developed by Fuji Research Institute Corporation.

In both the atmospheric and ocean components, Yin-Yang grid system presented in Kageyama (2004) and Arakawa C grid is used. The atmospheric component utilizes the terrain following vertical coordinate with Lorenz type variables distribution in Gal-Chen (1975). The ocean component uses the z-coordinate system for the vertical direction. In discretization of time, the 2nd, 3rd and 4th Runge-Kutta schemes and leap-frog schemes with Robert-Asselin time filter are available. The 3rd Runge-Kutta scheme presented in Wicker (2002) is adopted for the atmosphere component. In the ocean component, leap-frog schemes with Robert-Asselin time filter is used for the ocean component. For momentum and tracer advection computations, several discretization schemes introduced in Peng (2004) are available. In this study, the 5th order upwind scheme is used for the atmosphere and central difference is utilized in the ocean component. The vertical speed of sound in the atmosphere is dominant comparing with horizontal speed, because vertical discretization is tend to be finer than horizontal discretization.

From those reasons, horizontally explicit vertical implicit (HEVI) scheme in Durran (1991)^[15] is adopted in MSSG-A.

Conservation scheme was discussed in Peng (2006)^[16] and no side effects of over lapped grid system such as Yin-Yang grid were presented due to validations results of various benchmark experiments in Takahashi (2004a,b)^{[17] [18]} and Takahashi (2005)^[19].

3. High performance computing in MSSG

ES2 has different architecture with points of memory latency, memory band width and penalty of bank complicit. Considered those characteristics of the architecture of ES2, MSSG is required to be improved computational performance by optimizing on the ES2.

Table 1 shows computational performance statistics of main modules of MSSG on ES2. 18GFLOPS per one CPU of ES2 has attained and is estimated by about 20% of the theoretical peak of ES2. In near future, especially, we are planning to optimize the performance of cloud micro physics processes using Assignable Data Buffer (ADB) architecture of ES2.

4. Physical performance improvements in MSSG

In this report, present several topics results on key issues in order to execute weather/climate seamless simulations/forecasting with MSSG.

4.1 Impacts of turbulence in clouds and validation results of cloud micro-physics in MSSG

There is a growing consensus that the collision growth rate of cloud droplets can be increased by cloud turbulence. We have investigated the turbulence impacts in turbulent convective clouds using the hybrid-bin method with our turbulent collision model in MSSG (MSSG-Bin model). In MSSG-Bin model, two kinds of convective clouds have been simulated; free (heat) convective clouds and forced (orographic) convective clouds. Preliminary results show that the turbulent collisions cause

Table 1 MSSG current status of computational performance on ES2.

EXCLUSIVE TIME [sec]	%	MFLOPS	V.OP RATIO	AVER. V.LEN	I-CACHE MISS	O-CACHE MISS	BANK CONFLICT		PROC. NAME
							CPU PORT	NETWORK	
19777.543	99.7	18592.9	99.54	236.1	256.595	772.348	262.653	6554.572	(A1) main loop
4479.512	22.6	22277.2	99.51	239.2	90.681	198.871	74.955	1697.248	(A2) N-S HEVI
2632.633	13.3	24765.7	99.50	238.7	26.207	71.759	52.430	821.099	(A2) N-S eq.(large)
4649.974	23.4	34140.6	99.80	238.7	16.851	60.720	20.966	566.511	(A2) tracer eq.
3996.377	20.1	7798.0	99.20	213.7	87.334	272.048	57.238	1878.027	(A2) physics
285.278	1.4	1471.8	99.36	230.4	8.858	15.927	10.138	198.995	(A2) boundary
596.373	3.0	584.6	99.40	224.2	5.130	8.725	13.396	445.971	(A2) boundary (side)
235.785	1.2	6361.6	99.11	239.6	0.385	1.991	5.099	93.416	(A2) z2ps
1073.107	5.4	305.1	81.38	172.9	1.550	3.569	1.977	218.644	(A2) output
130.365	0.7	23363.6	99.42	238.4	0.399	1.103	22.172	65.026	(A2) RKG
504.566	2.5	646.3	98.62	239.8	0.295	0.326	0.012	352.960	(A2) diagno
448.958	2.3	13480.8	99.24	227.6	16.439	33.263	4.128	192.399	(A2) subfield
734.071	3.7	1083.8	79.70	236.7	0.406	99.532	0.134	23.240	(A2) recalc dt
0.317	0.0	2.1	90.13	236.1	0.037	0.091	0.001	0.013	(A2) restart

significant changes on the droplet size spectra.

Fig. 2 shows surface precipitation distribution in time with MSSG-Bin model. It shows the discrepancy of the distribution and turbulent collision model reveals the impact with increasing

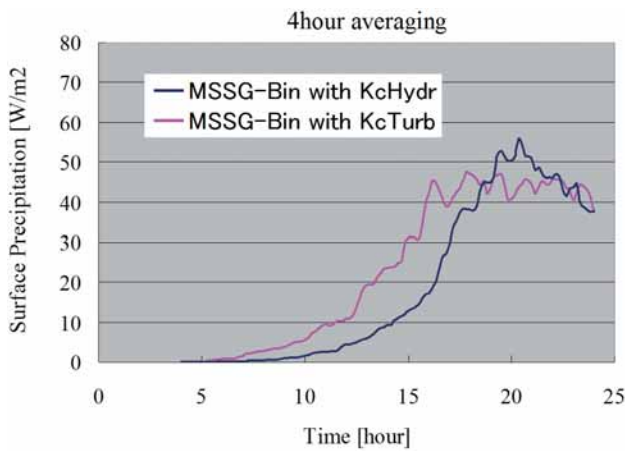


Fig. 2 Impacts of surface precipitation distribution during development of cloud.

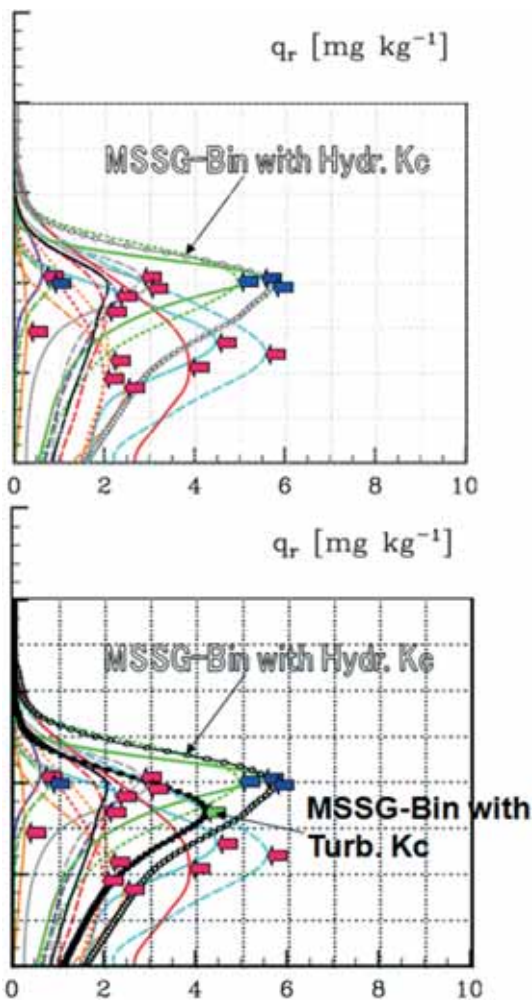


Fig. 3 Turbulent collisions impacts of precipitation throughout RICO mode comparison. Above: without the effects of turbulence. Below: with effects of turbulence collision.

of the volume of precipitation by the effect of turbulent droplet collisions in cloud development.

As the results of experiments in RICO (shallow Cu) case, turbulent collisions significantly weaken the updraft, consequently decrease turbulence intensity due to quick removal of water, make be lower the cloud height and shorten the rain initiation time. Fig. 3 presents a part of the results of experiments.

4.2 Advanced scheme to simulate weather/climate in urban area

High performance solver for fully compressible fluid is applied to atmospheric flow field in MSSG to resolve and understand mechanism of heat transfer in urban canyon.

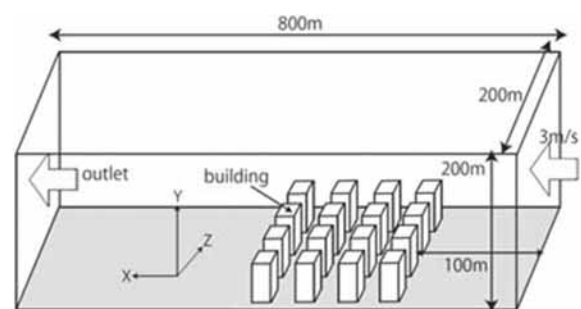


Fig. 4 Schematic view of canyon case.

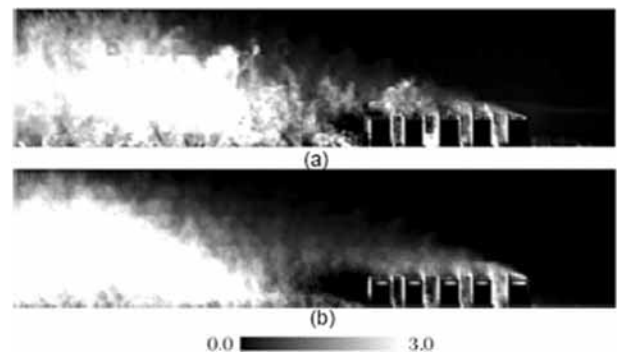


Fig. 5 Time averaged vertical heat flux distributions, (a) with Boussinesq approximation (BS), and (b) with fully compressive formulation (CP).

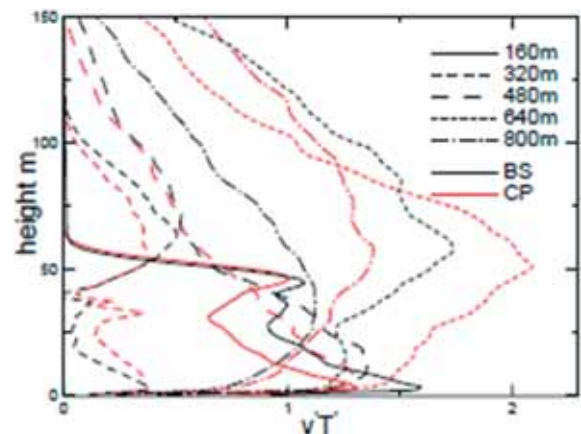


Fig. 6 Vertical heat flux profiles in four stream wise points.

Implementation of efficiency and applicability of the fully compressible formulation is investigated in the atmospheric boundary layer with simplified buildings (Fig. 4). Simulations with conventional scheme using Boussinesq approximation are also performed under the same condition to validate differences and shortcomings of the incompressible solver. As the results from the experiments, vertical heat flux is tend to increase at the vicinity of the ground, which is induced by fluid expansion. Incompressible solver overestimates turbulence intensity while fully compressible solver can capture the effect of turbulence suppression due to the increase of kinematic viscosity as caused from heat transfer as shown in Fig. 5 and Fig. 6. This suggests that fully compressible formulation is required to represent the mechanism of heat transfer in urban area.

4.3 Validation of physical performance of MSSG-O

MSSG-O model which is an oceanic component of MSSG is developed to simulate oceanic flows on various spacial and time

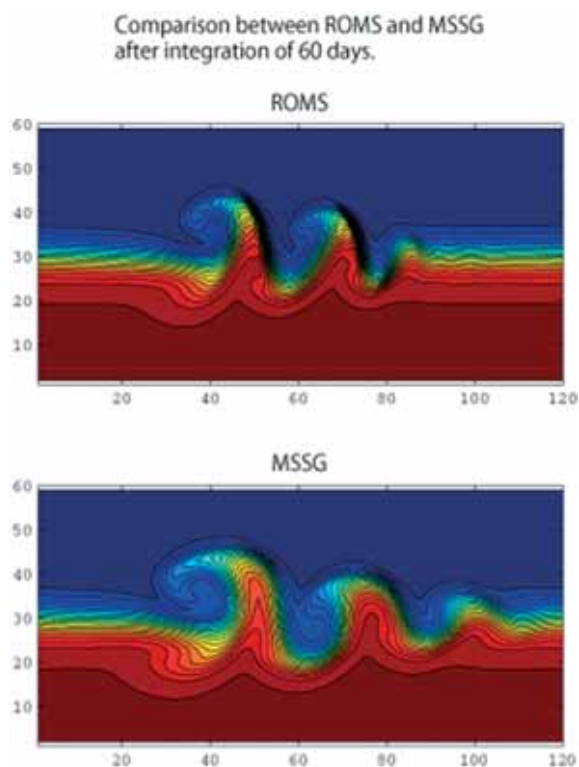


Fig. 7 Development of disturbance of sea surface temperature.

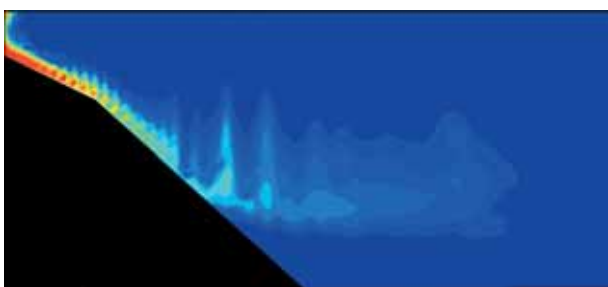


Fig. 8 Development of Dynamics of turbulent bottom gravity currents in MSSG-O.

scales with numerical stability and reasonable precision. For this fiscal year, various idealized model validation experiments were pursued to examine the capability of the model. One of validation plan was focusing on "Non-hydrostatic term" and the validation results are introduced in this report.

Non-hydrostatic capability of MSSG-O is tested by simulating dense overflows around Antarctic. To test the feature in presence of wind-driven circulation, we examined the interaction of overflow and the wind-driven coastal current. MSSG-O simulations results suggest that coastal currents can modify the pressure gradient of the overflow and change the strength of water mass exchange between the open ocean and the marginal sea. Past non-hydrostatic model studies have focused on simulating single oceanic process. Our model simulation is new that it now includes interaction of two processes (wind-driven circulation and overflow).

Figs. 7 and 8 are validation results of MSSG-O, which is set up with non-hydrostatic term. Fig. 6 shows development of disturbances in MSSG-O which are comparable to previous results^[22]. Fig. 8 represents bottom gravity current and K-H instabilities^{[23][24]} above the bottom in the ocean.

5. Near future work

In this report, we showed computational performance of MSSG and advances of model development. At the same time, we now begin forecasting of weather/climate in urban area under the condition of climate variability. It will be further clear that interaction process between weather and climate as previous studies pointed out. Detail analysis is required for each scale phenomena in order to understand those mechanics. In addition, implementation of dynamic AMR (adaptive mesh refinement) schemes on MSSG has been almost completed. Multi-scale and multi-physics simulations with MSSG will be begun in order to predict climate variability in near future.

References

- [1] Satomura, T. and Akiba, S., 2003: Development of high- precision nonhydrostatic atmospheric model (1): Governing equations, *Annals of Disas. Prev. Res. Inst.*, Kyoto Univ., 46B, 331-336.
- [2] Lilly, D. K., 1962: On the numerical simulation of buoyant convection, *Tellus*, 14, 148-172.
- [3] Smagorinsky, J. , Manabe, S. and Holloway, J. L. Jr., 1965: Numerical results from a nine level general circulation model of the atmosphere, *Monthly Weather Review*, 93, 727-768.
- [4] Zhang, D. and Anthes, R. A., 1982: A High-Resolution Model of the Planetary Boundary Layer - Sensitivity Tests and Comparisons with SESAME-79 Data, *Journal of Applied Meteorology*, 21, 1594-1609.
- [5] Reisner, J., Ramussen R. J., and Bruinjtjes, R. T., 1998: Explicit forecasting of supercooled liquid water in winter

- storms using the MM5 mesoscale model, *Quart. J. Roy. Meteor. Soc.* 124, 1071-1107.
- [6] Kain, J. S. and Fritsch, J. M., 1993: Convective parameterization for mesoscale models: The Kain-Fritsch Scheme, *The Representation of Cumulus Convection in Numerical Models of the Atmosphere, Meteor. Monogr.*, 46, Amer. Meteor. Soc., 165-170.
- [7] Fritsch, J. M., and Chappell, C. F., 1980: Numerical prediction of convectively driven mesoscale pressure systems, Part I: Convective parameterization, *J. Atmos. Sci.*, 37, 1722-1733.
- [8] Marshall, J., Hill, C., Perelman, L. and Adcroft, A., 1997a: Hydrostatic, quasi-hydrostatic, and nonhydrostatic ocean modeling, *Journal of Geophysical Research*, 102, 5733-5752.
- [9] Marshall, J., Adcroft, A., Hill, C., Perelman, L. and Heisey, C., 1997b: A finite-volume, incompressible Navier-Stokes model for studies of the ocean on parallel computers, *Journal of Geophysical Research*, 102, 5753-5766.
- [10] Stuben, K., 1999: A Review of Algebraic Multigrid, *GMD Report 96*.
- [11] Davies, H. C., 1976: A lateral boundary formulation for multi-level prediction models, *Quart. J. R. Met. Soc.*, 102, 405-418.
- [12] Gal-Chen, T. and Somerville, R. C. J., 1975: On the use of a coordinate transformation for the solution of the Navier-Stokes equations, *Journal of Computational Physics*, 17, 209-228.
- [13] Wicker, L. J. and Skamarock, W. C., 2002: Time-splitting methods for elastic models using forward time schemes, *Monthly Weather Review*, 130, 2088-2097.
- [14] Peng, X., Xiao, F., Takahashi, K. and Yabe T., 2004: CIP transport in meteorological models, *JSME international Journal (Series B)*, 47(4), 725-734.
- [15] Durrant, D., 1991: Numerical methods for wave equations in Geophysical Fluid Dynamics, Springer.
- [16] Peng, X., Feng Xiao, F. and Takahashi, K., Conservation constraint for quasi-uniform overset grid on sphere, *Quarterly Journal Royal Meteorology Society*. (2006), 132, pp. 979-996.
- [17] Takahashi, K. et al., 2004a: Proc. 7th International Conference on High Performance Computing and Grid in Asia Pacific Region, 487-495.
- [18] Takahashi, K., et al., 2004b. "Non-hydrostatic Atmospheric GCM Development and its computational performance", http://www.ecmwf.int/newsevents/meetings/workshops/2004/high_performance_computing-11th/presentations.html
- [19] Takahashi, K, et al. 2005: Non-hydrostatic atmospheric GCM development and its computational performance, *Use of High Performance computing in meteorology, Walter Zwiefelhofer and George Mozdzynski Eds., World Scientific*, 50-62.
- [20] Kageyama, A. and Sato, T., 2004: The Yin-Yang Grid: An Overset Grid in Spherical Geometry, *Geochem. Geophys. Geosyst.*, 5, Q09005, doi:10.1029/2004GC000734.
- [21] Blackadar, A. K., 1979: High resolution models of the planetary boundary layer, *Advances in Environmental Science and Engineering*, 1, Pfafflin and Ziegler, Eds., Gordon and Breach Publ. Group, Newark, 50-85.
- [22] Kelmann and Kase (1987) "Numerical Modeling of Meander and Eddy Formation in the Azores Current Frontal Zone", *JPO*.
- [23] Jones, H., and J. Marshall, 1993: Convection with Rotation in a Neutral Ocean: A Study of Open-Ocean Deep Convection. *J. Phys. Oceanogr.*, 23, 1009-1039.
- [24] Özgökmen, T.M., and E.P. Chassignet, 2002: Dynamics of two-dimensional turbulent bottom gravity currents. *J. Phys. Oceanogr.*, 32/5, 1460-1478.

気候変動に適応可能な環境探索のための マルチスケールシミュレーション

プロジェクト責任者

高橋 桂子 海洋研究開発機構 地球シミュレータセンター

著者

高橋 桂子^{*1}, 大西 領^{*1}, 杉村 剛^{*1}, 馬場 雄也^{*1}, 木田新一郎^{*1}, 後藤 浩二^{*2}, 淵上 弘光^{*3}

^{*1} 海洋研究開発機構 地球シミュレータセンター

^{*2} NEC 株式会社

^{*3} NEC インフォマティックシステム株式会社

A coupled atmosphere-ocean-land model has been developed in the Earth Simulator Center, which is designed to model multi-scale interactions among the atmosphere, the ocean and the coupled system. In this project of this fiscal year, we focused on introducing computational optimization architecture to the MSSG to be run with maximizing the computational power of the Earth Simulator 2. At the results, the computational performance of MSSG attained about 30% of the theoretical peak of ES2. Cloud micro-physics with turbulence effects, characteristics of heat transfer in urban area and non-hydrostatic physical performance in the oceanic component of MSSG is validated and present those results in this report.

キーワード: Coupled atmosphere-ocean model, multi-scale, multi-physics, high performance computing, the Earth Simulator

本年度は、サブテーマ(1)~(4)は、ES2上における計算性能最適化であり、ベクトル長、通信に関わる並列化性能の問題点をコンポーネントごとに詳細な計算性能解析を行い、MSSGの大気、海洋、および結合バージョンそれぞれについての計算性能最適化を行った。計算性能最適化は、理論ピーク性能値に対して約20%の計算性能を達成し(平成21年11月現在)、MSSGの従来の物理的性能に影響を与えないことを確認した。

加えて、MSSGの物理的性能向上のためのモデル開発、および検証結果、研究成果の一部を紹介する。

- MSSG-Aにおける雲物理計算手法の高度化
都市エアロゾルが対流雲の発達への影響評価を行い、乱流衝突効果がGCCNもともに有意なインパクトを与えることを明らかにした。

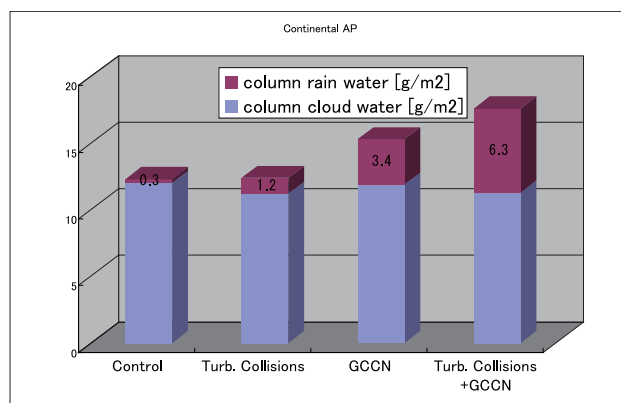


Fig. 1 都市エアロゾルが対流雲の発達への影響。

- 大気境界層内に密度成層が存在する場合の都市スケールの水平・鉛直混合過程の解明
熱フラックスによりシアード支配から対流支配へと遷移する過程において特徴的渦構造があることを明らかにした。

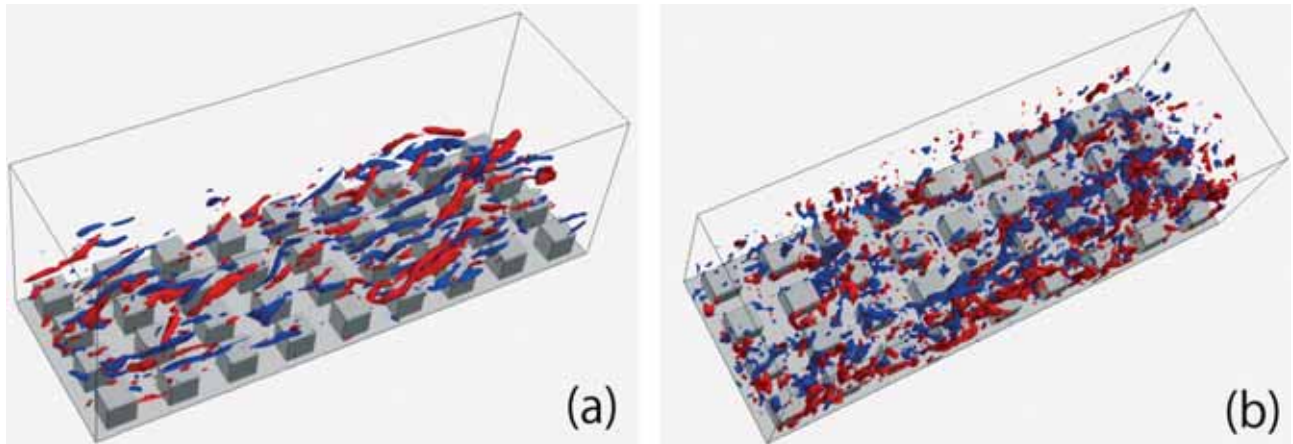


Fig. 2 遮蔽物の配置と渦構造の相違。(a) は中立条件から底面に境界条件として熱フラックスを与えない場合、(b) 底面に境界条件として熱フラックスを与えた場合。

- MSSG-O における非定常擾乱発達過程の検証
60 日後の海面温度の変化の様子を示す。波の発達など擾乱の発達していく様子よく再現されており、他のモデルとの比較においても何ら遜色がないことを示した。

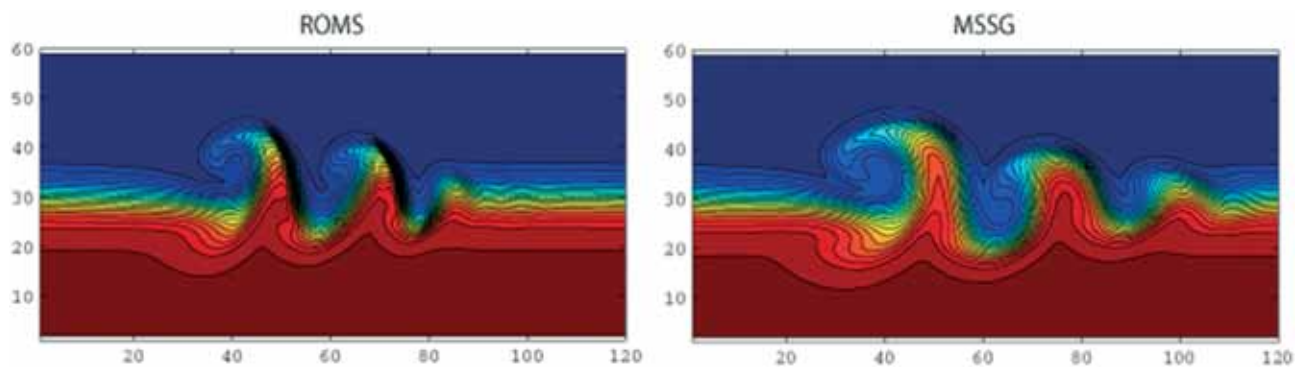


Fig. 3 ROMS と MSSG の 60 日後の海面温度分布。擾乱の発達過程がいずれにおいても再現されている。

Development of a High-Resolution Coupled Climate Model for Global Warming Studies

Project Representative

Akira Noda

Research Institute for Global Change, Japan Agency for Marine-Earth Science and Technology

Authors

Akira Noda^{*1}, Ayako Abe-Ouchi^{*2,1}, Megumi O. Chikamoto^{*1}, Yoshio Kawatani^{*1},

Yoshiki Komuro^{*1}, Masao Kurogi^{*1}, Rumi Ohgaito^{*1}, Kumiko Takata^{*1} and Yukio Tanaka^{*1}

*1 Research Institute for Global Change, Japan Agency for Marine-Earth Science and Technology

*2 Atmosphere and Ocean Research Institute, The University of Tokyo

The purpose of this project is to further develop physical models for global warming simulations, and to investigate mechanisms of changes in global environment as a successor of a previous ES joint project. We have obtained the following results this year.

Relative contribution of equatorially trapped wave modes and internal gravity waves in driving the QBO is discussed by using a high-resolution (T213L256) atmospheric GCM MIROC-AGCM, and it is shown that the gravity waves play a crucial role in driving the QBO in its westward shear phase.

A sub-grid scale parameterization for sea-ice thickness distribution is introduced to ice-ocean coupled models and it is shown that the horizontal pattern of sea-ice thickness becomes more realistic using the parameterization.

The glacial ocean carbon cycle simulation using climate fields obtained from MIROC shows that the atmospheric $p\text{CO}_2$ is reduced by 20 ppm. In the factorial analysis of the ocean carbon cycle, this reduction is mainly caused by the enhanced gas solubility associated with lowering sea surface temperature, whereas it is less contributed by the ocean stratification and the expanded sea ice.

A sub-grid snow-cover model SSNOWD is introduced into MATSIRO (land surface component of MIROC), and it is shown that the biases in simulated snow-cover ratio over eastern Siberia and the Rocky Mountains are significantly reduced.

Keywords: Atmosphere-Ocean-Land coupled model, offline biogeochemical model, stratospheric QBO

1. Introduction

This project is a successor of one of the previous ES-joint projects named ‘Development of a High-resolution Coupled Atmosphere-Ocean-Land General Circulation Model for Climate System Studies.’ The purpose of this project is to further develop physical models for global warming simulations, and to investigate mechanisms of changes in global environment.

To achieve the purpose, we focus on the development of ice sheet model, permafrost model and sea ice model, improvement of subcomponent models for atmosphere, ocean and land-surface processes in the climate model MIROC, as well as sensitivity studies using climate models relevant to global warming and paleo-climate.

2. Simulation of QBO using a high-resolution Atmospheric GCM

The relative contribution of equatorially trapped wave modes (EQWs) and internal gravity waves in driving the QBO is investigated using the T213L256 AGCM. Here EQWs are defined with order $n = -1$ to 2 with zonal wavenumber $s \leq 11$ (s

is zonal wavenumber) and equivalent depths of 2–90 m, while gravity waves have $s \geq 12$. Figure 1a presents a time-height cross section of the EP-flux divergence due to all resolved wave components averaged for 10°S–10°N. A QBO-like oscillation is obvious. The period is shorter than the observed value, but the amplitude and bottom levels of the QBO-like oscillation are realistic.

Figure 1b shows the time series of the EP-flux divergence due to all waves, eastward EQWs, westward EQWs, and gravity waves as well as the forcing due to the residual circulation at 30 hPa averaged for 10°S–10°N. Generally, the forcing due to the residual circulation is opposite to, and smaller than, the total wave forcing. In the eastward shear phase, peaks of eastward forcing due to the eastward EQWs and gravity waves are almost coincident. The contributions of eastward EQWs and gravity waves to the eastward forcing are ~25–50% and ~50–75%, respectively. In the westward shear phase, westward EQWs contribute ~10% at most to QBO driving. On the other hand, the contribution by Rossby waves propagating from the winter hemisphere is about 10–20% (not shown). Consequently, gravity

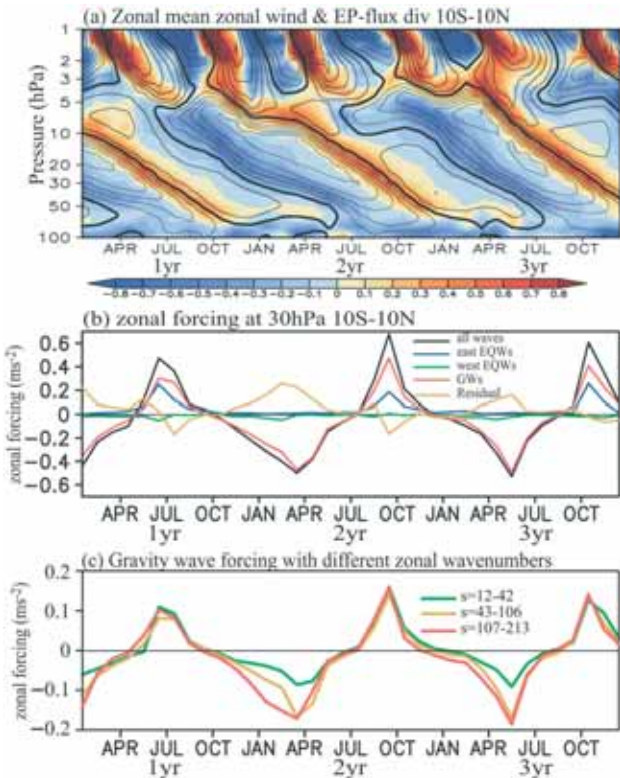


Fig. 1 Time-height cross-section of zonal-mean zonal wind (contour) and EP-flux divergence (shaded) at 10°S-10°N. Red and blue colors correspond to eastward and westward forcing, respectively. Eastward and westward winds are shown with solid and dashed lines. (b) Time variation of EP-flux divergence due to all waves (black), eastward EQWs (blue), westward EQWs (green), gravity waves (red), and forcing due to the residual circulation (yellow) at 30 hPa averaged from 10°S to 10°S. (c) The same as (b), but for EP-flux divergence due to $12 \leq s \leq 42$ (green), $43 \leq s \leq 106$ (yellow), and $107 \leq s \leq 213$ (red). Note that the range of the ordinate axis of (c) is different from that of (b).

waves play a crucial role in driving the QBO in its westward shear phase.

In order to investigate the horizontal scales of gravity waves driving the QBO, time series of EP-flux divergence are shown separately for the components of $12 \leq s \leq 42$, $43 \leq s \leq 106$, and $107 \leq s \leq 213$ (Fig. 1c). The eastward forcing due to each component is comparable in the eastward shear phase. In contrast, components with $42 \leq s \leq 213$ (horizontal wavelength ≤ 1000 km) are dominant for westward forcing in the QBO westward shear phase.

3. Development of Sea-ice model and Ocean GCM

We have introduced a sub-grid scale parameterization for ice thickness distribution (ITD) into an ice-ocean coupled model COCO. In the previous COCO, we employed a traditional two-category sea-ice model, in which all the sea ice in a horizontal grid has the same thickness. The new sea-ice model calculates the evolution of the sub-grid scale ITD following *Bitz et al.* [1].

The new ITD parameterization mainly affects on thermodynamics of sea ice. We perform a sensitivity experiment, in which the ITD parameterization is used but sea ice thickness is presumed to be uniform in a specific grid in diagnosing vertical heat flux through sea ice. The result shows that the ITD parameterization makes sea ice thicker, especially in the Arctic Ocean (figure not shown).

The ITD parameterization is also applied to MIROC5, the newest version of MIROC (Model for Interdisciplinary Research on Climate). In Figure 2, summertime Arctic sea-ice thickness is compared between pre-industrial simulations by using MIROC5 and older version (MIROC3). The horizontal pattern of sea-ice thickness becomes realistic (thick ice along the Canadian Archipelago and the north coast of Greenland) in MIROC5. Since sea-ice is very sensitive to climatic change and

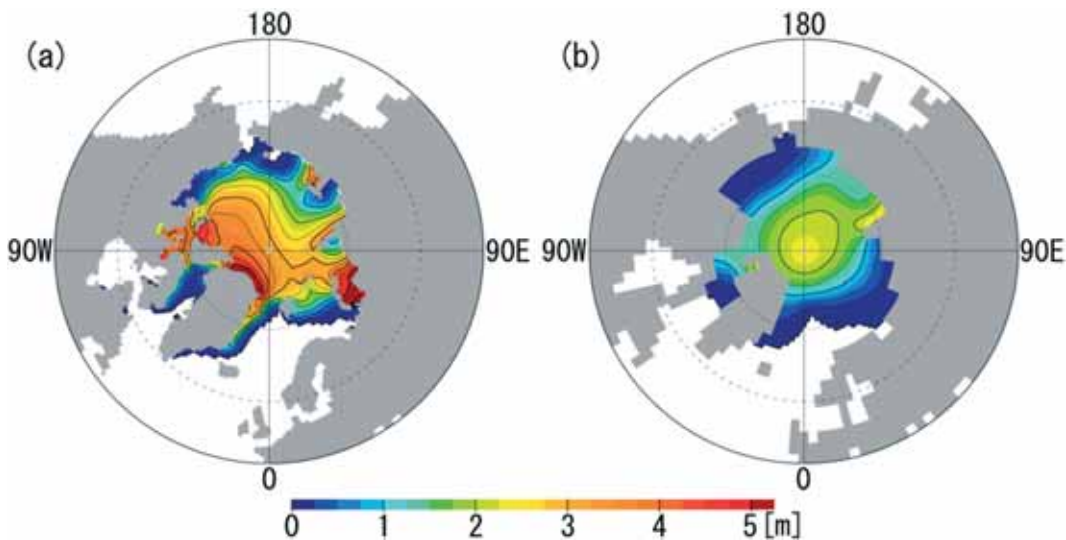


Fig. 2 Sea ice thickness in September, from simulations under pre-industrial boundary conditions. (a) MIROC5 simulation (T85 atmosphere and approx. 1-degree ocean), (b) MIROC3 simulation (T42 atmosphere and approx. 1-degree ocean).

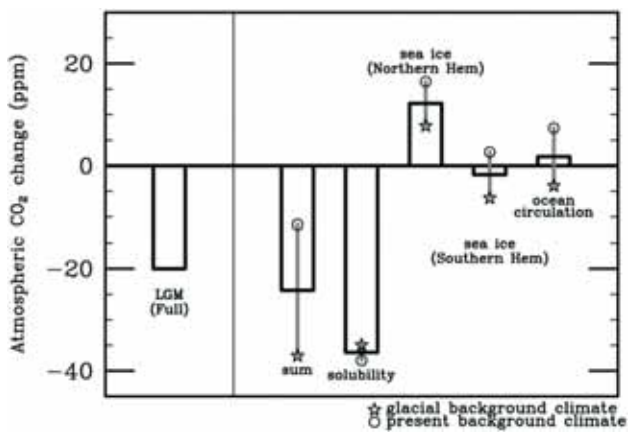


Fig. 3 Atmospheric $p\text{CO}_2$ responses to the climate dynamics of the glacial experiment. Thick bars are the average of the factorial estimates under the glacial and present background climate.

variability, the improvement of sea-ice fields will contribute to present and future climate simulations.

4. Glacial-interglacial simulations of the ocean carbon cycle using GCM

To investigate the glacial-interglacial atmospheric $p\text{CO}_2$ variability due to the climate dynamics change, we conducted factorial experiments of the marine carbon cycle under the glacial climate condition. The prescribed climate fields are obtained from runs of a coupled Atmosphere-Ocean General Circulation Model (AOGCM), MIROC, following the Paleoclimate Modeling Intercomparison Project 2 protocol. This is a new approach to evaluate the marine carbon cycle sensitivity to glacial climate factors of sea surface temperature, ocean circulation and sea ice using the fully coupled AOGCM.

In our simulations, atmospheric $p\text{CO}_2$ is reduced by 20 ppm (Fig. 3). This is mainly caused by enhanced gas solubility associated with lowering sea surface temperature. On the other hand, the ocean stratification and the expanded sea ice have relatively small effects on the atmospheric $p\text{CO}_2$. Compared with the paleo-proxy data, the modest enhancement of Southern Ocean stratification in our glacial simulation would reduce the ability of oceanic carbon uptake. In addition, the sea-ice coverage in the North Atlantic increases the atmospheric $p\text{CO}_2$ through less gas solubility, which is partly counteracted by the $p\text{CO}_2$ drawdown through prevent degassing of DIC-rich deep water in the Southern Ocean. It is the interaction between ocean circulation and sea-ice coverage that is a key factor accounting for the observed glacial $p\text{CO}_2$ drawdown.

We extended this method to model-data comparisons for the representation of North Pacific Ocean circulation during the deglaciation [3]. In our simulation, a North Atlantic freshwater discharge enhances the North Pacific deepwater formation, which is consistent with paleoclimate proxy records.

5. Land-surface modeling in GCM

Snow-cover ratio plays an important role in land surface energy balance because energy fluxes are calculated separately in snow-covered and snow-free portions in a grid cell in the land surface model (MATSIRO) of MIROC, and because albedos of snow-covered/free surfaces are very different. The snow cover ratio had been diagnosed with a simple function of snow water equivalent (SWE), which increases in accordance with SWE (OLD scheme). However, the snow cover ratio depends on sub-grid distribution of snow, which is affected by some factors, e.g., vegetation type and sub-grid topography. Therefore, a model of sub-grid snow cover ratio where such factors (SSNOWD; Liston, 2004 [2]) were considered was incorporated in MATSIRO and its effects were examined. In SSNOWD, a sub-grid snow distribution type is assigned for each grid cell in according to vegetation type and sub-grid topography (i.e., standard deviation of sub-grid variation in elevation), and a sub-grid ratio is prognosticated. CGCM experiments were performed with OLD and SSNOWD schemes, and the results

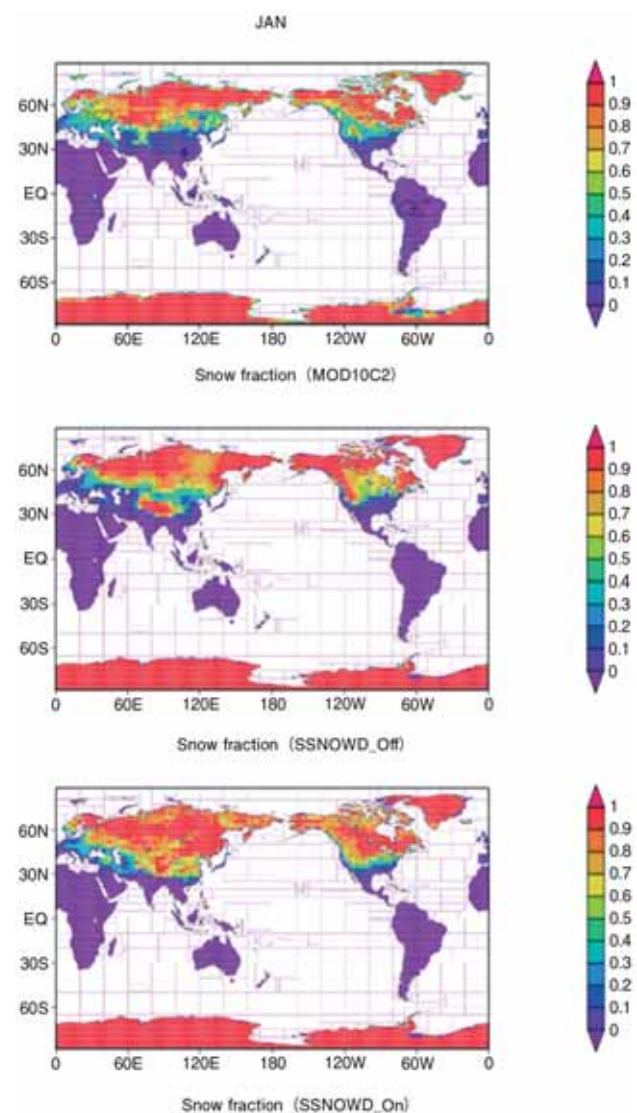


Fig. 4 Sub-grid snow distribution in January by satellite observation (upper), with OLD (middle), and with SSNOWD (lower).

were compared with a satellite observation data (Fig 4). With OLD scheme, the sub-grid snow cover ratio was underestimated in eastern Siberia, because snow amount is small and snow cover ratio is high there. Besides, the snow cover ratio was overestimated in Rocky Mountains with OLD because of the high snow amount in the mountainous region due to low temperature at high altitude. Those biases are significantly reduced with SSNOWD.

References

- [1] Bitz, C. M., M. M. Holland, A. J. Weaver, and M. Eby, (2001): Simulating the ice-thickness distribution in a coupled climate model. *J. Geophys. Res.*, 106, 2441-2463.
- [2] Liston, G., (2004): Representing subgrid snow cover heterogeneities in regional and global models. *J. Clim.*, 17, 1381-1397.
- [3] Chikamoto, M. O., L. Menviel, A. Abe-Ouchi, R. Ohgaito, A. Timmermann, Y. Okazaki, N. Harada, and A. Oka: Variability in North Pacific intermediate and deep water ventilation during Heinrich events in two coupled climate models, submitted.

地球温暖化予測研究のための高精度気候モデルの開発研究

プロジェクト責任者

野田 彰 海洋研究開発機構 地球環境変動領域

著者

野田 彰^{*1}, 阿部 彩子^{*2,1}, 近本めぐみ^{*1}, 河谷 芳雄^{*1}, 小室 芳樹^{*1}, 黒木 聖夫^{*1},
大垣内るみ^{*1}, 高田久美子^{*1}, 田中 幸夫^{*1}

*1 海洋研究開発機構 地球環境変動領域

*2 東京大学 大気海洋研究所

本研究は、地球温暖化予測のための各種物理モデルの開発を進めながら、地球環境の変動メカニズムの解明を行う。具体的には1)氷床モデル・凍土モデル・海氷モデルの開発、2)大気、海洋、陸面の物理過程の評価と改良、3)地球温暖化予測ならびに古気候再現に関わる気候モデルの感度実験、を行う。

本年度は以下の成果を得た。

中層大気を含む気候モデルの中では世界トップクラスの水平鉛直解像度である、T213L256AGCM の出力結果を解析し、QBO の駆動に対して、赤道域にトラップされた重力波モード（赤道波）と3次元的に伝播可能な内部重力波の役割分担について明らかにした。更に内部重力波に適用可能な3次元 wave flux を用いて、wave forcing の3次元分布を解析した。

サブグリッドスケールの海氷厚さ分布を海氷-海洋モデル COCO 及び結合モデル MIROC に導入した。MIROC5 を用いた工業化以前の境界条件を用いた全球シミュレーションでは、北極域の海氷場がより現実的になった。

MIROC を用いた氷期実験の気候場における大気中二酸化炭素分圧と海洋炭素循環の応答メカニズムを調べた。氷期気候場は、大気中の二酸化炭素分圧を約 20ppm 低下させた。この低下には、水温低下に伴い二酸化炭素の海水への溶解度が強まることが大きく寄与し、大西洋の熱塩循環の弱化や海氷の拡大による影響は小さいことが解析から示唆された。

MIROC5 の陸面水文過程では、1グリッドにおいて積雪域と無積雪域のエネルギーフラックスを別々に算定しているため、積雪のサブグリッド被覆率は地表面の熱収支に大きな影響を及ぼす。これまでは積雪水当量とともに増大する関数を用いて診断されてきた（OLD スキーム）。これを、植生や地形を考慮して、積雪のサブグリッド被覆率を予報するスキーム（SSNOWD）を導入したところ、OLD スキームでは過小評価されてきた東シベリアでの積雪被覆率や、過大評価されてきたロッキー山脈での積雪被覆率が衛星観測による積雪被覆率に近づくことが明らかになった。

キーワード:大気海洋陸面結合モデル, オフライン海洋生物地球化学モデル, 成層圏準二年振動(QBO)

Simulations of Atmospheric General Circulations of Earth-like Planets by AFES

Project Representative

Yoshi-Yuki Hayashi

Department of Earth and Planetary Sciences, Kobe University

Authors

Yoshi-Yuki Hayashi

Department of Earth and Planetary Sciences, Kobe University

Masahiro Takagi

Department of Earth and Planetary Science, University of Tokyo

Yoshiyuki O. Takahashi

Department of Earth and Planetary Sciences, Kobe University

Medium and high resolution simulations of the Martian atmosphere have been performed by using a GCM (General Circulation Model) based on the AFES (Atmospheric GCM for the Earth Simulator), and an accurate radiative transfer model for the Venus atmosphere has been constructed to extend the model toward the calculations of the Venus atmosphere. Our aim is to have insights into the dynamical features of atmospheric small and medium scale disturbances in the Earth-like atmospheres and their roles in the general circulations. Confirmation of the results of Martian simulations obtained until last fiscal year is also an important task because a bug in estimation of surface fluxes was found in the model. The results of the simulation with horizontal grid size of about 44 km show that many kinds of atmospheric small and medium scale disturbances, such as, medium scale vortices in the lee of Alba Patera and small scale vortices in low latitudes, are represented. It is confirmed that these features are qualitatively similar to those reported until last year. The analysis of distribution function of surface stress suggests that the small scale disturbances in low latitude are important to generate large surface stress. Toward the high resolution simulations of the Venus atmosphere with realistic radiative forcing, an accurate radiative transfer model of the Venus atmosphere has been constructed. In order to construct the model, four absorption line profiles of CO₂ proposed by past studies were tested and the most promising line profile that leads to a reasonable temperature structure has been determined for a new radiation model. Incorporation of this model into the AFES will produce the first reliable general circulation simulation of Venus atmosphere.

Keywords: planetary atmospheres, superrotation, dust storm, Earth, Mars, Venus

1. Introduction

The structure of the general circulation differs significantly with each planetary atmosphere. For instance, the atmospheres of the slowly rotating Venus and Titan exemplify the superrotation, while the weak equatorial easterly and the strong mid-latitude westerly jets are formed in the Earth's troposphere. The global dust storm occurs in some years on Mars, but a similar storm does not exist in the Earth's atmosphere. Understanding the physical mechanisms causing such a variety of structures of the general circulations of planetary atmospheres is one of the most interesting and important open questions of the atmospheric science and fluid dynamics.

The aim of this study is to understand the dynamical processes that characterize the structures of each planetary atmosphere by simulating circulations of those planetary atmospheres by using general circulation models with the common dynamical core of the AFES [1]. Appropriate physical processes are adopted for each planetary atmosphere. In our project so far, we have been mainly performing simulations under condition of Mars. In addition, the accurate radiation

model of the Venus atmosphere has been constructed toward performing the simulations of the Venus atmosphere with realistic radiative forcing. In the followings, the particular targets of each simulation, the physical processes utilized, and the results obtained are described briefly.

2. Mars simulation

2.1 Targets of simulations

It is well known that a certain amount of dust is always suspended in the Martian atmosphere and the radiative effect of dust has important impact on the thermal budget of the Martian atmosphere. However, the physical mechanisms of dust lifting have not been well understood. It has been implied that the effects of wind fluctuations caused by small and medium scale disturbances would be important for the dust lifting processes. Until the last fiscal year, the features of disturbances and dust lifting amount at northern fall and summer were investigated. However, a bug in estimation of surface momentum and heat fluxes was found in the model. The disturbances near the surface may be strongly affected by the surface momentum and heat

fluxes. In this fiscal year, after fixing the bug, the simulations are performed to confirm the features of atmospheric disturbances reported by the last year, and the distribution function of surface stress in the model is examined to have implications on effects of atmospheric disturbances on dust lifting.

2.2 Physical processes

The physical processes used for the Mars simulations are introduced from the Mars GCM [2, 3] which has been developed in our group so far. The implemented physical processes are the radiative, the turbulent mixing, and the surface processes. Before performing simulations, a bug found in estimation of surface process was fixed. By the use of this GCM, the simulations in northern fall condition are performed. Resolutions of simulations are T79L96 and T159L96, which are equivalent to about 89 and 44 km horizontal grid sizes. In the simulation performed in this fiscal year, the atmospheric dust distribution is prescribed, and the dust is uniformly distributed in horizontal direction with an amount corresponding to visible optical depth of 0.2. But, the dust lifting parameterization [4] is included in the model, and the possibility of dust lifting can be diagnosed in the model.

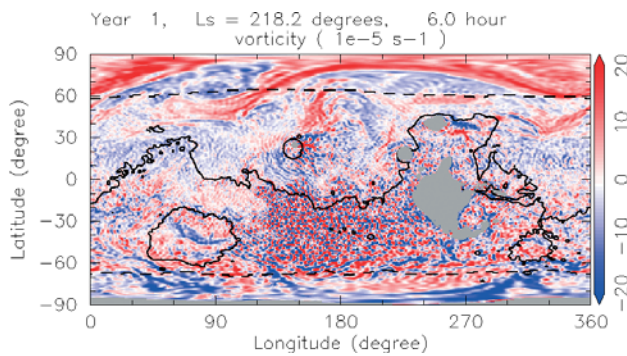


Fig. 1 Global distribution of vorticity at the 4 hPa pressure level at northern fall with the resolution of T159L96. Unit of vorticity is 10^{-5} s^{-1} . Also shown is the areoid (solid line) and low latitude polar cap edge (dashed line). Gray areas represent mountains at the 4 hPa pressure level.

2.3 Results

Figure 1 shows a snapshot of global distribution of relative vorticity at the 4 hPa pressure level at northern fall obtained from T159L96 simulation. In the simulation, many kinds of atmospheric disturbances can be observed. One of the most striking features is the baroclinic wave whose zonal wavenumber is 2-3. Associated with this wave, fronts are observed as elongated vorticity features. In addition to this large scale wave, small scale disturbances can also be observed. One of examples is medium scale vortices in the lee of Alba Patera around 255°E , 40°N . Analysis of circulation around Alba Patera suggests the interaction between mean wind and mountain and diurnally varying slope wind would cause this vortex generation. Small scale disturbances of another type are a lot of small scale vortices in low latitude. These vortices are generated in the afternoon and dissipated in the night. It is suggested that these would be an appearance of convective activity represented in the model. These results are qualitatively similar to those reported until last year although the calculation of surface flux is changed by fixing the bug.

The distribution functions of surface stress are analyzed to examine the effects of small and medium scale disturbances on dust lifting. Figure 2 shows the distribution functions of

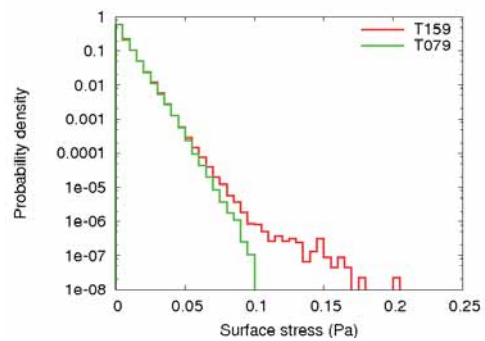


Fig. 2 Distribution functions of surface stress obtained from T159L96 resolution simulation (red), and T79L96 resolution simulation (green).

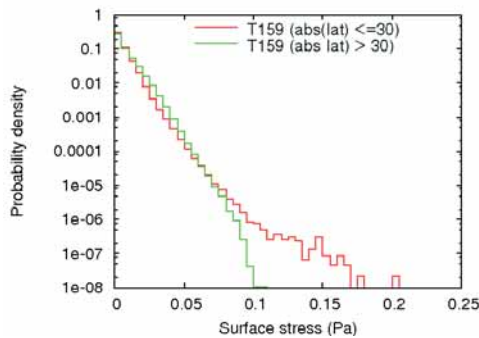


Fig. 3 Latitudinal dependence of distribution function from T159L96 simulation, equatorward of 30 degree latitude (red) and poleward of 30 degree latitude (green).

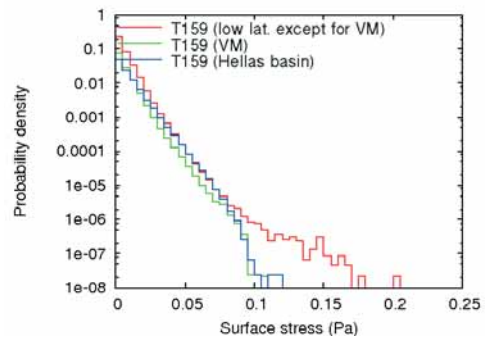


Fig. 4 Regional dependence of distribution function of surface stress at low latitude except for Valles-Marinieris (VM) (red), VM (green), and Hellas basin (blue).

surface stress obtained from T159L96 and T79L96 resolution simulations. The distribution function from T159L96 simulation shows a large surface stress tail. The maximum surface stress in T159L96 simulation is about 1.5-2 times larger than that in T79L96 simulation. Diagnostics of possibility of dust lifting by dust lifting parameterization included in the model shows that the large surface stress shown in T159L96 simulation causes the dust lifting in the model.

In order to have implications for phenomena causing high surface stress, the latitudinal dependence of distribution function is examined. It is shown that the large surface stress tail is generated in low latitude region (Fig. 3). This simply implies the importance of disturbances in low latitude. At the same time, this also implies that the baroclinic waves and fronts in northern middle and high latitude do not play important roles in view of generating large surface stress.

Finally, the regional dependence of distribution function is examined by picking up two characteristic topography features, Hellas basin and Valles-Marineris (VM). However, it is shown that the large surface stress tail is not observed in distribution functions in these regions (Fig. 4). The analysis of circulation implies the importance of steep slope to generate atmospheric disturbances. But, disturbances in such regions do not have significant impact in view of generating large surface stress in our model and in our current resolution.

3. Venus simulation

3.1 Targets of simulations

Numerical simulations of the Venus atmospheric circulation have been actively made in recent years [5, 6, 7, 8, 9]. In most models used in these simulations, the radiative transfer process is represented by the Newtonian cooling. However, this approximation cannot be justified for the Venus atmosphere whose opacity is extremely large in the infrared region. In order to investigate the Venus atmospheric circulation, we

must develop a radiative transfer model applicable to the Venus atmosphere and to the AFES.

3.2 A new radiative transfer model

The Venus atmosphere consists of the vast amount of carbon dioxide (CO_2), which leads to high pressure and high temperature in its lower atmosphere. In this situation, representation of the pressure broadening of CO_2 absorption lines is quite important for constructing an accurate radiative transfer model. The broadening of the absorption line is usually represented by the Lorentz profile. However, it is well known that the infrared absorption due to CO_2 is overestimated by the Lorentz profile, and several profiles have been proposed as a substitute for the Lorentz profile. In the present study, the following line profiles are used to obtain temperature profiles in the radiative and radiative-convective equilibrium states [10, 11, 12, 13]: Lorentz profile, profile by Tonkov et al. (1996), profile by Fukabori et al. (1986), and profile by Meadows and Crisp (1996). Collision induced absorption (CIA) is also taken into account [14]. It is assumed that the H_2O absorption line is represented by the Lorentz profile.

A radiative transfer model constructed in the present study is based in the correlated k-distribution method. A wavenumber region of $0\text{-}6000\text{ cm}^{-1}$ is taken into account, and divided into 30 channels. It is assumed that the H_2SO_4 cloud is optically "grey" and its optical thickness is 10. An atmospheric layer of $0\text{-}80\text{ km}$ is divided into 50 layers in the following calculations. A vertical profile of the solar heating is based on the observations [15]. Vertical convection is represented by the vertical eddy viscosity based on the mixing length theory. Radiative and radiative-convective equilibrium temperature profiles are obtained for the following conditions:

- Case 1: CO_2 only (CIA is excluded)
- Case 2: Case 1 + CIA
- Case 3: Case 2 + H_2O

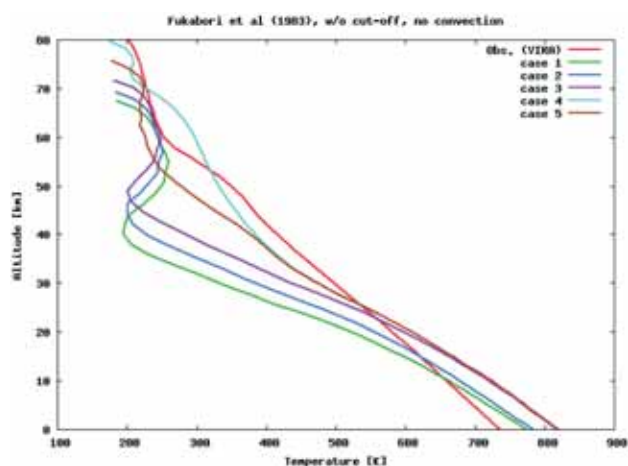


Fig. 5 Radiative equilibrium temperature profiles obtained for the cases 1-5 by using the Fukabori line profile. The red line shows the observed temperature profile.

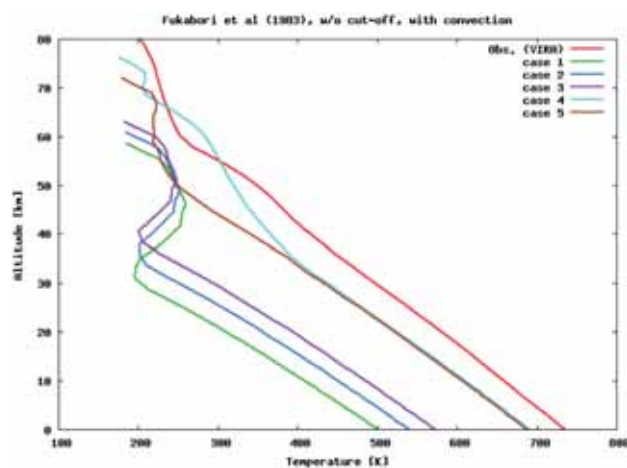


Fig. 6 The same as Fig. 5, but for the radiative-convective equilibrium.

- Case 4: Case 3 + H₂SO₄ cloud (constant $k\rho$)
- Case 5: Case 3 + H₂SO₄ cloud (constant k).

In this report, results obtained by the Fukabori profile are shown in Figs. 5 and 6. These results and others (not shown here) can be summarized as follows:

- Temperature profiles close to the observed one can be obtained by using the line profiles of Fukabori et al. [12] and Meadows and Crisp [13].
- Realistic radiative transfer model for the Venus atmosphere may be constructed by these line profiles.
- In the radiative equilibrium states, the temperature profiles are super-adiabatic from the surface to 10-80 km (the top level depends on the CO₂ line profiles). The temperature at the surface is much higher than the observed one.
- In the radiative-convective equilibrium states, a convective layer is formed from the surface to 30-50 km. The temperature at the surface strongly depends on the temperature at the cloud bottom.

See Takagi et al. [16] for more details of the new radiative transfer model.

In order to simulate the Venus atmospheric circulation and investigate the generation mechanism of the atmospheric superrotation, we are going to carry out numerical simulations with the AFES combined with the new radiative transfer model.

References

- [1] Ohfuchi, W., H. Nakamura, M. K. Yoshioka, T. Enomoto, K. Takaya, X. Peng, S. Yamane, T. Nishimura, Y. Kurihara, and K. Ninomiya, 10-km Mesh Meso-scale Resolving Simulations of the Global Atmosphere on the Earth Simulator - Preliminary Outcomes of AFES (AGCM for the Earth Simulator) -, *Journal of the Earth Simulator*, 1, 8, 2004.
- [2] Takahashi, Y. O., H. Fujiwara, H. Fukunishi, M. Odaka, Y.-Y. Hayashi, and S. Watanabe, Topographically induced north-south asymmetry of the meridional circulation in the Martian atmosphere, *J. Geophys. Res.*, 108, 5018, doi:10.1029/2001JE001638, 2003.
- [3] Takahashi, Y. O., H. Fujiwara, and H. Fukunishi, Vertical and latitudinal structure of the migrating diurnal tide in the Martian atmosphere: Numerical investigations, *J. Geophys. Res.*, 111, E01003, doi:10.1029/2005JE002543, 2006.
- [4] Newman, C. E., S. R. Lewis, and P. L. Read, Modeling the Martian dust cycle 1. Representation of dust transport processes, *J. Geophys. Res.*, 107, 5123, doi:10.1029/2002JE001910, 2002.
- [5] Yamamoto, M and M. Takahashi, Dynamics of Venus' superrotation: The eddy momentum transport processes newly found in a GCM, *Geophys. Res. Lett.*, 31, L09701, doi:10.1029/2004GLO19518, 2004.
- [6] Takagi, M and Y. Matsuda, Effects of thermal tides on the Venus atmospheric superrotation, *J. Geophys. Res.*, 112, D09112, doi:10.1029/2006JD007901, 2007.
- [7] Lee, C., S. R. Lewis, and P. L. Read, Superrotation in a Venus general circulation model, *J. Geophys. Res.*, 112, E04S11, doi:10.1029/2006JE002874, 2007.
- [8] Hollingsworth, J. L., R. E. Young, G. Schubert, C. Covey, and A. S. Grossman, A simple-physics global circulation model for Venus: Sensitivity assessments of atmospheric superrotation, *Geophys. Res. Lett.*, 34, L05202, doi:10.1029/2006GL028567, 2007.
- [9] Kido, A and Y. Wakata, Multiple equilibrium states appearing in a Venus-like atmospheric general circulation model, *J. Meteor. Soc. Japan*, 86, 969-979, 2008.
- [10] Pollack, J. B., J. B. Dalton, D. Grinspoon, R. B. Wattson, R. Freedman, D. Crisp, D. A. Allen, B. Bezaud, C. DeBergh, L. P. Giver, Q. Ma, and R. Tipping, Near-Infrared Light from Venus' Nightside: A Spectroscopic Analysis, *Icarus*, 103, 1-42, 1993.
- [11] Tonkov, M. V., N. N. Filippov, V. V. Bertsev, J. P. Bouanich, Nguyen Van-Thanh, C. Brodbeck, J. M. Hartmann, C. Boulet, F. Thibault, and R. Le Doucen, Measurements and empirical modeling of pure CO₂ absorption in the 2.3- μ m region at room temperature: far wings, allowed and collision-induced bands, *Applied Optics.*, 35, 4863-4870, 1996.
- [12] Fukabori, M., T. Nakazawa, and M. Tanaka, Absorption properties of infrared active gases at high pressures. I CO₂, *J. Quantitative Spectroscopy and Radiative Transfer*, 36, 265-270, 1986.
- [13] Meadows, V. S. and D. Crisp, Ground-based near-infrared observations of the Venus nightside: The thermal structure and water abundance near the surface, *J. Geophys. Res.*, 101, 4595-4622, 1996.
- [14] Moskalenko, N. I., Yu. A. Il'in, S. N. Parzhin, and L. V. Rodionov, Pressure-induced IR radiation absorption in atmospheres, *Izvestiya, Atmos. Oceanic Phys.*, 15, 632-637, 1979.
- [15] Tomasko, M. G., L. R. Dose, P. H. Smith, and A. P. Odell, Measurements of the flux of sunlight in the atmosphere of Venus, *J. Geophys. Res.*, 85, 8167-8186, 1980.
- [16] Takagi, M., K. Suzuki, H. Sagawa, P. Baron, J. Mendrok, Y. Kasai, and Y. Matsuda, Influence of CO₂ line profiles on radiative and radiative-convective equilibrium states of the Venus lower atmosphere, *J. Geophys. Res.*, in press.

AFES を用いた地球型惑星の大気大循環シミュレーション

プロジェクト責任者

林 祥介 神戸大学 大学院理学研究科

著者

林 祥介 神戸大学 大学院理学研究科

高木 征弘 東京大学 大学院理学系研究科

高橋 芳幸 神戸大学 大学院理学研究科

大気大循環モデル AFES (AGCM (Atmospheric General Circulation Model) for the Earth Simulator) に基づく GCM を用いて、火星大気の中高解像度大気大循環シミュレーションを実施した。また、金星大気計算への拡張を目指して、高精度の金星大気放射モデルを構築した。我々の研究の目的は、地球型惑星大気における中小規模擾乱の力学的特徴と、その大気大循環への影響を調べることである。また、昨年度に地表面におけるフラックスの計算においてバグが発見されたため、昨年度までの火星大気シミュレーションの結果を確認することも今年度の重要な目的である。水平格子点間隔約 44 km の解像度での火星大気シミュレーションを行った結果、アルバ・パテラ領域の風下での中規模渦や低緯度での小規模渦群といった様々な大気擾乱が表現された。これらの特徴は、昨年度までに見られていたものと定性的に同様であることが確認された。計算結果を用いて地表面応力の分布関数について解析を行ったところ、低緯度で生じる小規模擾乱が大きな値の地表面応力を生成する上で重要であることが示唆された。また、現実的な加熱強制を与えた金星大気の高解像度大気大循環シミュレーションの実施に向けて、高精度の放射モデルを構築した。モデル構築においては、先行研究で提案された 4 つの CO₂ 吸収線型をテストし、理にかなった温度構造の得られる吸収線型を決定した。この放射モデルを AFES に導入して計算を行うことにより、初めての信頼に足る金星大気の大気大循環実験を行いたい。

キーワード: 惑星大気, スーパーローテーション, ダストストーム, 地球, 火星, 金星

Study on the Diagnostics and Projection of Ecosystem Change Associated with Global Change

Project Representative

Michio J. Kishi

Research Institute for Global Change, Japan Agency for Marine-Earth Science and Technology

Authors

Yasuhiro Yamanaka^{*1,2}, Akio Ishida^{*1}, Yoshikazu Sasai^{*1}, Maki Noguchi Aita^{*1},
Taketo Hashioka^{*1}, Hiroshi Sumata^{*2} and Takafumi Hirata^{*2}

*1 Research Institute for Global Change, Japan Agency for Marine-Earth Science and Technology

*2 Faculty of Environmental Earth Science, Hokkaido University

In this project we will improve the ability to simulate the present status of ocean climate and ecosystems and clarify effects of climate variability on marine biogeochemical cycles and ecosystems by using multiple ocean general circulation models (GCMs) with multiple ecosystem models including marine biogeochemical cycles. Taking advantage of our high-resolution general circulation model, we have investigated the impact of fine scale physical variability on the marine ecosystem and found that cyclonic eddies affected approx. 20% of biological production in the Kuroshio Extension region. We also have developed an advanced ecosystem model including some key biogeochemical processes, e.g., optimal nutrient uptake kinetics of phytoplankton, iron cycle and aggregation processes for sinking particles. The new model is used for an international project on model intercomparison "The MARine Ecosystem Model Intercomparison Project (MAREMIP)". We have also begun developing a model including stable isotope compositions of carbon and nitrogen to simulate the trophic position of consumers in the food web.

Keywords: Ecosystem, Biogeochemical Cycles, Global Change, Ocean General Circulation Model

1. High resolution modeling of biogeochemical cycles and ecosystems

This study has made progress by using a high resolution model, the Ocean general circulation model For the Earth Simulator (OFES) including a simple ecosystem model (Nutrient-Phytoplankton-Zooplankton-Detritus, or NPZD type), with a horizontal resolution of 0.1 degrees. Using the OFES-NPZD model, we have published scientific results on the effects of the mesoscale eddies on the marine ecosystem in the Kuroshio Extension (KE) region [1]. The model reproduces high chlorophyll concentration corresponding to low sea surface height (SSH) associated with cyclonic eddies (Fig. 1), because the cyclonic eddies lift nutrient-rich water into the euphotic zone. The number of the cyclonic eddies and area-averaged surface chlorophyll concentration within the cyclonic eddies are shown in Fig. 2. On average two cyclonic eddies per year are detached to the south of the KE jet and they propagate westward. The area-averaged surface chlorophyll concentration within the cyclonic eddies is considerably higher (by two to seven times) than that outside the eddies (Fig. 2b, c). This gives an indication of the impact of the eddies on the overall chlorophyll concentration. The cyclonic eddies contribute about

20% of the area averaged surface chlorophyll concentration in this region.

2. Process modeling in marine ecosystems

Using a 3-D marine ecosystem model NEMURO (North Pacific Ecosystem Model for Understanding Regional Oceanography), we published scientific results on the projection of marine ecosystems under global warming climate [2]. Maximum biomass during the spring bloom under global warming climate is found to occur 10 to 20 days earlier than under the pre-industrial climate. A study on the impact of global warming on Japanese common squid in the Sea of Japan was also published [3].

To improve the ability of the model to simulate marine ecosystems, we have advanced the model formulation for nutrient uptake by phytoplankton based on physiological acclimation. The optimal uptake kinetics describes observed nitrate uptake rates over wide ranges of nutrient concentrations better than the widely applied classical Michaelis-Menten equation [2]. We also improved the particles sinking process to simulate the dependence of aggregation on the size of particles. The iron cycle in the model is also revised. Implementing these

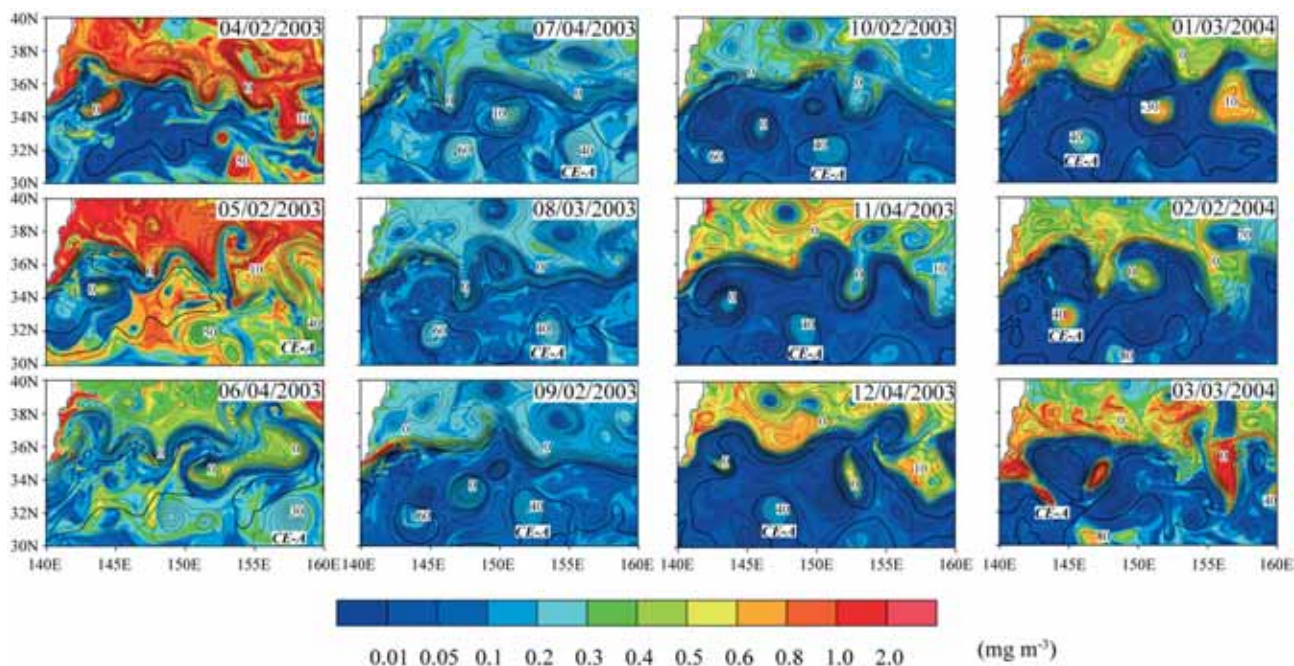


Fig. 1 Snapshots of surface Chlorophyll-a (color) and SSH (contour) from April 2003 to March 2004. In spring, the chlorophyll concentration reaches its highest value (2.0 mg m^{-3}) for the year, especially in the subpolar region and cyclonic eddies in the subtropical region. The high chlorophyll ($0.8\text{-}1.0 \text{ mg m}^{-3}$) associated with the cyclonic eddies is at the same level as in the subpolar region.

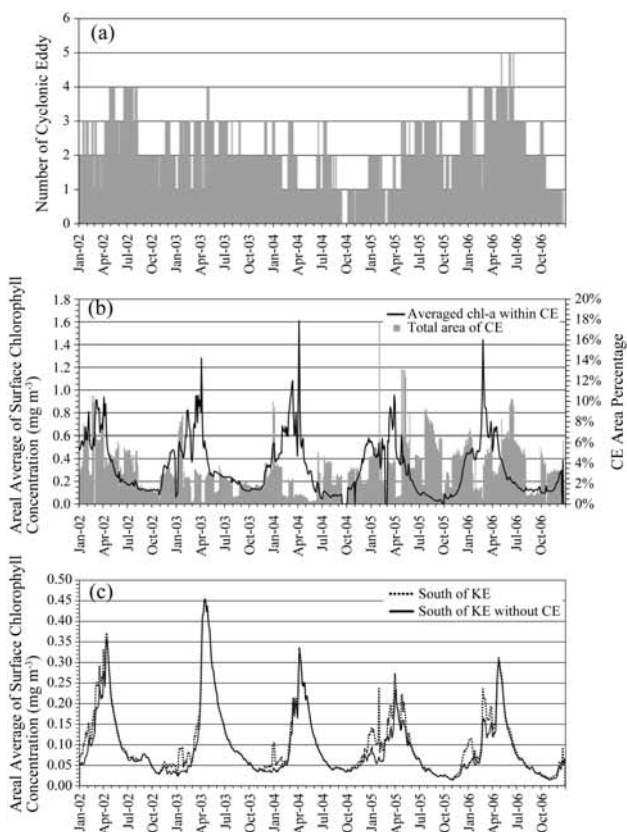


Fig. 2 (a) Number of cyclonic eddies (CEs) produced in the model, (b) areal average of the surface chlorophyll concentration within CEs (black line) and total surface area of CEs (grey bar), (c) the areal average of the surface chlorophyll concentration south of the KE jet (dashed line) and without CEs area (solid line).

new formulations and schemes in a 3-D model, we performed numerical experiments to investigate the performance of the new model. Using the new model we started a hindcast experiment for the MARine Ecosystem Model Intercomparison Project (MAREMIP) Phase 1. The offline version of the 3-D model developed in Hokkaido University [5] was transplanted on the Earth Simulator and tuned for long-term integration. We also started developing a model including stable isotope compositions of carbon and nitrogen to simulate the trophic position of consumers in the food web. Using the observed data in the northwestern North Pacific, we evaluated the trophic level and material flow related with the food habit of one key species in the Oyashio region.

References

[1] Sasai, Y., K. J. Richards, A. Ishida, H. Sasaki (2010): Effects of cyclonic mesoscale eddies on the marine ecosystem in the Kuroshio Extension region using an eddy-resolving coupled physical-biological model, *Ocean Dynamics*, DOI 10.1007/s10236-010-0264-8.

[2] Hashioka, T., T. Sakamoto, Y. Yamanaka (2009): Potential impact of global warming on North Pacific spring blooms projected by an eddy-permitting 3-D ocean ecosystem model, *Geophysical Research Letters*, 36, L20604, doi:10.1029/2009GL038912.

[3] Kishi, M. J., K. Nakajima, M. Fujii and T. Hashioka (2009): Environmental factors which affect growth of Japanese Common Squid, *Todarodes pacificus*, analyzed by a bioenergetics model coupled with a lower trophic

- ecosystem model. *Journal of Marine Systems*, 78, 278-287.
- [4] Smith, S. Lan, Y. Yamanaka, M. Pahlow and A. Oschlies (2009) Optimal uptake kinetics: physiological acclimation explains the pattern of nitrate uptake by phytoplankton in the ocean, *Marine Ecology Progress Series*, 384 Feature Article, p. 1-12.
- [5] Sumata, H. T. Hashioka, T. Suzuki, N. Yoshie, T. Okunishi, M. N. Aita, T. T. Sakamoto, N. Okada and Y. Yamanaka (2010) Effect of eddy transport on the nutrient supply into the euphotic zone simulated in an eddy-permitting ocean ecosystem model, *Journal of Marine Systems*, doi:10.1016/j.jmarsys.2010.07.002.

地球環境変化に伴う生態系変動の診断と予測に関する研究

プロジェクト責任者

岸 道郎 海洋研究開発機構 地球環境変動領域

著者

山中 康裕^{*1,2}, 石田 明生^{*1}, 笹井 義一^{*1}, 相田(野口)真希^{*1}, 橋岡 豪人^{*1}, 須股 浩^{*2},
平田 貴文^{*2}

*1 海洋研究開発機構 地球環境変動領域

*2 北海道大学 大学院地球環境科学研究科

本プロジェクトでは、空間解像度や複雑さの異なる複数の海洋生態系モデル、海洋大循環モデルを用いて、現在の気候条件における生態系変動再現実験、及び、温暖化気候における将来予測実験を通して、生態系の変動特性の定量化、生態系の将来予測、海域による海洋生態系の違いや卓越種の再現を目指した生態系モデル開発を実施する。今年度は高解像度海洋大循環・海洋生態系結合モデルを用いて、黒潮続流域における渦による海洋生態系へのインパクトを定量的に調べ、低気圧性渦が黒潮続流の南の生物量に約20%寄与していることを明らかとした。また、いくつかの鍵となる生物地球化学過程(植物プランクトンの栄養塩取り込み過程や鉄循環の導入、沈降粒子の凝集過程など)を導入した新モデルを開発し、中解像度の海洋大循環モデルに結合することで、国際研究計画MAREMIP(MARine Ecosystem Model Intercomparison Project)のPhase 1に対応して実験に着手した。さらに、オフライン版の3次元海洋生態系モデルのES2への移植、テスト計算を実施した。

キーワード:生態系,物質循環,気候変動,高解像度海洋大循環モデル

Computational Fluid Dynamics Simulation of Daytime and Nighttime Summer Temperatures in 23 Special Wards of Tokyo

Project Representative

Yasunobu Ashie

National Institute for Land and Infrastructure Management

Authors

Yasunobu Ashie

National Institute for Land and Infrastructure Management

Takaaki Kono

Building Research Institute

Keiko Takahashi

The Earth Simulator Center, Japan Agency for Marine-Earth Science and Technology

Computational fluid dynamics simulations of air temperature fields were performed in the entire area of 23 special wards of Tokyo at 05:00, 14:00, and 22:00 local standard time on July 31, 2005. Comparisons with simulation results and observations showed the same tendency in the air temperature distributions at 14:00 and 22:00, where air temperatures in the coastal areas were cooler than those in the inland areas; while at 5:00, air temperatures in the coastal areas were hotter than those in the inland areas. The root mean square errors of air temperature between simulation results and observations were 0.5°C at 05:00, 1.1°C at 14:00, and 0.4°C at 22:00, respectively.

Keywords: urban heat island, CFD, air temperature, daytime and nighttime, summer, 23 special wards of Tokyo

1. Introduction

Recently, countermeasures against the urban heat island (UHI) effect, such as reduction of anthropogenic heat release and enhancement of urban ventilation, have become increasingly important in Tokyo. Evaluations of urban ventilation require construction of a high-resolution computational fluid dynamics (CFD) system, which takes into account complex urban morphology. The morphological complexity arises from multiscale geometry consisting of buildings, forests, and rivers, which is superimposed on varying topography. Given this morphological background, we have been developing a high-resolution CFD system and have performed simulations of wind and air temperature fields in the 23 special wards of Tokyo using a horizontal grid spacing of 5 m^[1]. In fiscal year 2009, we performed CFD simulations of daytime and nighttime summer temperature fields in the wards and compared the results with the actual observations.

2. Date and time of analysis

The CFD simulations were performed for 05:00, 14:00, 22:00 local standard time on July 31, 2005. This date was selected for two reasons. First, the UHI effect becomes the most severe during the day in summer. Second, the results of the current analysis can be compared against large-scale simultaneous meteorological observations—Metropolitan Environmental Temperature and Rainfall Observation System (METROS)

managed by Tokyo Metropolitan Government. In this study, air temperature data of METROS, observed at Stevenson screens located at elementary schools across Tokyo's 23 wards, are used. Figure 1 shows the horizontal computational domain of

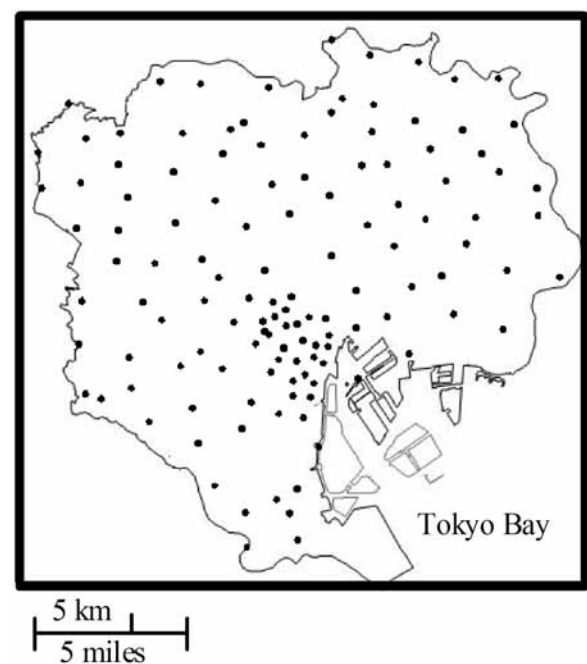


Fig. 1 Horizontal computational domain. Black dots indicate observation points (METROS).

33 km × 33 km. In the figure, observation points of METROS are indicated by black dots.

3. Calculation of surface temperatures

Although it is desirable to estimate the surface temperatures of buildings and other objects on the ground by performing a fully coupled conduction, radiation, and convection heat transfer simulation in three-dimensional space, the following simplified method is adopted in the present study. First, an unsteady heat conduction analysis is performed for individual cover types, which include asphalt and grassland. In the analysis, one-dimensional vertical heat conduction is assumed and evaluated according to the meteorological condition on the day of the simulation. The surface temperature of a cover type is calculated for both, the case with no shading from the sun and the case with shading from the sun. Subsequently, from the solar position at the hour of the analysis, the sunlit and shaded conditions of the urban surfaces are determined in every grid cell of the three-dimensional computational domain. The sunlit and shaded conditions of the urban surfaces are determined by taking into account the building arrangement within the city to be investigated by the CFD analysis. Finally, the surface temperature of the urban surface within an individual grid cell is assigned according to the surface cover types and the sunlit and shaded conditions.

When the surface-heat energy budget is solved, values for parameters such as albedo, emissivity, and evaporation efficiency are required. Ichinose et al. (1999)^[2] evaluated values for five parameters relevant to the surface-heat energy budget (i.e., albedo, evaporation efficiency, density, specific heat, and thermal diffusion coefficient) of 10 land cover types. Ihara et al. (2003)^[3] evaluated values for a different set of five parameters relevant to the surface-heat energy budget (i.e., albedo, emissivity, thermal diffusion coefficient, heat capacity, and thermal conductivity) of eight land cover types. This study uses relevant parameters and corresponding values from Ichinose et al. (1999)^[2] and Ihara et al. (2003)^[3]. These are summarized in

Table 1. Although the thermal diffusivity value is influenced by wind speed, it is set at a constant of $11.6 \text{ W m}^{-2} \text{ K}^{-1}$ (Yoshida et al., 2000)^[4]. The mass transfer coefficient is estimated using Lewis's law.

The surface temperatures of buildings and other objects on the grounds are estimated by performing a heat balance analyses using the parameters in Table 1 and meteorological observation data (AMeDAS, Tokyo); the estimated surface temperatures are used as boundary conditions for CFD simulations.

4. Comparisons of simulation results with observations

Figure 2 compares the horizontal distribution of the air temperature at 126 points of METROS from simulation results with those from METROS's observations. Here, simulation results at 2 m above the ground are depicted. In addition, data at a point over the sea ($35^{\circ} 27' 52.09'' \text{ N}$, $139^{\circ} 52' 28.35'' \text{ E}$) observed by Ministry of Environment (MOE)^[5] are depicted. At 05:00 in Fig. 2 (a), air temperatures in the coastal areas are higher than those in the inland areas. At 14:00 in Fig. 2 (b), air temperatures are lower in the eastern areas and higher in the central and northern areas of the inland. At 22:00 in Fig. 2 (c), air temperatures of the north side of inland areas and those of the central areas obviously become higher than those of other areas and form an inverted triangular shaped region of higher temperature. Simulation results and observations are almost identical. The root mean square errors of air temperature between simulation results and observations are 0.5°C at 05:00, 1.1°C at 14:00, and 0.4°C at 22:00, respectively.

Figure 3 shows the frequency distributions of the maximum differences in the simulated air temperatures within an area of $100 \text{ m} \times 100 \text{ m}$ at and around each observation point. At 05:00 and 22:00, areas with the maximum air temperature differences within 1°C account for 90 percent or more. However, at 14:00, areas with the maximum air temperature differences above 1°C account for 90 percent or more, indicating a great unevenness in air temperature distributions.

Table 1 Values of parameters relevant to the surface energy budget

Land use classification adopted for the present study	Building sites	Asphalt	Grassland	Water	Trees
Albedo [-] (Ichinose et al. 1999)	0.18	0.18	0.16	0.08	0.16
Surface emissivity [-] (Ihara et al. 2003)	0.96	0.91	0.95	0.93	0.95
Evaporation efficiency [-] (Ichinose et al. 1999)	0.05	0.05	0.30	1.00	0.30
Density [kg m^{-3}] (Ichinose et al. 1999)	2.4×10^3	2.1×10^3	1.8×10^3	1.0×10^3	1.8×10^3
Specific heat [$\text{J kg}^{-1} \text{K}^{-1}$] (Ichinose et al. 1999)	882	882	1176	4200	1176

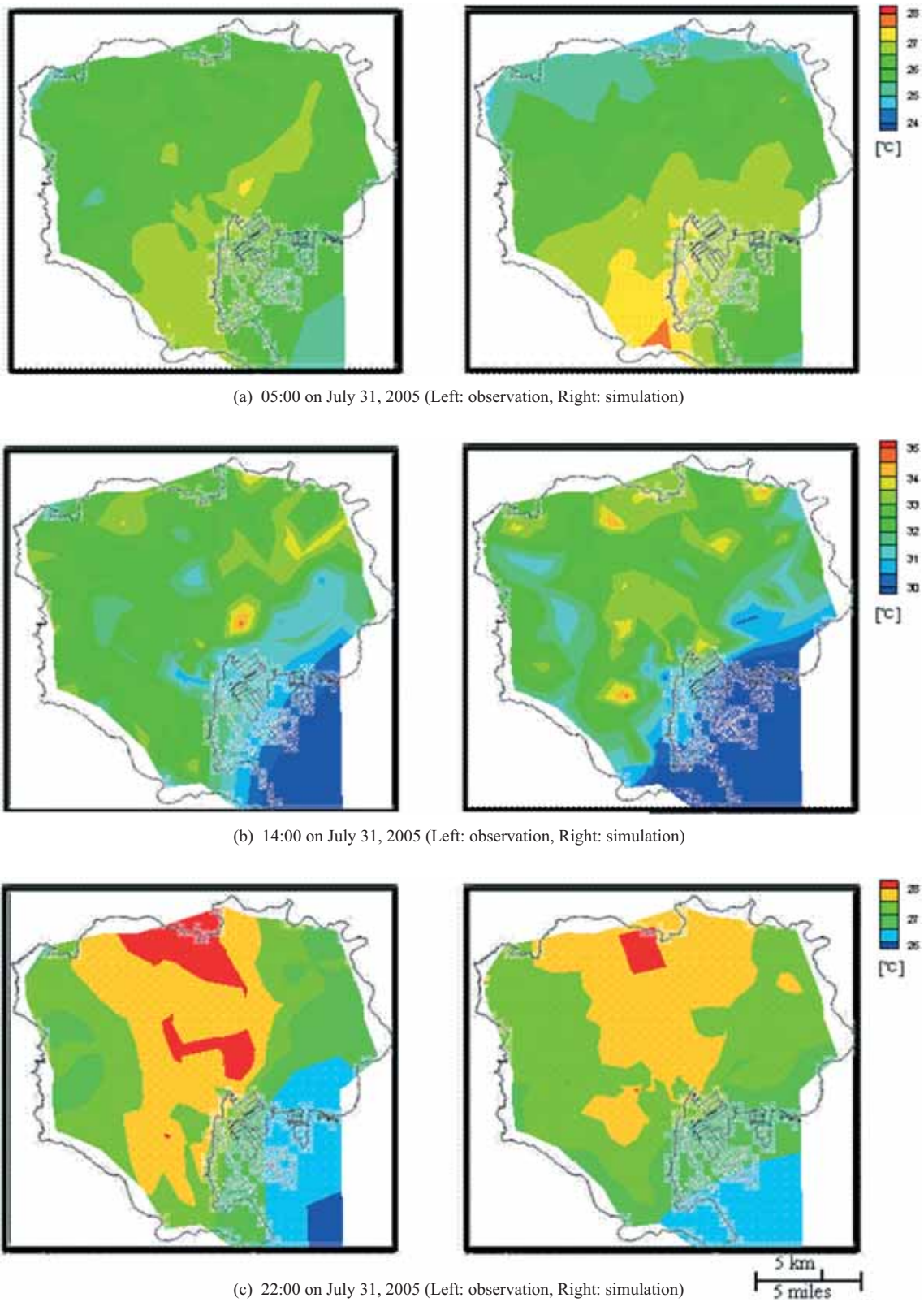


Fig. 2 Horizontal distribution of air temperature

Observation: observation data at 126 METROS observation points and one MOE observation point^[5]. Simulation: simulation results at 2 m above the ground at the observation points.

5. Future work

Figure 4 shows the pathlines of fluid particles that flow through the points at $Y = 18000$ m with 3000 m spacing in the X direction and 50 m spacing in the Z direction from $Z = 50$ m to 250 m at 05:00. Here, the color of the pathline indicates air temperature. Wind direction prevails from the north at $Y = 33000$ m. The figure shows that the pathlines reach near the height of the computational domain ($Z = 500$ m) in the region of 27°C or higher in Fig. 2 (a, Right). It is possible that the

overestimation of air temperature in this region is caused by the suppression of vertical mixing of heat due to the influence of the upper computational domain. The same symptom is confirmed in the distribution of pathlines at 14:00 (not shown here).

Therefore, we believe that to improve the reproducibility of the air temperature distribution, it is important to improve the reproducibility of the development of the atmospheric boundary layer. In the future, we plan to improve our simulation model to be able to deal with unsteady-state conditions. In addition, we

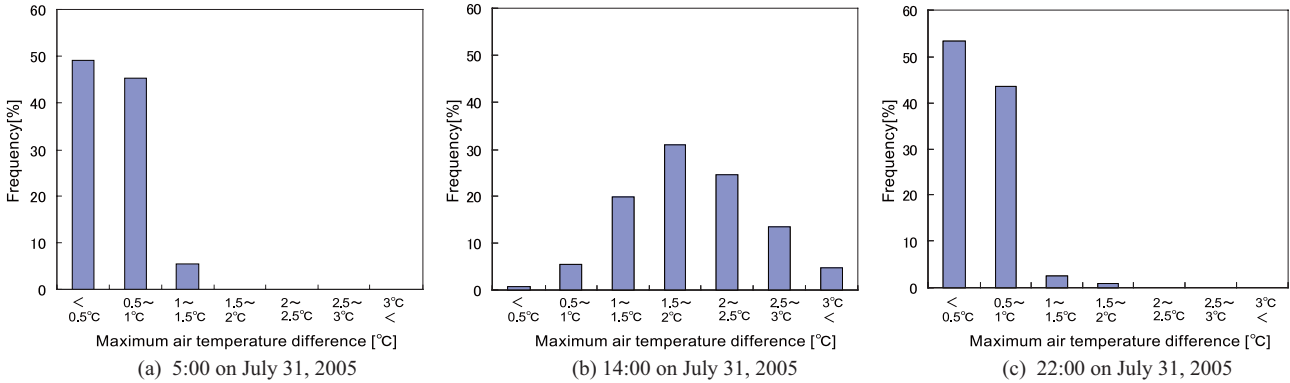


Fig. 3 Frequency distribution of the maximum difference in the simulated air temperatures in areas of $100\text{ m} \times 100\text{ m}$ at and around the observation points. (2 m above the ground).

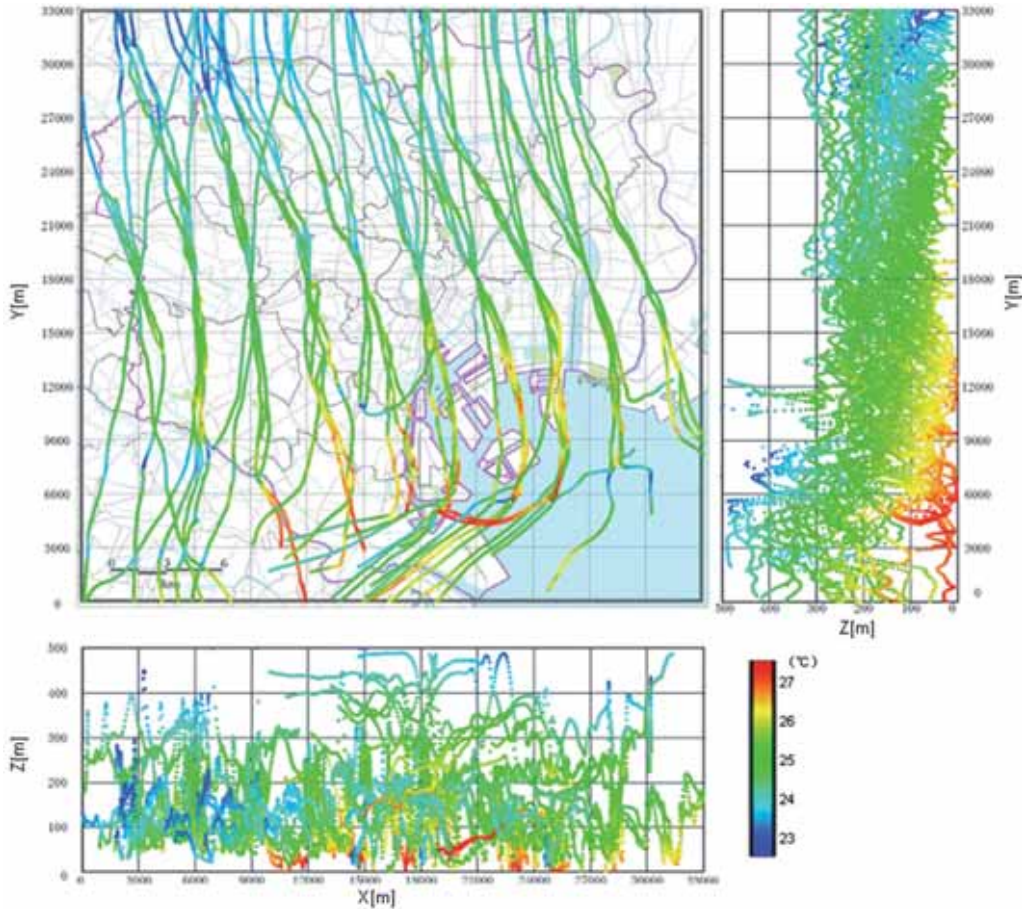


Fig. 4 Pathline distribution at 05:00 on July 31, 2005 (trajectory of a fluid particle that flows through points at $Y = 18000$ m with 3000 m spacing in the X direction and 50 m spacing in the Z direction from $Z = 50$ m to 250 m).

are planning to study the influence of the upper boundary of a computational domain.

6. Summary

We performed CFD simulations of air temperature fields in the entire area of the 23 special wards of Tokyo at 05:00, 14:00, and 22:00. By comparing the simulation results and the observations, we confirmed that both show the same air temperature distribution tendencies: at 14:00 and 22:00, air temperatures in the coastal areas were cooler than those in the inland areas; while at 05:00, air temperatures in the coastal areas were hotter than those in the inland areas. The root mean square errors of air temperature between simulation results and observations were 0.5°C at 05:00, 1.1°C at 14:00, and 0.4°C at 22:00, respectively.

References

- [1] K. Hirano, T. Kono, and Y. Ashie: "Large-scale CFD simulation of heat island phenomenon and countermeasures in Tokyo," Annual report of the earth simulator center April 2007-March 2008, The Earth Simulator Center (JAMSTEC), 2008.
- [2] T. Ichinose, K. Shimodozono, and K. Hanaki: "Impact of anthropogenic heat on urban climate in Tokyo," *Atmospheric Environment* 33: 3897-3909, 1999.
- [3] T. Ihara, H. Aida, Y. Yoshida, T. Handa, R. Matsuhashi, and H. Ishitani: "Evaluation of CO₂ Emissions Reduction Effect from the Building by Introducing High Light-Reflective and High Heat-Emissive Paint considering Urban Thermal Environment," Proc. 19th conf. on energy, Economy, and Environment, 655-660, 2003. (in Japanese)
- [4] S. Yoshida, S. Murakami, A. Mochida, R. Ooka, Y. Tominaga, and S. Kim: "Influence of green area ratio on outdoor thermal environment with coupled simulation of convection, radiation and moisture transport," *Journal of architecture planning and environmental engineering, Transactions of AIJ* 529: 77-84, 2000. (in Japanese)
- [5] Ministry of Environment: http://www.env.go.jp/air/life/heat_island/wm/index.html

東京 23 区の夏期昼夜間における熱環境の数値シミュレーション

プロジェクト責任者

足永 靖信 国土技術政策総合研究所

著者

足永 靖信 国土技術政策総合研究所

河野 孝昭 建築研究所

高橋 桂子 海洋研究開発機構 地球シミュレータセンター

東京 23 区全域を対象にして臨海部から内陸に至る 33km 四方の領域の熱環境について CFD 解析を実施した。個々の建築物を陽的に解像する為に水平メッシュ解像度を 5m とし、総メッシュ数は約 50 億である。夏期の 3 時刻(5 時、14 時、22 時)を対象にして解析を行い得られた気温分布を 127 点の観測値と比較した。各時刻の気温分布は観測と計算がほぼ一致した傾向を示し、内陸と比較すると 14 時と 22 時には湾岸地域の気温が低く、5 時には湾岸地域の気温が逆に高かった。RMS 誤差は 5 時 : 0.5 、 14 時 : 1.1 、 22 時 : 0.4 であった。風速の計算結果を用いて流跡線を作成し、東京 23 区における昼夜間の 3 次元的な流れ構造を検討した。ただし、今回の CFD 解析は定常状態を仮定しているため、より現実に近い条件で検討を進めるためには、モデルの非定常化を行うとともに、適切な解析領域高さを設定する必要がある。

キーワード: ヒートアイランド, CFD, 気温, 昼夜, 夏期, 東京 23 区

Study of Cloud and Precipitation Processes Using a Global Cloud-system Resolving Model

Project Representative

Masaki Satoh

Atmosphere and Ocean Research Institute, University of Tokyo / Research Institute for Global Change, Japan Agency for Marine-Earth Science and Technology

Authors

Masaki Satoh^{*1,2}, Hirofumi Tomita^{*1}, Tomoe Nasuno^{*1}, Akira T. Noda^{*1}, Shin-ichi Iga^{*1}, Hiroaki Miura^{*1,2}, Kazuyoshi Oouchi^{*1}, Hiroshi Taniguchi^{*1}, Yohei Yamada^{*1}, Wataru Yanase^{*2}, Chihiro Kodama^{*1}, Masayuki Hara^{*1}, Yasutaka Wakazuki^{*1}, Kazuaki Yasunaga^{*1} and Tatsuya Seiki^{*2}

*1 Research Institute of Global Change, Japan Agency for Marine-Earth Science and Technology

*2 Atmosphere and Ocean Research Institute, The University of Tokyo

In order to well understand the cloud-precipitation system over the globe, we have been conducting the global cloud resolving simulations. In this fiscal year, we updated several physical schemes to represent more precise mechanism of cloud and precipitation processes and validated the new schemes. Changing the microphysical scheme from three categories to six categories, the climatology of cloud is improved. Using the new schemes, we tried to conduct the simulation of typhoon Fengsheng, which is known as its difficult prediction. In this case, we found that the track is sensitive not only to the initial conditions but also to the planetary boundary layer scheme.

Keywords: cloud and precipitation processes, global cloud-system resolving model

1. Introduction

For the future precise projection of cloud-precipitation processes over the globe, it is very important to investigate and understand its essential processes in the present climate. Our subject is to clarify the essential mechanism of cloud-precipitation system over the globe, time scale of which ranges from the diurnal to the seasonal cycles. For this study, we use the global cloud-system resolving model NICAM (Satoh et al. 2008[1]) and conducts long integrations of half year for medium resolution (~10 km) and short integration of 10 days for the highest resolution (3.5 km).

Another important aspect of our project is collaboration with ongoing international observation projects, e.g., YOTC (Year Of Tropical Convection), AMY (Asia Monsoon Year). Comparing with observational data obtained by such observations, we quantitatively estimate our numerical results and exchange information each other. Furthermore, based on these knowledges, we improve the physical schemes of NICAM.

In FY2009, we first performed several sensitivity studies of newly implemented physical schemes, focusing on the cloud properties. After that, we mainly conducted the simulations of Typhoon Fengshen (TY0806), investigating the dependency of physical schemes and initial conditions.

2. Update of physical schemes in NICAM

From this fiscal year, we replaced several physical schemes by newly developed ones. For the microphysics, three categories scheme (Grabowski 1998[2]) is replaced by six categories Lin-type scheme (Tomita 2008[3]). For the PBL scheme, we implemented the Mellor-Yamada-Nakanizhi-Niino (MYNN) level 2.5 (Mellor and Yamada 1974[4], Nakanishi and Nino 2004[5], Noda et al. 2010[6]). The land process model is also changed from the bucket model to MATSIRO model (Takata et al. 2003[7]).

Figure 1 shows the comparison of results between old and new physics runs for the cloud amount by ISCCP simulator. The bias of lower cloud amount that appears in the old physics is drastically improved in the new physics. The mid-level cloud amount in the new physics is also improved over the tropical region. On the other hand, the upper cloud amount of the new physics increases slightly comparing with the old physics and seems to be worse than the old physic. However, we found that this upper cloud amount is sensitive to microphysics parameters, for example, the threshold value in the process of change from ice to snow, and it can be tuned by the relatively easy way. Figure 2 shows the zonal mean of ice water contents. This figure indicates that the new physics improves the excessive cloud ice

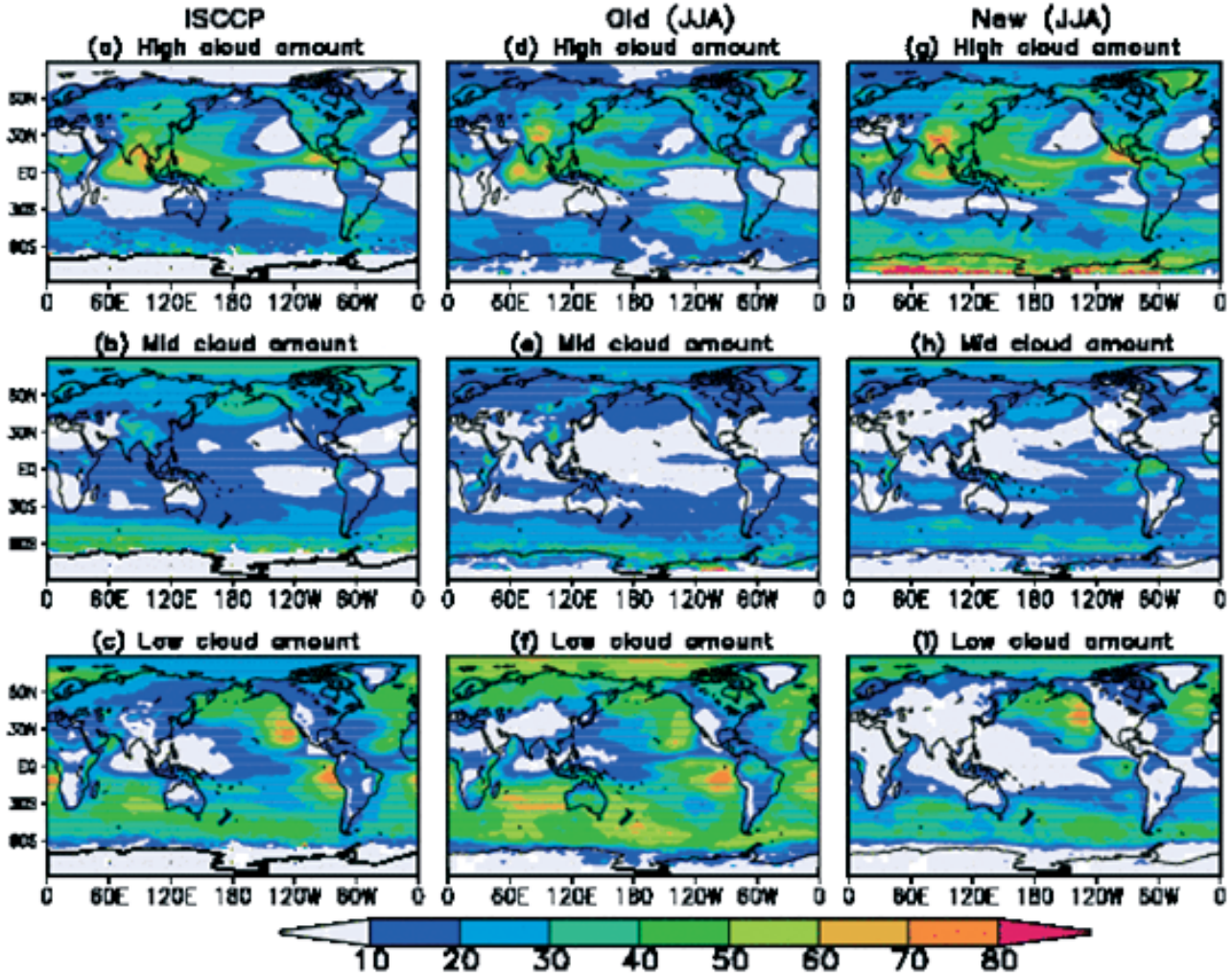


Fig. 1 The comparison of cloud amount between old and new physics runs and the observation (ISCCP).

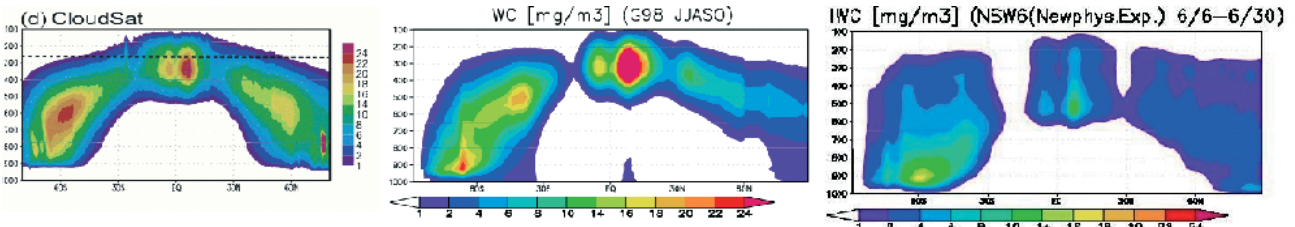


Fig. 2 The comparison of zonal mean ice water contents between old and new physics runs and the observation (CloudSat).

over the tropics that appears in the old physics.

3. Simulation of Typhoon Fengshen (TY0806)

In order to evaluate the performance of NICAM, series of simulations of field campaigns led by JAMSTEC (e.g., Mirai Indian Ocean cruise for the Study of the MJO-convection Onset [MISMO], Pacific Area Long-term Atmospheric observation for Understanding of climate change [PALAU] 2008) have been executed. In FY2009, we have conducted numerical simulations of typhoon Fengshen (TY0806), generation process of which had been observed during intensive observation period of PALAU2008 (Yamada et al. 2009[8]). The observation period was also included in an international project Year of Tropical Convection (YOTC). Research collaboration and contributions

to international community is planned with the simulations of Fengshen.

Fengshen is known as one of the most difficult typhoons to forecast their tracks in 2008 (Fig. 3). Based on studies using NICAM with stretched grid system (Yanase et al., 2009[9], Fig. 3, red line), we have investigated sensitivity of typhoon tracks to turbulent processes in the model.

The simulations were performed with horizontal mesh size of 14 km and vertically 40 layers for 10-day period. Physical processes were renewed as described in section 2. As to the turbulent processes, MYNN level 2 / 2.5 schemes were used for sensitivity study. The level 2 scheme was used as default (hereafter referred to as ‘standard mixing’). In this study vertical diffusion coefficient used for level 2.5 scheme leads to larger

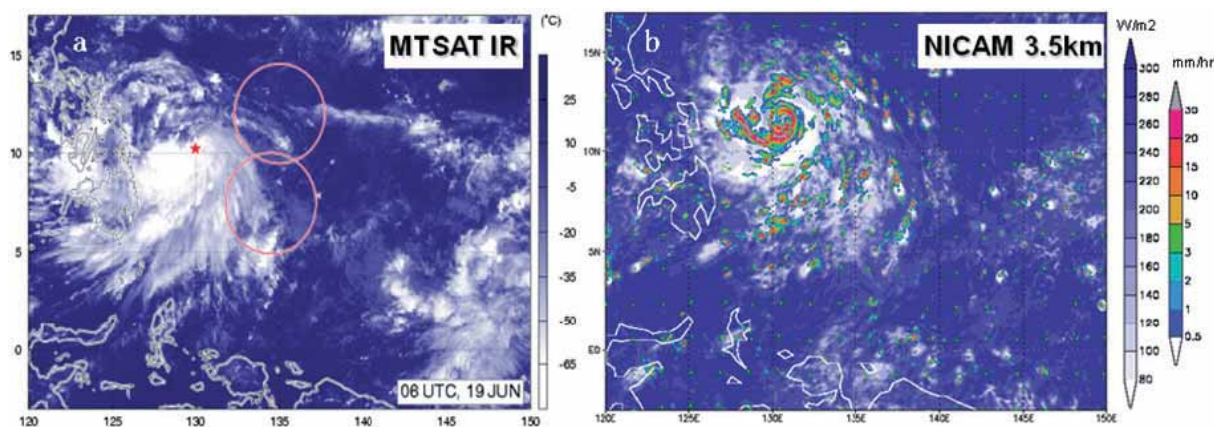


Fig. 6 Horizontal view of Fengshen (a) observed by Multi-functional Transport Satellite (MTSAT) and (b) simulated by 3.5-km mesh NICAM. In (b) color shows surface rainfall intensity.

title of which is "Development of a High-Resolution Coupled Atmospheric-Ocean-Land General Circulation Model for Climate System Studies". In order to enhance the understanding of the cloud process using the global cloud-system resolving model NICAM, the current project study derived from it and was restarting from this fiscal year, based on the results from the previous project. In this year, we first replaced the old physical schemes by the new ones to more precisely represent the cloud-precipitation system over the globe. The climatology for the new physics is in good agreement with observation, comparing with the old ones. We were mainly focusing on the Typhoon Fengshen and performed the several simulations changing the resolution, initial conditions, and physical schemes. We found that in this difficult prediction case the results depends not only on initial condition but also on the planetary boundary schemes. The results will be discussed much more intensively with the other international communities.

We also continue to analyze the simulation data which are not only obtained in this year but also obtained in the ES era. Especially, the convective momentum transports in the Madden-Julian Oscillation are currently analyzed. The diurnal cycles over the ocean and land are also intensively examined. Although we cannot describe the detail of the analysis due to space limitation, we will report them for the other publications or the next year report.

References

- [1] Satoh, M., T. Matsuno, H. Tomita, H. Miura, T. Nasuno, and S. Iga, "Nonhydrostatic Icosahedral Atmospheric Model (NICAM) for global cloud resolving simulations", *J. Comput. Phys.*, doi:10.1016/j.jcp.2007.02.006, the special issue on Predicting Weather, Climate and Extreme events. 2008
- [2] Grabowski, W. W., "Toward cloud resolving modeling of large scale tropical circulation: A simple cloud microphysics parameterization", *J. Atmos. Sci.*, 55, 3283-3298.
- [3] Tomita, H., "New microphysics with five and six categories with diagnostic generation of cloud ice," *J. Meteor. Soc. Japan*, 86A, 121-142, 2008
- [4] Mellor, G. L and T. Yamada, "A hierarchy of turbulence closure models for planetary boundary layers," *J. Atmos. Sci.*, 61, 1521-1538, 1974.
- [5] Nakanishi, M. and H. Niino, "An improved Mellor-Yamada Level-3 model with condensation physics: Its design and verification," *Boundary-Layer Meteor.*, 112, 1-31, 2004.
- [6] Noda, A. T., K. Oouchi, M. Satoh, H. Tomita, S. Iga, and Y. Tsushima, "Importance of the subgrid-scale turbulent moist process: Cloud distribution in global cloud-resolving simulations," *Atmos. Res.*, 96, 208-217, doi, "10.1016/j.atmosres.2009, 2010.
- [7] Takata K., S. Emori and T. Watanabe, "Development of the minimal advanced of the surface interaction and runoff," *Global Planetary Change*, 38, 209-222, 2003.
- [8] Yamada, H., W. Yanase, R. Shirooka, K. Yoneyama, M. Satoh, and M. Yoshizaki, "Observation and numerical simulation of generation process of TY0806 (Fengshen)," 95, A204, Spring meeting of Meteorological Society of Japan, Tsukuba, 28-31 May, 2009.
- [9] Yanase, W., H. Hamada, M. Satoh, and A. T. Noda, "Simulation of generation process of Typhoon Fengshen (2008)," 95, P399, Spring meeting of Meteorological Society of Japan, Tsukuba, 28-31 May, 2009.

全球雲解像モデルを用いた雲降水プロセス研究

プロジェクト責任者

佐藤 正樹 東京大学 大気海洋研究所

海洋研究開発機構 地球環境変動領域

著者

佐藤 正樹^{*1,2}, 富田 浩文^{*1}, 那須野智江^{*1}, 野田 暁^{*1}, 伊賀 晋一^{*1}, 三浦 裕亮^{*1,2},
大内 和良^{*1}, 谷口 博^{*1}, 山田 洋平^{*1}, 柳瀬 亘^{*1}, 小玉 知央^{*1}, 原 政之^{*1},
若月 泰孝^{*1}, 安永 数明^{*1}, 清木 達也^{*2}

*1 海洋研究開発機構 地球環境変動領域

*2 東京大学 大気海洋研究所

全球での雲降水システムのよりよい理解のため、我々はこれまで、全球雲解像シミュレーションを行ってきた。今年度は、より正確な雲降水プロセスを表現するため、物理過程のいくつかについてスキームを刷新し、テストを行った。雲微物理スキームを3カテゴリースキームから6カテゴリースキームに変更したところ、雲量についての気候値が改善した。これらの新しいスキームを使って、台風 Fengshen の計算を行った。この台風は進路の予測が難しいことで知られているものである。様々な初期条件と物理スキームを使って計算を行ったところ、このケースの場合、進路は、初期条件だけではなく、境界層スキームに非常に依存することが分かった。この Fengshen 再現実験においては、最高解像度の 3.5km の実験も実施し、現在解析中である。

キーワード: 雲降水プロセス, 全球雲解像モデル

Observing System Research Using Ensemble-based Data Assimilation Methods

Project Representative

Takeshi Enomoto

Earth Simulator Center, Japan Agency for Marine-Earth Science and Technology

Authors

Takeshi Enomoto^{*1}, Takemasa Miyoshi^{*2}, Jun Inoue^{*3}, Qoosaku Moteki^{*3}, Miki Hattori^{*3} and Shozo Yamane^{*4}

*1 Earth Simulator Center, Japan Agency for Marine-Earth Science and Technology

*2 Department of Atmospheric and Oceanic Science, University of Maryland

*3 Research Institute for Global Change, Japan Agency for Marine-Earth Science and Technology

*4 Department of Environmental Systems Science, Doshisha University

A data assimilation system for global atmospheric observations has been developed using an ensemble method. This system is composed of the Atmospheric General Circulation model for the Earth Simulator (AFES) and the Local Ensemble Transform Kalman Filter (LETKF). It assimilates global atmospheric observations from public data archives efficiently on the Earth Simulator. The new architecture of the renovated Earth Simulator required re-optimization of AFES and LETKF. The dynamical core of the AFES has been optimized to run twice as fast. The optimized version of LETKF achieved a bump of more than three times. A stream from 1 January 2008 is being conducted to give preliminary results. Smoother fields in the polar regions are achieved by the updated LETKF. Predicted precipitation compares well with satellite observations. Analysis error estimated as analysis ensemble spread is used to evaluate atmospheric observations and to study atmospheric predictability. Observing system experiments are conducted to clarify the influence of pressure observations by Arctic drifting buoys and to identify the planetary-scale propagation of the impact of additional dropsonde observations in the Indian Ocean. Precursory signals are found in various atmospheric phenomena in which the analysis ensemble spread increases prior to the events.

Keywords: Atmospheric General Circulation Model, Ensemble Kalman Filter, Observing System Experiment, Atmospheric Predictability, Optimization

1. Introduction

Japan Agency for Marine-Earth Science and Technology (JAMSTEC) conducts field campaigns in many parts of the world every year. In order to better capture the climate system of the Earth as a whole not only the observations of ocean and atmosphere by research vessels and buoys but also those of land and cryosphere are becoming increasingly important. In addition in-situ and remote sensing observations are investigated by researchers at JAMSTEC. The aim of the project is to apply the simulation techniques to help evaluating the various observations and to develop methodologies for observing system design.

The observing systems are defined by types, distributions, intensity and frequency of observations. Traditionally the observing systems are designed based on the feature of the phenomena in question. The data assimilation system provides an objective tool for designing an optimal observing system.

To achieve our aim an ensemble-based data assimilation

system is developed. First it is applied to the assimilation of global atmospheric observations and then it will be applied to other data such as greenhouse gases, land or cryospheric data. Ensemble-based techniques have advantages in assimilating various processes in the climate system since it does not require adjoint models. The climate system, or even a component of it, is so complex that the adjoint models required by the variational techniques are difficult to obtain.

Another important task of the project is evaluation of observations. The value of observations in a particular field campaign is quantified in experiments to test sensitivity to input observations (observing system experiments, OSEs). The analysis error is obtained as the analysis ensemble spread in an ensemble-based data assimilation system. The change in the analysis error represents improvement or degradation of the analysis in OSEs.

The multi-year plan of the project is as follows:

- production of ensemble global atmospheric datasets,

- evaluation of field campaigns by OSEs and
- application of the ensemble-based data assimilation techniques to greenhouse gases, land or cryosphere data.

For the fiscal 2009, 2-year global atmospheric analysis and about 1.5-year equivalent of OSEs and the development of ensemble-based data assimilation techniques were planned. However we were unable to conduct our research and development as scheduled due to a delay in the development of the data assimilation system. After finding a problem related to a compiler bug and applying a workaround, preliminary assimilation experiments from 1 January 2008 were conducted. The delay hindered production runs and OSEs.

The plan of this report is as follows. The overview of the data assimilation system is given and optimization for the Earth Simulator 2 is described in Section 2. Scientific achievements are outlined in Section 3. Concluding remarks are found in Section 4.

2. Development of an ensemble data assimilation system

2.1 System overview

The atmospheric data assimilation system is composed of AFES [1] [2][3] and LETKF [4] [5] [6] [7]. Both AFES and LETKF are updated from those used to produce ALERA (AFES-LETKF experimental ensemble reanalysis) [6]. The planned dataset to be produced with the new system will be called ALERA2. The specifications of ALERA and ALERA2 are summarized in Table 1.

The horizontal resolution is somewhat coarser (about 100 instead of 80 km). The T119L48 (triangular truncation wavenumber at 119, 48 model levels) is used in other simulations such as CFES mini [8] and parameters in physical schemes are determined through experiments. The AFES 3.x [9] T119L48 outperforms AFES 2.x T159L48 used in ALERA in forecast experiments of August 2004. Improvements can be mainly attributable to introduction of the new grid condensation scheme. In addition a more sophisticated the land surface scheme MATSIRO [10] is used to obtain land variables.

The ensemble size is increased from 48 to 63. In addition

Table 1 Specifications of ALERA and ALERA2.

	ALERA [6]	ALERA2
Resolution	T159L48	T119L48
Ensemble size	40	63
Covariance localization	21x21x13	400km/0.4 ln p
Spread inflation	0.1	
Observation dataset	JMA	NCEP
SST	NOAA 1° weekly OI [12]	NOAA 1/4° daily [13]

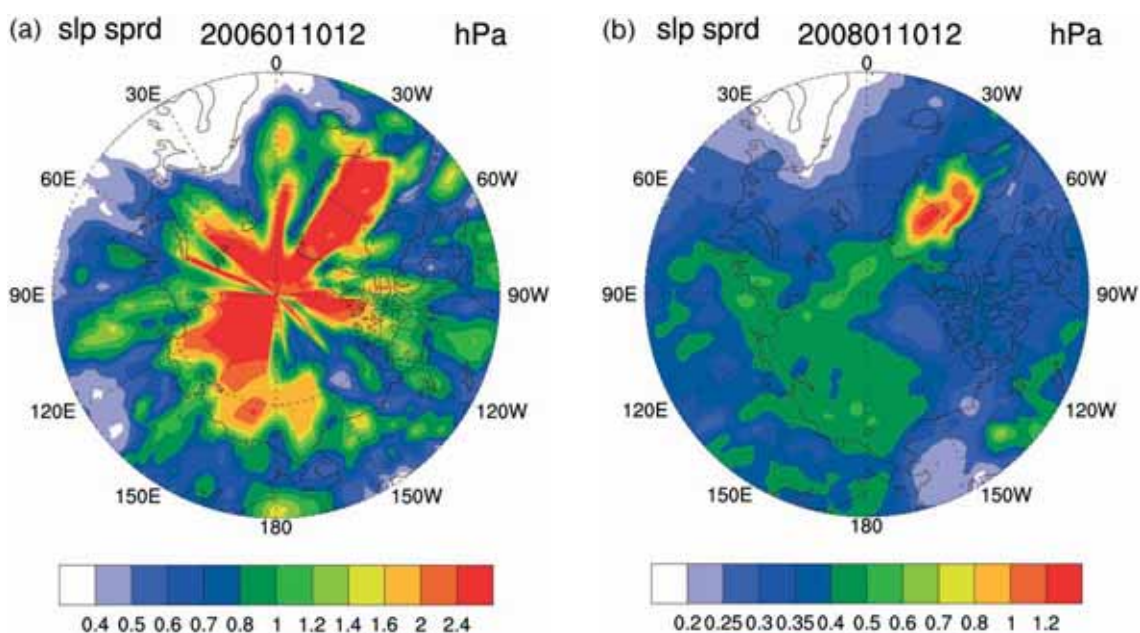


Fig. 1 Snapshots of the analysis ensemble spread of the sea-level pressure (hPa) (a) in ALERA (12 UTC 10 January 2006) and (b) in ALERA2 (12 UTC 10 January 2008). The choice of the date is arbitrary.

the control run from the ensemble mean is conducted. The differences between the guess (6-hr forecast without assimilation) mean and the control indicate the nonlinearity.

The new LETKF assimilates observations with weights based on physical distances without local patches [7] (Fig. 1). ALERA suffers from discontinuities of the analysis ensemble spread of the sea-level pressure due to the local patches converging toward the pole. Such noise is absent in ALERA2 and the analysis ensemble spread is smooth in the polar regions.

ALERA provides the analysis and guess of prognostic

variables (wind, temperature, dew point depression) and limited diagnostic variables (geopotential height and sea-level pressure) [6]. As a result the investigation tends to be limited within the dry dynamics. In ALERA2 6-hr forecast of selected variables such as precipitation and surface fluxes are provided. Figure 2 shows daily total (grid-scale and convective) precipitation. Although there are differences in the representation of weak rain, the simulated precipitation associated with extratropical cyclones and tropical convection compares very well with satellite estimates [11] both in terms of distribution and in

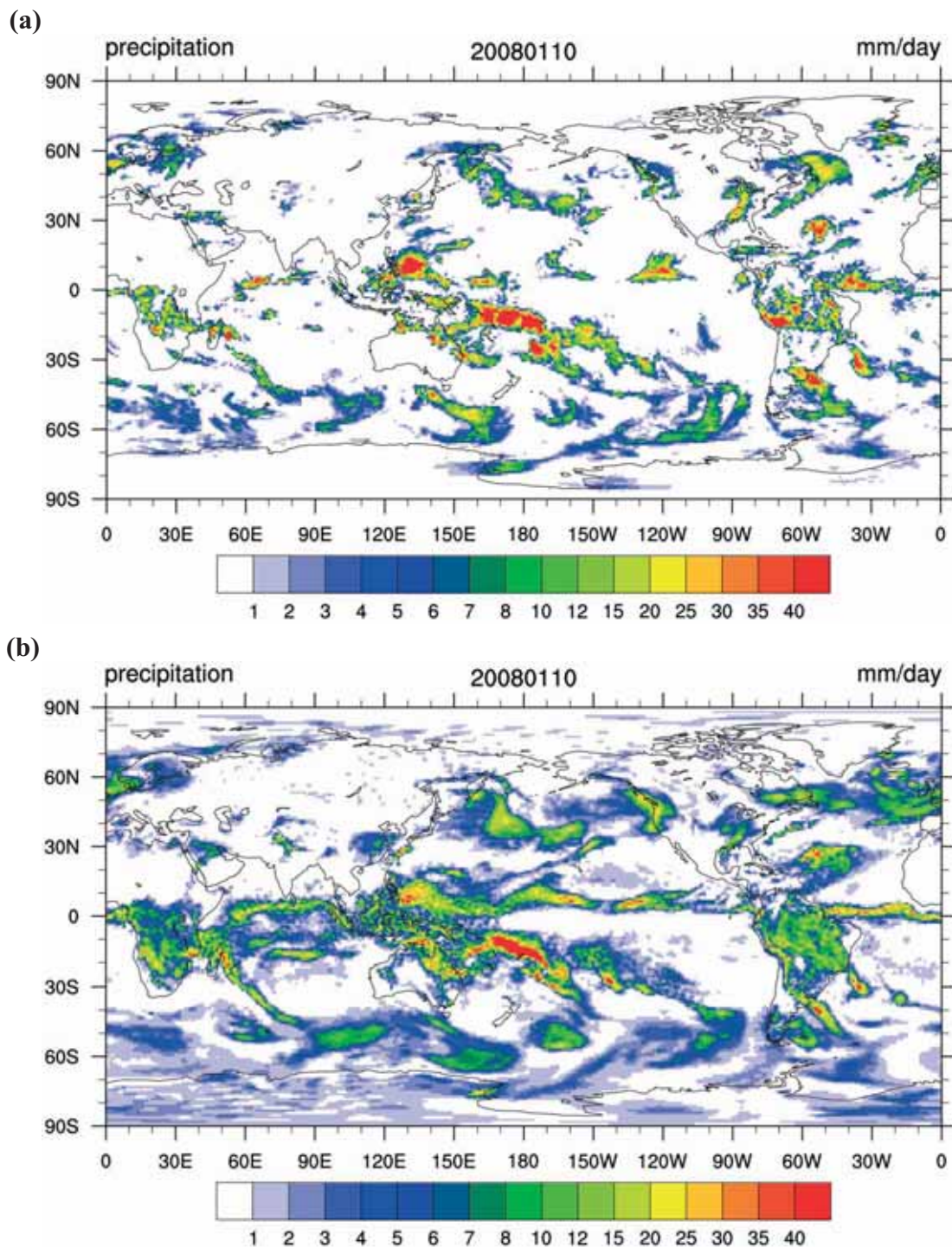


Fig. 2 Daily precipitation of 10 January 2008 from (a) Global Precipitation Climatology dataset [11] and ALERA2.

intensity. Increase of output variables encourages investigation of statistical features of atmospheric phenomena that are represented in physics schemes such as radiation, condensation and convection.

Global atmospheric observations compiled by the National Centers for Environmental Prediction (NCEP) are obtained from the University Corporation for Atmospheric Research (UCAR). This dataset includes most of the observations used for numerical weather prediction at NCEP. ALERA [6] uses the National Oceanic and Atmospheric Administration (NOAA) optimum interpolation (OI) 1° weekly sea-surface temperature (SST) dataset [12]. ALERA2 uses a spatiotemporally higher resolution NOAA 1/4° daily OI SST [13].

2.2 Optimization

Eight nodes are used to produce 64 member ensemble forecast. Thus each processor runs a process of AFES and intra-node parallelism (i.e. microtasking) is not used. AFES is shared by a few projects and optimization has been done collaboratively. In this project the dynamical core has been optimized. In the Legendre analysis some work arrays are eliminated to reduce memory access. The manual unrolls in the Legendre synthesis are replaced by the matrix-vector multiplication calls. The associated Legendre functions now stored by even or odd of $n+m$ and their derivatives are eliminated and replaced by the recurrence formula. Note that other methodologies may help at other resolutions since the optimizations above are adhoc and are found by trial and error. As a result of optimization one-day integration of AFES T119L48 takes 29 s a half of 58 s required by the unoptimized

version.

LETKF suffered from a serious problem: LETKF failed produce analysis in several upper layers. The optimization flags were found to cause the problem. Unoptimized LETKF produced reasonable analysis but run significantly slower to retard efficient development. A workaround was then found to use BLAS rather than macro replacements by the compiler. In addition loops of the number of the observations are expanded for vectorization. The optimized LETKF run more than three times faster (1,267 s vs 4,046 s) with real observations.

3. Scientific achievements

3.1 Observing system experiments Observing system experiments

The pressure observation in the Arctic Ocean is mainly conducted by Arctic drifting buoys. An OSE to evaluate pressure observations has been conducted for about a half years to reveal its importance [14] [15]. The influence is not limited to the surface but extends the lower troposphere as shown in Fig. 3 [14]. Information from ALERA has been used to determine the location of POPS (Polar Ocean Profiling System) buoys installed by JAMSTEC. Our findings have attracted attention of the International Arctic Buoy Programme (IABP).

OSEs have been conducted to evaluate sonde observations conducted during MISMO (Mirai Indian Ocean cruise for the Study of the MJO-convection Onset) [16]. These observations act to reduce the analysis error near the observation sites in the central Indian Ocean (Fig. 4a, b). The difference between the two indicates that the improvement extends globally in the form of equatorial waves. The eastern flank of the influence reaches

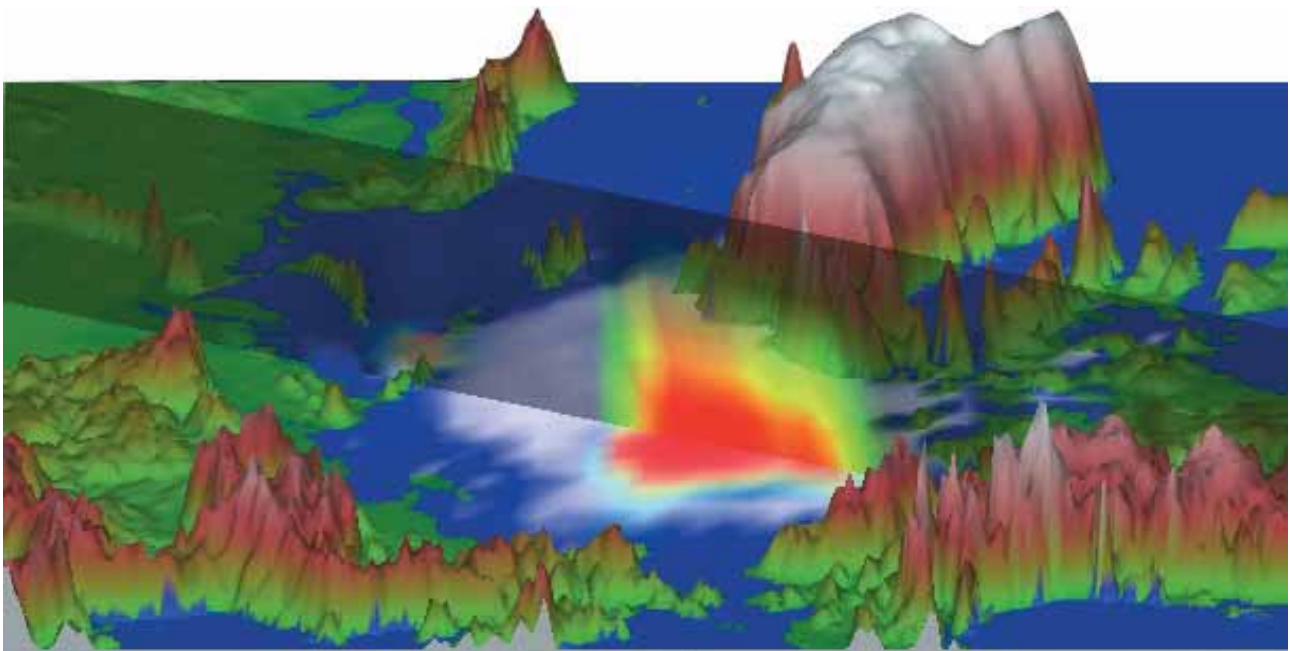


Fig. 3 Three-dimensional visualization of the difference in ensemble spread of the sea-level pressure and in the geopotential height field [15]. In the diagram, the warmer the color, the lower the accuracy of estimates, due to removal of observations. Sea-level pressure observations affect the estimates of geopotential height fields and temperature in the lower troposphere. Sea ice is drawn in white.

the western Pacific and affects the representation of the typhoon genesis.

3.2 Atmospheric predictability

The ensemble analysis is useful in the research on atmospheric predictability. The analysis error is similar to the bred vector and contains information on nonlinear growth. The analysis error is expected to be realistic since it is distributed around the analysis ensemble mean, which is the best estimate of the truth. Investigation of the analysis ensemble spread reveals the increase of the analysis ensemble spread prior to the onset of various atmospheric phenomena: typhoon genesis, westerly bursts, monsoon onset and even stratospheric sudden

warming [17].

In the Southern Vietnam the north easterlies and westerlies prevail during the winter and summer monsoons, respectively. Figure 5 shows the 30-day running average of the zonal wind and its analysis error in this region. Prior to the set up of the westerly core with its vertical extension the analysis error increases in the middle troposphere. Although the precursory signals are expected features implied by the linear perturbation theory the precise mechanisms behind the phenomena are not yet known and requires further studies. Increased output variables in ALERA2 will help investigations.

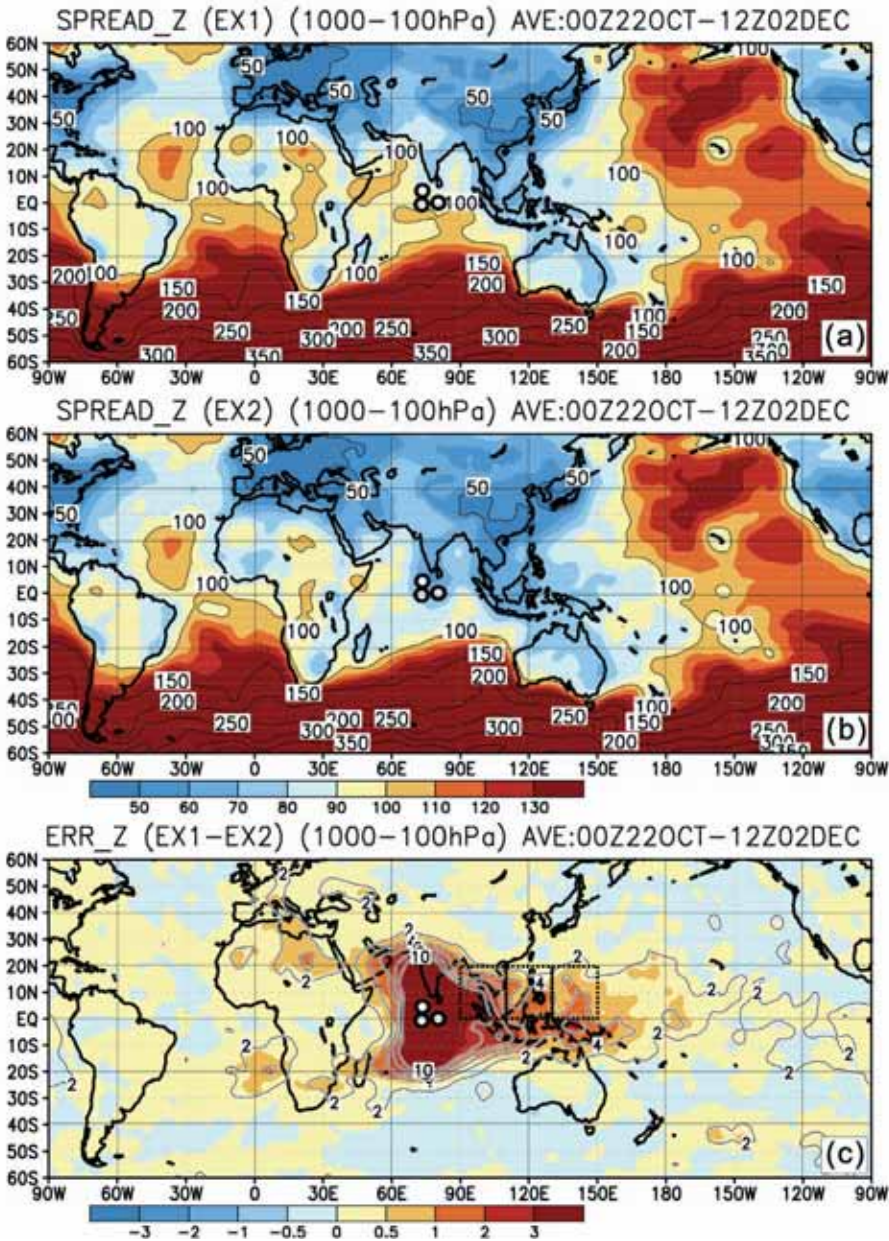


Fig. 4 Distribution of the analysis ensemble spread of the geopotential height vertically integrated from 1000 to 10 hPa and averaged during 0 UTC 22 October and 12 UTC 2 December 2006 (a) in ALERA, (b) in ALERA with additional sonde observations and (c) the difference between the two ((a)-(b)) [16]. The three open circles at the centre of each panel are the observation sites.

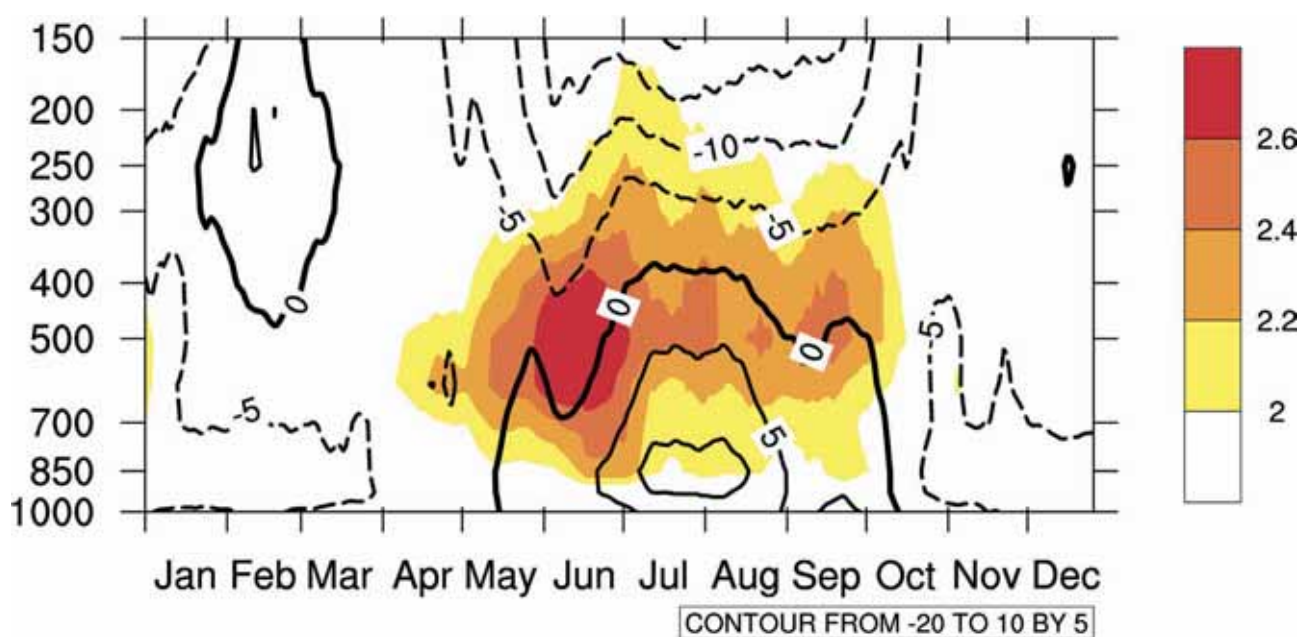


Fig. 5 The 30-day running average of the zonal wind (contour) and its analysis error (colour shades) in the Southern Vietnam (10–15°N, 107.5°–110°E). Produced by M. Hattori [17].

4. Concluding remarks

An ensemble-based data assimilation system has been developed using updated versions of AFES and LETKF. The code has been optimized for the new Earth Simulator to obtain 2x to 3x speed up. Preliminary results show realistic distribution of atmospheric variables including precipitation and much smoother analysis ensemble spread in the polar regions. OSEs conducted with the original Earth Simulator are investigated to obtain new insights into the polar and equatorial dynamics. ALERA has been investigated to identify precursory signals are found in various atmospheric phenomena. Delayed production runs and OSEs will be conducted in the new fiscal year. Applications of the ensemble methods to cryosphere, land and greenhouse gases are being prepared and data assimilation experiments are planned on the Earth Simulator.

Acknowledgement

ALERA was produced under the collaboration among the Japan Meteorological Agency, Japan Agency for Marine- Earth Science and Technology, and Chiba Institute of Science. The atmospheric observation datasets are compiled by the National Centers for Environmental Prediction and obtained from the data archive at the University Corporation for Atmospheric Research (UCAR), USA. The National Oceanic and Atmospheric Administration optimum interpolation 1/4 degree daily sea surface temperature analysis (Reynolds et al. 2007) is also obtained from UCAR.

References

- [1] Numaguti, A., M. Takahashi, T. Nakajima, and A. Sumi, 1997: Description of CCSR/NIES atmospheric general

circulation model. *CGER'S supercomputer monograph report*, National Institute for Environmental Studies, **3**, 1-48.

- [2] Ohfuchi, W., H. Nakamura, M. K. Yoshioka, T. Enomoto, K. Takaya, X. Peng, S. Yamane, T. Nishimura, Y. Kurihara, and K. Ninomiya, 2004: 10-km mesh meso-scale resolving simulations of the global atmosphere on the Earth Simulator: Preliminary outcomes of AFES (AGCM for the Earth Simulator). *J. Earth Simulator*, **1**, 8-34.
- [3] Enomoto, T., A. Kuwano-Yoshida, N. Komori, and W. Ohfuchi, 2008: Description of AFES 2: Improvements for high-resolution and coupled simulations. In *High Resolution Numerical Modelling of the Atmosphere and Ocean*, K. Hamilton and W. Ohfuchi (eds.), chapter 5, pp. 77-97, Springer, New York.
- [4] Hunt, B., E. J. Kostelich and I. Szunyogh, 2007: Efficient data assimilation for spatiotemporal chaos: a local transform Kalman filter. *Physica D*, **230**, 112-126.
- [5] Miyoshi, T., S. Yamane and T. Enomoto, 2007: The AFES-LETKF experimental ensemble reanalysis: ALERA. *SOLA*, **3**, 45-48., doi:10.1029/2010GL042723.
- [6] Miyoshi, T. and S. Yamane, 2007: Local ensemble transform Kalman filtering with an AGCM at a T159/L48. *Mon. Wea. Rev.*, **135**, 3841-3861.
- [7] Miyoshi, T., S. Yamane and T. Enomoto, 2007: Localizing the error covariance by physical distances within a local ensemble transform Kalman filter (LETKF). *SOLA*, **3**, 89-92, doi:10.2151/sola.2007-023.
- [8] Sasaki, H., T. Enomoto, N. Komori, A. Kuwano-Yoshida, K. Tsuboki, J. Inoue, B. Taguchi and W. Ohfuchi, 2009:

- Understanding and forecasting high-impact phenomena in the atmosphere and ocean. *Annual Report of the Earth Simulator Center April 2008–September 2008*, Earth Simulator Center, JAMSTEC, Yokohama, Japan, 23-28.
- [9] Kuwano-Yoshida, A., T. Enomoto and W. Ohfuchi: An improved PDF cloud scheme for climate simulations. *Quart. J. Roy. Meteor. Soc.*, in press.
- [10] Takata, K., S. Emori and T. Watanabe, 2003: Development of the minimal advanced treatments of surface interaction and runoff, *Global and Planetary Change*, **38**, 209-222.
- [11] Huffman, G. J., R. F. Adler, M. M. Morrissey, D. T. Bolvin, S. Curtis, R. Joyce, B. McGavock and J. Susskind, 2001: Global precipitation at one-degree daily resolution from multisatellite observations. *J. Hydrometeor.*, **2**, 36-50.
- [12] Reynolds, R. W., N. A. Rayner, T. M. Smith, D. Stokes and W. Wang, 2002: An improved in situ and satellite SST analysis for climate. *J. Climate*, **15**, 1609-1625.
- [13] Reynolds, R. W., L. Churning, T. M. Smith, D. B. Chelton, M. G. Schlax, and K. S. Casey, 2007: Daily high-resolution-blended analyses for sea surface temperature, *J. Climate*, **20**, 5473-5496.
- [14] Inoue, J., T. Enomoto, T. Miyoshi and S. Yamane, 2009: Impact of observations from Arctic drifting buoys on the reanalysis of surface fields. *Geophys. Res. Lett.*, **36**, L08501, doi:10.1029/2009GL037380.
- [15] Inoue, J. and T. Enomoto, 2009: Reduced Arctic Sea Ice Hinders Accurate Climate Monitoring—Impact of Depleted Arctic Drifting Buoy Network—, press release, Japan Marine-Earth Science and Technology, 2 April, Yokosuka, Japan.
- [16] Moteki, Q., K. Yoneyama, R. Shirooka, H. Kubota, K. Yasunaga, J. Suzuki, A. Seki, N. Sato, T. Enomoto, T. Miyoshi and S. Yamane: The influence of observations propagated by convectively coupled equatorial waves, *Q. J. Roy. Meteor. Soc.*, in revision.
- [17] Enomoto, T., M. Hattori, T. Miyoshi and S. Yamane, 2010: Precursory signals in analysis ensemble spread. *Geophys. Res. Lett.*, **37**, L08804, doi:10.1029/2010GL042723.

アンサンブル同化手法を用いた観測システムの最適化に関する研究

プロジェクト責任者

榎本 剛 海洋研究開発機構 地球シミュレータセンター

著者

榎本 剛^{*1}, 三好 建正^{*2}, 猪上 淳^{*3}, 茂木 耕作^{*3}, 服部 美紀^{*3}, 山根 省三^{*4}

*1 海洋研究開発機構 地球シミュレータセンター

*2 メリーランド大学 大気海洋科学部

*3 海洋研究開発機構 地球環境変動領域

*4 同志社大学 環境システム学科

シミュレーション技術を応用した観測システム研究を実施し、効率的な観測システムの設計に役立てるため、アンサンブル手法を用いた全球大気データ同化システムを開発した。このシステムは、地球シミュレータ用大気大循環モデル (AFES) と局所アンサンブル変換カルマンフィルタ (LETKF) から構成され、公開されている全球大気観測データを地球シミュレータ上で効率的に大気大循環モデルに同化することができる。本年度は、まず AFES 及び LETKF を更新された地球シミュレータに最適化した。AFES の力学過程は最適化の結果実行時間を半減させることに成功した。LETKF は最適化の結果 1/3 以下の実行時間を達成した。このシステムを用いて、2008 年 1 月 1 日からの同化実験を開始し、初期的な結果が得られた。LETKF の改良により、極付近のノイズが一掃された。降水量の 6 時間予報値は、衛星観測とよく対応している。アンサンブル同化手法を用いると、解析誤差がアンサンブルスプレッドとして推定される。解析誤差は、観測を評価し観測システム設計に役立てることができる。本年度は、北極海の漂流ブイによる気圧観測の影響が対流圏下層に広がっていることやインド洋での追加のゾンデ観測の影響が惑星規模に及ぶこと等を明らかにした。また、大気予測可能性に関し、さまざまな大気現象に先行して解析誤差が増大する現象を発見した。

キーワード: 大気大循環モデル, アンサンブル・カルマンフィルタ, 観測システム実験, 大気予測可能性, 最適化

Process Studies and Seasonal Prediction Experiment Using Coupled General Circulation Model

Project Representative

Yukio Masumoto

Research Institute for Global Change, Japan Agency for Marine-Earth Science and Technology

Authors

Jing-Jia Luo^{*1,2}, Wataru Sasaki^{*1,2}, Swadhin Behera^{*1,2}, Hirofumi Sakuma^{*1,2}, Takeshi Izumo^{*1}, Sebastien Masson^{*4}, Antonio Navarra^{*3}, Silvio Gualdi^{*3}, Simona Masina^{*3}, Alessio Bellucci^{*3}, Annalisa Cherchi^{*3}, Pascal Delecluse^{*5}, Gurvan Madec^{*4}, Claire Levy^{*4}, Marie-Alice Foujols^{*4}, Arnaud Caubel^{*4}, Guy Brasseur^{*6}, Erich Roeckner^{*6}, Marco Giorgetta^{*6}, Luis Kornbluh^{*6}, Monika Esch^{*6}, Toshio Yamagata^{*2} and Yukio Masumoto^{*1}

*1 Research Institute for Global Change, Japan Agency for Marine-Earth Science and Technology

*2 Application Laboratory, Japan Agency for Marine-Earth Science and Technology

*3 Centro Euro-Mediterraneo per i Cambiamenti Climatici, INGV

*4 Laboratoire D'oceanographie et du Climat (LOCEAN)

*5 Météo France

*6 Max Planck Institute for Meteorology

The SINTEX-Frontier coupled ocean-atmosphere GCM is developed under EU-Japan collaborative framework to understand the climate variability and predictability. After successfully predicting the third-in-a-row positive Indian Ocean Dipole (IOD) event of 2008, SINTEX-F1 realistically predicted the 2009 El Niño event and its termination. The model has been consistent in predicting all of the recent IOD and El Niño/Southern Oscillation events to become the leading climate prediction model in the world.

In addition to the real-time predictions, the model is used in sensitivity experiments to understand climate processes. In one such study, by activating and suppressing air-sea coupling in tropical Pacific and Indian Oceans in the SINTEX-F1 prediction experiments, it is found that the extreme IOD event of 1994 played a key role in driving the El Niño Modoki of that year. It is also noted that the El Niño Modoki occurs more frequently in recent decades, coincident with a weakened atmospheric Walker circulation. Extreme IODs may also significantly enhance El Niño events and their onset forecasts as found in this sensitivity study supported by an observational study. SINTEX-F1 model simulations were also used in several process studies to understand the role of air-sea interactions in regional climate variations.

Keywords: SINTEX-F1, IOD, ENSO, Prediction, 2009

1. INTRODUCTION

Climate variability in recent years has significantly affected socio-economic conditions in many parts of the world. The variability in the Indian Ocean seems to have changed recently. In a rare occasion in the history of climate research, we witnessed three consecutive positive Indian Ocean Dipole (IOD) events back to back from 2006 to 2008. This change in the IOD behavior has caused a huge deviation in the way the Indian Ocean used to influence surrounding regions. In 2007, Australian farmers lost billions of Australian dollars in spite of a La Niña development in the Pacific since the positive IOD of 2007 destroyed the La Niña-related favorable conditions over

the eastern part of Australia. The consecutive positive IOD events in 2006, 2007, and 2008 caused the serious "Big Dry" in southeastern Australia and prepared the background for the "Black Saturday" forest fires there in February 2009 (Yamagata and Behera 2009; Yamagata et al. 2009). Therefore, it has become very important to understand these decadal shifts in the IOD and El Niño/Southern Oscillation (ENSO) variations using available observation and numerical simulations.

The SINTEX-F1 coupled general circulation model (CGCM) has emerged as one of the leading CGCM in the world to provide real-time predictions of seasonal to interannual climate variations. The model has successfully predicted

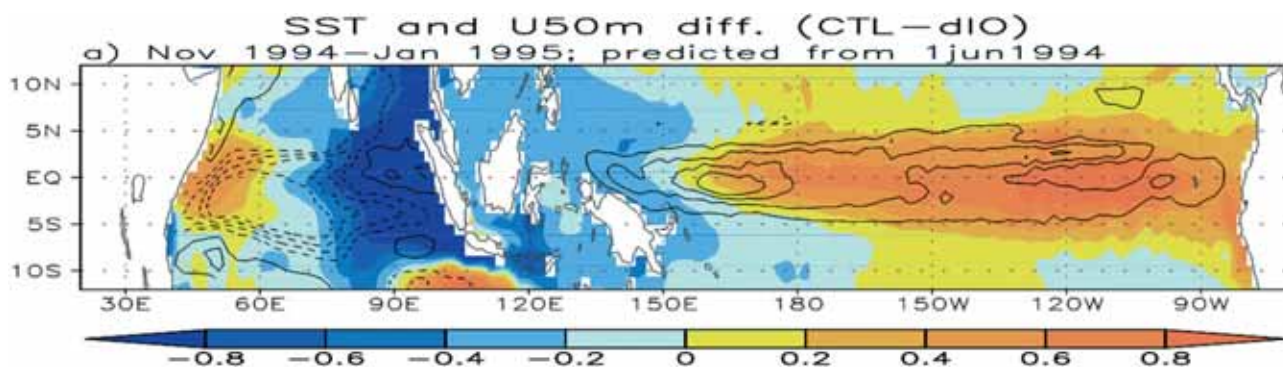


Fig. 1 Development of an El Niño Modoki event in 1994 associated with the positive IOD in the Indian Ocean from November 1994 to January 1995 period. Differences in anomalies of SST and surface zonal winds are shown in shading and contours respectively. The predictions were initiated on 1 June 1994.

all past ENSO and IOD events. In a recent study (Luo et al. 2010), it is also shown that the model is capable of predicting the ENSO Modoki, which is recently identified as one of the leading modes of variability in the tropical Pacific. In addition to the good predictions at long lead times, the realistic simulation results of SINTEX-F1 are helpful in understanding the processes associated with climate phenomena. Besides the climate variations in the tropical regions, the model results are useful in understanding the slow processes in higher latitudes. The high-resolution version of the model, the SINTEX-F2, is under development and the model results are expected to help in understanding of finer scale climate processes.

2. CLIMATE PREDICTIONS

Real time climate forecasts for 12 to 24 lead months are continuously performed by using SINTEX-F1 CGCM and

predictions are updated every month. The model has successfully predicted the evolution of the 2009 El Niño event following the La Niña conditions of 2008. In addition to the phase of the evolution, the model was able to realistically predict a moderate amplitude warm event in 2009 and its quick termination in early 2010. Because of its continuous success in the predictions of past IOD and ENSO events, the model predictions of the 2009 El Niño received a lot of attentions of news media and general public, in addition to the research community. The forecast results were distributed to many research scientists and operational forecast centers (e.g. IRI, APCC, CLIVAR, IIT) and made available to general public through the JAMSTEC website. The high performance of the real time forecasts were applauded by Australian (The Weekly Times) and Indian (The Hindu Business Line) news papers in addition to several news papers and television channels in Japan.

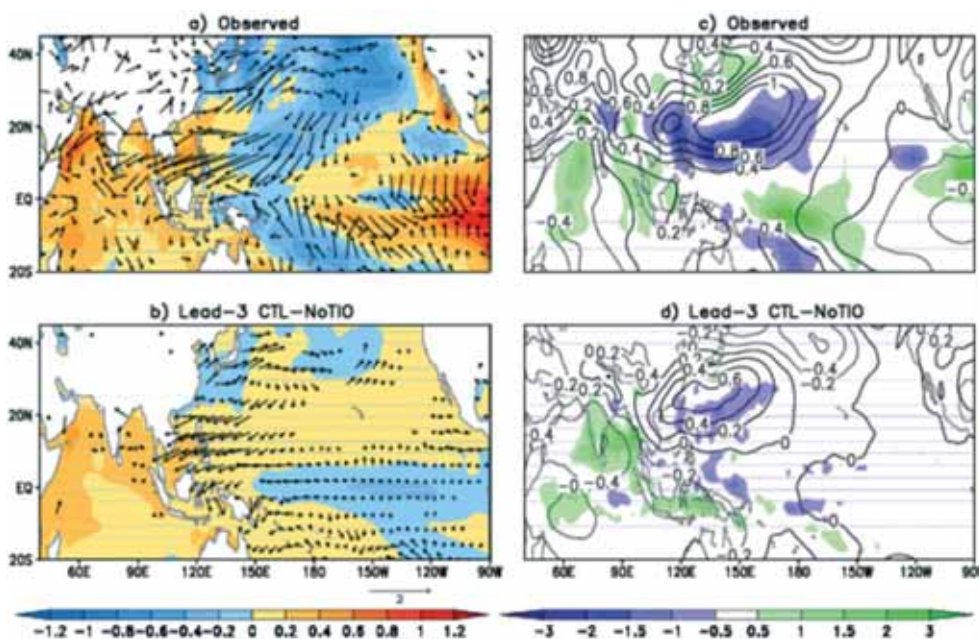


Fig. 2 Anomalies of a) observed SST and surface wind, and c) observed precipitation (shaded) and sea level pressure (contour) during June-August 1998. b-d) As in (a, b), but for the difference of model anomalies between control and no-Indian Ocean integrations at 3-month lead.

The model predictions were further tested by activating and/or suppressing air-sea coupling in tropical Pacific and Indian Oceans (Luo et al. 2010) to understand their individual and combined roles in ENSO and IOD developments. It is found that the extreme IOD event of 1994 played a key role in driving the El Niño Modoki event in that year (Fig. 1), which is in contrast to the traditional point of view, which suggests that El Niño dominates the Indo-Pacific climate variations. Luo et al. (2010) also noted that El Niño Modoki is more frequently observed in recent decades, coincident with a weakened atmospheric Walker circulation. Extreme IODs may also significantly enhance El Niño events and their onset forecasts as found in their analysis and that of Izumo et al. (2010), which was mainly based on observational data analysis.

3. PROCESS STUDIES

The simulation results of SINTEX-F1 CGCM were used in several process studies. Chowdary et al. (2009) found that the SINTEX-F1 retrospective forecasts capture major modes of atmospheric variability over the Northwest Pacific during June-August including a rise in sea level pressure, an anomalous anticyclone at the surface, a reduction in subtropical rainfall, besides increased rainfall over the northeast and East Asia. In the sensitivity experiment, when the sea surface temperature in the tropical Indian Ocean is fixed to monthly climatology, the Northwest Pacific anticyclone during June-August weakened considerably and condensed its westward extension (Fig. 2). Without an interactive tropical Indian Ocean, the anomaly correlation for anticyclone prediction dropped significantly. Several other studies have reported high performance of the SINTEX-F in the predictions of the intraseasonal variations including the monsoon intraseasonal oscillations (Wang et al. 2009; Lee et al. 2009, Ajayamohan et al. 2009). Further, these intraseasonal variations are shown to have interactions with

climate modes such as IOD and ENSO (Rao et al. 2009; Kug et al. 2009; Lin et al. 2009).

In another study of the tropical Atlantic, it is found that SINTEX-F1 produces a realistic pattern of precipitation variability there. Model simulations have reproduced the two rainfall maxima along the African coast and over the Gulf of Guinea (Fig. 3) realistically. However, the model simulated rainfall variability was found to be somewhat stronger than the observation. The model simulations also showed decent variability in SST off the Namibian/Angolan coast but almost no variability in equatorial cold tongue region.

4. SINTEX-F2 DEVELOPMENT

The real-time forecasts and model simulation studies were affected to some extent by the change in the computational environment following the installation of ES2 in place of ES1. Both SINTEX-F1 and SINTEX-F2 are being optimized to achieve higher level of computational performances on ES2. In the process of development, when ocean model resolution is increased to a quarter degree (ORCA025), it is found that biases related to the equatorial Pacific cold tongue and northern Atlantic are reduced besides better simulations of El Niño and IOD events. Several sensitivity experiments were also carried out to understand the role of vertical mixing parameterization in the behavior of the simulated cold tongue SST.

ACKNOWLEDGEMENT

We appreciate the support extended by the Earth Simulator in achieving our project goals.

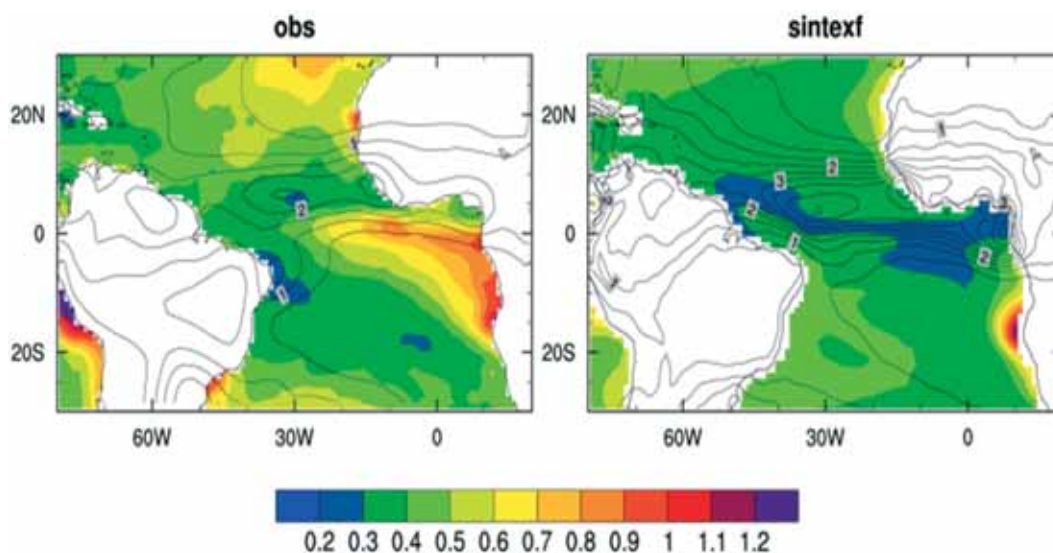


Fig. 3 Standard deviations of SST and precipitation from observations (left) and SINTEX-F simulations (right).

References

- [1] Ajayamohan, R. S., S. A. Rao, J.-J. Luo, and T. Yamagata, 2009: Influence of Indian Ocean Dipole on boreal summer intraseasonal oscillations in a coupled general circulation model. *JGR-Atmosphere*, 114, D06119, doi:10.1029/2008JD011096.
- [2] Chowdary, J. S., S.-P. Xie, J.-J. Luo, J. Hafner, S. Behera, Y. Masumoto, and T. Yamagata, 2009: Predictability of Northwest Pacific climate during summer and the role of the Tropical Indian Ocean. *Climate Dynamics*, DOI: 10.1007/s00382-009-0686-5.
- [3] Izumo T., J. Vialard, M. Lengaigne, C. de Boyer Montégut, S.K. Behera, J.-J. Luo, S. Cravatte, S. Masson, and T. Yamagata, 2010: Influence of the state of the Indian Ocean Dipole on following year's El Niño. *Nature Geoscience*, 3, 168 - 172.
- [4] Kug, J.-S., K. P. Sooraj, F.-F. Jin, and J.-J. Luo, 2009: Impact of Indian Ocean Dipole on fast atmospheric variability over the Indian Ocean. *Atmospheric Research*, 94, 134-139, DOI: 10.1016/j.atmosres.2008.10.022.
- [5] Lee, J.-Y., et al., 2009: How is the performance on mean climate related to seasonal prediction skill in coupled climate models? *Clim. Dyn.*, in press.
- [6] Lin, A., T. Li, X. Fu, and J.-J. Luo, 2009: Impact of air-sea interactions over the Indian Ocean on the climatological state of tropical atmospheric circulation in boreal summer. *Chinese J. Atmos. Sci.*, 33(6), 1123-1136.
- [7] Luo, J.-J., 2009: Indian Ocean Dipole [in "State of the climate in 2008"]. *Bull. Am. Meteor. Soc.*, 90, S92-S94.
- [8] Luo, J.-J., R. Zhang, S. Behera, Y. Masumoto, F.-F. Jin, R. Lukas, and T. Yamagata, 2010: Interaction between El Niño and extreme Indian Ocean Dipole. *J. Climate*, 23, 726-742.
- [9] Rao, S. A., J.-J. Luo, S. K. Behera, and T. Yamagata, 2009: Generation and termination of Indian Ocean Dipole events in 2003, 2006 and 2007. *Climate Dynamics*, 33, 751-767.
- [10] Wang, B., et al., 2009: Advance and prospectus of seasonal prediction: assessment of the APCC/CliPAS 14-model ensemble retrospective seasonal prediction (1980-2004). *Climate Dynamics*, 33, 93-117, DOI 10.1007/s00382-008-0460-0.
- [11] Yamagata T and S. K. Behera, 2009: International Symposium on the Application of Climate Information, *EOS*, 90, 17, p148.
- [12] Yamagata, T., J.-J. Luo, S. Masson, et al. 2009: Process studies and seasonal prediction experiment using coupled general circulation model. *Earth Science*, in press.

大気海洋結合モデルを用いたプロセス研究と季節予測実験

プロジェクト責任者

升本 順夫 海洋研究開発機構 地球環境変動領域

著者

羅 京佳^{*1,2}, 佐々木 亘^{*1,2}, スワディン ベヘラ^{*1,2}, 佐久間弘文^{*1,2}, タケシ イズモ^{*1},
 Sebastien Masson^{*4}, Antonio Navarra^{*3}, Silvio Gualdi^{*3}, Simona Masina^{*3}, Alessio Bellucci^{*3},
 Annalisa Cherchi^{*3}, Pascal Delecluse^{*5}, Gurvan Madec^{*4}, Claire Levy^{*4}, Marie-Alice Foujols^{*4},
 Arnaud Caubel^{*4}, Guy Brasseur^{*6}, Erich Roeckner^{*6}, Marco Giorgetta^{*6}, Luis Kornbluh^{*6}, Monika Esch^{*6},
 山形 俊男^{*2}, 升本 順夫^{*1}

*1 海洋研究開発機構 地球環境変動領域

*2 海洋研究開発機構 アプリケーションラボ

*3 Centro Euro-Mediterraneo per i Cambiamenti Climatici, INGV

*4 Laboratoire D'oceanographie et du Climat (LOCEAN)

*5 Meteo France

*6 Max Planck Institute for Meteorology

気候変動ならびにその予測可能性研究のための日欧研究協力に基づき、SINTEX-Frontier 大気海洋結合大循環モデルの開発を推進している。その第一版の SINTEX-F1 は、3年連続で発生したインド洋ダイポールモード現象 (IOD) の3年目に当たる2008年の IOD の予測に成功したばかりでなく、2009年に発生したエルニーニョ現象とその終息についても現実的に予測している。このモデルは、近年発生した全ての IOD およびエルニーニョ / 南方振動現象の予測で一定の成功を収めており、世界の気候変動予測研究を先導するモデルとしての地位を確立している。

また、SINTEX-F1 モデルは気候変動のメカニズムを解明するための感度実験などにも利用されている。熱帯太平洋あるいはインド洋での経年的な大気海洋結合過程を取り入れた場合と取り入れなかった場合の感度実験から、1994年に発生した非常に強い IOD が太平洋でのエルニーニョもどきの発生に対して重要な役割を果たしていることが示されると共に、インド洋での IOD が太平洋のエルニーニョ現象の発生とその後の発展に対しても寄与していることが明らかとなった。さらに、近年のウォーカー循環の弱化和関連して、エルニーニョもどきの発生が多発する傾向があることも分かった。

キーワード: SINTEX-F1, IOD, ENSO, 予測, 2009

Global Elastic Response Simulation

Project Representative

Seiji Tsuboi

Institute for Research on Earth Evolution, Japan Agency for Marine-Earth Science and Technology

Authors

Seiji Tsuboi

Institute for Research on Earth Evolution, Japan Agency for Marine-Earth Science and Technology

Akiko To

Institute for Research on Earth Evolution, Japan Agency for Marine-Earth Science and Technology

We pursue accurate numerical techniques to obtain theoretical seismic waves for realistic three dimensional (3-D) Earth models using Spectral-Element Method. We have tried to solve forward problem, that is, to calculate synthetic seismic waveform for fully 3-D Earth model. We introduce a heterogeneous region at Earth's core-mantle boundary by combining a small, strongly anomalous region to a large, weakly anomalous region. We calculate synthetic seismograms for this model and found that Sdiff phase, which is diffracted S-wave at core-mantle boundary, is followed by a significant postcursor. This is consistent with the anomalous Sdiff waveforms which sample beneath Hawaii. We use antipodal seismic observations to review the Earth's Core based on our synthetic seismograms. Our results imply that there may be anomalous structure at the Earth's inner core-outer core boundary.

Keywords: Synthetic seismograms, 3-D velocity structure of the Earth, Spectral Element Method

1. Evidence of a thick and localized ultra low shear velocity zone inside the Pacific slow region at the base of the mantle [5]

Prominent postcursors to S/Sdiff waves with delays as large as 26 s are observed in Northern America for Papua New Guinea events. These waves sample the northern side of the Pacific large low shear velocity province revealed by global shear velocity (V_s) tomographic models. The emergence of

the postcursors strongly depends on the epicenter-to-station azimuth, indicating that the waveforms are, in general, strongly affected by 3-dimensional (3D) heterogeneities. We limit our focus to an azimuthal range around 60° where the records show a relatively small azimuthal variation, suggesting a relatively small 3D effect there. In this azimuthal range we attempt 2D structural modeling along the great circle plane towards stations in southern US.

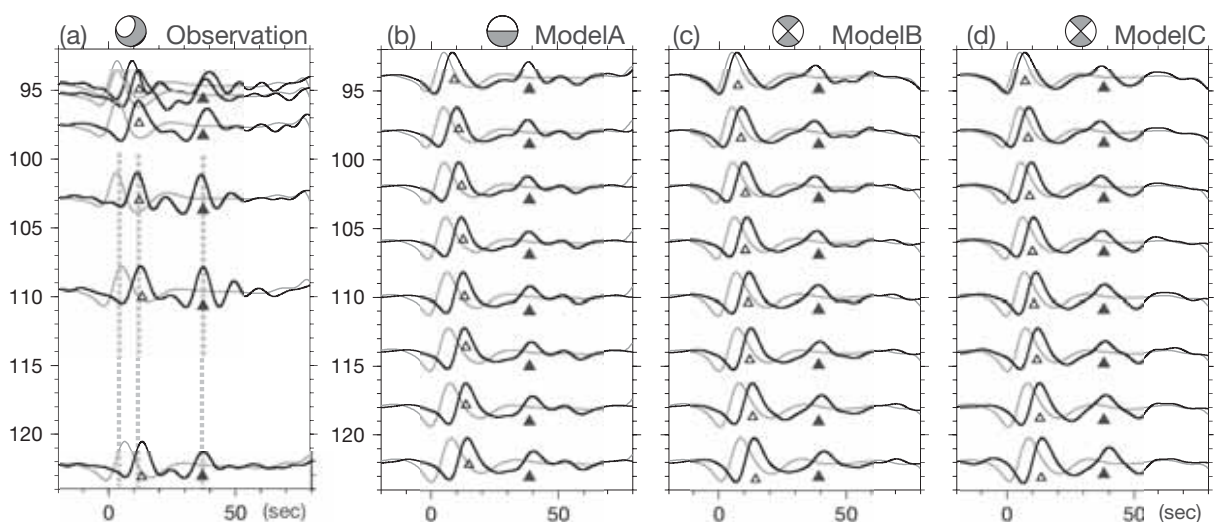


Fig. 1 (a) S/Sdiff waveforms of event 20030612 recorded at station azimuths between 60° and 63° are aligned in the order of distance and shown by solid lines [5]. The PREM synthetics are shown by grey lines. The main Sdiff phase and postcursor is indicated by open and solid reversed triangle. Three vertical grey dashed lines show a constant slowness of 8.3 s/deg fitted to the observed main Sdiff phase, postcursor and the synthetic Sdiff predicted by PREM. Each trace is normalized by its maximum amplitude. Records are bandpass filtered between 0.03 and 0.125 Hz. (b-d) Synthetic waveforms calculated by SEM for Model A, Model B and Model C [5]. They are filtered and normalized in the same way as for the observed waveforms. Model parameters are given in Table 1. Configuration of LWAR and SSAR of the three models are shown in Fig. 2 (b-d).

Figure 1a shows observed Sdiff waveforms obtained at the station azimuth between 60° and 63°. They are aligned in order of epicentral distance. The arrivals of the main Sdiff phase (open reversed triangles) and the postcursors (reversed solid triangles) are both characterized by a slowness of about 8.3s/deg, which is in an agreement with the slowness of Sdiff for PREM. This agreement indicates that the main Sdiff and the postcursor are both core-diffracted waves that depart from the same location on the CMB where the structure is similar to PREM. Therefore, the 26 sec delay of the postcursor relative to the main Sdiff phase has to be attributed to the effect of an anomalous body located between the source and the entering point of Sdiff ray path to the CMB, which is at an approximate distance of 50° from the source.

First, we perform 2D ray-tracing to examine whether a single

anomalous body placed on the CMB can generate two Sdiff ray paths, with a travel time difference of 26 sec. Although diffracted waves cannot be handled by ray theory, we assume that Sdiff is generated when the ray enters the CMB tangentially. We demonstrate eventually that this is a good approximation by showing results of waveform modeling. We examined 270 different models, which are parameterized by the location of the source-side border of the anomalous body and the 1D Vs profile within it. 1D Vs profiles are expressed by the height, the Vs gradient at the top of the slow anomaly region and the Vs reduction inside the region. The height is changed from 151 km to 551 km above the CMB. The Vs reductions at the base of the mantle examined are 3, 6 and 9% with respect to PREM. The sidewalls of the anomalous body are kept perpendicular to the CMB to limit the number of parameters. Figure 2a shows one

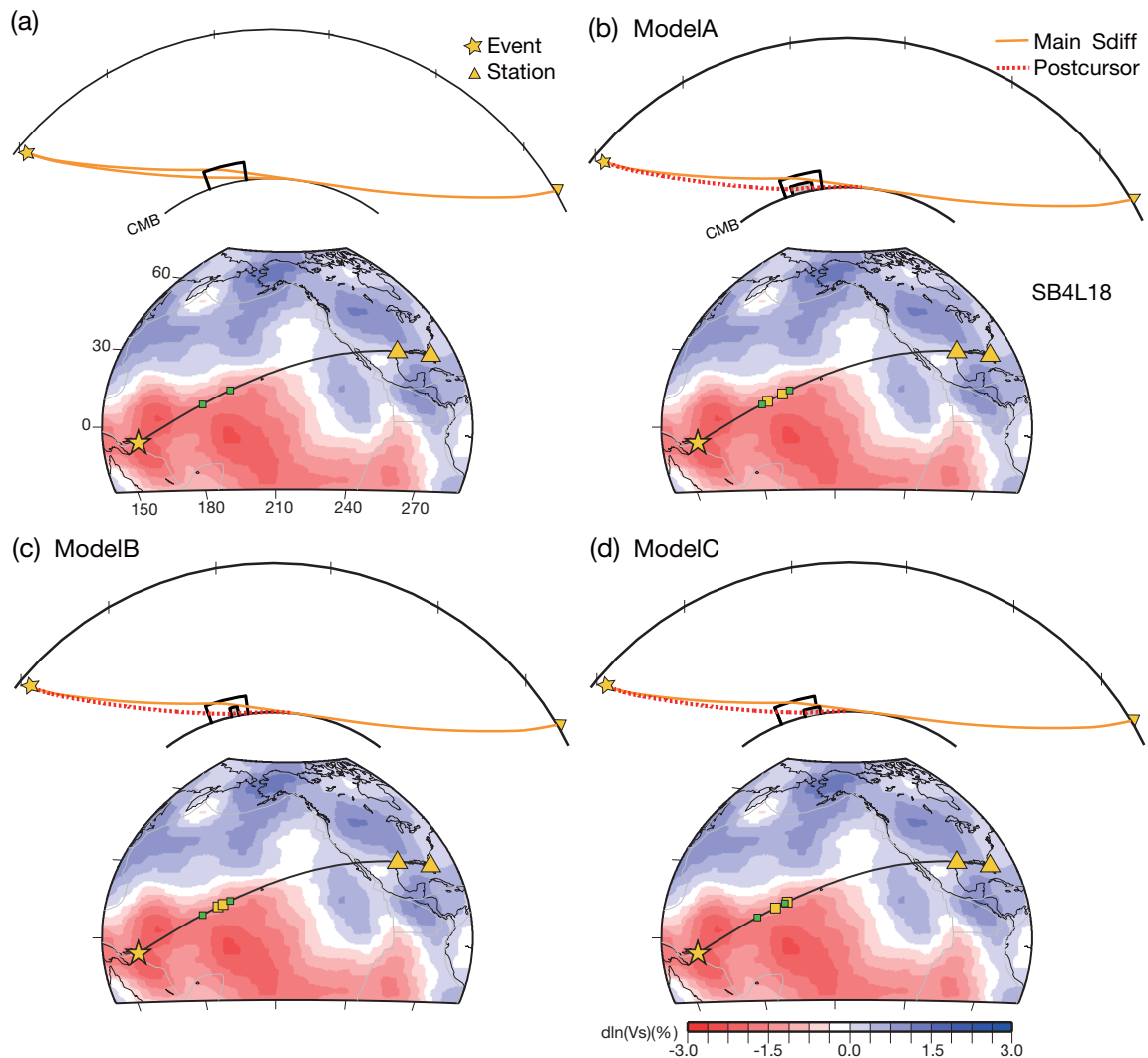


Fig. 2 Top Panel: A cross-section of a model with one slow anomaly region, which generates two Sdiff ray paths. The two Sdiff paths are shown by orange lines. The travel time difference of the two paths is only 0.7 seconds. The anomaly region is 351 km high and has 6% Vs reduction at the base of the mantle. Vs linearly decreases from 351 km to 251 km above the CMB below which it is constant down to the CMB. The two side walls are located at 30° and 42° from the source. Bottom panels: The location of the slow anomaly region is plotted on the Vs tomographic maps of SB4L18 [6]. The locations of the side walls are indicated by green diamonds. (b-d) Models with two types of slow anomaly regions, which generate two Sdiff ray paths, whose arrival times are approximately 26 seconds apart. The locations of the side walls of LWAR and SSAR are shown by green and yellow diamonds respectively on the tomography maps.

of the models, which provides two Sdiff ray-paths by placing a slow anomalous body on the CMB. One Sdiff ray enters the anomalous body from its top and the other enters from its side. However, the travel time difference of the two paths is only 0.7 seconds, which are two orders of magnitude smaller than the observed arrival time difference of 26 seconds. The largest arrival time difference between the two paths among the models examined is 2.2 seconds, which is far less compared to the observation. By tilting the side walls, the time difference increases only 0.5 seconds or so.

In order to obtain models that provide the observed travel time difference of 26 seconds, we combine a small, strongly anomalous region (hereafter called SSAR), to a large, weakly anomalous region (hereafter called LWAR). We conducted 2D ray tracing for thousands of models by systematically changing the V_s profile and the locations of the source-side walls of LWAR and SSAR. Figure 2 (b-d) are three of the successful models. Model parameters are given in Table 1. The path of the main Sdiff enters LWAR from its top and does not sample SSAR. The path of the secondary arrival enters SSAR from its source-side wall, samples SSAR horizontally and exits from its station-side wall.

Figure 1 (b-d) show synthetic waveforms calculated for models shown in Fig. 2 (b-d). Waveforms are calculated by Spectral Element Method (SEM) at periods down to 5 seconds [1][2]. The method can handle strong 3D heterogeneity and is well adapted to the spherical geometry of the CMB. It is an adequate method to investigate the diffracted waves, which interact with the strong heterogeneities near the CMB [3]. The synthetic waveforms for all the three models have two Sdiff arrivals of the same polarity, which are approximately 26 seconds apart. The slowness values are those as expected from PREM, at least beyond the distance of 100° . These features are consistent with the observations.

The observed waveforms cannot be explained by placing one anomaly region on the CMB, in which the V_s profile is given as a function of depth. A laterally localized region with extremely low V_s , with more than 25% V_s reduction (SSAR) should exist inside or at the edge of the larger slow anomaly region with less than several percents of V_s reduction (LWAR). Such an internal

structure is required to generate two Sdiff arrivals that are approximately 26 s apart. The localized SSAR should be more than 100 km high in thickness in order to generate the secondary arrival. The data we have analyzed sample the northern edge of the Pacific large low shear velocity province (LLSVP). LWAR obtained in this study constitutes a part of the Pacific LLSVP. The analyses of the limited data show that SSAR can be placed either at the edge or inside of the LWAR. Further investigations are required to determine the absolute locations of SSAR and LWAR.

2. Antipodal Observations of Earth's Core

We use antipodal seismic observations to review the Earth's Core, where the seismic energy broadly samples the Inner Core and lowermost Outer Core. The data set contains several station-event pairs ($\Delta > 179^\circ$), including Algeria-Tonga, Brazil-Indonesia, and China-Chile. The seismic waves that travel the Earth's Inner Core are categorized as PKIKP, which penetrates the center of the Earth, and PKIKPK, which reflects once at the Inner Core – Outer Core boundary. We model global seismic wave propagation generated by the earthquake by using a spectral-element method (SEM) [1]. The spectral-element

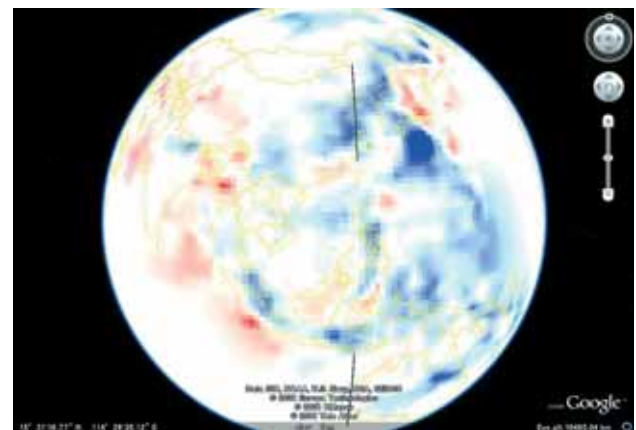


Fig. 3 P-wave seismic velocity model of GAP-P1. The region at depth 600 km is shown in blue if the P-wave velocity is faster than the average and shown in red if the P-wave velocity is slower than the average. This figure is created at: http://www.jamstec.go.jp/pacific21/google_earth/

Parameters of the models examined by SEM.

Model	LWAR			SSAR		
	Height	Mid-height	Wall locations	Height	dV_s/V_s^{*1}	Wall locations
ModelA	351	251(km)	$30^\circ 42^\circ$	171	-18, -48, -18	$32.5^\circ 39^\circ$
ModelB	351	251	$30^\circ 42^\circ$	171	-60	$36.7^\circ 39^\circ$
ModelC	351	301	$28^\circ 40^\circ$	131	-25, -52	$36^\circ 41^\circ$

Table 1 Parameters of the models examined by SEM. Synthetic waveforms are shown in Fig. 1. *Height*: Height of the slow anomaly region above the CMB. V_s starts to decrease linearly with respect to depth from this height. *Mid-height*: Height at which the V_s gradient with respect to depth changes. V_s decrease linearly from Height to Mid-height. Below Mid-height V_s is kept constant down to the CMB. dV_s/V_s : V_s reduction at the CMB with respect to PREM. *1 In ModelA, the anomaly dV_s/V_s of SSAR laterally changes from -18% at the both side edges to -48% at the center. In ModelC, the anomaly of SSAR changes laterally from -25% at the source-side edge to -52% at the station side edge.

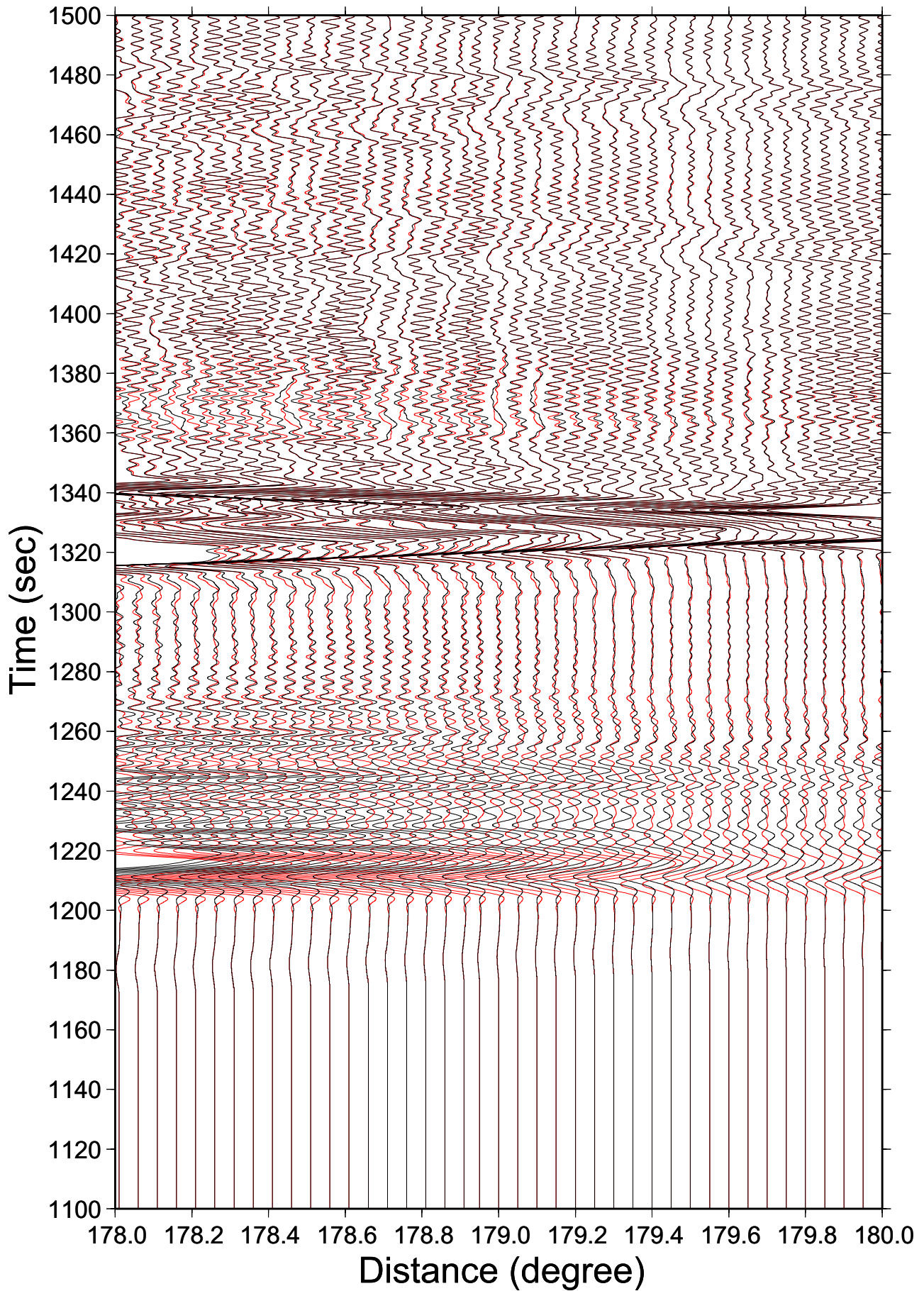


Fig. 4 Comparison of vertical component synthetic seismograms computed at Algeria station for Tonga earthquake with epicentral distance from 178 to 180 degrees. Red traces are the synthetic seismograms computed for standard Inner Core and Outer Core structure. Red traces are synthetic seismogram computed for modified Inner Core structure with the P-wave velocity reduced by 2% from PREM model below depth 1020 km.

method can take into account three-dimensional variations inside the Earth, such as P-wave velocity, S-wave velocity and density, attenuation, anisotropy, ellipticity, topography and bathymetry, and crustal thickness. [1] We use P-wave velocity model GAP-P1 of the mantle[4] (Fig. 3), model CRUST2.0 of the crust, and topography and bathymetry model ETOPO5. The only factor which is not taken into account in this realistic three-dimensional model is the effect of the seismic wave propagation in the ocean layer. Following the previous work [2], the simulations are performed on 1014 processors, which require 127 nodes of Earth Simulator 2 (ES2). We use a mesh with a total of 13.5 billion global integration grid points, which corresponds to an approximate grid spacing of 2.0 km along the Earth's surface and should enable us to get synthetic seismograms accurate up to 3.5 seconds. The inner core and outer core structure used in the first experiment is the same as that of PREM. The result shows that the general features of observed seismograms are reproduced well by the synthetics but those waves, such as PKIKP are not modeled well. Then for the second experiment, we have reduced the P-wave velocity by 2% inside the Inner Core from the PREM model. Figure 4 shows comparison of the synthetics computed for the original PREM model and reduced P-wave velocity model. The figure demonstrates that PKIKP waves, which arrive at around 1240 sec, show significant amplification and suggests there may exist lower P-wave velocity layer inside the Inner core.

References

- [1] Komatitsch, D., J. Ritsema, and J. Tromp, 2002. The Spectral-Element Method, Beowulf Computing, and Global Seismology. *Science*, 298 1737- 1742.
- [2] Tsuboi, S., Komatitsch, D., Ji C., and Tromp, J., 2003. Broadband modeling of the 2002 Denali Fault earthquake on the Earth Simulator. *Phys. Earth Planet. Inter.*, 139 305-312.
- [3] Capdeville, Y., To, A., and Romanowicz, B., 2003. Coupling spectral elements and modes in a spherical earth: an extension to the "sandwich" case. *Geophys. J Int.*, 154 44-57.
- [4] Obayashi, M., H. Sugioka, J. Yoshimitsu, and Y. Fukao, 2006. High temperature anomalies oceanward of subducting slabs at the 410-km discontinuity, *Earth Planet. Science Lett.*, 243, 149-158.
- [5] To, A., Fukao Y., and Tsuboi S., 2010. Evidence of a thick and localized ultra low shear velocity zone inside the Pacific slow region at the base of the mantle., submitted to *Phys. Earth Planet. Inter.*
- [6] Masters, G., Laske, G., Bolton, H. , and Dziewonski, A., 2000. The Relative Behavior of Shear Velocity, Bulk Sound Speed, and Compressional Velocity in the Mantle: Implications for Chemical and Thermal Structure, "Earth's Deep Interior", AGU Monograph 117, AGU, Washington D.C.

全地球弾性応答シミュレーション

プロジェクト責任者

坪井 誠司 海洋研究開発機構 地球内部ダイナミクス領域

著者

坪井 誠司 海洋研究開発機構 地球内部ダイナミクス領域

藤 亜希子 海洋研究開発機構 地球内部ダイナミクス領域

スペクトル要素法により現実的な3次元地球モデルに対する理論地震波形記録を計算した。今年度は、地球の核マントル境界で回折するS波であるSdiff波に見られる顕著な後続波を説明することを考えた。観測されるSdiff波の性質から、核マントル境界に局在する地震波速度異常を考え、そのモデルに対する理論地震波形を計算した。得られた理論地震波形には観測波形に見られるSdiff波の後続波が現れており、用いたモデルが定性的に観測を説明できることを示している。Sdiff波の後続波の振幅を定量的に説明するためには、さらにモデルを改良する必要があることが分かった。地震の対蹠点における地震波の観測を説明するために、理論地震波形を計算した。スペクトル要素法を対蹠点の理論地震波形計算に用いる利点は、地球の中心が特異点とならず安定して理論波形を計算出来る点にある。対蹠点で観測される地震波形には、地球の中心を通過してくる波や、内核 - 外核境界で回折や反射してくる波があり、内核 - 外核境界の性質を調べるために適している。最近の観測では、対蹠点の地震波形でこれまでの地球モデルでは説明できないものがあることが報告されている。ここでは、内核 - 外核境界に異常な地震波速度構造を導入すると、そのような地震波を説明できる可能性があることが分かった。

キーワード:理論地震波形記録, 3次元地球内部構造, スペクトル要素法

Simulation Study on the Dynamics of the Mantle and Core in Earth-like Conditions

Project Representative

Yozo Hamano

Institute for Research on Earth Evolution, Japan Agency for Marine-Earth Science and Technology

Authors

Ataru Sakuraba^{*1}, Futoshi Takahashi^{*2}, Masaki Matsushima^{*2}, Takatoshi Yanagisawa^{*3}, Yasuko Yamagishi^{*3} and Yozo Hamano^{*3}

*1 Department of Earth and Planetary Science, School of Science, University of Tokyo

*2 Department of Earth and Planetary Sciences, School of Science and Engineering, Tokyo Institute of Technology

*3 Institute for Research on Earth Evolution, Japan Agency for Marine-Earth Science and Technology

Thermal convection in the outer core and the mantle is the origins of various Earth's activities and essentially important in the Earth's evolution. We investigate the core convection using low-viscosity geodynamo models. A physical interpretation is given for different behaviors of two geodynamo models: a uniform-surface-temperature model and a uniform-heat-flux model. The thermal boundary condition for the core surface temperature regulates the thermal wind and generation of the toroidal magnetic field. The geomagnetic westward drift and torsional oscillations are simulated to understand mechanisms of short-term geomagnetic field variations. In the mantle convection, we use a three-dimensional spherical-shell code that includes effects of phase transitions, temperature-dependent viscosity with plastic yielding near the surface, and viscosity increase in the lower mantle, and find that, with realistic Rayleigh numbers, these three effects cause plate-like behaviors and slab stagnation and penetration around the transition zone.

Keywords: mantle convection, core convection, geodynamo, geomagnetic secular variation, slab stagnation

1. Introduction

Our group is composed of three subgroups, aiming for comprehensive understanding of the dynamics of the Earth's mantle and core as a combined solid-Earth system. The geodynamo group simulates thermal convection of the fluid outer core and a resultant generation process of the geomagnetic field. In order to reach the core conditions, we have made attempts to reduce viscous effects in the dynamo model by decreasing the Ekman number ($E = \nu/2\Omega c^2$; ν : kinematic viscosity, Ω : Earth's angular velocity, c : core radius) and the magnetic Prandtl number ($Pm = \nu/\eta$; η : magnetic diffusivity). The mantle convection group focuses on dynamical behaviors of the Earth's mantle and simulates infinite-Prandtl-number thermal convection. Particular attention has been paid on integrating realistic mantle properties (e.g., variable viscosity, phase transition, plate behaviors) into the model and reproducing the images obtained from seismic tomography. The geomagnetism and geoelectricity group aims to model electromagnetic properties of the Earth by comparison of simulated and observed data. Here we report some results of the geodynamo and mantle convection groups.

2. Geodynamo simulations

2.1 Impact of the boundary condition for the core-surface temperature

We have shown that, in low-viscosity geodynamo models of $E = 5 \times 10^{-7}$ and $Pm = 0.2$, which are one of the lowest-viscosity models, the solutions are dramatically different between a case where the core-surface temperature is laterally uniform and a case where the heat flux is laterally uniform at the core surface [1,2]. The uniform-surface-temperature model (USTM) produces sheet-like, high-wavenumber convection and a comparatively weak magnetic field that is almost stationary in time. The uniform-heat-flux model (UHFM) allows a large-scale convection pattern and a strong magnetic field that, driven by a zonal flow, moves retrograde like the geomagnetic westward drift. As the mantle convection is too slow to homogenize the core-surface temperature in the core's convective timescale, the USTM is geophysically unrealistic. The numerical results indicate that the USTM is not only theoretically inappropriate but fails to reproduce geomagnetic field behaviors. Other low-viscosity USTMs [3,4] resemble our USTM, but previous higher-viscosity USTMs [5] seem to have characteristics similar

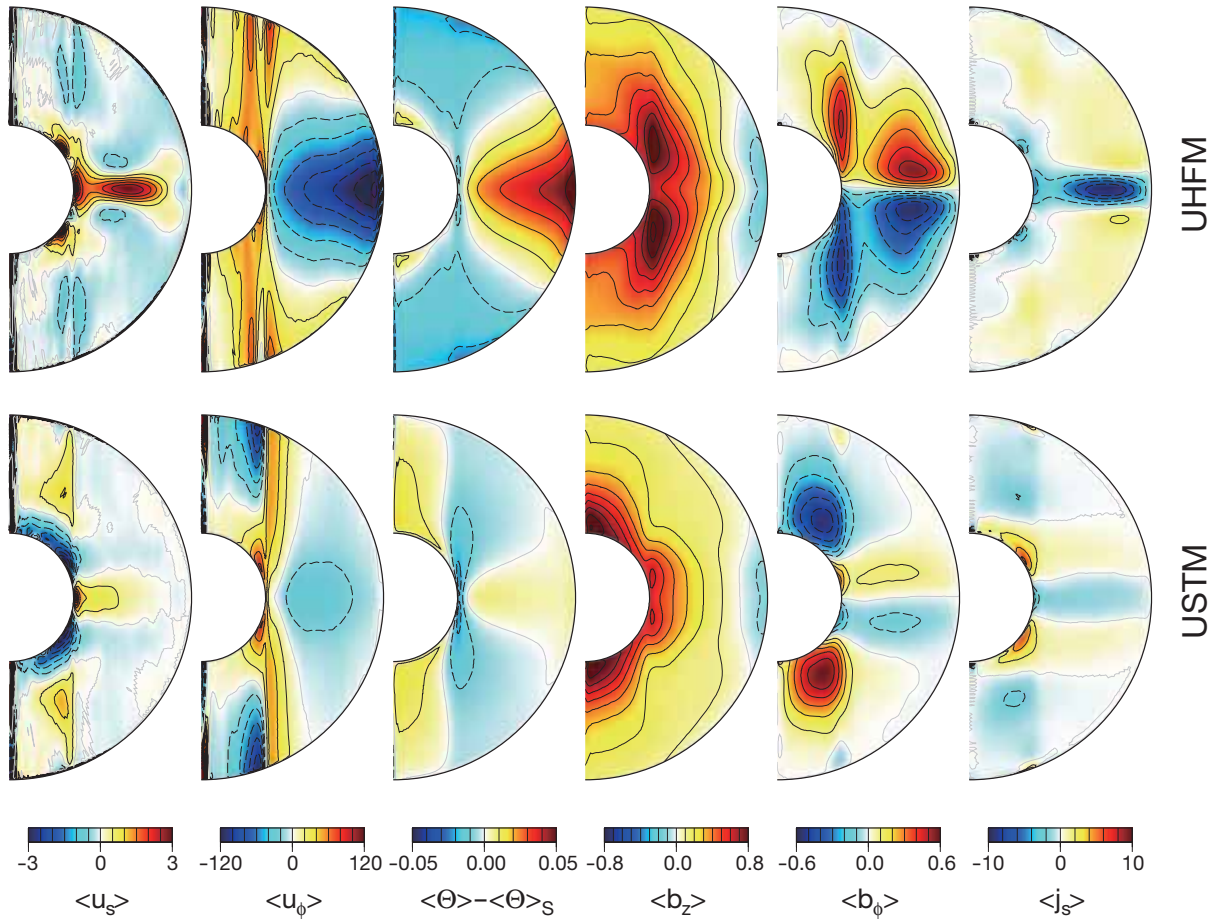


Fig. 1 The time-averaged axisymmetric structures of the solutions of the UHF (top) and the UST (bottom). Shown from left to right are the cylindrically radial and azimuthal velocities, the spherically asymmetric part of the temperature, the axial and azimuthal magnetic fields, and the radial electric current density.

to our UHF, implying that the thermal boundary condition has a great impact only when the viscosity is low enough.

When averaged in time and longitude, the temperature perturbation, $\langle \Theta \rangle$, is a solution of the heat conduction equation with the source term, $C(r, \theta) = -\langle u_r \rangle dT_c/dr - \langle \mathbf{u} \cdot \text{grad}(\Theta) \rangle$, where T_c is the reference temperature, \mathbf{u} is the flow velocity and $\langle \rangle$ denotes the time and azimuthal average. Even when $C(r, \theta)$ is the same, the amplitude of $\langle \Theta \rangle$ strongly depends on the boundary condition, because this elliptic boundary-value problem is intrinsically sensitive to the choice between the Dirichlet-type (UST) and the Neumann-type (UHF) boundary conditions. Suppose that initially there is a radial upwelling flow, $\langle u_r \rangle$, along the equatorial plane and that the nonlinear terms are negligibly small. The flow creates a positive $C(r, \theta)$ to heat up the equatorial region. We have confirmed that, when a simple flow distribution is assumed, the UHF produces $\langle \Theta \rangle$ several times greater than the UST in which the temperature variation along latitude is exactly zero at the surface. The greater $\langle \Theta \rangle$ in the UHF produces a stronger azimuthal thermal wind and a stronger toroidal field because of the omega-effect. The resultant stronger Lorentz force in the UHF, which is eastward to decelerate the thermal wind, requires a stronger radial upwelling flow, $\langle u_r \rangle$, at the equatorial

plane because the major counter force to the Lorentz force is only the Coriolis force. Therefore, the initially imposed radial flow can grow by generating a strong toroidal magnetic field in the UHF. This positive feedback makes the difference between the two models bigger and bigger until the nonlinear term cancels the heat source term $C(r, \theta)$. The UST is less effective to drive a thermal wind, so the toroidal magnetic field cannot grow outside the tangent cylinder. These scenarios well describe the time-averaged axisymmetric structures of the two solutions (Fig. 1) and explain why the UST became a weak-field dynamo [6].

2.2 Magnetic field changes of short timescales

The geomagnetic field changes in various timescales. As observational geomagnetic data during the past several hundreds years are relatively abundant, there is a possibility to make a detailed comparison between the model and such short-term data and obtain some information about the deep Earth. One of the most notable short-term geomagnetic field changes is the westward drift, whose phase velocity is estimated to be up to about 17 km/yr at the core surface and the signal is concentrated in a narrow equatorial belt [7]. In order to see such a short-timescale phenomenon, we performed geodynamo simulations

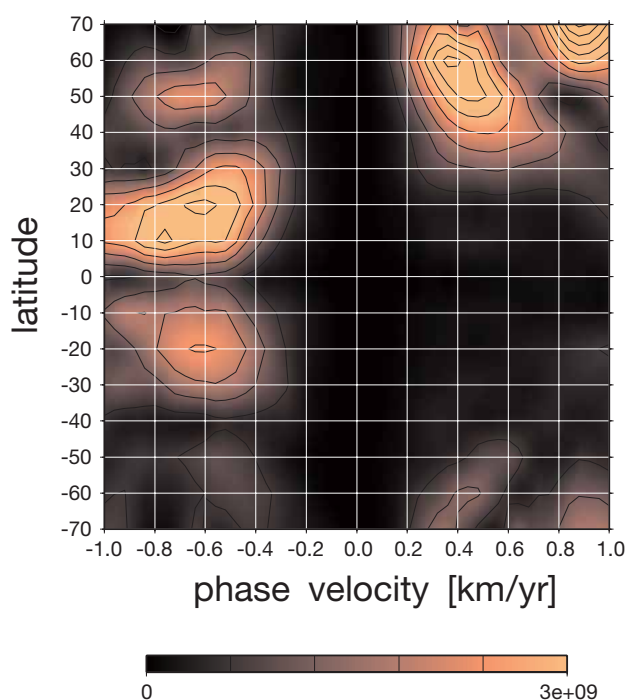


Fig. 2 The signal power of the radial component of the core-surface magnetic field moving in the azimuthal direction is plotted as a function of the phase velocity (a positive value means eastward propagation) and the latitude, obtained from the UHFMM with $E = 2.5 \times 10^{-7}$, $Pm = 0.2$, $Ra = \alpha\beta g c^2 / 2\Omega\eta = 6400$ (α : thermal expansivity, β : temperature gradient at the core surface, g : acceleration due to gravity at the core surface).

using the UHFMM and decreasing the Ekman number to 2.5×10^{-7} . We used a spectral method with the maximum spherical harmonic degree of 359. We plotted the core-surface field as a function of time and longitude at various latitudes and made a wave analysis in the ϕ - t plane to obtain the phase velocity of the strongest signal. The result indicates that the field propagation is most evident within the latitudes of ± 30 degrees similar to the geomagnetic data (Fig. 2). The phase velocity can be converted

to a dimensional value of 0.7 km/yr, if $\eta = 3 \text{ m}^2/\text{s}$. There are some signals in the high latitudes that are both eastward and westward. The simulated westward drift is too slow to account for the observational data, implying that the Rayleigh number ($Ra = 6400$ in this case) should be much higher to drive a stronger thermal wind.

Another interesting short-term geomagnetic variation is caused by the torsional oscillations of the Earth's core. Provided that viscous and inertial forces are neglected, the integral of the azimuthal component of the Lorentz force over an axial cylindrical surface has to be zero (the Taylor's constraint). The angular velocity of the cylinder's rotation obeys a wave equation with some assumption, whose phase velocity is proportional to the root-mean-square magnetic field perpendicular to the cylindrical surface. It has been argued that the torsional waves cause decadal geomagnetic field variations that could be related to the change of the angular momentum of the mantle [8]. Figure 3 shows the time derivative of the zonal velocity averaged over an axial cylindrical surface of radius s . We made a wave analysis in the s - t plane to obtain the phase velocity, similar to the case of the westward drift. The result shows that the ingoing waves (toward the z axis) are more evident outside the tangent cylinder and the outgoing waves are seen near the equator, implying that the waves are excited around $s = 0.75$ and propagated to both directions, but they are absorbed at both ends of the tangent cylinder (Fig. 4). The phase velocity is slightly slower than the theoretical estimate, which may imply that a modification is needed to the theory of the torsional waves.

2.3 Improvement of geodynamo models

We made efforts to improve the numerical method and the model equations. We employ either the Chebyshev spectral or the finite difference methods to resolve the radial convective structure. In general, the former is more accurate with the same

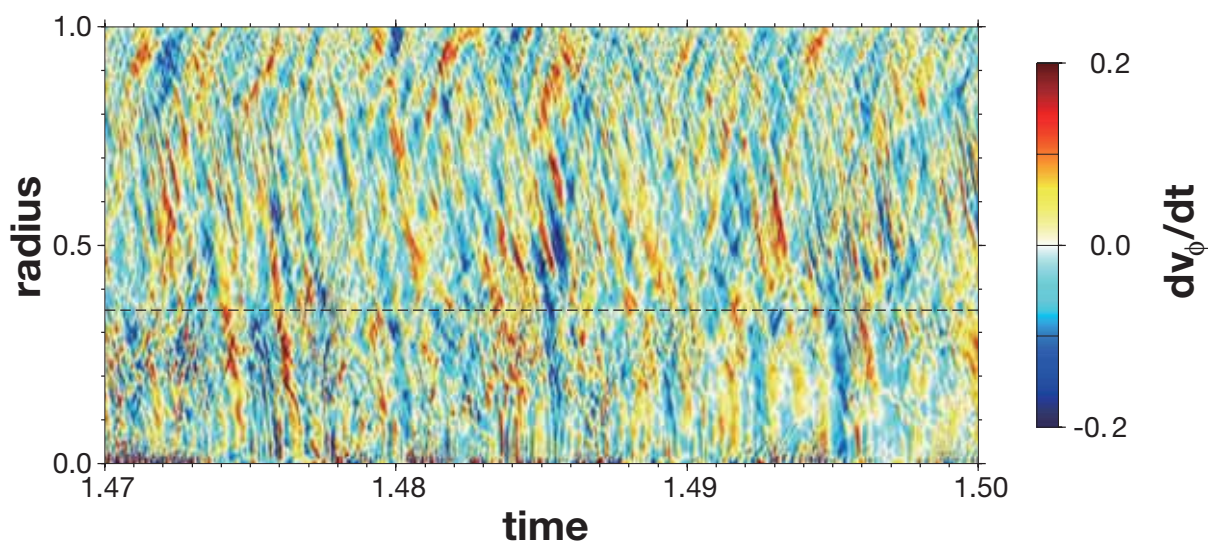


Fig. 3 The surface average of the time derivative of the azimuthal velocity as a function of the time and the cylinder's radius.

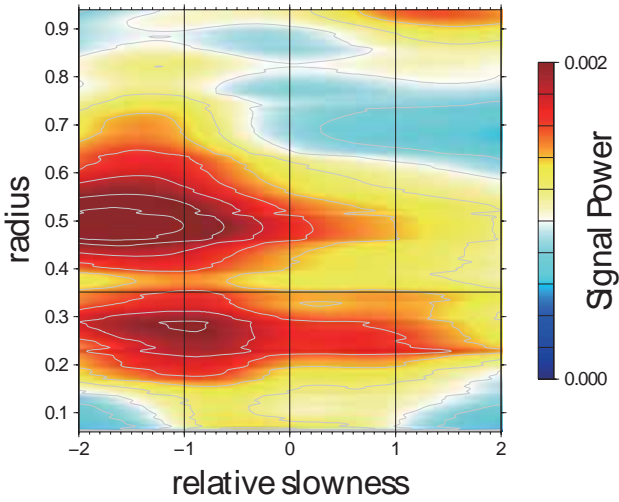


Fig. 4 The result of a wave analysis of the data shown in Fig. 3. The signal power is plotted as a function of the radius and the slowness that is normalized by the theoretically predicted slowness of the torsional wave.

degree of freedom (spectral modes or grid points), but the latter could be superior in computational speed. We modified the finite difference method by using the combined compact difference scheme [9] to cope with speed and accuracy. Preliminary calculations of the dynamo benchmark test show that the solution has 4th-order accuracy and the numerical integration is stable. We so far used the Boussinesq approximation for the core convection, which might be however inappropriate because of finite compressibility of the core fluid. We attempted to modify the Boussinesq equations using the incompressible approach proposed by Anufriev and Hejda [10]. We introduced the dissipation number and the ratio of the adiabatic heat flow to the actual heat flow at the core surface. By changing these numbers, we succeeded in simulating a thermally stable layer at the top of the core.

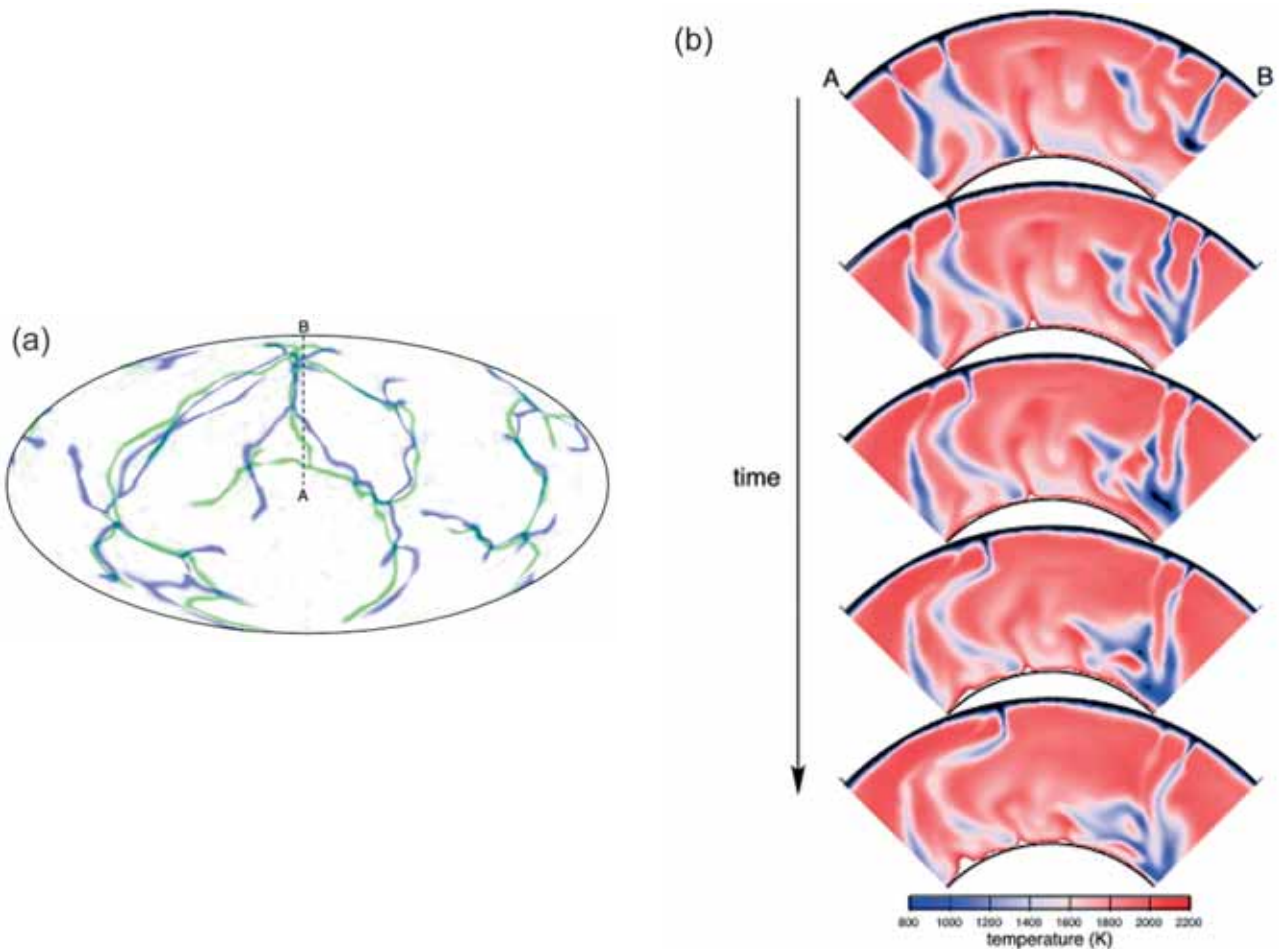


Fig. 5 Movement of the positions of convergence regions at the surface between 200 million years (a), and variation of the convection pattern in a vertical cross section (b). Rayleigh number is 2×10^7 . Temperature dependency of viscosity with plastic yielding and phase transitions at 410 km and 660 km depth are included. Viscosity of the lower mantle is 40 times higher than the upper mantle. In (a), green: original positions of convergence regions (corresponding to the first frame in (b)), blue: 200 million years later (corresponding to the last frame in (b)). The broken line with A and B indicates the position of the vertical cross section in (b). In (b), temperature is shown by color-scale and the time interval for each frame is 50 million years. Stagnation of the subducted slab around the transition zone occurs with the horizontal migration of the downwelling flow in the upper mantle.

3. Simulations of mantle convection

The Earth's mantle is composed of solid rocks but it flows like a viscous fluid in a geologic time scale. This convective flow of the mantle is emerging as the motion of tectonic plates on the Earth's surface. The motion of surface plates causes earthquake, volcanism and mountain building at the plate margins. And as the mantle flow transports the heat from the hot interior, the whole of the Earth has been cooling through its history. It also controls the boundary conditions of the outer core. Hence, mantle convection is the key process for understanding the activity and evolution of our planet. Seismic tomography reveals the natural mode of convection in the Earth is whole mantle with subducted plates (slabs) clearly seen as continuous features into the lower mantle. Simultaneously existing alongside these deep slabs are stagnant slabs which are, if only temporarily, trapped in the upper mantle (recent review [11]). Previous numerical models of mantle convection have observed a range of behavior for slabs in the transition zone depending on viscosity stratification and mineral phase transitions, but typically only exhibit flat-lying slabs in the transient state with artificial setting of plate boundary or trench migration is imposed.

We simulated fully dynamical and self-consistent thermal convection in high-resolution 3-D spherical shell models which range up to Earth-like conditions in Rayleigh number, and succeeded in spontaneous generation of plate-like behavior with slab stagnation. We examined the influence of three factors: phase transitions, temperature dependent viscosity with plastic yielding at shallow depth, and viscosity increase in the lower mantle, and clarified the condition for generating stagnant slabs [12]. For the evaluation of the effect of the 660 km phase transition, the regime diagram of convection pattern in an isoviscous mantle is established. It suggests that the present Earth is in the intermittent convection mode. The temperature dependent viscosity with plastic yielding spontaneously produces plate-like behavior with very localized convergence zones at the surface. This plate-like structure can stagnate in the transition zone with the combination of 660 km phase transition and viscosity increase in the lower mantle. The model including these three factors with adequate values generates the coexisting state of stagnant and penetrating slabs around the transition zone (Fig. 5), which are characteristics of mantle convection revealed by seismic tomography. The key mechanism to generate stagnant slabs is the partly decoupled state of the upper and lower mantle flow due to the phase transition.

Acknowledgement

We thank Prof. P. H. Roberts for discussion.

References

- [1] A. Sakuraba and P.H. Roberts, "Generation of a strong magnetic field using uniform heat flux at the surface of the core", *Nature Geoscience*, vol.2, pp.802-805, 2009.
- [2] A. Sakuraba, et al., "Generation of a strong dipole magnetic field in a geodynamo model with low viscosity", *Annual Report of the Earth Simulator Center April 2008 - September 2008*, pp.69-74, 2009.
- [3] A. Kageyama, T. Miyagoshi, and T. Sato, "Formation of current coils in geodynamo simulations", *Nature*, vol.454, pp.1106-1109, 2008.
- [4] F. Takahashi, M. Matsushima, and Y. Honkura, "Scale variability in convection-driven MHD dynamos at low Ekman number", *Phys. Earth Planet. Inter.*, vol.167, pp.168-178, 2008.
- [5] F.H. Busse and R.D. Simitev, "Parameter dependences of convection-driven dynamos in rotating spherical shells", *Geophys. Astrophys. Fluid Dyn.*, vol.100, pp.341-361, 2006.
- [6] A. Sakuraba and P.H. Roberts, "On thermal driving of the geodynamo", submitted to *Proceedings of the 11th Scientific Assembly of IAGA, Sopron, Hungary*, 2009.
- [7] C.C. Finlay and A. Jackson, "Equatorially dominated magnetic field change at the surface of Earth's core", *Science*, vol.300, pp.2084-2086, 2003.
- [8] R. Holme, "Large-scale flow in the core", in *Treatise on Geophysics*, vol. 8, pp.107-130, Elsevier, 2007.
- [9] P.C. Chu and C. Fan, "A three-point combined compact difference scheme", *J. Comp. Phys.*, vol.140, pp.370-399, 1998.
- [10] A.P. Anufriev and P. Hejda, "Earth's core convection: Boussinesq approximation or incompressible approach?", submitted to *Geophys. Astrophys. Fluid Dyn.* 2010.
- [11] Y. Fukao, M. Obayashi, T. Nakakuki, and Deep Slab Project Group, "Stagnant slab: A review", *Annual. Rev. Earth Planet. Sci.*, vol.37, pp.19-46, 2009.
- [12] T. Yanagisawa, Y. Yamagishi, Y. Hamano, and D. R. Stegman, "Mechanism for generating stagnant slabs in 3-D spherical mantle convection models at Earth-like conditions", *Phys. Earth Planet. Inter.* (in press).

実地球環境でのマントル・コア活動の数値シミュレーション

プロジェクト責任者

浜野 洋三 海洋研究開発機構 地球内部ダイナミクス領域

著者

櫻庭 中^{*1}, 高橋 太^{*2}, 松島 政貴^{*2}, 柳澤 孝寿^{*3}, 山岸 保子^{*3}, 浜野 洋三^{*3}

*1 東京大学大学院理学系研究科 地球惑星科学専攻

*2 東京工業大学大学院理工学研究科 地球惑星科学専攻

*3 海洋研究開発機構 地球内部ダイナミクス領域

地球のマントルとコアで起こっていると考えられる熱対流は、固体地球に生起するさまざまな活動の根本原因であり、地球の進化を知る上で重要である。コアの熱対流については、計算可能なもっとも低粘性の地球ダイナモモデルをもちいて研究をおこなった。これまでの研究で、粘性パラメータをじゅうぶん低く抑えると、コア表面の温度境界条件が解の性質を大きく変えること、コア表面温度を一定にするような、地球物理的に不適切な境界条件の下では、地球のような強い双極子磁場の生成がさまたげられることを明らかにした。その原因について解析をおこなったところ、温度境界条件がコア内部に吹く西向き温度風をコントロールし、結果としてトロイダル磁場の生成に影響を与えていることがわかった。地磁気の短時間変動の原因をあきらかにするため、これまでよりも低い粘性パラメータをもちいた数値シミュレーションをおこなった。粘性をあらゆるエクマン数と磁気プラントル数はそれぞれ 2.5×10^{-7} および 0.2 である。シミュレーションで再現されるコア表面磁場の西方移動は赤道付近に集中しており、これは地磁気の特徴とよく似ている。そのメカニズムはコア内部の西向き温度風によるものと考えられる。しかし位相速度は地磁気のそれよりも著しく遅く、今後さらにレイリー数をあげるなどの必要があろう。さらにコアのねじれ振動に似た振動現象がシミュレーションでも再現されていることをあきらかにした。また地球ダイナモモデルの改良もおこなった。動径方向の空間差分を結合コンパクト差分に置き換えることで、より高い精度が実現されることを確認し、低粘性に起因する薄い境界層の表現に寄与することが期待された。

マントル対流のシミュレーションでは、3次元球殻において、粘性の温度依存性と浅部での降伏現象、マントル鉋物の相転移、下部マントルでの粘性増加、という3つの要素を組み込んで、地球マントルに相当するレイリー数の計算を実行した。その結果、地震波トモグラフィーで見えているような遷移層に滞留（スタグナント）するスラブと突き抜けるスラブとの共存状態が自然に再現されるとともに、表面での沈み込み位置の移動に伴って滞留構造が形成されていく過程を明らかにすることに成功した。滞留構造を生み出す鍵となるのは、負のクラペイロン勾配を持つ相転移により浮力が減じられるため上下マントルの流れが非結合状態になり得ること、そして粘性差により上下マントルに大きな流速の違いが生じること、である。

キーワード: マントル対流, コア対流, 地球ダイナモ, 地磁気永年変化, スタグナントスラブ

Development of a Predictive Simulation System for Crustal Activities in and around Japan - VII

Project Representative

Chihiro Hashimoto Graduate School of Environmental Studies, Nagoya University

Authors

Chihiro Hashimoto^{*1}, Eiichi Fukuyama^{*2}, Toshiko Terakawa^{*1}, Takeshi Sagiya^{*1},
Kengo Nakajima^{*3}, Toshinori Sato^{*4} and Mitsuhiro Matsu'ura^{*5}

*1 Graduate School of Environmental Studies, Nagoya University

*2 National Research Institute for Earth Science and Disaster Prevention

*3 Information Technology Center, The University of Tokyo

*4 Faculty of Science, Chiba University

*5 Institute of Statistical Mathematics, Research Organization of Information and Systems

Our research group aims to develop a physics-based predictive simulation system for crustal activities in and around Japan, which consists of a combined simulation model for quasi-static stress accumulation and dynamic rupture propagation and the associated data assimilation software. In the first phase (2003-2005), we constructed a prototype of the combined simulation model on a realistic 3-D structure model. In the second phase (2006-2008), we tested the validity and applicability of the combined simulation model, and demonstrated that the physics-based computer simulation is useful for the quantitative evaluation of strong ground motions that will be produced by potential interplate earthquakes. We also developed the associated data assimilation software; that is, a GPS data inversion method to estimate interplate coupling rates, a CMT data inversion method to estimate crustal stress fields, and a GPS inversion method to estimate 3-D elastic/inelastic strain fields. In 2009, applying the GPS data inversion method to interseismic GPS data (1996-2000) in the southwestern part of Japan, we estimated the slip-deficit rate distribution on the Eurasian-Philippine Sea plate interface along the Nankai trough and the Ryukyu trench, and revealed that a high slip-deficit rate belt extends from the Suruga Bay to the Bungo Channel. On the basis of the inversion results, we computed stress accumulation rates in the seismogenic region, and performed a numerical simulation for the dynamic rupture of a potential Nankai-trough earthquake by using the boundary integral equation method.

Keywords: GPS data inversion, interplate coupling, stress accumulation, dynamic rupture propagation, combined simulation

1. Introduction

The occurrence of earthquakes can be regarded as the releases of tectonically accumulated elastic strain energy through dynamic fault ruptures. Given this, the entire earthquake generation process generally consists of tectonic loading, quasi-static rupture nucleation, dynamic rupture propagation, and fault strength recovery. We can now quantitatively describe the entire earthquake generation process with coupled nonlinear equations, consisting of a slip-response function, a fault constitutive law, and relative plate motion. The slip-response function, which relates fault slip to shear stress change, is a solution of the equation of motion in continuum mechanics. The fault constitutive law, which prescribes shear strength change with fault slip and contact time, is an energy balance equation in fracture zones. The relative plate motion is a driving force of the coupled nonlinear system. Thus, the essence of earthquake

generation modeling is quite simple, but it is not easy to develop a predictive simulation model, because the actual world is complex in structure and also in material properties.

In the first phase (2003-2005) of the project, we constructed a realistic 3-D model of plate interface geometry in and around Japan, represented by the superposition of about 30,000 bi-cubic splines [1]. On this structure model we developed a quasi-static stress accumulation model and a dynamic rupture propagation model. Then, given the past fault-slip history, we performed the combined simulation of quasi-static stress accumulation and dynamic rupture propagation for the 1968 Tokachi-oki earthquake ($M_w=8.2$), and demonstrated that when the stress state is close to a critical level, dynamic rupture is rapidly accelerated and develops into a large earthquake, but when the stress state is much lower than the critical level, started rupture is not accelerated [2]. So, the problem is how to know the past

fault-slip history and how to monitor the present stress state. In the case of Japan, fortunately, we have nation-wide dense geodetic and seismic observation networks such as GEONET operated by GIS (Geographical Survey Institute of Japan) and F-net operated by NIED (National Research Institute for Earth Science and Disaster Prevention).

In the second phase (2006-2008), we developed the associated data assimilation software; that is, a GPS data inversion method to estimate interplate coupling rates [3], a CMT data inversion method to estimate crustal stress fields [4], and a GPS data inversion method to estimate 3-D elastic/inelastic strain fields [5]. Applying the GPS data inversion method [3] to GEONET data (GSI) in the Hokkaido-Tohoku region for the interseismic calm period of 1996-2000, we estimated the slip-deficit rate distribution on the North American-Pacific plate interface, and revealed that the inverted five slip-deficit peaks almost completely coincide with the source regions of 10 large interplate earthquakes ($M_w > 7.5$) occurred along the Kuril-Japan trench in the last century [6]. Based on the inversion results, we performed the combined simulation of quasi-static stress accumulation, dynamic rupture propagation and seismic wave propagation for the 2003 Tokachi-oki earthquake ($M_w = 8.1$), and demonstrated that the physics-based computer simulation is useful for the quantitative evaluation of strong ground motions that will be produced by potential interplate earthquakes [7].

2. Interplate slip-deficit rate distribution along the Nankai trough inverted from GPS data

In 2009, applying the GPS data inversion method [3] to horizontal velocity data at GEONET stations in the southwestern part of Japan for the interseismic calm period of 1996-2000 (Fig. 1), we estimated precise slip-deficit rate distribution on the Eurasian-Philippine Sea plate interface along the Nankai trough and the Ryukyu trench. In the analysis, we took the changes in distance between adjacent GPS stations as data, instead of horizontal velocities, to remove the effect of block rotation. In practice, we composed a triangle network from 512 GPS stations with the Delaunay triangulation (the inset of Fig. 1), and used 1265 side-length change data for the inversion analysis.

In Fig. 2, we show the inverted slip-deficit rate distribution on the Eurasian-Philippine Sea plate interface together with the tsunami source regions of the 1944 Tonankai ($M = 7.9$) and 1946 Nankai ($M = 8.0$) earthquakes. From this figure we can see that a high slip-deficit rate belt in the depth range of 5-30 km extends along the Nankai trough from the Suruga Bay to the Bungo Channel. The 1944 Tonankai and 1946 Nankai earthquakes were shallow thrust-type submarine earthquakes accompanied by tsunamis. The tsunami source region of the 1946 event extends from the Kii peninsular to the west of the Tosa Bay, but not to the Bungo Channel, which agrees with the coseismic slip distribution estimated from the inversion analysis of triangulation and levelling data [8]. The discrepancy between

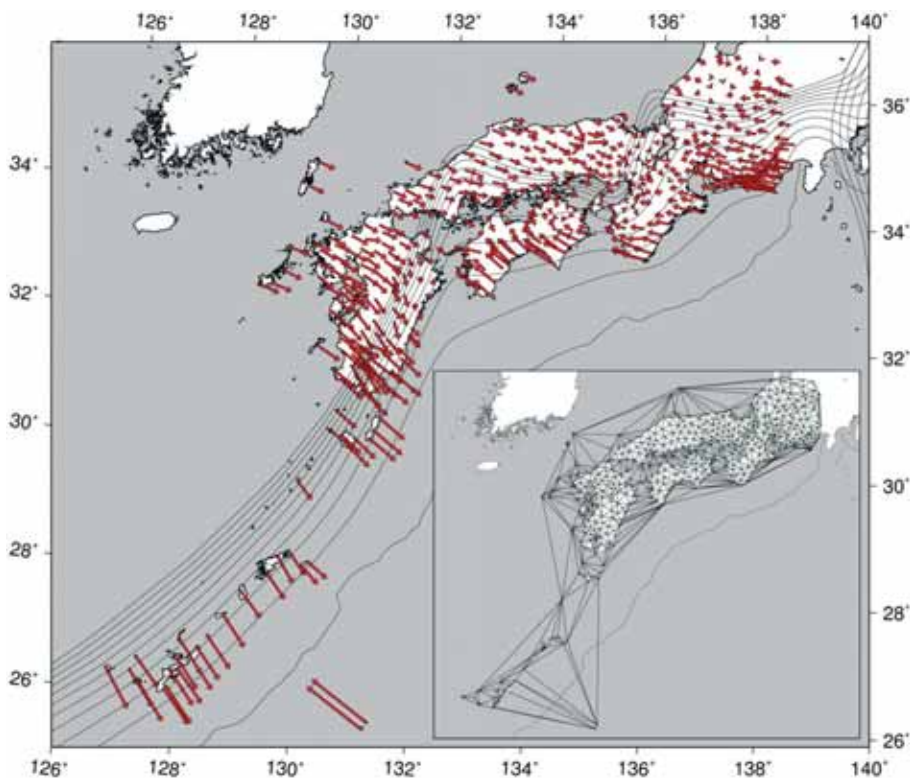


Fig. 1 Interseismic GPS velocity data in the southwestern part of Japan (Hashimoto, Sagiya & Matsu'ura, SSJ 2009 Fall Meeting). The red arrows indicate horizontal velocity vectors. The plate interface geometry is shown by the iso-depth contours at the interval of 10 km. The inset shows the triangle network composed of 512 GPS stations with the Delaunay triangulation.

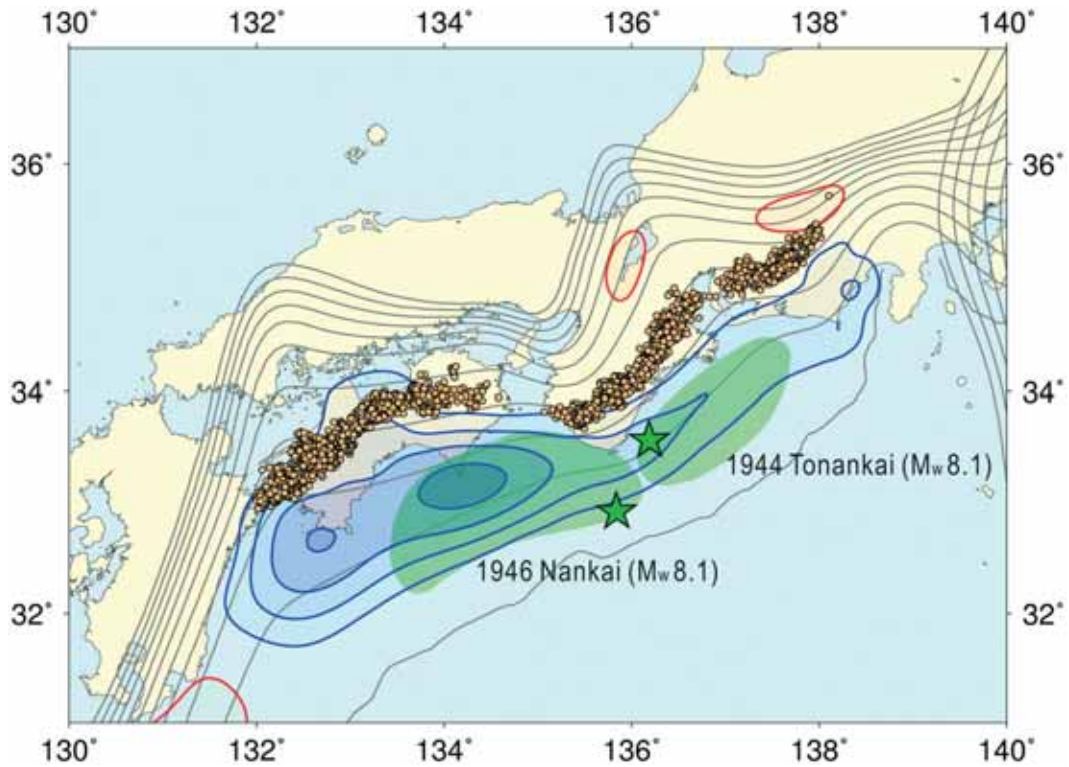


Fig. 2 The slip-deficit rate distribution inverted from GPS data (Hashimoto, Sagiya & Matsu'ura, SSJ 2009 Fall Meeting). The blue contours indicate the slip-deficit rate at the interval of 2 cm/yr. The green stars and green areas indicate the epicentres and tsunami source regions of the 1944 Tonankai and 1946 Nankai earthquakes. The small orange circles indicate the location of deep low-frequency tremors [9,10].

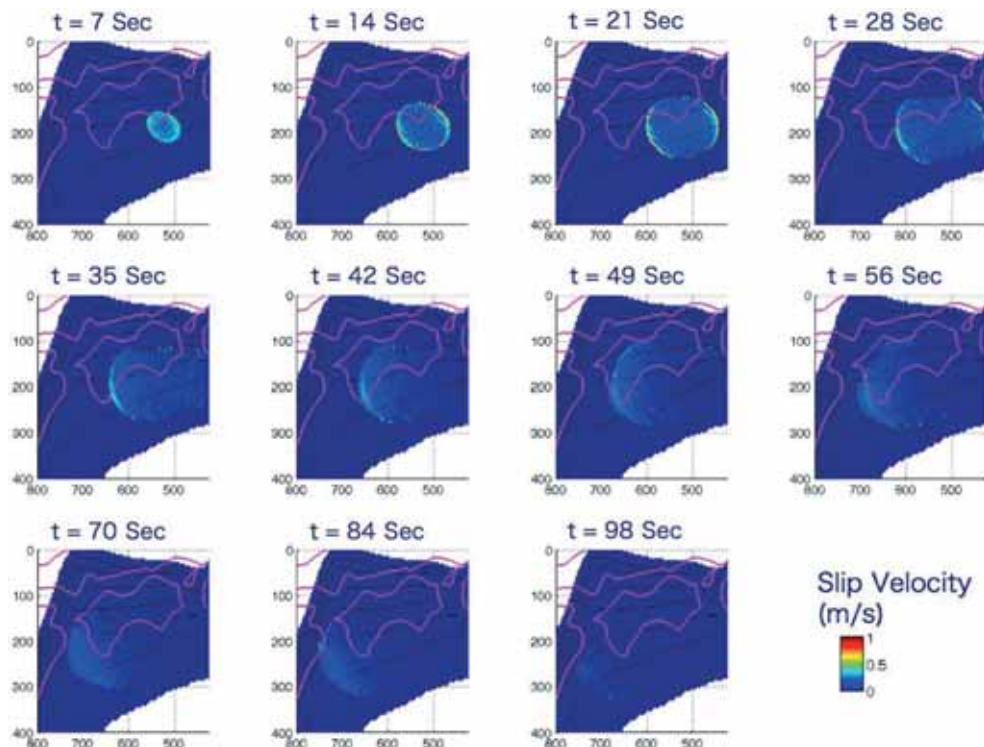


Fig. 3 Dynamic rupture simulation for a potential Nankai-trough earthquake (Hok, Fukuyama & Hashimoto, SSJ 2009 Fall Meeting). A series of snapshots shows slip velocity distribution at each time step. The dynamic rupture started near the Muroto promontory propagates westward and develops into a large earthquake that releases the tectonically accumulated stress completely.

the interseismic slip-deficit rate distribution and the coseismic slip distribution of the 1946 event suggests complexity in the past fault-slip history and the present stress state about the Bungo Channel.

3. Dynamic rupture simulation for a potential Nankai-trough earthquake

On the basis of the inversion results, we performed a numerical simulation for the dynamic rupture of a potential Nankai-trough earthquake by using the boundary integral equation method. In the numerical simulation, first, we computed the stress distribution on the plate interface just before the initiation of dynamic rupture by multiplying the inverted slip-deficit rates by an assumed interseismic period after the 1946 event. Then, we forced the dynamic rupture to start by giving small amount of stress drop. If we assume a uniform frictional property over the seismogenic region, the started dynamic rupture is accelerated and extends over the whole slip-deficit zone (Fig. 3). The dynamic rupture process is essentially controlled by the frictional property (peak strength and critical displacement) of faults as well as the initial stress state. The present numerical results shows that the started dynamic rupture extends to the Bungo Channel, which agrees with the case of the 1854 Ansei Nankai earthquake ($M=8.4$), but not with the case of the 1946 Showa Nankai earthquake. For the reliable prediction of potential interplate earthquakes along the Nankai trough, it is crucial to specify the spatial distributions of peak strength and critical displacement over the plate interface and reveal the background tectonic stress field around the plate interface through the integrated analysis of the past fault-slip history in the southwestern part of Japan.

References

- [1] C. Hashimoto, K. Fukui, and M. Matsu'ura, "3-D modelling of plate interfaces and numerical simulation of long-term crustal deformation in and around Japan," *Pure Appl. Geophys.*, vol.161, pp.2053-2068, 2004.
- [2] M. Matsu'ura, "Quest for predictability of geodynamic processes through computer simulation," *Computing in Science & Engineering*, vol.7, pp.43-50, 2005.
- [3] M. Matsu'ura, A. Noda, and Y. Fukahata, "Geodetic data inversion based on Bayesian formulation with direct and indirect prior information," *Geophys. J. Int.*, vol.171, pp.1342-1351, 2007.
- [4] T. Terakawa and M. Matsu'ura, "CMT data inversion using a Bayesian information criterion to estimate seismogenic stress fields," *Geophys. J. Int.*, vol.172, pp.674-685, 2008.
- [5] A. Noda and M. Matsu'ura, "Physics-based GPS data inversion to estimate 3-D elastic and inelastic strain fields," *Geophys. J. Int.*, doi: 10.1111/j.1365-246X.2010.04611.x, 2010.
- [6] C. Hashimoto, A. Noda, T. Sagiya, and M. Matsu'ura, "Interplate seismogenic zones along the Kuril-Japan trench inferred from GPS data inversion," *Nature Geoscience*, vol.2, pp.141-144, 2009.
- [7] E. Fukuyama, R. Ando, C. Hashimoto, S. Aoi, and M. Matsu'ura, "A physics-based simulation of the 2003 Tokachi-oki, Japan, earthquake toward strong ground motion predictions," *Bull. seism. Soc. Am.*, vol.99, pp.3150-3171, 2009.
- [8] T. Yabuki and M. Matsu'ura, "Geodetic data inversion using a Bayesian information criterion for spatial distribution of fault slip," *Geophys. J. Int.*, vol.109, pp.363-375, 1992.
- [9] K. Obara and H. Hirose, "Non-volcanic deep low-frequency tremors accompanying slow slips in the southwest Japan subduction zone," *Tectonophysics*, vol.417, pp.33-51, 2006.
- [10] K. Obara and H. Hirose, "Discovery of slow slip families associated with the subduction of the Philippine Sea plate in southwest Japan," *Bull. seism. Soc. Japan*, vol.61, pp.S315-S327, 2009 (in Japanese with English abstract).

日本列島域の地殻活動予測シミュレーション・システムの開発 -

プロジェクト責任者

橋本 千尋 名古屋大学 大学院環境学研究科

著者

橋本 千尋^{*1}, 福山 英一^{*2}, 寺川 寿子^{*1}, 鷺谷 威^{*1}, 中島 研吾^{*3}, 佐藤 利典^{*4}, 松浦 充宏^{*5}

*1 名古屋大学 大学院環境学研究科

*2 防災科学技術研究所 地震研究部

*3 東京大学 情報基盤センター

*4 千葉大学 理学部 地球科学科

*5 情報・システム研究機構 統計数理研究所

本研究プロジェクトは、複雑なテクトニック環境の下にある日本列島及びその周辺域を一つのシステムとしてモデル化し、プレート運動に伴う長期的な地殻変形から大地震の発生まで、時間・空間スケールの著しく異なる地殻活動現象を統一的且つ定量的に予測する並列シミュレーション・システムを開発し、モデル計算と観測データを併合した日本列島域の地殻活動予測シミュレーションを行うことを目的としている。

地殻活動予測シミュレーション・システムは、日本列島域の3次元標準構造モデル (CAMP Standard Model; Hashimoto, Fukui & Matsu'ura, PAGEOPH, 2004) 上に構築された、準静的応力蓄積モデル、動的破壊伝播モデル、及び地震/地殻変動データの解析・同化ソフトウェアから成る。平成20年度には、モデル計算と観測データの融合に向け、直接的及び間接的先験情報を考慮したGPSデータの逆解析手法 (Matsu'ura, Noda & Fukahata, GJI, 2007) を北海道-東北地域の地震間 (1996-2000) のGPS速度データに適用して北米-太平洋プレート境界の詳細なすべり遅れ分布を求め (Hashimoto, Noda, Sagiya & Matsu'ura, Nature Geoscience, 2009) その結果に基づいて2003年十勝沖地震の準静的応力蓄積 動的破壊伝播 地震波動伝播の連成シミュレーションを行ない、将来的に発生が予想されるプレート境界地震による地震動を定量的に予測することが可能なことを示した (Fukuyama et al., BSSA, 2009)。平成21年度は、上記のGPSデータ逆解析手法を西南日本域に適用してユーラシア-フィリピン海プレート境界の固着-すべり状態を推定し、駿河湾から豊後水道にかけて帯状に分布する東海・東南海・南海地震の震源域のすべり遅れレートの詳細な分布を明らかにした (Hashimoto, Sagiya & Matsu'ura, SSJ 2009 Fall Meeting)。また、GPSデータから推定したプレート境界のすべり遅れレートに基づいて震源域の応力分布を計算し、境界積分方程式法による仮想南海地震の動的破壊伝播の予測シミュレーションを試みた (Hok, Fukuyama & Hashimoto, SSJ 2009 Fall Meeting)。一方、内陸地震発生メカニズムの解明に向けては、CMTデータから地殻応力を推定する逆解析手法 (Terakawa & Matsu'ura, GJI, 2008) をF-netの15,000の地震データに適用して日本列島全域の3次元地殻応力パターンを明らかにした (Terakawa & Matsu'ura, BSSJ, 2009)。また、GPSデータから地殻内の3次元弾性/非弾性歪み速度場を推定する逆解析手法を確立し、新潟-神戸歪み集中帯の変形様式を明らかにした (Noda & Matsu'ura, GJI, 2010)。

キーワード: GPSデータインバージョン, プレート間カップリング, 応力蓄積, 動的破壊, 連成シミュレーション

Numerical Simulation of Seismic Wave Propagation and Strong Motions in 3D Heterogeneous Structure

Project Representative

Takashi Furumura

Center for Integrated Disaster Information Research, The University of Tokyo
Earthquake Research Institute, The University of Tokyo

Author

Takashi Furumura

Center for Integrated Disaster Information Research, The University of Tokyo
Earthquake Research Institute, The University of Tokyo

We developed a procedure for integrated simulation of seismic wave and tsunami for mitigation of earthquake and tsunami disasters associated with large subduction-zone earthquakes occurring in the Nankai Trough. We firstly calculate ground motion due to the earthquake by solving equation of motions with heterogeneous source-rupture model and 3-D heterogeneous subsurface structural model. We then calculate tsunami generation and propagation in heterogeneous bathymetry by solving the 3-D Navier-Stokes equation. Ground motion and tsunami simulations are combined through an appropriate dynamic boundary condition at the sea floor. Thanks to the Earth Simulator supercomputer, we have been able to reproducing strong ground motion and tsunamis caused by the M8.0 Tonankai earthquake in 1944.

Keywords: Earthquake, 1944 Tonankai earthquake, Long Period Ground motions, Strong Ground Motions, Tsunami

1. Introduction

Large magnitude (M) >8 earthquakes have repeatedly occurred in the Nankai Trough every 100-200 years. Strong ground motion and tsunamis due to the 1944 M8.0 Tonankai and the 1946 M8.0 Nankai earthquakes seriously damaged areas from Kyushu to Tokai, killing over 2,500 persons in total. Over 60 years have been passed since these events, so the next Nankai Trough earthquake is predicted to occur within the next 30 years.

To better understand and mitigate earthquake and tsunami disasters from such earthquakes, we must be able to realistically simulate these phenomena by employing supercomputers to calculate equation of motion that describe seismic wave propagation and the Navier-Stokes (N-S) equation that describe water flow with detailed source-rupture models, high-density three-dimensional (3-D) subsurface structural models, and high-resolution bathymetry data.

The dynamic seafloor displacement due to the earthquake causes an initial tsunami on the sea surface above the source area. However, ground-motion and tsunami simulations are usually conducted independently using different source and structural models even though they are relating very closely. Current tsunami simulations are often based on approximation equations such as linear long-wave theory (LLW) rather than directly solving N-S equations. For these reasons, understanding of strong ground motion and tsunamis associated with the Nankai-Trough earthquakes remains insufficient.

Therefore, we have developed an integration simulation model combining ground motion and tsunami simulation that accurately represents strong ground motion and tsunamis caused by the Nankai Trough earthquakes. In this integrated simulation, the ground motion and tsunami due to heterogeneous source-rupture process and propagating in 3-D subsurface structure can be simulated consistently. Such coupled ground motion and tsunami simulation was developed and first applied to the 1993 M7.8 Hokkaido-Nansei Oki earthquake simulation by Ohmachi et al. (2001) [1], who used the boundary element method (BEM) for calculating dynamic seabed displacement caused by complex fault-rupture in a homogeneous half-space subsurface structure, then tsunami simulation was conducted by solving the N-S equation in 3-D based on the finite-difference method (FDM). Following this pioneering study, we developed an alternative integrated simulation model using a realistic 3-D heterogeneous subsurface structure model and high-resolution bathymetric data by efficient large-scale parallel simulation using supercomputers. We calculate dynamic ground displacement and coseismic seafloor deformation by FDM simulation of equations of motion in 3-D. Then, the results of seafloor ground motion are used for tsunami generation and propagation simulation as an input in the FDM simulation of 3-D N-S equations.

2. Ground Motion and Tsunami Simulations of the 1944 Tonankai earthquake

2.1 Ground Motion Simulation

Seismic wave propagation and strong ground motions can be solved by parallel 3-D FDM simulation of equation of motions (Furumura and Chen, 2004, [2]) based on a domain-partitioned procedure. The simulation model covers 496 x 800 km and extends 141 km deep, which has been discretized using a uniform mesh of 0.4 x 0.4 x 0.2 km. A structural model of the Earth's crust and upper-mantle beneath central Japan is constructed based on the model of sedimentary structures and the shape of the subducting Philippine-Sea Plate. Both are constructed by based on reflection and refraction experiments, deep land drilling, and gravity data. The source-slip model for the 1944 Tonankai earthquake is derived by an inversion using a near-field strong motion waveform. The inferred fault model is 180 x 90 km, and maximum slip of 4 m radiates seismic waves with a total seismic moment of $M_0=1.0 \times 10^{21}$ Nm ($M_w=8.0$; Fig. 1).

The results of the FDM simulation for the seismic wave propagation from the 1944 Tonankai earthquake demonstrate the strength of horizontal velocity ground motion at time $T=15s$, 40s, 90s, and 120s from when the earthquake begins (Fig. 3). A sequence of snapshots clearly shows the spread of seismic waves from the source fault where the fault ruptures spreading from southwest to northeast at a speed slightly less than S-wave speed.

The development of the long-period ground motion at a period of $T=3-6$ s is clearly developed at the rupture front due to the directivity of the rupturing fault. Later time frames ($T=90s$ and 120s) capturing significant amplification of long-period

ground motion in large sedimentary basins such as those beneath Osaka, Nagoya, and Tokyo, where thick sedimentary rocks of over $h=3000$ m cover rigid bedrock (Fig. 3).

2.2 Tsunami Simulation

We then use ground motion simulation results in dynamic seafloor movement caused by the 1944 Tonankai earthquake in tsunami generation and propagation simulation which is described by 3-D Navier-Stokes equations for incompressible flow. Our simulation treats offshore tsunamis because the boundary condition on the sea surface cannot account for tsunami wavefront breaking and tsunami run-up. In order to solve the Navier-Stokes equations, we use the conventional SOLA technique developed by Hirt et al. (1975) [3], which has been widely used for simulating flow of fluid in 3-D. In simulation, velocities and pressure components in cells on the staggered-grid are updated iteratively at each time step to satisfy the following continuity conditions for incompressible fluid at a satisfactory level.

The dynamic vertical seafloor movement on the sea floor derived by the simulation of ground motion is introduced into the tsunami simulation, with the velocity boundary condition at the seafloor during source rupture time. The vertical flow of water due to seafloor movement above the source region lifts the sea surface, which is the initial tsunami developed by the earthquake. The developed initial tsunami distribution at the sea surface is usually smoother than the shape of coseismic seafloor deformation caused by the earthquake because a thick cover of seawater and finite source-duration time works as a sort of high-cut filter to remove large-wave number components from the shape of initial tsunami developed at sea surface (Kajiura,

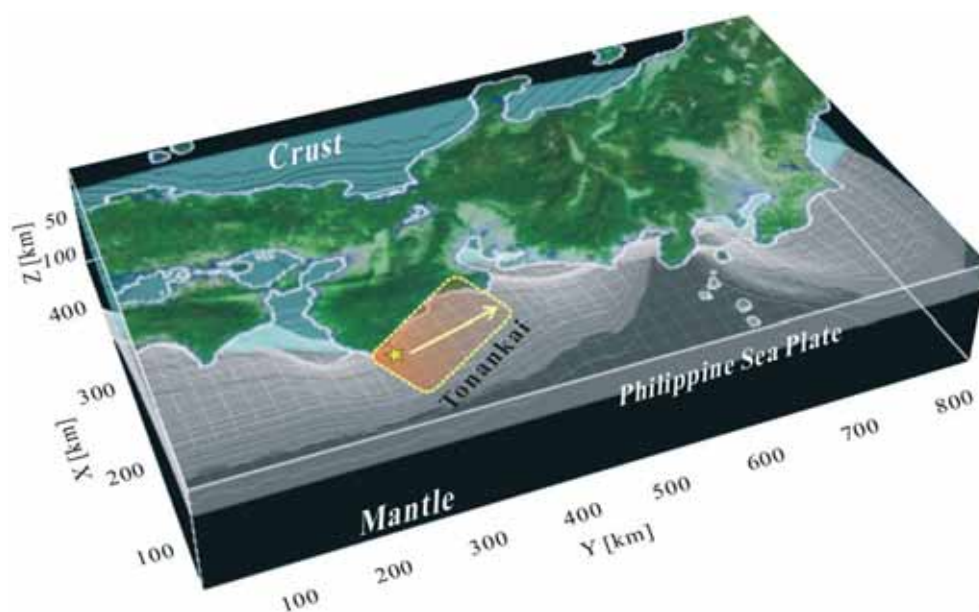


Fig. 1 Source (orange area) model of the 1944 Tonankai ($M_w=8.1$) earthquake and 3D structural model of Nankai Trough subduction zone used for 3D simulation of seismic wave propagation and tsunami propagation simulation.

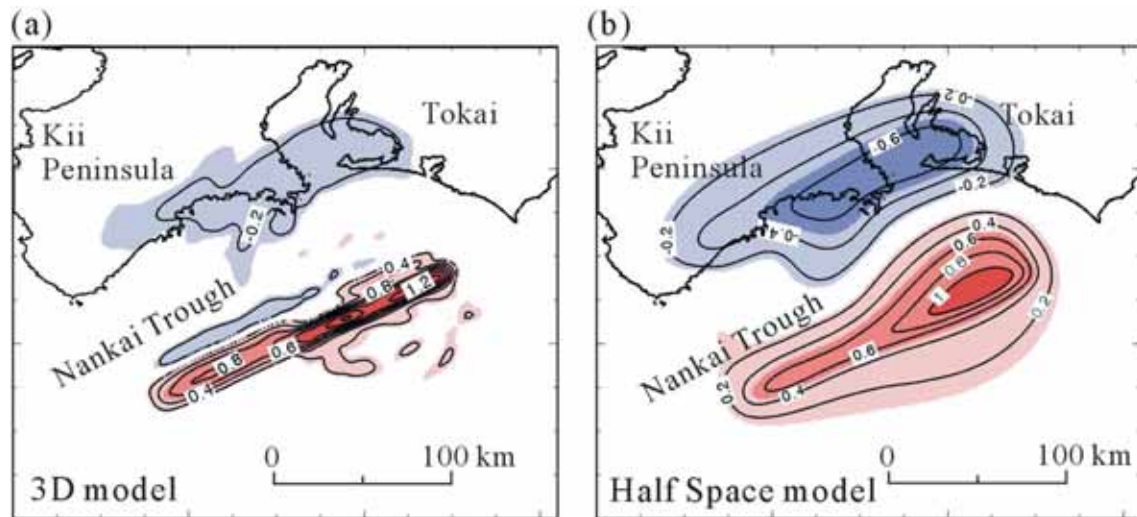


Fig.2 Coseismic deformation of seafloor with uplift (red) and subsidence (blue) of seafloor derived in 3-D simulation of seismic wave propagation using (a) a 3-D heterogeneous structural model and (b) a homogeneous half-space model.

1963, [4]; Saito and Furumura, 2009, [5]). Our 3-D N-S tsunami simulation simulates such all effects naturally and accurately.

The most consuming FDM simulation calculation of the 3-D N-S equation based on the SOLA algorithm is for updating velocity and pressure components at individual cells together with surrounding cells iteratively at each time step. Such an iteration calculation sequence is, however, inefficient in extracting the power of the vector computing hardware such as employed in the Earth Simulator. Thus, it is still necessary to modify present tsunami simulation code suitable for vector computing. For parallel simulations we here used a single-level flat MPI model in which single-threaded MPI processes are

executed on each processor core.

Model of the 3-D tsunami simulation was 500 x 1200 km and 10 km deep, discretized into 1000 * 2400 * 100 grid points with a grid of 500 m horizontally and 100 m deep. We also used digital bathymetric data of J-EGG 500, provided by the Japan Oceanographic Data Center, in the tsunami simulation.

Figure 2 illustrates coseismic seafloor displacement distribution derived by ground motion simulation for the 1944 Tonankai earthquake using the 3-D heterogeneous subsurface structure model for the Nankai-Trough subduction zone (Fig. 1) and that derived by using a homogeneous half-space model assuming rigid bedrock ($V_p=8$ km/s, $V_s=4.6$ km/s). Note that

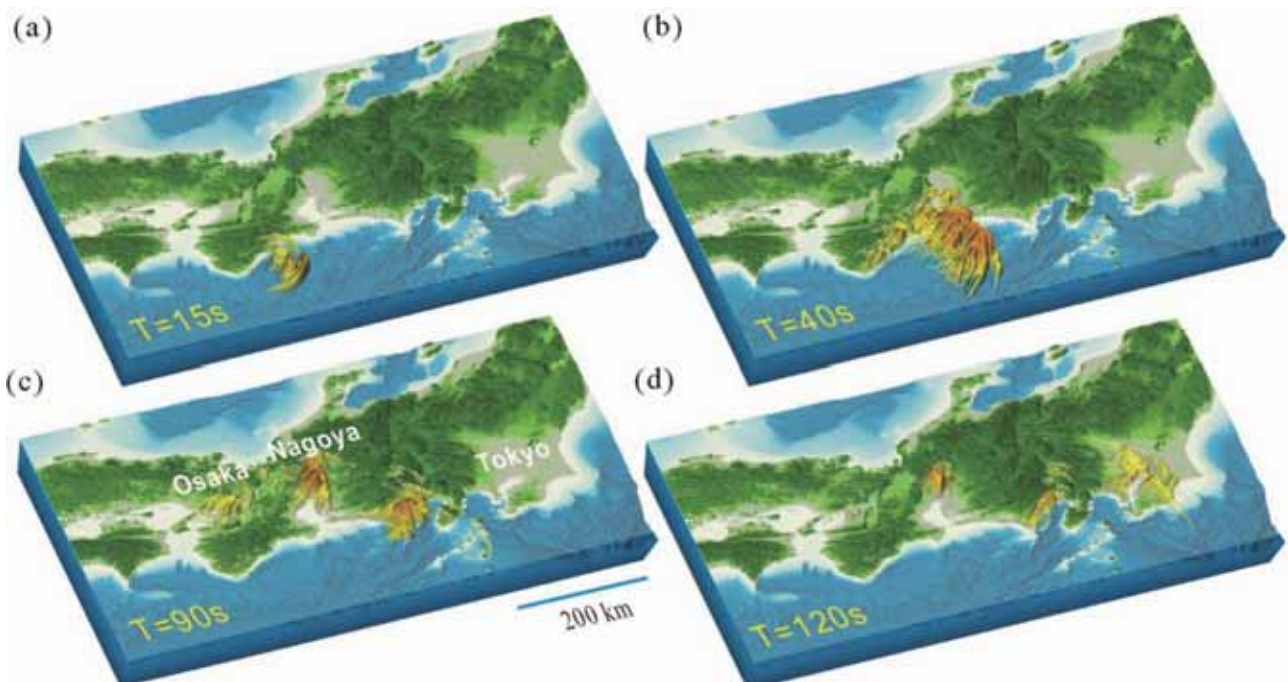


Fig.3 Snapshot of ground motion for the 1944 Tonankai Earthquake derived by 3D FDM simulation of seismic wave propagation.

present tsunami simulation usually assumes such static seafloor elevation in a homogeneous half-space structure using a conventional computer code such as developed by Okada (1985) [6], rather than considering complex seafloor movement due to the actual 3-D heterogeneous structure.

Sea floor elevation results due to low-angle thrust faulting at the top of the shallowly dipping Philippine-Sea Plate show large uplift in the seafloor along the trench of the Nankai Trough and subsidence of ground surface at the eastern coast of the Kii Peninsula. Such coseismic displacement distribution pattern derived by the 3-D model shows a large seafloor elevation in a relatively narrow zone about 20 km wide and 180 km long (Fig. 2a). On the other hand the coseismic displacement pattern derived by simulation using the half-space model is spreading to the wider area of about 80 km and 200 km (Fig. 2b). Maximum seafloor elevation derived by the 3-D and homogeneous half-space subsurface models is almost same at 1.2 m and 1.0 m, respectively.

The tsunami derived by the simulation for the 1944 Tonankai earthquake at time $T = 10, 20, 30,$ and 40 minutes after when the earthquake began had a tsunami wavefield for sea surface uplift and subsidence (Fig. 4). The large slip at the northeastern part of the fault plane and fault rupture propagation from southwest to northeast produced large tsunamis eastward of the source region of the Tonankai earthquake. Some 10 minutes after the earthquake, a large tsunami arrived at the eastern Kii Peninsula and Tokai coast. As the tsunami propagated coastally, the tsunami height increases dramatically. Tsunamis over 2 m high hit the Pacific Ocean coast 10-20 min after the earthquake. Some 20 min after the earthquake the head of the tsunami had spread

to the Izu Islands 300 km east of the hypocenter and to Cape Muroto in Shikoku, and by 40 min the tsunami propagated to the Boso Peninsula and Cape Shiono. As time passed, scattering of tsunami due to multiple reflections in heterogeneous bathymetry and around the islands modified the tsunami waveform very dramatically, leading to complex and long-term sea surface disturbances.

We compared tsunami simulation results for the 3-D N-S model to those from conventional tsunami simulation based on 2-D linear long-wave (LLW) theory. The LLW model effectively treats tsunamis in shallow seas with depth (H) less than the tsunami wavelength (L) ($H < 10\text{-}20 \times L$). In our tsunami simulation for the LLW model, the initial tsunami for the sea surface elevation distribution is assumed to be identical to that of sea bottom elevation, which is also reasonable for considering tsunami generation in shallow seas with sea depth H less than 10 times of the sea bottom deformation area S_a ($H < 10 \times S_a$; Saito and Furumura, 2010, [5]). Note that the linear theory (Kajiura, 1963, [4]) can also be used for more accurate estimation of initial tsunami distribution on the sea surface caused by the sea floor deformation in deep sea.

Simulated tsunami waveforms at Mera, Uchiura, Matsuzaka, and Tosa Shimizu stations are shown in Fig. 5 which have been applied a high-cut filter with a cut-off frequency of $f_c=0.0167$ Hz (cut-off period of $T_c=1$ min) to remove high-frequency signals. The tsunami waveform derived by the half-space subsurface structure model shows a smooth, longer-wavelength tsunami compared to that from the heterogeneous 3-D structural model as is easily expected from the seafloor displacement distribution pattern shown in Fig. 2. On the other hand the

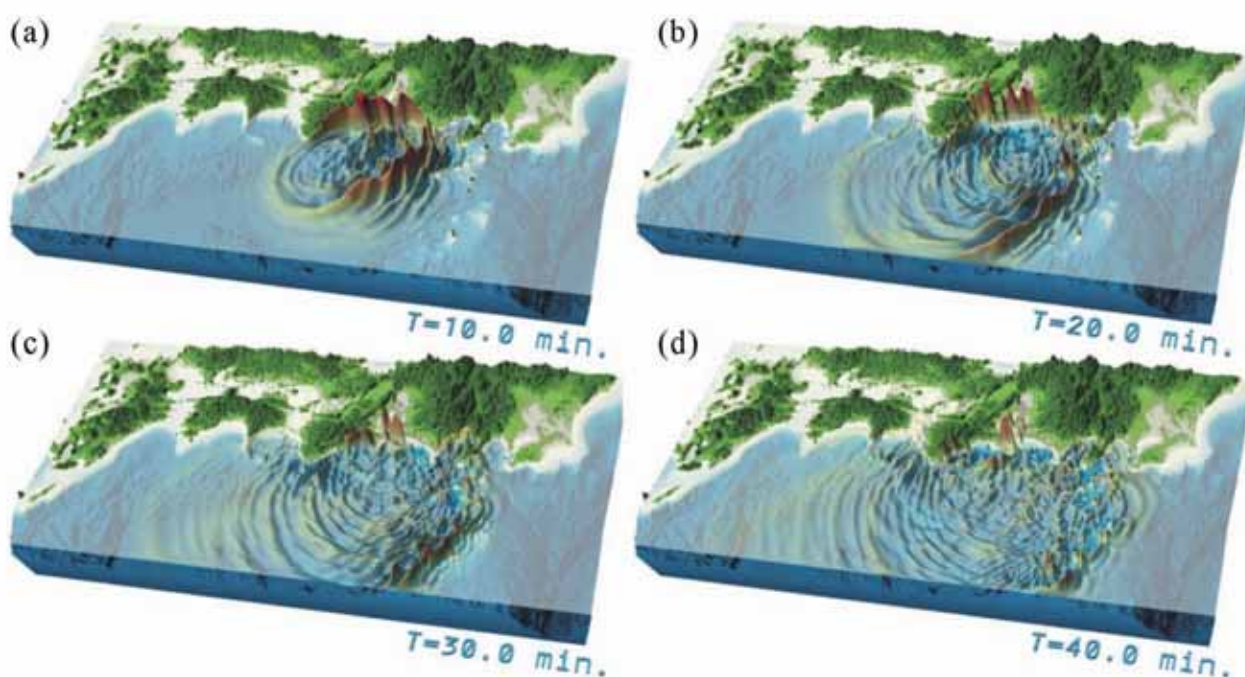


Fig.4 Snapshots of tsunami from the 1944 Tonankai Earthquake derived by the 3D Navier-Stokes equation simulation.

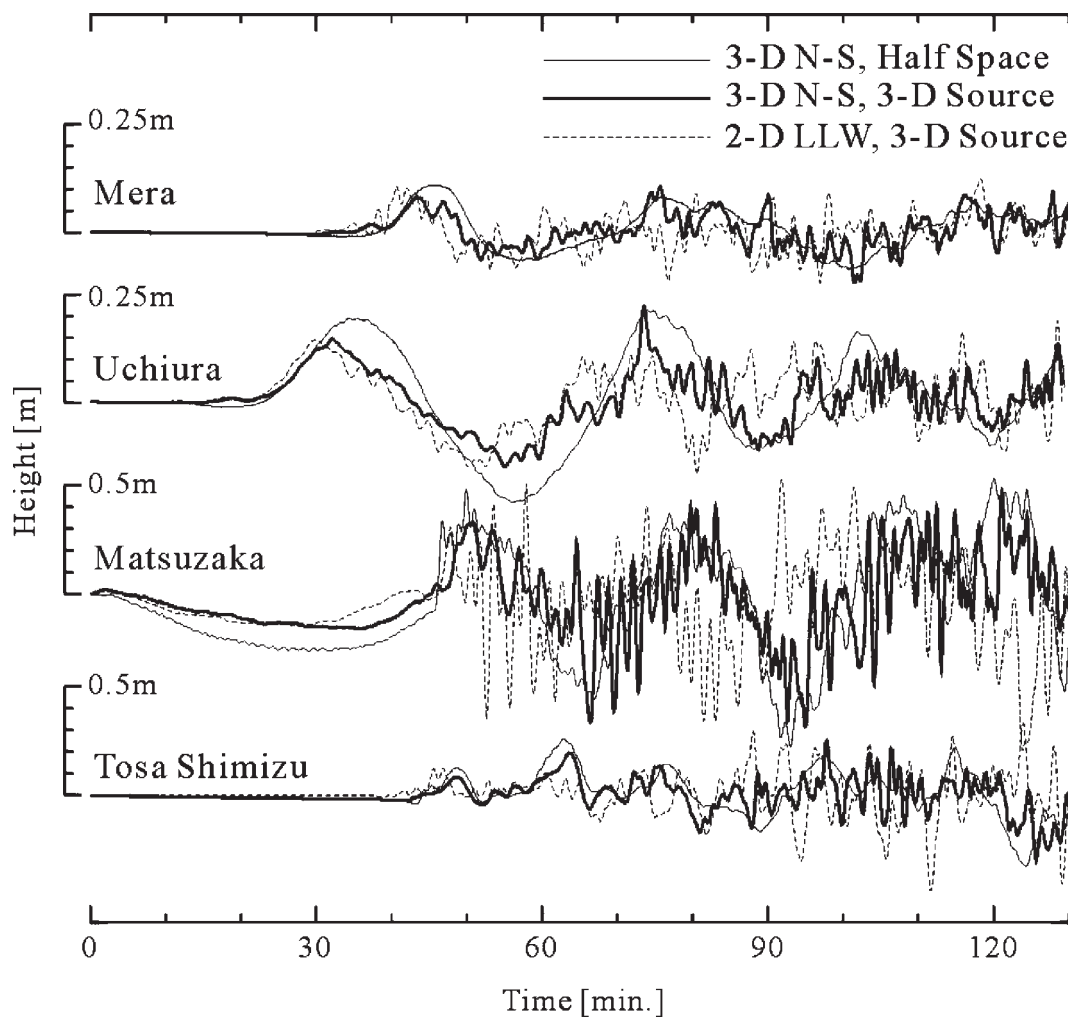


Fig.5 Simulated tsunami waveform at Mera, Uchiura, Matsuzaka, and Tosa Shimizu (stations in Fig. 5) derived by simulation using 3-D N-S and source models assuming a 3-D heterogeneous structure (thick lines) (Fig. 2a) and a homogeneous half-space model (thin lines) (Fig. 2b) and 2-D LLW model (dashed lines).

tsunami waveform derived by the simulation from the 3-D N-S model shows a somewhat smoother wave shape than that for the 2-D LLW model because the cover of thick sea water above the source acts high-wavenumber cut filter. A finite source-rupture time for the earthquake also removes large wave number components from the initial tsunami distribution on the sea surface. Some delay in tsunami arrival of 3-5 min in the 3-D N-S simulation in the tsunami record of distant Mera and Tosa Shimizu stations is due to the dispersion of tsunami propagating in deep Nankai Trough. Such effects are not accounted for in the 2-D LLW model.

3. Conclusion

Large ($M > 8$) earthquakes occurring in the Nankai Trough might be causing significant disasters from Kyushu to Tokai along Japan's Pacific Ocean coast due to large, long-term ground shaking of long-period ground motions in sedimentary basins and tsunamis along the coastal zone. Coseismic vertical movements associated with large earthquakes also have caused rise and subsidence in coastlines near the source

area. Downtown Kochi, Shikoku, sank after the 1946 Nankai earthquake due to coastal subsidence - exceeding 0.5 m. Such coseismic displacement is expected to cause additional coastal disasters with enhanced tsunami inundation and tidal wave effects.

To mitigate such earthquake-related disasters anticipated in future Nankai-Trough earthquakes, integrated ground motion and tsunami simulation using high-performance computers and reliable simulation models is indispensable.

By using present ES supercomputers, we have reproduced long-period ground motion, coseismic deformation, and tsunamis during the 1944 Tonankai earthquake very efficiently. Simulation and observation results agreed well for long-period ground motion developing in central Tokyo, indicating the effectiveness of the present simulation model for modeling long-period ($T > 2$ s) ground motion for the past and future earthquakes.

Acknowledgement

This study was conducted under the joint research project

of the Earth Simulator Center with title "Numerical simulation of seismic wave propagation and strong ground motions in 3-D heterogeneous media" The author acknowledge to the Earth Simulator Center for providing large computer resources.

References

- [1] Ohmachi, T., H. Tsukiyama, and H. Matsumoto, "Simulation of tsunami induced by dynamic displacement of seabed due to seismic faulting," *Bull. Seism. Soc. Am.*, 91, pp. 1898-1909, 2001.
- [2] Furumura, T. and L. Chen, "Large scale parallel simulation and visualization of 3D seismic wavefield using the Earth Simulator," *Computer Modeling and Engineering Sciences*, 6, pp.143-168, 2004.
- [3] Hirt, C.W., B. D. Nichols, and N. C. Romero, "SOLA - A numerical solution algorithm for transient fluid flows," *Los Alamos National Laboratory report LA-5852*, 1975.
- [4] Kajiura, K., "The leading wave of a tsunami," *Bulletin of the Earthquake Research Institute*, 41, pp. 545-571, 1963.
- [5] Saito, T., and T. Furumura, "Scattering of linear long-wave tsunamis due to randomly fluctuating sea-bottom topography: coda excitation and scattering attenuation", *Geophys. J. Int.*, 178, 877-888, 2010.
- [6] Okada, Y., "Surface deformation due to shear and tensile faults in a half space", *Bull. Seismol. Soc. Am.*, 75, pp. 1135-1154, 1985.

3 次元不均質場での波動伝播と強震動シミュレーション

プロジェクト責任者

古村 孝志 東京大学 大学院情報学環総合防災情報研究センター
東京大学 地震研究所

著者

古村 孝志 東京大学 大学院情報学環総合防災情報研究センター
東京大学 地震研究所

南海トラフ巨大地震による強震動と津波を高精度に評価し、災害の予測と軽減に資することを目的に、地震と津波の連成シミュレーションコードを開発した。本シミュレーションでは、まず震源モデルと地下構造モデルを用いて地震動と地震地殻変動を運動方程式の3次元差分法計算により評価する。次に、求められた海底面及び陸の地殻変動を入力として、津波の発生と伝播を3次元ナビエストークス式の差分法計算により行う。地震と津波の連成シミュレーションにより、不均質な地下構造で発生する地震が作り出す地殻変動を正しく評価することができ、そして地震から津波にいたる海溝型巨大地震の災害を時間を追って考えることができるようになる。従来の津波評価では地殻変動は均一な地下構造を用いた評価が一般的であり、また津波伝播計算には線形長波モデルが用いられることが多かった。本シミュレーションにより、3次元的に不均質の強い海底下での特異な地殻変動と、深い海を伝わる津波の分散波の特徴を表現することができるようになり、南海トラフ地震による津波の継続時間を含めた津波波形の評価に威力を発揮するものと期待される。ナビエストークス式計算のベクトル化効率が悪く、コードチューニング等による改善が課題として残される。

Development of Advanced Simulation Methods for Solid Earth Simulations

Project Representative

Akira Kageyama

Graduate School of System Informatics, Kobe University

Authors

Akira Kageyama^{*1}, Mamoru Hyodo^{*2}, Mikito Furuichi^{*2}, Takehiro Miyagoshi^{*2},
Masanori Kameyama^{*3} and Nobuaki Ohno^{*4}

*1 Graduate School of System Informatics, Kobe University

*2 Institute for Research on Earth Evolution, Japan Agency for Marine-Earth Science and Technology

*3 Geodynamics Research Center, Ehime University

*4 Earth Simulator Center, Japan Agency for Marine-Earth Science and Technology

Geodynamo: We have found a new convection regime of the core that exhibits a dual structure in the low viscous frontier of numerical simulation of geodynamo; sheet-like radial plumes inside and a westward cylindrical zonal flow outside. The dual convection structure with the zonal flow is stable under a self-generated strong magnetic field. **Mantle convection:** We have improved our numerical code "ACuTEMan" by employing the truncated anelastic liquid approximation (TALA). This has enabled us to successfully incorporate the effects of adiabatic compression on thermal convection in Cartesian domains. **Plate-mantle unified system:** we have developed an iterative solution technique for solving the Stokes flow problem with a large and sharp contrast in viscosity, for example, between the upper mantle, tectonic plate and sticky air for free surface treatment. Our method with Schur complement approach with mixed precision arithmetic is very robust against large and sharp viscosity contrast, given by the one to several grid resolutions.

Keywords: Geodynamo simulation, Yin-Yang grid, Mantle convection, Anelastic Liquid Approximation, Schur complement, Double-double.

1. Geodynamo simulation

Zonal jets are omnipresent in nature. Well known examples are those in atmospheres of giant planets, alternating jet streams in the Earth's ocean, and zonal flow formation in nuclear fusion devices. A common feature of these zonal flows is that they are spontaneously generated in turbulent systems. Since the Earth's outer core is also believed to be in a turbulent state, it is an interesting question if a vigorous zonal flow exists in the liquid iron of the outer core. We have found, in the low viscous frontier of numerical simulation of geodynamo, a new convection regime of the core that exhibits a dual structure; sheet-like radial plumes inside and a westward cylindrical zonal flow outside. The dual convection structure with the zonal flow is stable under a self-generated, strong dipole magnetic field.

Convection motion of the Earth's liquid core generates the geomagnetic field through the magnetohydrodynamic (MHD) dynamo process. Computer simulation of the geodynamo has successfully reproduced the Earth's dipole magnetic field and its reversals, and various scaling laws are reduced. The convection motion in those simulations are basically composed of

columnar cells aligned to the rotation axis. Recently, we have performed geodynamo simulations on the Earth Simulator with the highest spatial resolution ever achieved. The fine resolution has enabled us to investigate the numerical frontier of the low viscous simulation. One of the most important non-dimensional parameters of the core defined with the viscosity is Ekman number Ek . We have reported that when Ek is sufficiently small (of the order of 10^{-7}), the convection motion is composed of sheet-like plumes rather than columns [1].

In this fiscal year, we have found that the sheet-like plumes are surrounded by a zonal flow (Fig. 1). The simulation model and results are reported in our recent paper [2]. In the zonal flow region, the radial flow component in the cylindrical coordinate, v_r , is feeble while the azimuthal component, v_ϕ , is dominant. The zonal flow is westward. We call this convection structure--the sheet plumes inside and the zonal flow outside--as "dual convection". We have found that the dual convection state always appear when Ek is small and the Rayleigh number, Ra , is sufficiently large.

To prove the stability of the dual convection under the

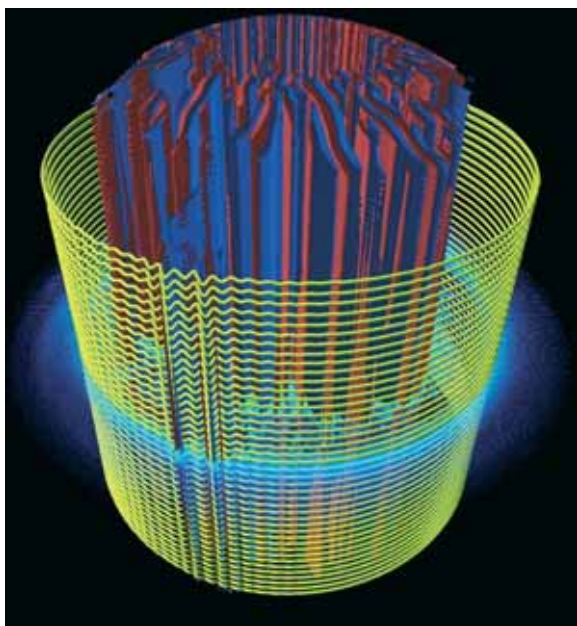


Fig. 1 Convection structure viewed from equator. Red and blue surfaces are positive (red) and negative (blue) isosurfaces of axial vorticity. The yellow lines are streamlines.

strong magnetic field, we would have to continue the run for much longer time, but it is practically impossible because the simulation would take for years with our the total grid size of 511 (in radial) \times 514 (in latitudinal) \times 1538 (in longitudinal) \times 2 (Yin and Yang).

We have therefore made a survey to find a parameter set in which the dual convection structure is formed under a coarser grid resolution $255 \times 258 \times 770 \times 2$, by which the simulation can be performed in much more swiftly. With this grid size, we were able to integrate the calculation for sufficiently long time to confirm the stability of the dual convection structure. The dual convection structure is stable even under self-generated strong magnetic field.

The zonal flow is generated and maintained by the non-linear coupling of the velocity components, or the Reynolds stress. Small scale flows ejected from the inner plumes transport the westward angular momentum at the zonal flow radius. The three-dimensional structure of the zonal flow is fairly uniform in the direction of the rotation axis. The flow appears as in a thin zone in the equatorial plane is actually a cross section of a thin cylinder of westward flows.

It is known from numerical simulations of planetary atmospheres that relatively strong azimuthal flows are formed in a rotating spherical shell convection under the stress-free boundary condition for the spherical boundaries. In contrast to those systems, the core is "capped" by the mantle. Our simulation suggests that convection in a spherical vessel may be closer than we had expected to the planetary atmospheres and oceans when viscosity or Ekman number is sufficiently small.

2. Development of mantle convection simulation code with adiabatic compression

In this FY, we developed a simulation code of mantle convection in a three-dimensional Cartesian domain which includes of the effect of adiabatic compression of mantle materials [3]. In most of numerical models of mantle convection, including our previous ones [4,5], the effects of adiabatic compression is ignored simply because of the numerical difficulty, although it has been commonly acknowledged that there occurs a significant compression of mantle materials by an extremely high pressure (exceeding 100GPa) expected in the Earth's interior. Here, by improving the thermodynamic treatment of the convecting fluid, we successfully incorporated the effects of adiabatic compression on thermal convection in Cartesian domains.

In this study, we improved our numerical code "ACuTEMan" by employing the truncated anelastic liquid approximation (TALA). The term "truncated" means that the effect of compression by dynamic pressure is ignored in the buoyancy force. This assumption is sufficiently validated by the fact that the dynamic pressure due to the fluid motion is much smaller than the static pressure by the overburden load. Compared to the well-known incompressible and/or Boussinesq approximation, the TALA enables us to include the effects of (i) the change in reference (i.e., zero-motion) density with pressure (or depth) and (ii) the conversion from mechanical to thermal energies such as an adiabatic (de)compression and viscous dissipation (or frictional heating). In particular, the first effect is taken into account through the change in the definition of thermal buoyancy and the divergence-free constraints on the mass flux (not on velocity). In the actual numerical model, the effect of adiabatic compression is expressed by a nondimensional parameter called "dissipation number", which is a measure of a ratio of the scale-height of density change to the thickness of the convecting layer. By conducting series of calculations of steady-state and time-dependent convection with systematically varying the Rayleigh and dissipation numbers, we confirmed that accurate results are successfully reproduced even for the cases with viscosity variations of several orders of magnitude. The present numerical code was chosen as one of the benchmark programs for a thermal convection of compressible fluids in two-dimensional Cartesian geometry.

3. Development of robust Stokes flow solver against viscosity jump by Schur complement approach with mixed precision arithmetic.

We develop an iterative solution technique for solving the Stokes flow problem with a large and sharp contrast in viscosity, for finite volume discretization in three dimensions. Robustness and scalability of the solver against viscosity contrast is important to treat the problems of the realistic geodynamical modeling. The large viscosity jump of the property on the sharp

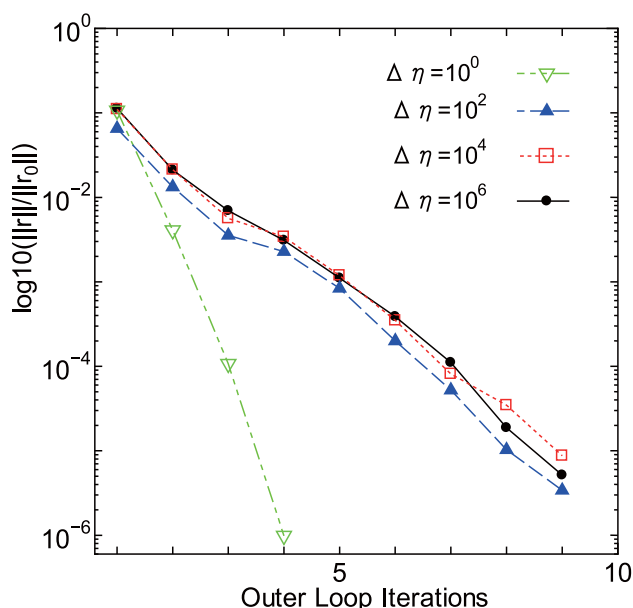


Fig. 2 Convergence history of the outer iterations by BFBt preconditioner for the falling block problems with different viscosity contrast.

interface is expected at the boundary interface, for example, between the upper mantle and the tectonic plate, or the treatment of free surface by the sticky air [6,7]. We use the Schur complement reduction with the Krylov subspace method. For the pre-conditioning of Schur complement, we employ scaled BFBt pre-conditioner as a scalable approach against the strong variation of viscosity profile. In addition, in order to improve the convergence of Krylov subspace method for momentum equation required for BFBt pre-conditioner, we propose to use a mixed precision technique. We implement quad precision arithmetic on Earth Simulator 2 by using the double-double precision method.

In order to see the performance of our iterative method, we solve the falling block benchmark test with a high viscosity jump $\Delta\eta$ within one discretized grid length. Figure 2 shows a history of outer solver residual. This plot presents that the number of iteration with the scaled BFBt pre-conditioner shows good scalability against the viscosity jump in the finite volume discretization.

References

- [1] Akira Kageyama, Takehiro Miyagoshi, and Tetsuya Sato, Formation of current coils in geodynamo simulations, *Nature*, vol. 454 pp. 1106-1109, 2008.
- [2] Takehiro Miyagoshi, Akira Kageyama, and Tetsuya Sato, Zonal flow formation in the Earth's core, *Nature*, vol. 463, pp. 793-796, 2010.
- [3] Scott D. King, Changyeol Lee, Peter E. van Keken, Wei Leng, Shijie Zhong, Eh Tan, Nicola Tosi, and Masanori Kameyama, A Community Benchmark for 2D Cartesian Compressible Convection in the Earth's Mantle, *Geophys. J. Int.*, vol. 180, pp. 73-87, 2010.
- [4] Masanori Kameyama, Akira Kageyama, and Tetsuya Sato, Multigrid iterative algorithm using pseudo-compressibility for three-dimensional mantle convection with strongly variable viscosity, *J. Comput. Phys.*, vol. 206, pp. 162-181, 2005.
- [5] ACuTEMan: A multigrid-based mantle convection simulation code and its optimization to the Earth Simulator, *J. Earth Simulator*, vol. 4, pp. 2-10, 2005.
- [6] Furuichi, M., Kameyama, M., and Kageyama, A., 2008. Three-Dimensional Eulerian method for large deformation of viscoelastic fluid: Toward plate-mantle simulation, *J. Comput. Phys.* 227, 4977-4997.
- [7] Furuichi, M., Kameyama, M. and Kageyama, A., 2009, Validity test of a Stokes flow solver by fluid rope coiling: toward plate-mantle simulation, *Phys. Earth Planet. Interiors*, 176, 44-53

先端的固体地球科学シミュレーションコードの開発

プロジェクト責任者

陰山 聡 神戸大学大学院 システム情報学研究科

著者

陰山 聡^{*1}, 兵藤 守^{*2}, 古市 幹人^{*2}, 宮腰 剛広^{*2}, 亀山 真典^{*3}, 大野 暢亮^{*4}

*1 神戸大学大学院 システム情報学研究科

*2 海洋研究開発機構 地球内部ダイナミクス領域

*3 愛媛大学 地球深部ダイナミクス研究センター

*4 海洋研究開発機構 地球シミュレータセンター

我々の最終的な目標は、地球シミュレータを駆使した大規模計算機シミュレーションを通じて、地球ダイナモとマン
トル対流をはじめとする地球内部全体の構造とダイナミクスを理解することである。そのために必要となる大規模並列
計算手法や基本数値アルゴリズムの独自開発にも積極的に取り組んでいる。

地球ダイナモシミュレーション：本年度は前年度に引き続き、低エクマン数領域の地球ダイナモシミュレーションを
追求した。その結果、前年度に発見したシート状のブルーム対流の周囲に西向きに流れる帯状流が形成されることを見
出した。帯状流を伴うこの2重対流構造は、MHD ダイナモ作用で生成された磁場の下でも安定に存在することを確認し
た。エクマン数とレイリー数をさまざまに変えた計算を行った結果、この構造はエクマン数が低くレイリー数が高い場
合にのみ現れる事が分かった。

マントル対流シミュレーション：ACuTE法の改良を行い、地球深部の高圧力条件下におけるマントル物質の(静的な)
断熱圧縮及び粘性散逸の効果を取り入れる事を可能にした。ここで開発・改良したプログラムは、非弾性流体近似に基
づいたマントル対流シミュレーションのベンチマークプログラムとして採用された。

プレート・マントル統合シミュレーション：プレートとマントルの間にある鋭い粘性差、ならびに数値惑星に向けた
自由境界表面を動的に取り扱う事を目的として、鋭い粘性差(ジャンプ)に対して有効なストークス流れソルバーの開
発を行った。具体的にはシュアー補行列を用いて、ストークス流れの行列問題を速度と圧力に分離し、対角項で規格化
されたBFBt前処理行列を用いることにより、速度と圧力の結合する反復法の収束性を粘性差に対してスケラブルな
ものにした。また局所的にdouble-double methodによる4倍精度演算を取り入れることで、計算時間をあまり増やすこと
なく効率的に粘性差に対してロバストな反復法を構築することに成功した。

キーワード:地球地球ダイナモ, インヤン格子, マントル対流, 非弾性流体近似, シュアー補行列, 混合4倍精度

Numerical Determination of the Efficiency of Entrainment in Volcanic Eruption Columns

Project Representative

Takehiro Koyaguchi Earthquake Research Institute, University of Tokyo

Authors

Yujiro Suzuki Institute for Research on Earth Evolution, Japan Agency for Marine-Earth Science and Technology

Takehiro Koyaguchi Earthquake Research Institute, University of Tokyo

Entrainment of air by turbulent mixing plays a central role in the dynamics of eruption clouds; the amount of entrained air controls eruption styles and heights of eruption columns. The efficiency of entrainment is quantified by the entrainment coefficient: the ratio between mean inward radial velocity at the edge and the mean vertical velocity. We directly determined the entrainment coefficient of eruption columns as a function of height on the basis of three-dimensional numerical simulations. The value of entrainment coefficient is similar to that for pure jets (~ 0.07) just above the vent, and approaches that for pure plumes ($0.10 - 0.15$) far from the vent. Between these two regions, we identify a new transitional zone with a significantly small entrainment coefficient (~ 0.05). This spatial variation in the entrainment coefficient is correlated with the change in vortical structure just above the vent.

Keywords: volcanic eruption cloud, pseudo-gas model, turbulent mixing, volcanic hazard

1. Introduction

During explosive eruptions, a mixture of volcanic gas and pyroclasts is released from a vent with a density larger than the atmospheric density. As the ejected material entrains ambient air through turbulent mixing, the density of the eruption clouds decreases because the entrained air expands by heating from the hot pyroclasts. Since the density of the mixture of the ejected material plus the entrained air changes with their mixing ratio, the efficiency of entrainment controls the dynamics and heights of eruption clouds [1-5]. If the amount of entrained air is sufficient, an eruption column convectively rises, whereas, if it is insufficient, a heavy pyroclastic flow spreads on the ground surface.

The flow of an eruption cloud is modeled as a free boundary shear flow. Here, we refer to turbulent free boundary shear flows driven by initial momentum as pure jets and those driven by buoyancy as pure plumes. When a pure jet or plume is ejected from a point source into a uniform environment, the flow is characterized by the self-similarity. Turbulent mixing in and around a strictly self-similar flow can be explained by the entrainment hypothesis that the entrainment velocity at the edge of a turbulent jet and/or plume, U_e , is proportional to the mean vertical velocity, W , at each height as $U_e = kW$ [1]. The proportionality constant, k , represents the efficiency of entrainment and is called the entrainment coefficient. Experimental studies suggest that pure jets and plumes are approximated by self-similar flows with constant k (~ 0.07 for

jets and $0.10 - 0.15$ for plumes) [6, 7].

Unlike pure jets or plumes, the flow of an eruption cloud is not self-similar. Its driving force changes with height because of the change in density. The flow near the vent has negative buoyancy and is driven by the initial momentum. As the eruption column rises, the density of the cloud decreases and the flow is primarily driven by positive buoyancy. Recent theoretical studies have suggested that the entrainment coefficient of such a non-self-similar flow is not necessarily constant [3]; however, no previous studies have succeeded in determining how the entrainment coefficient spatially varies in eruption clouds. The lack of knowledge of the spatial variation of entrainment coefficient has been a fundamental obstacle for understanding the entrainment mechanisms. In this study, we determine the value of k as a function of height (referred to as 'local k ') using three-dimensional (3-D) simulations of an eruption column.

2. Model for Determining k by 3-D Model

The simulations are based on a 3-D time-dependent fluid dynamics model that solves a set of partial differential equations describing the conservation of mass, momentum, and energy, and constitutive equations describing the thermodynamic state of the mixture of solid pyroclasts, volcanic gas, and air (see Suzuki et al. [4] for details). We assume that no particles separate from the eruption clouds when their size is sufficiently small (< 4 mm). In order to reproduce the general feature of turbulent mixing that the efficiency of entrainment is independent of the

Reynolds number [8], the grid sizes must be sufficiently smaller than the characteristic length scale of the flow. In the case of eruption columns, the characteristic length scale is represented by the radial scale of the flow at each height; it ranges from the vent diameter, D_0 , near the vent up to several tens of kilometers far from the vent. Suzuki et al. [4] showed that grid sizes smaller than $D_0/10$ correctly reproduce turbulent mixing near the vent. In order to effectively simulate the turbulent mixing with high spatial resolutions both near the vent and far from it, we have developed a 3-D code in which the domain is discretized on a non-uniform grid. The grid size is set to be sufficiently smaller than $D_0/10$ (typically $D_0/16$) near the vent, and to increase at a constant rate (1.01 for the vertical coordinate and 1.02 for the horizontal coordinate) with the distance from the vent up to $D_0/2$, such that the grid size is small enough to resolve the turbulent flow far from the vent.

From the 3-D simulations, we can directly determine local k using the following relationship [cf. 9, 10]:

$$k = Q_{in}/2\pi\rho_a LW, \quad (1)$$

where Q_{in} is the mass inflow of ambient air, ρ_a is the atmospheric density, and L is the radius of the eruption column at each height. The value of LW is given by

$$LW = \left(\int_0^\infty w^2 r dr\right)^{1/2}, \quad (2)$$

where w is the time-averaged vertical velocity, and r is the radial coordinate. In addition to the value of LW , the value of Q_{in} is required to estimate local k from Eq. (1).

The value of Q_{in} is estimated from the flow field that is averaged in time. The time-averaged flow field in and around the eruption column is divided into two regions with respect to flow directions. Inside the eruption column, the flow is predominantly vertical and the time-averaged radial velocity, u , is negligible. Outside the eruption column, on the other hand, the flow is approximately radial, and the time-averaged vertical velocity, w , is nearly zero. Using these features in the time-

averaged flow field, we can calculate the radial mass inflow around the eruption column:

$$Q_{in,1} = 2\pi\rho_a r u. \quad (3)$$

Because of the mass conservation of the radial mass inflow, $2\pi\rho_a r u$ remains constant regardless of r away from the column edge. This constant value outside the eruption column represents Q_{in} .

The value of Q_{in} can also be estimated from a method that utilizes the vertical mass flux inside the column, M as

$$Q_{in,2} = dM/dz, \quad (4)$$

where

$$M = \int_0^\infty 2\pi\rho w r dr. \quad (5)$$

When the flow of the eruption column reaches a steady-state, $Q_{in,2}$ must be equal to $Q_{in,1}$. In Section 3, we present the variation of local k based on $Q_{in,1}$; local k based on $Q_{in,2}$ is used to confirm the steadiness of flow as well as the consistency of the two methods.

Table 1 Input Parameters of the Simulations

Simulation	L_0 (m)	m_0 (kg s ⁻¹)	w_0 (m s ⁻¹)	T_0 (K)
Run 1	45	4.0×10^6	180	1053
Run 2	40	3.2×10^6	181	1053
Run 3	57	6.3×10^6	179	1053

3. Results

We carried out three simulations for explosive eruptions from a circular vent into a stationary atmosphere under the tropical condition (Table 1). An initial mass fraction of volcanic gas of $n_{g0}=0.06$ is assumed. The source conditions are set to be steady and pressure-balanced with a vent velocity equal to the sound velocity of the ejected material.

Our primary concern is how the efficiency of entrainment in eruption columns deviates from those for pure jets or plumes ejected from point sources. For this purpose, it is important to set vent radii sufficiently smaller than the length scale at

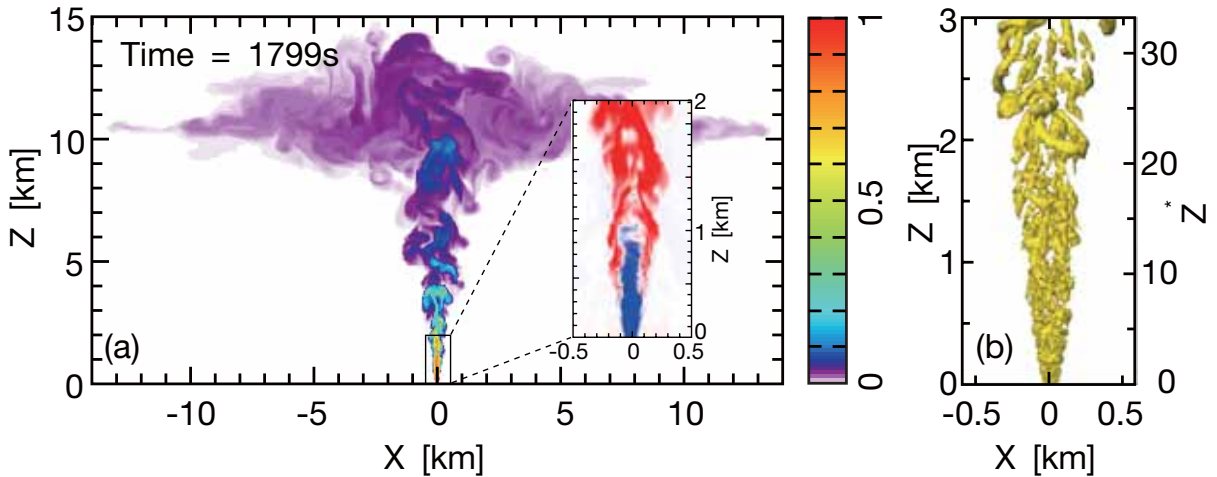


Fig. 1 Numerical results of an eruption column at 1799 s from the beginning of eruption in run 1. (a) Cross-sectional distributions of the mass fraction of magma and (inset) the density difference relative to the stratified atmospheric density at the same vertical position, $-\Delta\rho/\rho_a=1-\rho/\rho_a$, in $x-z$ space. (b) Isosurface of swirling strength (0.2).

which the initial upward momentum is lost (2-3 km) in the simulations. When the vent radius is greater than a few hundred meters, the eruption cloud loses its momentum before turbulent mixing fully develops from the edge to the core of the flow; as a result, the heavy unmixed core forms a radially suspended flow whose global feature is qualitatively different from those of typical turbulent jets or plumes [4, 11]. In order to avoid additional effects caused by such qualitative differences in flow patterns, we set vent radii to be less than 60 m in this study; the corresponding magma discharge rates range from 10^6 to 10^7 kg s^{-1} (see Table 1).

Our simulations have successfully reproduced the time evolutions of eruption columns (Fig. 1). The eruption cloud is ejected from the vent as a turbulent jet with a large density (3.47 kg m^{-3}) relative to the atmospheric density (1.16 kg m^{-3}). As the turbulent jet entrains ambient air, the eruption column rises as a buoyant plume. The radius of the eruption column linearly increases with height. After the eruption column reaches a maximum height, an umbrella cloud spreads radially, while the eruption column is stably sustained above the vent (Fig. 1a for run 1).

The eruption cloud entrains ambient air through unsteady flow due to turbulence in and around the column (inset in Fig. 1a). Near the vent, the entrainment is driven by shear between the cloud and air at the edge of the column; as a result, a concentric structure consisting of an inner flow and an outer shear layer develops. The outer shear layer has a lower density than that of air owing to expansion of entrained air. On the other hand, the inner flow, which is not mixed with ambient air, remains denser than air. The inner flow is eroded by the outer shear layer and disappears at a certain level (at a height of ~ 1 km for run 1). As the eruption column further ascends, the flow becomes highly unstable and undergoes a meandering instability.

Fig. 2a shows time-averaged distributions of the vertical velocity between 500 and 1799 s for run 1. The radial profile of the vertical velocity is set to be a top-hat shape as a boundary condition at the vent. The velocity profile near the vent ($z=0-2$ km) is subjected to an intense flow development from a top-hat to a Gaussian shape. Above 2 km, the velocity profile is approximated by a Gaussian shape.

From the profiles of w and $2\pi\rho_a r u$ (Fig. 2), we can identify the two distinct flow regions: the inside and outside of the eruption column. Outside the eruption column ($r > 2\sigma$ in Fig. 2), the value of $2\pi\rho_a r u$ remains constant. In this study, we estimate $Q_{\text{in},1}$ from the spatial average of $2\pi\rho_a r u$ in the range of $2\sigma < r < 3\sigma$ at each height for two directions. We confirmed that the value of $Q_{\text{in},1}$ is consistent with $Q_{\text{in},2}$ at each height (figures not shown).

Substituting $Q_{\text{in},1}$ into Eq. (1), we obtain the value of local k as a function of height (Fig. 3). The vertical profiles of k for different mass discharge rates ranging from 10^6 to 10^7 kg s^{-1} show a universal feature when the downstream distance from

the vent is normalized by D_0 . The value of k decreases with height from 0.07 to 0.05 just above the vent. The region of $3 < z^* < 15$ is characterized by a small value of $k \sim 0.05$. The value of k increases with height in the range of $15 < z^* < 30$, and approaches a constant value of 0.10 – 0.15.

The value of k decreases again with height above the level where the umbrella cloud begins to develop ($z^* > 60$); however, we do not consider this tendency further, because our estimation based on Eqs. (3) or (4) is no longer applicable for the region where an outward radial flow due to gravity current becomes predominant.

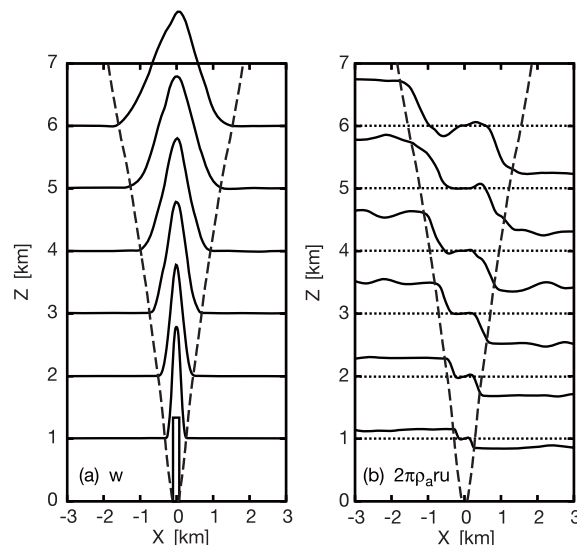


Fig. 2 Time-averaged radial profiles of (a) the vertical velocity and (b) the radial mass flux ($2\pi\rho_a r u$) at different heights in run 1. Dashed curves in the figures are the position of $r=2\sigma$. Note that the value of $2\pi\rho_a r u$ does not depend on x outside of the plume.

4. Discussion

The direct measurements of local k show that k is equal to that for pure jets (~ 0.07) just above the vent and approaches that for pure plumes (0.10 – 0.15) far from the vent. These features are consistent with the fact that eruption columns are driven by the initial momentum near the vent and by buoyancy far from the vent. Between these two regions we identify a transitional zone with a small local k (~ 0.05). The presence of this transitional zone is one of the most distinct characteristics of entrainment in eruption columns.

Figure 1b illustrates the change of vortical structures with height. Turbulence in the region where the concentric structure with a dense inner flow and an outer shear layer develops (corresponding to $z^* < 15$) consists of relatively small isotropic vortices, whereas turbulence far from the vent is characterized by large elongated hairpin structures. The position of the change in the vortical structure roughly coincides with the position where the value of k begins to increase. This suggests that the change in vortical structure accompanying the density change controls the efficiency of entrainment including the small local k

in the transitional zone.

In conclusion, we have revealed that the efficiency of entrainment significantly varies with height. This variation is considered to control column heights and the condition of column collapse. To gain a further understanding of the entrainment mechanism, 3-D numerical simulations will be a powerful tool for exploring the role of vortical structures in turbulent mixing.

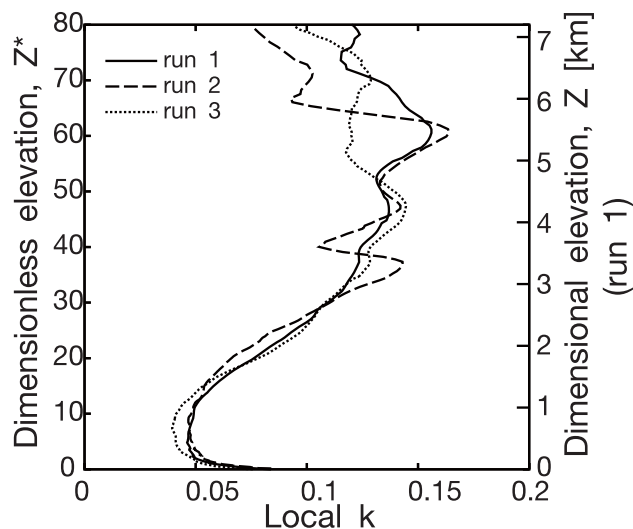


Fig. 3 The vertical distribution of the efficiency of entrainment (local k) for runs 1, 2, and 3.

Acknowledgement

A part of this work was performed under the inter-university cooperative research program of Earthquake Research Institute, University of Tokyo.

References

- [1] B. R. Morton, G. I. Taylor, and J. S. Turner, "Turbulent gravitational convection from maintained and instantaneous source", *Proc. R. Soc. London, Ser. A*, 234, 1-23, 1956.
- [2] A. W. Woods, "The dynamics of explosive volcanic eruptions", *Rev. Geophys.*, 33(4), 495-530, 1995.
- [3] E. Kaminski, S. Tait, and G. Carazzo, "Turbulent entrainment in jets with arbitrary buoyancy", *J. Fluid Mech.*, 526, 361-376, 2005.
- [4] Y. J. Suzuki, T. Koyaguchi, M. Ogawa, and I. Hachisu, "A numerical study of turbulent mixing in eruption clouds using a three-dimensional fluid dynamics model", *J. Geophys. Res.*, 110, B08201, 2005.
- [5] Y. J. Suzuki, and T. Koyaguchi, "A three-dimensional numerical simulation of spreading umbrella clouds", *J. Geophys. Res.*, 114, B03209, 2009.
- [6] P. N. Papanicolaou, and E. J. List, "Investigations of round vertical turbulent buoyant jets", *J. Fluid Mech.*, 195, 341-391, 1988.
- [7] H. Wang, and A. W. -K. Law, "Second-order integral model for a round turbulent buoyant jet", *J. Fluid Mech.*, 459, 397-428, 2000.
- [8] P. E. Dimotakis, "The mixing transition in turbulent flows", *J. Fluid Mech.*, 409, 69-98, 2000.
- [9] M. V. Pham, F. Plourde, and S. D. Kim, "Large-eddy simulation of a pure thermal plume under rotating conditions", *Phys. Fluids*, 18, 015101, 2006.
- [10] F. Plourde, M. V. Pham, S. D. Kim, and S. Balachandar, "Direct numerical simulations of a rapidly expanding thermal plume: Structure and entrainment interaction", *J. Fluid Mech.*, 604, 99-123, 2008.
- [11] A. Neri, and F. Dobran, "Influence of eruption parameters on the thermofluid dynamics of collapsing volcanic columns", *J. Geophys. Res.*, 99(B6), 11,833-11,857, 1994.

爆発的火山噴火における噴煙内部の乱流混合効率

プロジェクト責任者

小屋口剛博 東京大学 地震研究所

著者

鈴木雄治郎 海洋研究開発機構 地球内部ダイナミクス領域

小屋口剛博 東京大学 地震研究所

本プロジェクトでは、大規模数値シミュレーションを用いた固体地球と地球表層・大気にまたがる火山現象の理解と計算結果の防災への応用を目指している。本年は特に、火山噴煙内における乱流混合について研究を進めた。

爆発的火山噴火では、火山ガスと火山灰からなる噴出物が周囲の大気を混合し、取り込んだ大気を火山灰の熱で膨張させることで浮力を得て上昇する。この噴煙の最高到達高度、水平方向の広がり、火砕流の発生条件は、大気を取り込み量を定める乱流混合に支配される。一般に、乱流ジェットや乱流ブルームでは、平均上昇速度に対する周囲流体の取り込み速度の割合を混合効率の指標とし、エントレインメント係数 (k) と呼ぶ。密度成層のない流体中での乱流ジェットや乱流ブルームは自己相似性を持ち、 k は一定値をとることが知られている (乱流ジェット: 0.07、乱流ブルーム: 0.10 – 0.15)。大気が成層構造を持ち、非線形な密度変化をする噴煙の場合では、その混合効率は場所によって変化し、 k の値が一定とはならない可能性がある。そこで、数値シミュレーション結果に基づき、半径方向の大気流入量を直接測定することで取り込み速度と平均上昇速度の比から k の値を高さの関数として求めた。数値コードには一般座標系を適用し、火口付近と噴煙全体の流れのスケールや乱流混合を同時に再現できるようにした。

計算の結果、 k の値が高さによって大きく変化し、噴煙内で乱流混合の効率が変化することが分かった。火口の直上での k の値は 0.07 と密度成層のない流体中での乱流ジェットの値に近く、噴煙柱上部での k の値は 0.10 – 0.15 と乱流ブルームの値に漸近する。火口直上から噴煙柱上部の間には遷移領域が存在し、 k の値は 0.05 と非常に小さな値を取ることが新たに確認された。これらの k の値の高さ変化は、火口からの距離を火口直径で規格化したときに火口での噴火条件 (噴出率) に依存せず、噴煙に共通する性質であることが分かった。

3次元シミュレーション結果から密度構造や渦構造 (swirling strength) の3次元可視化を行い、乱流混合効率と渦構造の関係を調べた。噴煙柱下部では、流れの中心軸付近に大気とまだ混合していない高濃度噴煙の芯が残り、そこでの乱流は比較的小さく等方的な渦で構成されている。一方、噴煙柱上部では、中心軸付近まで大気との混合が進み、そこでの乱流は大きくて引き伸ばされたヘアピン構造で特徴付けられる。これらの渦構造が変化する高さは、 k の値が 0.05 から 0.10-0.15 に変化する高さとはほぼ一致することが分かった。

キーワード: 火山噴煙, 擬似ガスモデル, 乱流混合, 火山災害

Space and Earth System Modeling

Project Representative

Kanya Kusano

Institute for Research on Earth Evolution, Japan Agency for Marine-Earth Science and Technology

Authors

Kanya Kusano^{*1}, Yoji Kawamura^{*1}, Akio Kawano^{*1}, Shin-ichiro Shima^{*1}, Tooru Sugiyama^{*1} and Hiroki Hasegawa^{*1}

*1 Institute for Research on Earth Evolution, Japan Agency for Marine-Earth Science and Technology

Solar and astronomical dynamics as well as volcanic activity is widely believed to play some role for the variability of Earth's environment system in different time-scale. However, it is not well understood yet how the evolution of Earth's system is related to the outside as well as the interior of the Earth. The Earth Simulator Project "Space and Earth System Modeling" is newly established in order to advance our understanding of the environment variability caused by dynamics in space and in the deep interior of the Earth. In FY 2009, we have developed the several element models for space-earth environment system for the nucleation of aerosol, cloud, the acceleration of energetic particles, and aurora, respectively.

Keywords: space weather, space climate, multi-scale, multi-physics, plasma, cloud, aurora, nucleation, aerosols, particle acceleration, Earth Simulator

1. Introduction

Earth's environment is not isolated from the outside of the atmosphere as well as from the interior of solid earth. In fact, the several evidences indicate that there is clear correlation between the climate variation and sunspot activity. Also it is widely believed that giant volcanic eruption may impact the worldwide climate. However, the mechanism whereby the solar activity may affect the climate is not well understood yet. It is also a great issue for the study of geological history to reveal how the surface environment and the deep-interior of earth interact to each other.

Earth Simulator Project "Space and Earth System Modeling" was established in order to understand the mutual relationship between the surface environment and the activities in space and the interior of earth. In FY 2009, we have developed the several element models which will constitute a space climate simulation system. They are the molecular simulation of aerosol nucleation, the cloud simulation in terms of super-droplet method, the particle simulation of energetic particle acceleration, and the aurora simulation, respectively. In the following sections, we will explain about the detail of the each particular model.

2. Molecular Simulation of Aerosol Nucleation

It is an important research subject to quantitatively evaluate the production rate of atmospheric aerosols because atmospheric aerosols, which act as cloud condensation nuclei, significantly affect the Earth's climate. However, one cannot

still directly observe the nucleation process of atmospheric aerosols occurring at the nanometer scale. We are trying to quantitatively understand the nucleation process of aerosols using a combination of classical molecular dynamics simulations and ab initio quantum calculations.

In this fiscal year, we performed molecular dynamics simulations of binary nucleation in the vapor mixture composed of sulfuric acid and water (Fig. 1). By analyzing the simulation results, we estimated the nucleation rate and the critical cluster size. However, the densities of sulfuric acid and water under the simulation conditions are very large compared to those under atmospheric conditions, so as to observe the nucleation process within the limited simulation time. Thus, we cannot directly compare the nucleation rate estimated by the simulations with that observed in the atmosphere. For this reason, we are now analyzing a kinetic aerosol model, whose kinetic coefficients are determined in such a way that the values estimated from the simulation results are divided by the ratio of the density in the simulation to that in the atmosphere. The combination of molecular dynamics simulation and the kinetic aerosol model can provide us a powerful methodology to understand the aerosol nucleation.

3. Macro-Micro Interlocked Simulation of Cloud Formation and Precipitation

Although clouds play a crucial role in atmospheric phenomena, the accuracy and the reliability of numerical

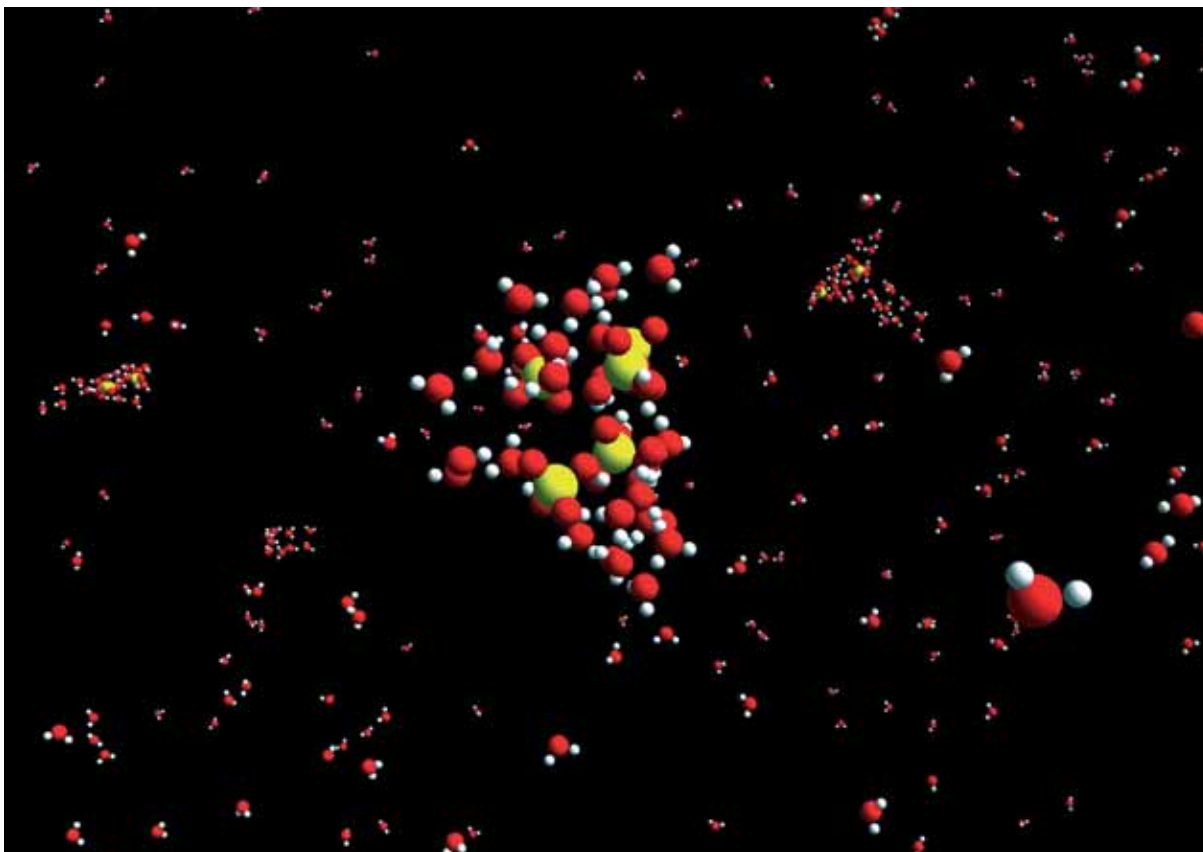


Fig. 1 Nucleation of sulfuric acid aerosols using molecular dynamics simulation.

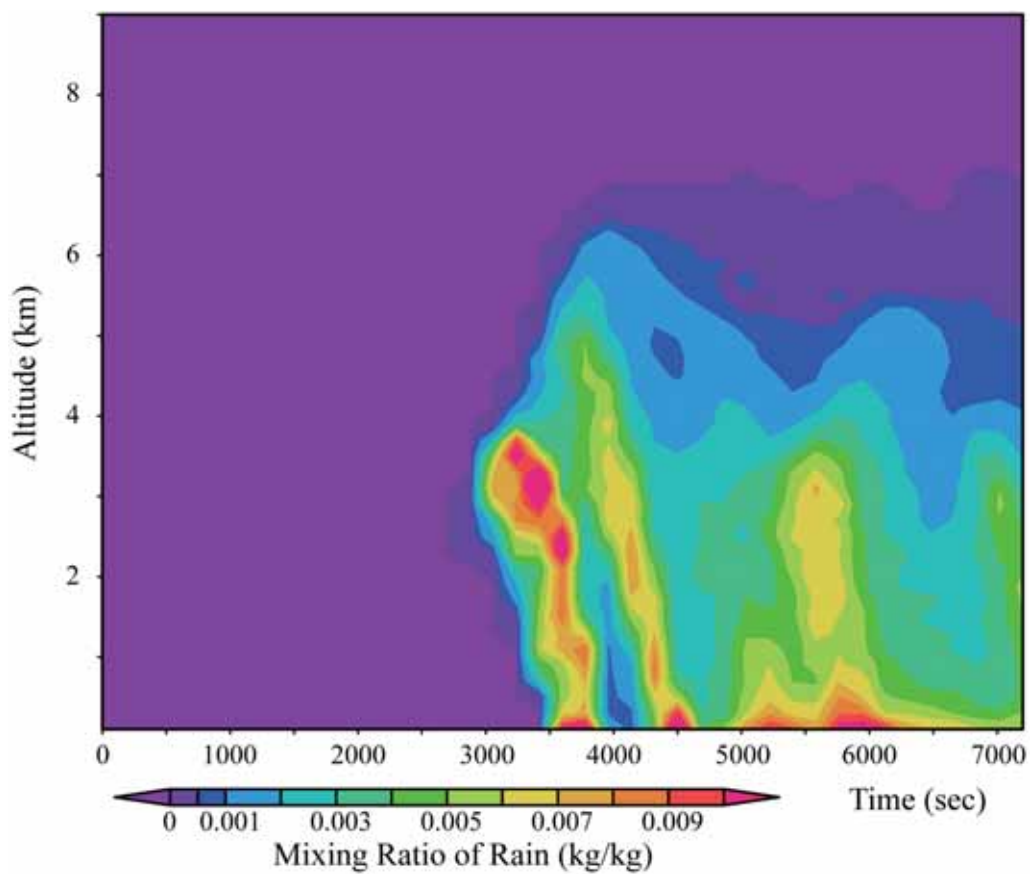


Fig. 2 Numerical simulation of cyclic development of a maritime convective cloud using the CReSS-SDM. This type of cloud was observed in a highly humid environment during the Baiu season around Miyakojima islands (D. Naito, 2005). We can see that the cyclic development of the cloud is successfully reproduced by the CReSS-SDM.

modeling of clouds are still limited. We have recently developed a novel, particle-based, probabilistic simulation scheme of cloud microphysics, named the Super-Droplet Method (SDM), which enables accurate numerical simulation of cloud microphysics with less demanding cost in computation [1].

In FY 2009, we have implemented the minimal components of the SDM to the Cloud Resolving Storm Simulator (CReSS), which is a well-established cloud-resolving model developed by K.Tsuboki and A.Sakakibara [2], and we call this new model the CReSS-SDM. Performance tuning has been carried out to use it on the Earth Simulator. As a result, the efficiency and the scalability of the CReSS-SDM have been improved. For example, the peak performance ratio is improved from 4% to 10% on average, and the vectorization of 99.54% and the parallelization of 99.977% were achieved on 128 nodes of the Earth Simulator. For testing the accuracy of the CReSS-SDM, its numerical output was compared with some observation and we confirmed that the oscillatory development of a shallow maritime precipitating cumulus, which are observed in Miyakojima island, is successfully reproduced (Fig. 2).

Currently, in order to simulate a one day behavior of 100 km-scale shallow maritime clouds, we are incorporating more detailed and advanced microphysical processes into the CReSS-SDM. In addition, to further accelerate the computation, we are constructing a general mathematical framework for a certain type of the Macro-Micro Interlocked Simulation, which is based on the mathematical idea that a macroscopic variable could be a set of coordinates on a certain invariant manifold embedded in the phase space of the microscopic model. The applicability of this framework to the cloud simulation is also under investigation.

4. Simulation of Energetic Particle Acceleration in Plasma

Energetic particles are widely observed in space and astrophysical plasmas. One of the possible accelerators is a collision-less shock wave. The diffusion-convection equation brings us knowledge about the particle acceleration, which is called diffusive shock acceleration (DSA) process [3]. However, since the wave amplitude observed around the shock is not small enough, the applicability of the quasi-linear theory to the DSA process is rather questionable. Therefore, the fully kinetic approach is necessary for more correct understanding of the shock acceleration process in large-amplitude wave. By using the Earth Simulator, we have performed a unprecedentedly large-scale simulation, in which the upstream region of the quasi-parallel shocks is elongated enough to include the accelerated particles within the simulation system. It means that the particles can hardly escape from the system boundaries and we can more precisely calculate the density and flux of the accelerated particles than the previous studies. Figure 3 shows the energy spectrum observed in the downstream region. The

spectrum clearly shows the power-law with high energy cut-off. Although the cut-off profile has been discussed as a result of the escaping particles in the previous studies, the high energy cut-off in this simulation should be recognized as a real phenomenon which can be observed in the shock system, because any particles do not escape out of the system. Therefore, the cut-off energy may be used as a measure to evaluate the simulation by comparing with the observation. Figure 4 shows that the cut-off energy increases with time.

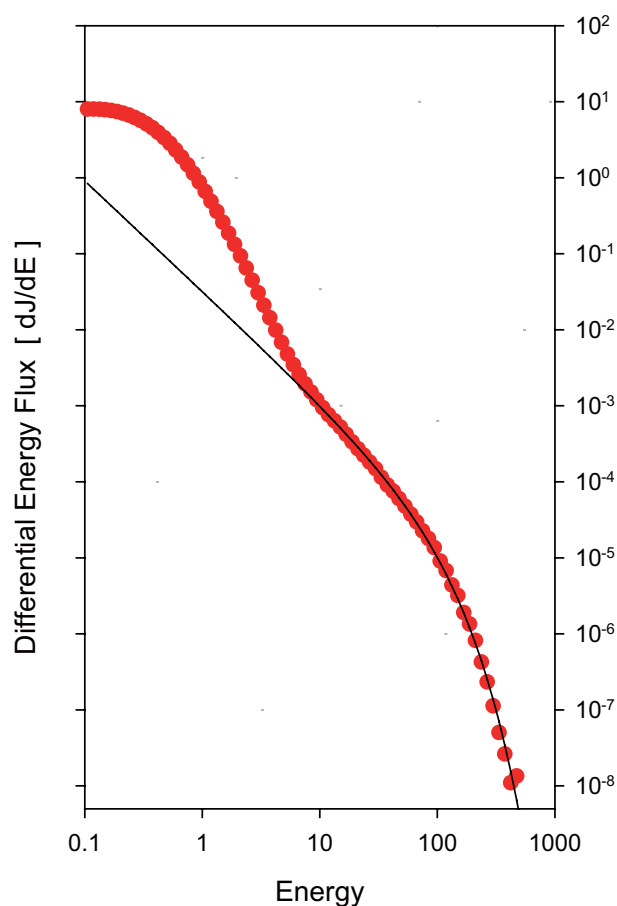


Fig. 3 Energy spectrum observed in the downstream region (red dots). The energy is normalized by the shock ram energy. Solid curve shows a fitting function of $E^{-1.45} \exp(-E/73.2)$, where E is the energy of particle.

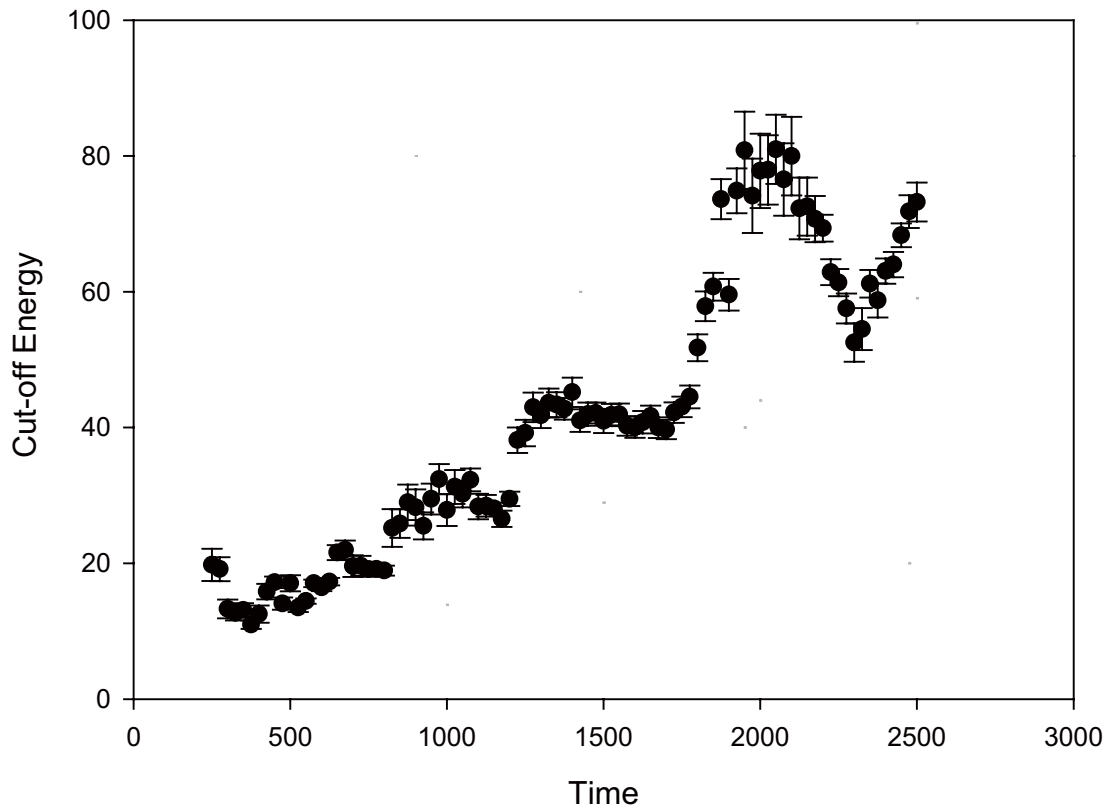


Fig. 4 Time profile of the cut off energy. It increases with time.

5. Multi-scale Simulation of Aurora

Aurora is a visible phenomena caused by the interaction between space and earth. We have investigated the process of quiet auroral arc formation. By using a three-dimensional magneto-hydro-dynamics (MHD) simulation of magnetosphere-ionosphere coupling system in a dipole coordinate, we have simulated that multiple longitudinally striated structures of the ionospheric plasma density and the field aligned current are formed as a result of the nonlinear ionospheric-feedback instability. The areas where these structures appear are consistent with the prediction by the theory of the ionospheric-feedback instability, in which the effects of the spatially non-

uniform electric field and non-uniform plasma density are taken into account [4]. Furthermore, we have developed the macro-micro interlocked (MMI) simulation that consists of the MHD model and the plasma particle simulation model for the calculation of auroral energetic electron production [5]. Figure 5 shows the snapshots of the brightened aurora arcs, where the light emission from oxygen is calculated based on the particle simulation data. In Fig. 5, the left and right panels represent the sights of simulated aurora from the ground level and from some high altitude, respectively.



Fig. 5 Synthetic auroral lights of oxygen atoms seen from the ground (left panel) and from a high altitude (right panel) obtained by the MMI simulation.

References

- [1] S. Shima, K. Kusano, A. Kawano, T. Sugiyama, and S. Kawahara, "The super-droplet method for the numerical simulation of clouds and precipitation: a particle-based and probabilistic microphysics model coupled with a non-hydrostatic model", *Quarterly Journal of the Royal Meteorological Society*, Volume 135 Issue 642, pp.1307-1320, 2009.
- [2] K. Tsuboki, and A. Sakakibara, "Large-Scale Parallel Computing of Cloud Resolving Storm Simulator", *Lecture Notes in Computer Science (Springer Berlin / Heidelberg)* Volume 2327, 2006.
- [3] T. Sugiyama, "Multi-scale and multi-physics plasma simulation and its application to the collisionless shock acceleration process", *The Japan Society of Plasma Science and Nucleation Fusion Research*, Vol. 85, pp.580-584, 2009.
- [4] H. Hasegawa, N. Ohno, and T. Sato, "Simulation of feedback instability in the coupled magnetosphere-ionosphere system", *J. Geophys. Res.*, in press.
- [5] T. Sato, H. Hasegawa, and N. Ohno, "Macro-micro interlocked simulation algorithm: An exemplification for aurora arc evolution", *Comput. Sci. Disc.*, Vol. 2, 015007, doi:10.1088/1749-4699/2/1/015007, 2009.

宇宙・地球表層・地球内部の関連モデリング

プロジェクト責任者

草野 完也 海洋研究開発機構 地球内部ダイナミクス領域

著者

草野 完也^{*1}, 河村 洋史^{*1}, 河野 明男^{*1}, 島 伸一郎^{*1}, 杉山 徹^{*1}, 長谷川裕記^{*1}

^{*1} 海洋研究開発機構 地球内部ダイナミクス領域

地球システムは内部（地殻、マントル、コア）、表層（大気、海洋）および外部（宇宙）が互いに影響を及ぼしながら変動進化する関連システムである。本プロジェクトは地球環境の大規模変動と宇宙及び地球内部ダイナミクスの関係を探るために、先進的な関連モデルを開発する目的で2009年度より開始された。本プロジェクトでは、特に宇宙線と雲の関係に注目しその物理的因果関係を定量的に解明するため、ミクروسケールからマクروسケールに至る様々な物理過程を可能な限り第1原理に基づいてモデル化すると共に、それらのモデルを総合した包括的な宇宙地球システムモデルを構築することを目指している。2009年度はプロジェクトの初年度として、エアロゾルの核形成に関する分子シミュレーション、超水滴法を利用した積雲成長シミュレーション、プラズマ中の高エネルギー粒子加速過程のシミュレーション、電磁流体力学モデルと粒子モデルを結合したマルチスケール・オーロラシミュレーションをそれぞれ開発した。

キーワード: 宇宙天気, 宇宙気候, マルチスケール, マルチフィジックス, プラズマ, 雲, オーロラ, 核形成, エアロゾル, 粒子加速, 地球シミュレータ

Chapter 2

■ Epoch-Making Simulation ■

Development of General Purpose Numerical Software Infrastructure for Large Scale Scientific Computing

Project Representative

Akira Nishida

Research Institute for Information Technology, Kyushu University

Author

Akira Nishida

Research Institute for Information Technology, Kyushu University

The Scalable Software Infrastructure Project was initiated as a national project in Japan, for the purpose of constructing a scalable software infrastructure for scientific computing. The project covered three areas: iterative solvers for linear systems, fast integral transforms, and their portable implementation.

Modular programming was adopted to enable users to write their codes by combining elementary mathematical operations. Implemented algorithms were selected from the viewpoint of scalability on massively parallel computing environments. Since the first release in September 2005, the codes have been used by thousands of research projects around the world.

Keywords: high performance computing, parallel algorithms, modular programming

1. Overview

Construction of a software Infrastructure for highly parallel computing environments requires precisely prediction of future hardware technologies, and design of scalable and portable software for these technologies.

The Scalable Software Infrastructure (SSI) Project was initiated in November 2002, as a national project in Japan, for the purpose of constructing a scalable software infrastructure [1], [2], [3]. Based on the policies, we have used various types of parallel computers, and carefully designed our libraries on them, to maintain portability and usability. The architectures include shared memory parallel computers, distributed-memory parallel computers, Linux-based PC clusters, and vector supercomputers. In 2003, we signed a contract with the IBM Watson Research Center on the joint study of the library implementation on massively parallel environments with tens of thousands of processors. Since 2006, the SSI project has been selected for a joint research with the Earth Simulator Center to port our libraries on massively parallel vector supercomputing environments. The results of the SSI project will be evaluated on larger supercomputers in the near future.

In the SSI project, we have studied object-oriented implementation of libraries, autotuning mechanisms, and scripting languages for the implemented libraries. The results were applied to a modular iterative solver library Lis and a fast Fourier transform library FFTSS. The libraries were written in C, and equipped with Fortran interfaces. We have also developed SILC, a simple interface for library collections, with an extension to the scripting language.

2. Lis: a Library of Iterative Solvers for Linear Systems

In the fields such as fluid dynamics and structural analysis, we must solve large-scale systems of linear equations to compute high resolution numerical solutions of partial differential equations. The subgroup released Lis, a library of iterative solvers and preconditioners for linear systems, with various sparse matrix storage formats. Supported solvers, preconditioners, and matrix storage formats are listed in Table 1-4. We present an example of the program using Lis in Fig. 1.

There are a variety of portable software packages that are applicable to the iterative solver of sparse linear systems. SPARSKIT is a toolkit for sparse matrix computations written in Fortran. PETSc is a C library for the numerical solution of partial differential equations and related problems, which is to be used in application programs written in C, C++, and Fortran. PETSc includes parallel implementations of iterative solvers and preconditioners based on MPI. Aztec is another library of parallel iterative solvers and preconditioners written in C. The library is fully parallelized using MPI. From the viewpoint of functionality, our library and all three of the libraries mentioned above support different sets of matrix storage formats, iterative solvers, and preconditioners. In addition, our library is parallelized using OpenMP to take multicore architectures into consideration. Feedbacks from the users have been applied to Lis, and Lis has been tested on various platforms from small PC clusters to massively parallel computers, including NEC's SX, IBM's Blue Gene, and Cray's XT series. The code of Lis has attained the vectorization ratio of 99.1% and the parallelization ratio of 99.99%. We show a comparison of the MPI version

Table 1 Solvers for linear equations

1.0.x	CG	Added in 1.1.x	CR
	BiCG		BiCR
	CGS		CRS
	BiCGSTAB		BiCRSTAB
	BiCGSTAB(l)		GPBiCR
	GPBiCG		BiCRSafe
	Orthomin(m)		FGMRES(m)
	GMRES(m)		IDR(s)
	TFQMR		MINRES
	Jacobi		
	Gauss-Seidel		
	SOR		

Table 2 Solvers for eigenproblems

Added in 1.2.x	Power Iteration
	Inverse Iteration
	Approximate Inverse Iteration
	Rayleigh Quotient Iteration
	Lanczos Iteration
	Subspace Iteration
	Conjugate Gradient
	Conjugate Residual

Table 3 Preconditioners

1.0.x	Jacobi	Added in 1.1.0	Crout ILU
	ILU(k)		ILUT
	SSOR		Additive Schwarz
	Hybrid		User defined preconditioner
	I+S		
	SA-AMG		
	SAINV		

Table 4 Matrix storage formats

Point	Compressed Row Storage
	Compressed Column Storage
	Modified Compressed Sparse Row
	Diagonal
	Ellpack-Itpack generalized diagonal
	Jagged Diagonal Storage
	Dense
	Coordinate
Block	Block Sparse Row
	Block Sparse Column
	Variable Block Row

```

LIS_MATRIX      A;
LIS_VECTOR      b,x;
LIS_SOLVER      solver;
int             iter;
double          times,itimes,ptimes;

lis_initialize(&argc, &argv);
lis_matrix_create(LIS_COMM_WORLD,&A);
lis_vector_create(LIS_COMM_WORLD,&b);
lis_vector_create(LIS_COMM_WORLD,&x);
lis_solver_create(&solver);
lis_input(A,b,x,argv[1]);
lis_vector_set_all(1.0,b);
lis_solver_set_optionC(solver);
lis_solve(A,b,x,solver);
lis_solver_get_iters(solver,&iter);
lis_solver_get_times(solver,&times, &itimes,&ptimes);
printf("iter = %d time = %e (p=%e i=%e)\n",iter,times, ptimes, itimes);
lis_finalize();

```

Fig. 1 Example of the C program using Lis.

of Lis and PETSc in Fig. 2, for solving a three-dimensional Poisson equation (size: one million, number of nonzero entries: 26 million) on an SGI Altix 3700 with 32 processors.

In our project, we have designed and implemented scalable and robust algorithms of iterative solvers for linear equations and their preconditioning, derived from physical applications. In recent years, multilevel algorithms for large-scale linear equations, such as the algebraic multigrid (AMG), have been investigated by many researchers. In most cases, multigrid methods show linear scalability, and the number of iteration counts is $O(n)$ for a problem of size n . The algebraic multigrid method is based on a principle similar to the geometric multigrid, which utilizes the spatial information on physical problems, but this method differs from the geometric multigrid by considering the coefficient as a vertex-edge incidence matrix. In addition, by using the information on the elements and their relations, this method generates coarser level matrices without higher frequency errors. The complexity of the algebraic multigrid is equivalent to the geometric multigrid and can be applied to irregular or anisotropic problems. We proposed an efficient parallel implementation of the algebraic multigrid preconditioned conjugate gradient method based on the smoothed aggregation (SAAMGCG) and found that the proposed implementation provides the best performance as the problem size grows [38]. Currently, the algebraic multigrid is the most effective algorithm for the general-purpose preconditioning, and its scalability is also remarkable. We have implemented the algebraic multigrid in Lis, and have tested it in massively parallel environments. We present the weak scaling results for a two dimensional Poisson equation of dimension 49 million on 1,024 nodes of a Blue Gene system in Fig. 3.

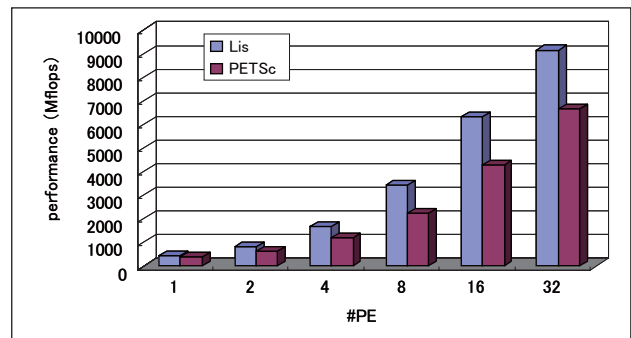


Fig. 2 Comparison of the MPI version of Lis and PETSc.

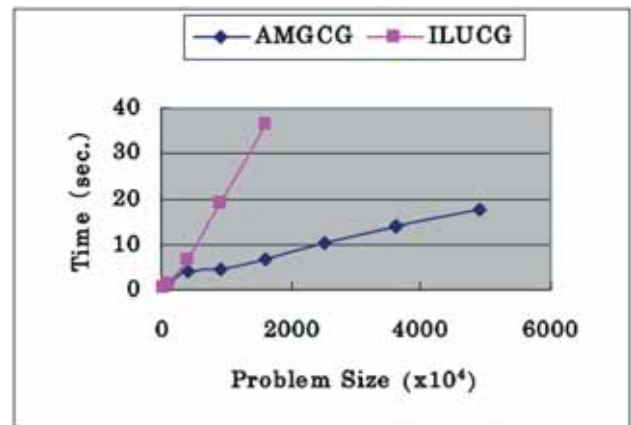


Fig. 3 Comparison of AMGCG and ILUCG.

The convergence of the Krylov subspace methods are much influenced by the rounding errors. Higher precision operations are effective for the improvement of convergence, although the arithmetic operations are costly. We implemented the quadruple precision operations on Lis, and accelerated them by using architecture specific SIMD instructions, such as Intel's SSE2 and IBM's FMA. To improve their performance, we also applied techniques such as loop unrolling. The computation time of our implementation is only 3.5 times as much as Lis' double precision, and 0.2 times as much as Intel Fortran's REAL*16.

Furthermore, we proposed the DQ-SWITCH algorithm, which efficiently switches the double precision iterations to the quadruple precision to reduce the computation time. The idea of the SIMD accelerated double-double precision operations has also been incorporated into Japan's next generation supercomputer project by RIKEN.

In the fields such as solid-state physics and quantum chemistry, efficient algorithms for eigenproblems for large-scale simulations derived from first principle calculation. There are several methods to compute eigenvalues of large-scale sparse matrices. Based on the observations, we proposed that the scalability of the conjugate gradient method can improve the performance of eigensolvers in parallel environments, where the extreme eigenvalues of a generalized eigenproblem can be solved by reducing these problems to the calculation of the local minimum of the Rayleigh quotient, combined with appropriate preconditioners, such as the algebraic multigrid. We have focused on the implementation of the existing major eigensolvers for sparse matrices on Lis, which was released as version 1.2.

The performance of iterative solvers is affected by the data structure of given matrices, the methodology of their parallelization, and the hierarchy of computer architectures. In the fiscal year 2009, we have studied the validity of the performance optimization of iterative solvers by benchmarking the FLOPS performance of matrix vector product kernels on given computing environments. Figure 4 shows the performance of a kernel `spmvtest1`, derived from a discretized 1-dimensional Poisson equation, for size up to 1,280,000 on a single node of SX-9 at JAMSTEC, and Fig. 5-7 show the performance for size up to 40,960,000 on the three scalar clusters at Kyushu University.

Although the scalar clusters show performance degradation after they reach their peak performance with the data size of 500kB to 1MB per core, SX-9 shows gradual performance increase until it reaches about 8-9GFLOPS per core (with the diagonal (DIA) format in this case), and keep it as the data size grows.

References

[1] A. Nishida, "SSI: Overview of simulation software infrastructure for large scale scientific applications (in Japanese)," IPSJ, Tech. Rep. 2004-HPC-098, 2004.
 [2] A. Nishida, "Experience in Developing an Open Source Scalable Software Infrastructure in Japan," Lecture Notes in Computer Science, vol. 6017, pp. 87-98, 2010.
 [3] A. Nishida, R. Suda, H. Hasegawa, K. Nakajima, D. Takahashi, H. Kotakemori, T. Kajiyama, A. Nukada, A. Fujii, Y. Hourai, S. L. Zhang, K. Abe, S. Itoh, and T. Sogabe, the Scalable Software Infrastructure for Scientific Computing Project, CREST, JST, 2009, <http://www.ssic.org/>.

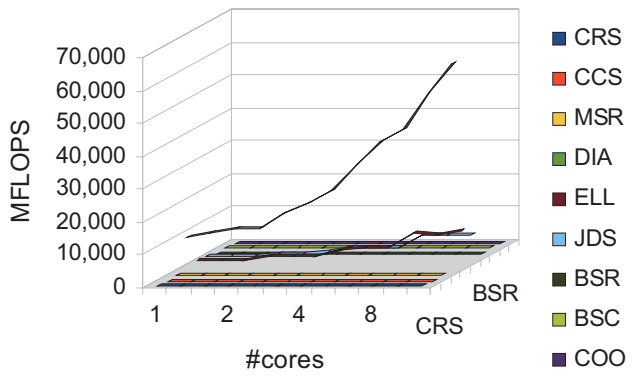


Fig. 4 Performance of `spmvtest1` on a single node of the Earth Simulator 2.

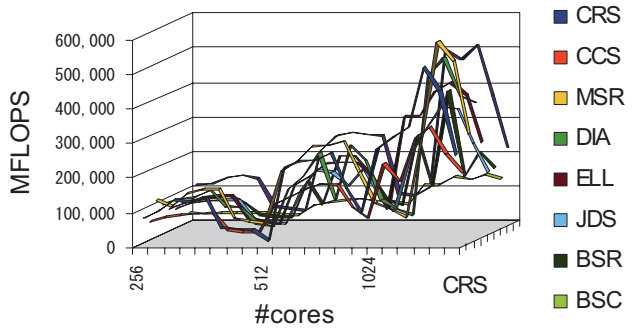


Fig. 5 Performance of `spmvtest1` on the Fujitsu PRIMEGY Cluster at Kyushu University.

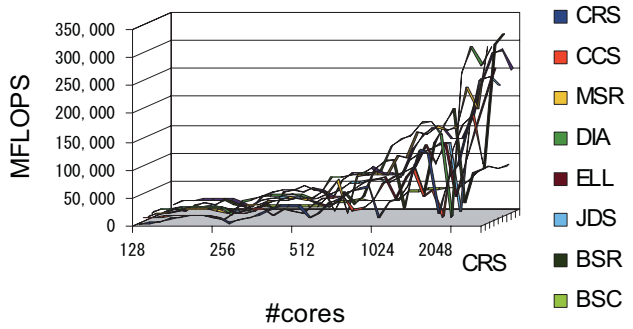


Fig. 6 Performance of `spmvtest1` on the Fujitsu PRIMEQUEST Cluster at Kyushu University.

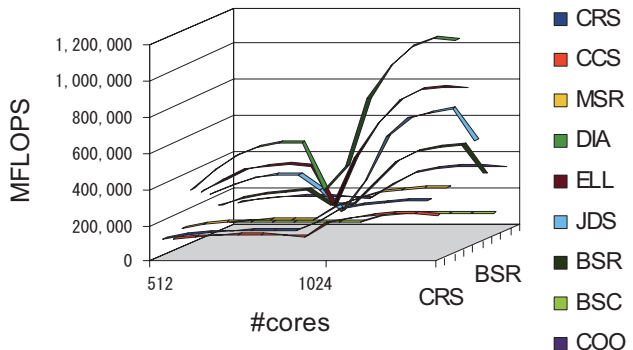


Fig. 7 Performance of `spmvtest1` on the Hitachi SR16000 Cluster at Kyushu University.

大規模科学計算向け汎用数値ソフトウェア基盤の開発

プロジェクト責任者

西田 晃 九州大学情報基盤研究開発センター

著者

西田 晃 九州大学情報基盤研究開発センター

本プロジェクトでは、従来それぞれの分野において別個に進められてきた並列アルゴリズムや実装に関する知見をもとに、大規模化が予想される今後の計算環境に対応したスケーラブルなソフトウェア基盤を整備することを目的として、反復解法、高速関数変換、及びその効果的な計算機上への実装手法を中心に、平成 14 年度より科学技術振興機構戦略的創造研究推進事業の一環として、多様な計算機環境を想定した開発を行っている。モジュール化されたインターフェースを採用し、複雑な機能を持つライブラリを容易に構築できるようにするとともに、スケーラビリティの観点から並列化に適したアルゴリズムを開発、実装し、高並列な環境での使用に耐えるライブラリを実現している。本研究の成果はネットワークを通じて広く一般に配布し、フィードバックをもとにより汎用性の高いソフトウェアとしていく方針を採っており、平成 17 年 9 月よりソースコードを無償公開するとともに、ユーザの要望を反映した更新を適宜行なっている。平成 18 年度からは、地球シミュレータセンター共同プロジェクトの一環として、高並列なベクトル計算機環境への最適化を実施し、その成果をライブラリとして公開している。

反復解法においては、疎行列ベクトル積が計算時間の大半を占めることが多く、性能の最適化は最も重要な課題のひとつである。しかしながら、疎行列ベクトル積の性能は、行列の形状、並列化手法、メモリの階層構造等によって大きく性能が変化するため、すべての場合に最適な解法を見出すのは難しい。そこで、本年度は様々なデータ格納形式・並列化手法における疎行列ベクトル積の性能を事前に評価するためのベンチマークプログラムを Lis 上に実装・公開し、その有効性を複数の計算環境を用いて評価した。本ベンチマークは局所的なものであるが、これによって解法の計算性能をある程度正確に見積もることが可能になった。

キーワード：高性能計算，並列アルゴリズム，モジュール化

Large Scale Simulations for Carbon Nanotubes

Project Representative

Syogo Tejima

Research Organization for Information Science & Technology

Authors

Syogo Tejima^{*1}, Satoshi Nakamura^{*1}, Yoshiyuki Miyamoto^{*2}, Yoshikazu Fujisawa^{*3} and Hisashi Nakamura^{*1}

*1 Research Organization for Information Science & Technology (RIST)

*2 R&D Unit Central Res. Labs. Green Innovation Research Laboratories, NEC Corporation

*3 Honda R&D Co., Ltd

CARBON NANOTUBE RESEARCH GROUP

Morinobu Endo, Eiji Osawa, Atushi Oshiyama, Yasumasa Kanada, Susumu Saito, Riichiro Saito, Hisanori Shinohara, David Tomanek, Tsuneo Hirano, Shigeo Maruyama, Kazuyuki Watanabe, Takahisa Ohno, Yutaka Maniwa, Yoshikazu Fujisawa, Yoshiyuki Miyamoto, Hisashi Nakamura

Nano carbon materials as nanotube and fullerene have a potential for applications to the advanced industries. For nano carbon materials, it has been recognized that large-scale simulation is a powerful and efficient tool to find and create new functional nano carbon materials.

Aiming at conducting the productive simulation for nano-materials, we have developed the large-scale simulation models such as tight-binding molecular dynamic model, *ab-initio* density functional theory (DFT), and time-dependent DFT model.

In this term, by utilizing these models effectively, we have studied various physical properties of nano-carbon and applications such as (1) Novel Functions of Mackay Crystal, (2) Structural relaxation of Nano Diamond, (3) Large-scale Simulation on Electron Conduction in Carbon Nanotubes at Finite Temperature, (4) Application of time-dependent density functional theory for irradiation of strong optical field on nano-carbons. Along these works, we have realized that the Earth Simulator is a very powerful tool for large-scale nano-material simulations.

Keywords: Large scale simulation, TB theory, ab initio theory, Time-dependent DFT, Carbon Nanotube, Fullerenes, Green energy, solar cell, photoelectric material

1. Introduction

Nano-carbon materials have been expected to bring breakthrough to material science and nanotechnology. A lot of potential applications of nanotube and fullerene to electronic devices have been attracted to scientists and engineers.

In the present days, large-scale numerical simulation by using supercomputer's computational performance has turned to be a very efficient tool and leverage for investigating their novel material properties. It now allows us to simulate complex nano-structures with more than ten thousand atom of carbon.

Aiming at using large-scale simulations on the Earth Simulator, we have developed an application package of *ab initio* DFT theory and parameterized tight-binding (TB) models. Especially, the TB model shows that it is very suitable for the very large systems even if it has a lack of symmetrical arrangement.

In this term, we have carried out simulation studies, in which there are three primary objectives as (1) design of innovative nonmaterial with the required properties; (2) obtain fundamental properties in nano-scale matter, and (3) develop new applications.

2. Physical studies on nano materials

2.1 Novel Functions of Mackay Crystal^[1]

The comprehensive simulation has been conducted so far on properties of the Mackay crystal, focusing on synthesis process through atomic arrangement of GSW and mechanical properties as stiffness, etc.. As Mackay crystals, it is well known that there are three different sizes and types. The crystal is classified as P, D, G-types, by the atomistic bonding configuration of hexagon or octagon on the surface curvature of the unit cell.

In this term, focusing P type crystal, the dependency of

energy band gap on the crystal size has been investigated through simulating the electronic band structure by DFT model.

This result indicates that Mackay crystal has a potential for highly efficient photoelectric material for solar cell. The energy band structures and electron density distribution are shown

in Figs. 1-3. These show that the band gaps are ranged from 0.05eV to 0.94 eV and the electron density depends on the size of atomic unit cell. The peak of electron density appears at octagon bonding and the lowest at hexagon in the direction to (111). It is the reason why the intrinsic electron density

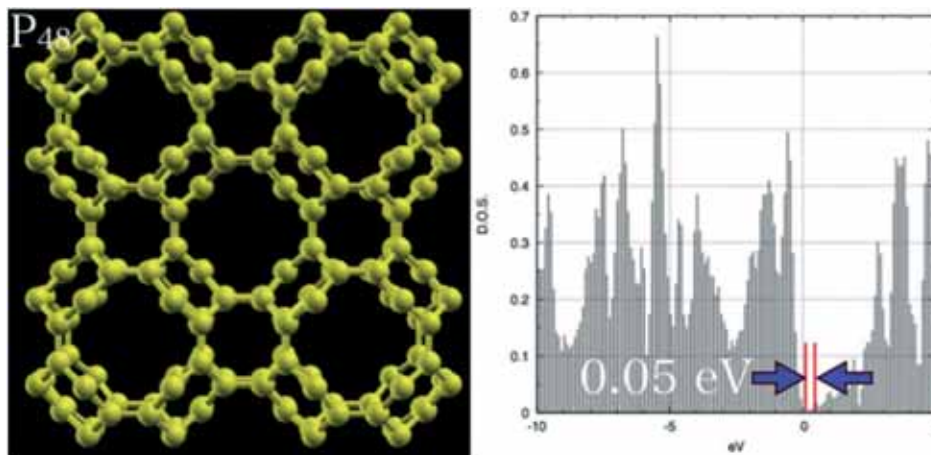


Fig. 1 Energetically optimized structure of P48 zigzag Mackay crystal and energy band structure.

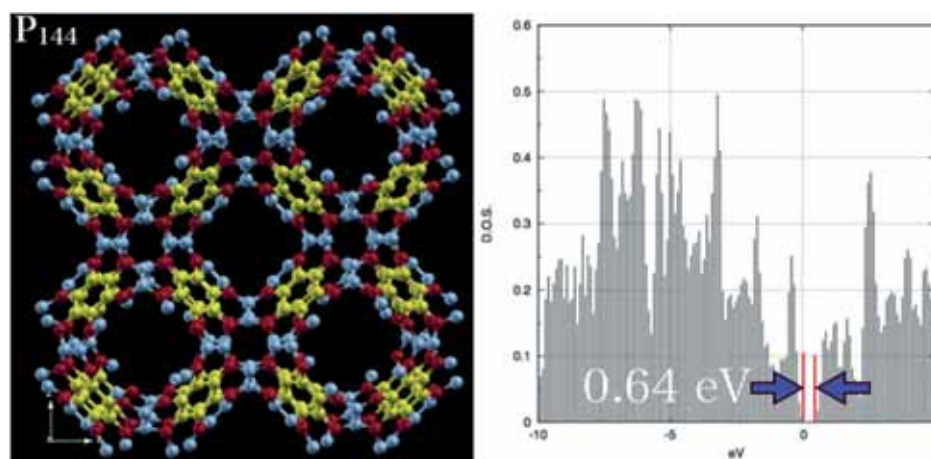


Fig. 2 Energetically optimized structure of P144 zigzag Mackay crystal and energy band structure. The color represents number of electrons, which decreases in the order of yellow and red.

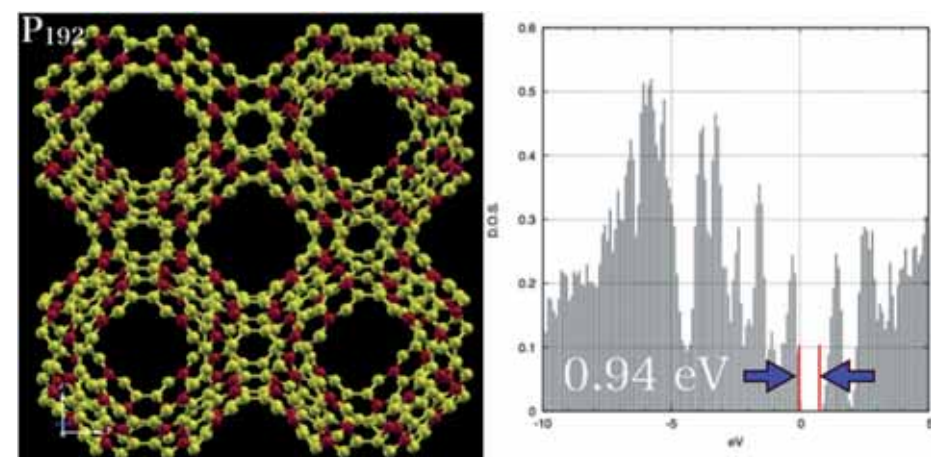


Fig. 3 Energetically optimized structure of P192 armchair Mackay crystal and energy band structure. The color represents number of electrons, which decreases in the order of yellow, red and aqua.

distribution and band gap are due to the existence of octagon forming the negative curvature of Mackey crystal.

Absorbable wavelengths of sun light depend on the energy band gap of the photo-electric material. By stacking Mackey crystal films with the different size, a tandem-type solar cell has been designed conceptually, which would be able to absorb the sun light with near infrared light. As the next step, the feasibility study of Mackey crystals for solar cell will be made by large-scale simulations.

2.2 Structural relaxation of Nano Diamond

Recently the fragment-diamond transformed into carbon-anions, so called as nano-diamond, was synthesized experimentally. Some researches & developments have been made by modifying the nano-diamond chemically to disperse or gel in solution for a drug delivery system. Presently there is no information on the characteristics of the surface of nano-diamond that leads us to select the adequate molecules to chemical modification.

For reliable and accurate simulations, DFT simulations have been carried out to describe the properties on size, temperature

and pressure dependence. The relaxation simulation has made on two sizes of nano-diamond by using DFT model. The initial structure is set in truncated octahedron and the number of atoms is 147 and 413 .

The structure of before- and after- relaxation are shown in Figs. 4 and 5 for C_{147} and C_{413} , respectively. It shows that the surface layer of the (111) is graphitized with sp^2 bond. The area of graphite layer increases as the size of the nano-diamond increases. The direction (100) consists of the diamond structure with sp^3 bond. The mixing state of sp^2 and sp^3 bonds is expected to generate the polarized electric fields with functional elements.

The polarized nano-diamond might be one of the functional elements for the drug delivery system or some fields. As a next step, large-scale simulation will be carried out on nano-diamond with thousand atoms.

2.3 Large-scale Simulation on Electron Conduction in Carbon Nanotubes at Finite Temperature^[2]

According to Moore's law, which states that the number of transistors in integrated circuit (IC) will double every 18 months, the rapid development of ICs has to a large extent

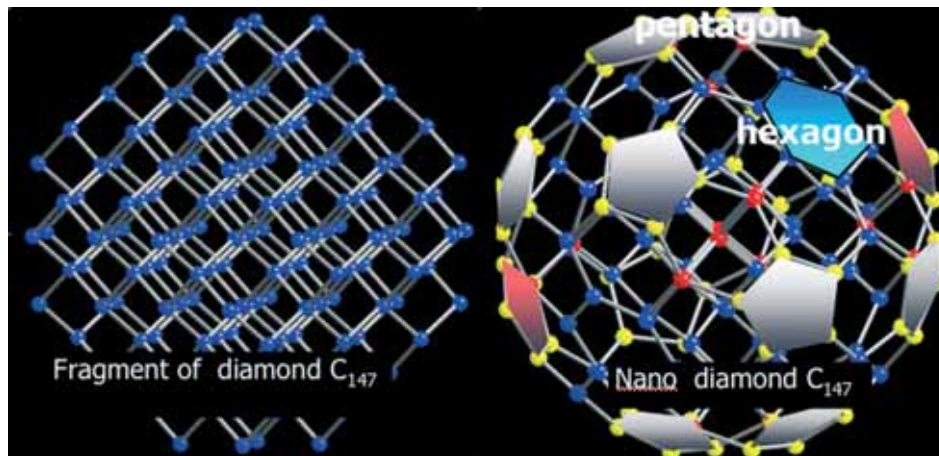


Fig. 4 C_{147} octahedral nanodiamond structure before (left) and after (right) the relaxation simulation.

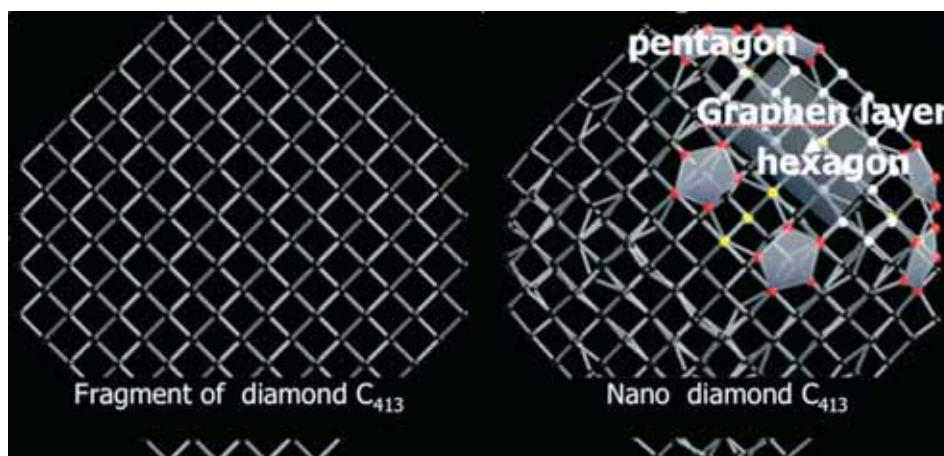


Fig. 5 C_{413} octahedral nanodiamond structure before (left) and after (right) the relaxation simulation.

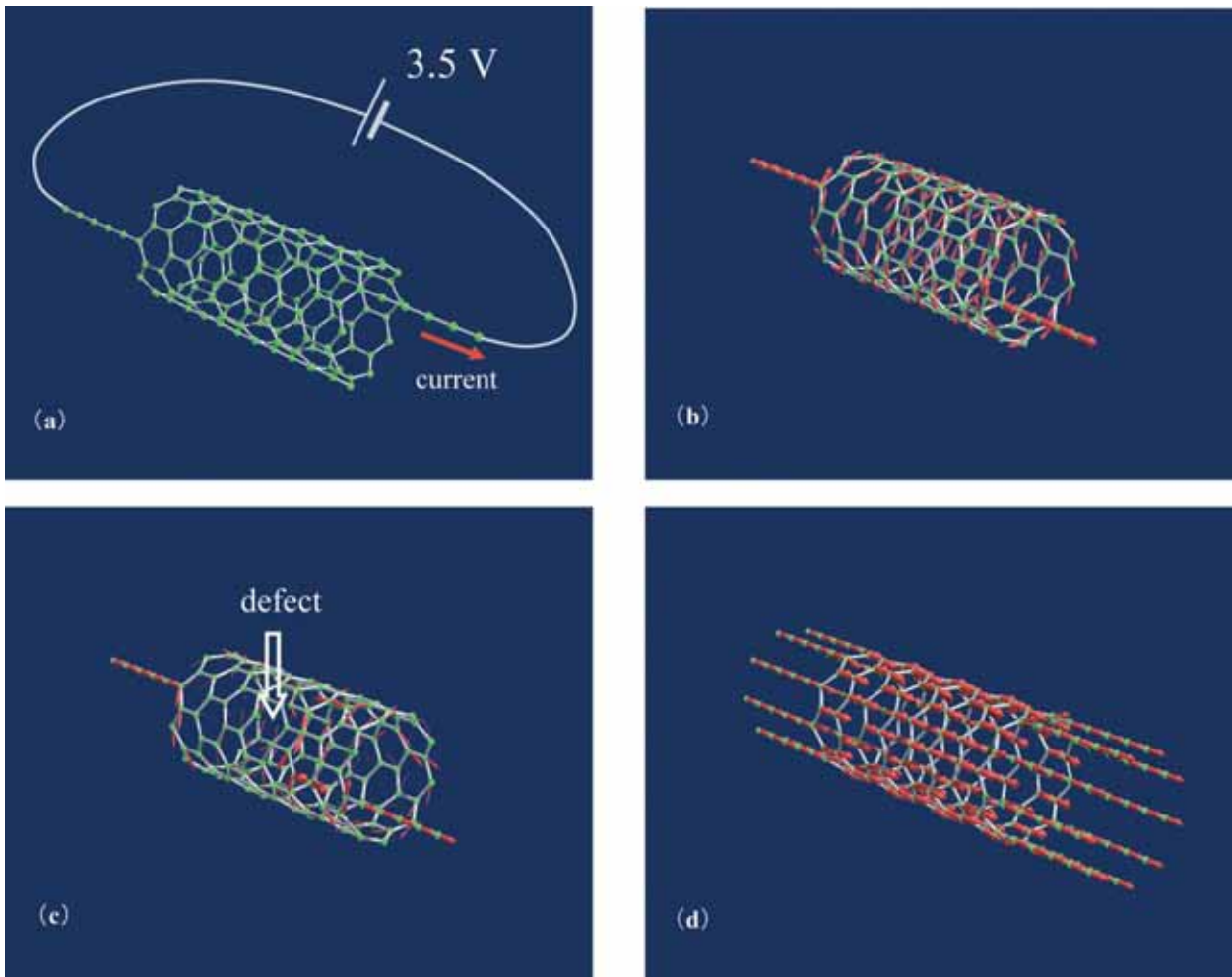


Fig. 6 (a) shows a schematic view of the system under consideration. Figures 1 (b), (c), and (d) show our simulation results under three different conditions: (b) The line connecting two electrode-junctions is not parallel to the axis of CNT. (c) Under the identical condition as Fig. (a) except for the existence of a defect in the CNT. (d) Many electrodes are attached on the CNT.

been enabled due to the improvement of a transistor design based on Silicon. By scaling down dimensions, the silicon-based technologies have been pushed close to its physical limits as soon as the end of this decade. Therefore it becomes crucial to develop technologies that will enable continued implementation of increasingly higher performance devices.

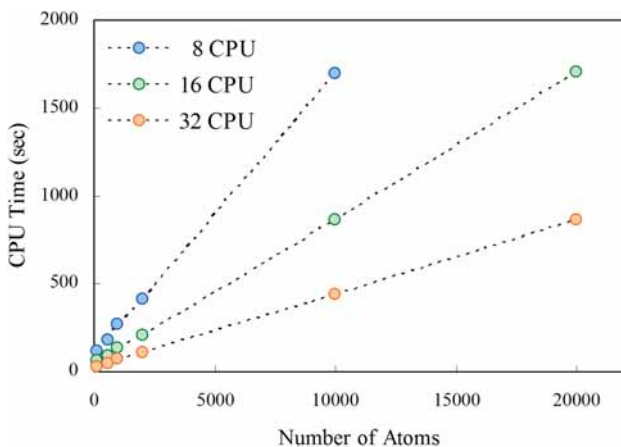


Fig. 7 CPU time versus the number of carbon atoms

Carbon nanotubes (CNTs) are considered attractive candidates for new technologies that could take the place of the silicon-based electronic.

It is still difficult, however, to manipulate CNTs experimentally; and besides the macroscopic Ohm's law breaks down due to the various effects caused by the microscopic size effect. In this context, it is necessary to study the transport behavior of CNTs using a quantum mechanical simulation. We have developed a simulation code by which electron transport simulations of nano- and meso-scale CNTs can be performed. We focused on the system under consisting of two semi-infinite electrodes and a scattering region sandwiched between these electrodes (see Fig. 6 (a)).

Using non-equilibrium Green's function (NEGF) technique, we obtain the following expression for electron current from j_1 site to j_2 site.

$$J_{j_1 \rightarrow j_2} = \frac{e}{\pi} \sum_{\xi_1, \xi_2} t_{j_2 \xi_2 j_1 \xi_1}(\{R\}) \int \{ f(\omega - \mu_R) - f(\omega - \mu_L) \} \times \sum_{\sigma} \text{Re} [G_{CC}^r(\omega) \{ -i\Gamma_L(\omega) \} G_{CC}^a(\omega)]_{(j_1, \xi_1, \sigma)(j_2, \xi_2, \sigma)} d\omega,$$

with $-i\Gamma_L(\omega) = \Sigma_L^r(\omega) - \Sigma_L^a(\omega)$,

$$G_{CC}(z) = \frac{I_{CC}}{zI_{CC} - H_{CC} - \Sigma_L(z) - \Sigma_R(z)},$$

$$\Sigma_L(z) = H_{CL} \frac{1}{z - H_{LL}} H_{LC},$$

$$\Sigma_R(z) = H_{CR} \frac{1}{z - H_{RR}} H_{RC}.$$

Here H_{CC} is the matrix describing the scattering region sandwiched between electrodes. Σ_L is the self-energy of the left-hand side electrode, and Σ_R the self-energy of the right-hand side. In this scheme, the large-dimensional matrix inversion to calculate the Green's function in the scattering region becomes the most heavy part of the model computationally. An embedding potential algorithm is implemented to obtain the equilibrium and non-equilibrium Green's functions.

Since the NEGF technique is also applicable to calculate the density of electrons, we determined NEGF self-consistently together with Poisson equation. The substitute charge method is considered to be a simple and effective method to solve the Poisson equation. The positions of substitute charges, however, are empirically determined. Therefore, in our solution method, both the positions and the values of charges are determined so that the differences of the potentials on boundary are least in a sense of the least square method. In this case, the implementation of least square method is made with Davidson-Fletcher-Powell algorithm.

These figures 6 (b), (c), and (d) show our simulation results at 300 (K). The arrows represent the electron current in CNTs

From figures 6 (b), (c), and (d), one can find the following results: When the line connecting two electrode-junctions is not parallel to the axis of the CNT, circular current occurs. On the other hand, under the same condition except for the existence

a defect in the CNT, circular current decreases. When many electrodes are attached on the CNT, current flows along the axis of the CNT and circular current does not occur.

Finally, CPU time versus the number of carbon atoms is shown in Fig. 7. One can see that our simulation code achieves the order (N) algorithm with respect to the size of the system. The sustained performance of 13 Tera flops was achieved, and the computing efficiency was seventeen percent of the peak performance.

2.4 Application of time-dependent density functional theory for irradiation of strong optical field on nano-carbons^[3]

In this term, we discovered field enhancement inside nanotube and pulse-laser induced exfoliation of graphene from graphite surfaces. These phenomena suggested the possibility of efficient photo-fabrication of nano-carbons with controlled manners. This term, we further investigated these two subjects.

As for the exfoliation of graphene from graphite surface, we searched more efficient process, i.e., faster exfoliation with lower energy cost of laser-shot, by tuning the shape of pulse laser in the time-axis. Last year, the assumed wavelength of the laser was 800 nm, and pulse width was 45 fs. In this year, we just shorten the pulse width as 10 fs and compared the dynamics shown in Fig. 1.

When we further shorten the pulse width, nothing happened on the surface. Therefore, we believe that the pulse width as 10 fs is optimized for graphene exfoliation which should be tested by experiments in future.

As for the photochemistry of molecule inside carbon nanotube, we rely on experience of last year which was the enhancement of the electric field (E-field) inside semiconducting

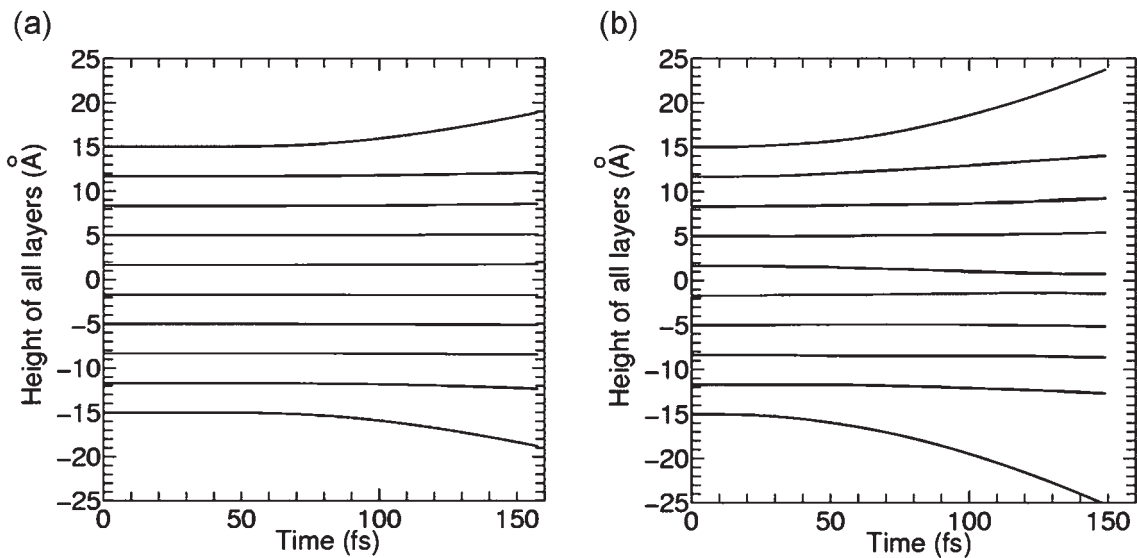


Fig. 8 Time evolution of heights of graphene layers (10-layer slab model having two surfaces on top and bottom) after irradiation of laser shot (a) with wavelength 800 nm, pulse width = 45 fs, and power per shot is about 87.9 mJ/cm², (b) with the same wavelength, pulse width 15 fs, and power 20 mJ/cm².

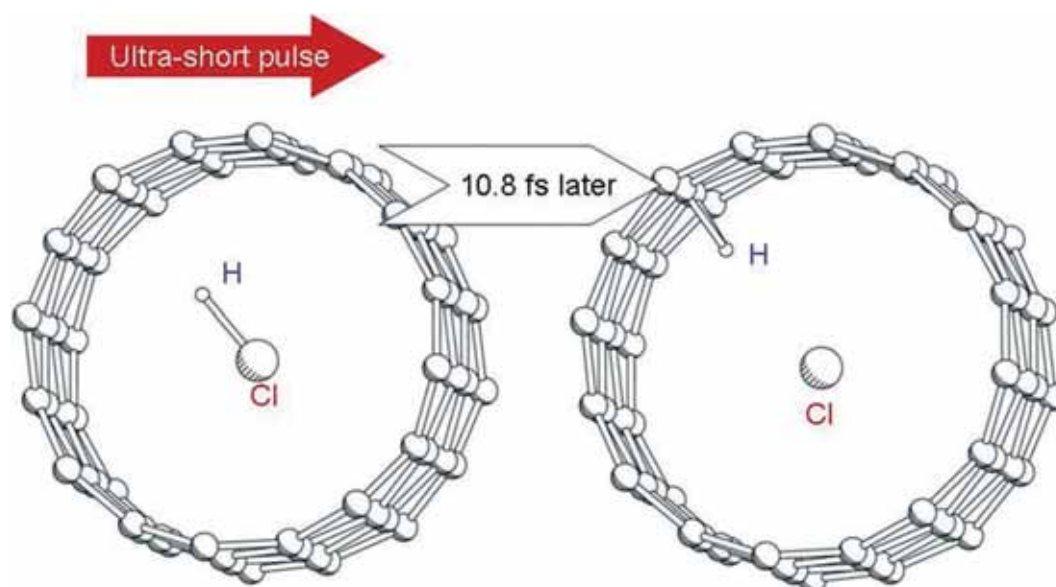


Fig. 9 Disintegration of an HCl molecule inside an (8,0) nanotube induced by very short pulse.

nanotube. We thus expect that trapping molecule inside semiconducting nanotube can make light illumination to molecule more efficient. We tested photo-induced disintegration of an HCl molecule inside an (8,0) nanotube.

Figure 9 shows the geometrical time-evolution of an HCl molecule inside an (8,0) nanotube after giving very short pulse shot with wavelength 800 nm, pulse width is 1 fs and maximum intensity of E-field is $12 \text{ V}/\text{\AA}$. (Such an extremely high E-field is available only at such very short pulse.) One can note spontaneous disintegration of HCl molecule and an ejected H atom is sticking nanotube wall, so the H atom is expected to reflect from the wall. According to our preliminary test, the nanotube itself is sustainable under such short pulse with the same field-intensity, but show significant shaking motion. We therefore think further simulation is needed to check whether the nanotube can remain and to check trajectory of reflected H atom. We believe this simulation will design efficient photo-chemical processes using encapsulation of molecules inside carbon nanotubes.

3. SUMMARY

Large-scale simulations have been carried out on nonmaterial by using *ab initio* density functional theory and the parameterized tight-binding models. These optimized models allowed us to simulate the properties with excellent performance on the Earth Simulator. It enables us to come across discoveries of novel phenomena in nano scale and find out some useful materials for clean energies.

References

- [1] S. Tejima, et al, Journal of the Surface Science Society of Japan, HYOMEN KAGAKU, vol.30, no.12, pp.673-679, 2009.
- [2] S. Nakamura, SC09, HCPNano09 Workshop, Oregon, November 15.
- [3] S. Miyamoto, et al, Phys. Rev. Lett., Vol.104, pp.208302-1-208302-4 (2010).

カーボンナノチューブの特性に関する大規模シミュレーション

プロジェクト責任者

手島 正吾 高度情報科学技術研究機構

著者

手島 正吾^{*1}, 中村 賢^{*1}, 宮本 良之^{*2}, 藤沢 義和^{*3}, 中村 壽^{*1}

*1 高度情報科学技術研究機構

*2 NEC R&D ユニット 中央研究所 グリーンイノベーション研究所

*3 本田技術研究所

1. 研究目的

優れた物性が予想されナノテクの基本材であるナノ炭素類（カーボンナノチューブ（CNT）、フラーレン、グラフェン）の電子・機械特性を従来不可能だった大規模シミュレーションにより推定し、科学技術及び産業界に提供すると共に、応用として特性の優れた新構造を発見し、基本材の拡充に寄与する目的で実施された。

2. 成果

これまで、我が国のナノチューブ研究で当面する課題解決に向けた応用シミュレーションを実施した。本年度さらに、グリーンエネルギーに関するシミュレーションを推進した。得られた結果を以下に示す。

- (1) これまでマッカーシー結晶の包括的な特性把握のために、合成法、機械特性などのシミュレーションを実施してきた。本年度は、電子構造特性のシミュレーションにより、マッカーシー結晶が太陽電池材料としての可能性があることが示された。サイズが異なる単位セルにそれぞれ 48、144、192 個の炭素をもつ P 型マッカーシー結晶のエネルギーバンド構造を第一原理計算で調べたところ、0.05eV から 0.94eV のエネルギーギャップを持つこと、原子が中性電荷からずれていることが明らかとなった。これらの理由は、マッカーシー結晶がもつ負のガウス曲面を維持するために基本となる 6 員環構造に 8 員環が混じり、特殊な電荷ポテンシャルが生じたためである。異なるバンドギャップをもつ積層半導体マッカーシー結晶は、応用として、広範囲の波長の光吸収を可能とする、高効率太陽が期待される。
- (2) タマネギ型構造をもち表面が活性で特徴的な性質をもつナノダイヤモンドが合成されゲル状の分散が可能となったことから、ドラックデリバリーシステムなどへの応用も進められている。この構造体はダイヤモンドクラスターの構造最適化により得られるが、分子化学修飾が可能な表面の性質は未だ詳細に得られていない。DFT 計算手法により、ナノダイヤモンドのサイズ依存性を、147、413 原子について調べた。その結果、(111) 方向は sp^2 結合による黒鉛化し、(100) 方向は sp^3 結合によるダイヤモンド構造であることが明らかとなった。サイズが大きくなると黒鉛層が大きくなる。 sp^2 と sp^3 の混在により、ナノダイヤモンドの電荷偏極が発生していると予測される。電荷偏極したナノダイヤモンドはドラックデリバリーシステム等への機能材料の一つと期待される。さらに大きなナノダイヤモンドの特性把握シミュレーションを予定している。
- (3) 電子デバイスとしてシリコンを使った微細加工は限界に達している。カーボンナノチューブは次世代の電子デバイスとして期待されている。しかし、未だカーボンナノチューブを実験で操作することは困難であるが、オームの法則からなずれなどの量子効果が観測されている。ナノスケールの伝導特性を把握する事は重要である。非平衡グリーン関数法により、各原子から原子への電子の流れの計算手法を開発した。代用電荷法でポアソン方程式の電荷分布を再現した。カーボンナノチューブに流れる電流の微細な様子はワーヤー電極の着ける位置、本数で代わり、条件によっては渦電流の発生が確認された。また、不純物効果も扱う事もできた。コード性能評価により、計算量は原子数に比例するオーダー N であり、大規模計算が可能であることを確認した。
- (4) 次世代電子材料として期待されるグラフェンの製造方法に関する知見をシミュレーションから得た。グラフェンの純度を損なわないように、化学物質の天下は行わず、グラファイト表面にフェムト秒レーザー照射を行うことにより、表面からの原子一層分のグラフェンをはがせることが、第一原理計算より判明した。

キーワード: 大規模シミュレーション, タイトバインディング理論, 時間依存密度汎関数法, オーダー N 法, カーボンナノチューブ, マッカーシー構造, ナノダイヤモンド, 量子伝導, グラファイト加工技術

Development of the Next-generation Computational Fracture Mechanics Simulator for Constructing Safe and Sustainable Society

Project Representative

Ryuji Shioya Faculty of Information Sciences and Arts, Toyo University

Authors

Ryuji Shioya Faculty of Information Sciences and Arts, Toyo University

Masao Ogino Faculty of Engineering, Kyusyu University

Hiroshi Kawai Faculty of Engineering, University of Tokyo

Hiroshi Okada Faculty of Science and Technology, Tokyo University of Science

The authors have been developing a crack propagation analysis system that can deal with arbitrary shaped cracks in three-dimensional solids. The system is consisting of mesh generation software, a large-scale finite element analysis program and a fracture mechanics module. To evaluate the stress intensity factors, a Virtual Crack Closure-Integral Method (VCCM) for the second-order tetrahedral finite element is adopted and is included in the fracture mechanics module. The rate and direction of crack propagation are predicted by using appropriate formulae based on the stress intensity factors. Combined with ADVENTURE system, a large-scale fully automatic fracture analysis can be performed on ES2.

Keywords: fracture mechanics, crack propagation analysis, finite element method, domain decomposition method, aging structure

1. Introduction

For the realization of sustainable society in the 21 century, assessment of gradually aging social infrastructure is becoming important. Fracture analysis has been one of the key numerical simulation for such problems. However, a three dimensional crack analysis of a real world, highly complicated structure has not been widely used yet, because of many obstacles including the lack of computational power.

The authors have been developing an open-source CAE system, ADVENTURE [1]. It is based on the hierarchical domain decomposition method (HDDM) with the balancing domain decomposition (BDD) pre-conditioner [2]. A general-purpose structural analysis solver, ADVENTURE Solid is one of the solver modules of the ADVENTURE system. It runs on The Earth Simulator (ES1) with a large scale model hundreds of millions of degrees of freedom [3, 4]. It can achieve vectorization ration 98%, parallel performance 70% (256 nodes) and 25% of the peak performance using an unstructured grid.

On the other hand, we have also been developing a system to support a three dimensional fracture analysis, especially a fatigue or SCC propagation analysis with many cracks of arbitrary complicated shape and orientation. To integrate the large scale structural analysis code with this fully automatic fracture analysis capability, a direct fracture simulation of a highly complicated realistic aging structure with explicit

modeling of cracks.

In this year, we conducted mainly two tasks, porting of automatic fracture analysis system on ES2 and performance tuning of ADVENTURE Solid for ES2.

2. Development of automatic fracture analysis system based on VCCM

Most of the fracture analyses have been performed by using the hexahedral finite elements. It takes an enormous amount of manual labor to generate a finite element model for a complex shaped three-dimensional structure with hexahedral finite elements. Thus, methodologies such as element free Galerkin method (EFGM), s-Version finite element method (s-FEM) and eXtended finite element method (x-FEM) were proposed to obviate the processes of mesh generation and were applied to the fracture mechanics problems.

Recently, Okada et al. [5, 6] have developed a virtual crack closure-integral method (VCCM) for tetrahedral finite elements. Based on the VCCM, an analysis system to perform crack propagation analysis system is being developed by present authors. The system is consisting of automatic mesh generation software, a large-scale finite element analysis program and a fracture mechanics module to evaluate the stress intensity factors by using VCCM. When crack propagation analysis is performed, the rate and direction of crack propagation need

to be predicted by using appropriate formulae based on the stress intensity factors. Mesh generation software that is a part of ADVENTURE project [1] is extended so that models with cracks can automatically be created. The cracks are regarded as local features in the three-dimensional analysis model ("local model"). They are inserted in an existing finite element model ("global model") without any cracks. Thus, the geometry representation of the structure is unchanged even though the shapes and the sizes of the cracks change as they grow. The crack models are represented by a number of nodal points and they are inserted in the global model. Hence, Delaunay triangulation technique is appropriately applied to generate the finite element mesh with the tetrahedral elements.

The crack propagation analysis system is consisting of parts/modules/programs for 1) model and crack geometry definition, 2) automatic finite element mesh generation with the second order tetrahedral finite elements, 3) finite element analysis using a parallel PC cluster, 4) evaluation for the stress intensity factors by using the virtual crack closure-integral method (VCCM) and 5) predictions for the direction and rate of crack propagation when the crack propagation analysis is performed, as depicted in Fig. 1.

First, the global model that has geometry information of the problem as whole is generated. This is called "base mesh". Only nodal point information of the base mesh is used to generate the crack model. The crack is inserted in the dense mesh region.

Second, the local model for the crack is generated. The procedures of generating the crack model are (1) defining the geometry of crack, (2) assigning the locations of nodal points in the plane of crack so that the model requirements for the VCCM computation is satisfied and (3) staking all the nodal points for the crack in the vertical direction. Nodal points are

inserted in the base mesh and a finite element model consisting of second-order tetrahedral finite elements is generated by using the Delaunay triangulation technique. Points with blue and red colors are those on the crack face and those at the crack front.

As an example, a fatigue crack in a circular bar subject to torsion is considered. The stress intensity factors are evaluated along the crack front. The kink angle and the rate of crack propagation are computed.

Finite element mesh for the initial state is shown in Fig. 2. It has a total of about 690,000 nodes and 500,000 elements and the numbers increase as the crack grows. The total numbers of nodes and elements after 15 steps of crack propagation were about 1,120,000 and 800,000, respectively. The growth of crack is shown in Fig. 3.

3. Performance Optimization of ADVENTURE Solid

As a programming style on a vector-type supercomputer such as ES1, ES2 and NEC SX-series, the length of an inner-most loop should be long enough to achieve high performance. On ES1, ADVENTURE Solid had an enough vector loop length to obtain roughly 30 - 40% of peak performance. However, on the new supercomputer, ES2, the vector loop length to obtain good enough vector performance on the current ADVENTURE Solid code has increased. As a result, peak performance ratio dropped to 4 - 5% with the current code. We planned a major revision of ADVENTURE Solid, so that it can regain a good enough vector length on ES2. To investigate the design detail, first we studied performance characteristics of ES2 in the context of the finite element method and the domain decomposition method.

ADVENTURE Solid is based on the hierarchical domain decomposition method (HDDM). In HDDM, a whole analysis domain is subdivided into many small subdomains. The parallelization of ADVENTURE Solid code is primarily based on subdomain-wise FEM calculation. On the FE analysis of each subdomain, a linear system of the subdomain stiffness matrix is solved. A skyline solver is employed for the solution of the relatively small system. In the current version of ADVENTURE Solid, this subdomain-wise skyline solver is identified as a hot spot. The inner-most loop of the hot spot is the double loop in forward and back substitution of the skyline solver. Its loop length, which means the band width of the skyline matrix, is not so large. It is usually about several hundreds.

To increase the vector loop length at the hot spot of ADVENTURE Solid, we tried an approach to move the loop over subdomains, which was located at outer-most, into the inner-most place. Then, the load balance issues among subdomain FEM calculation become important. In case of a large scale model, there can be tens of thousand of subdomains in total. Per processor, the number of subdomains is about 500 - 1000. Through the performance study on ES2, this number was found to be enough to achieve high vector performance.

If the inner-most loop is driven by the number of

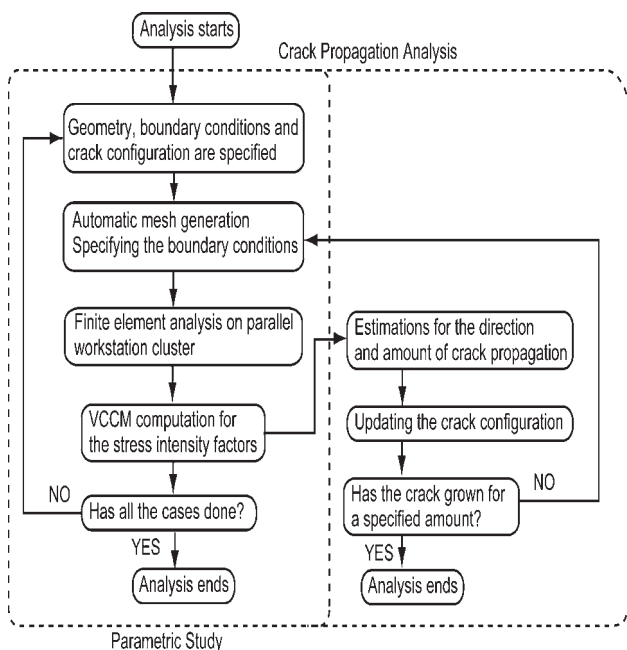


Fig. 1 Crack propagation system (programs and modules).

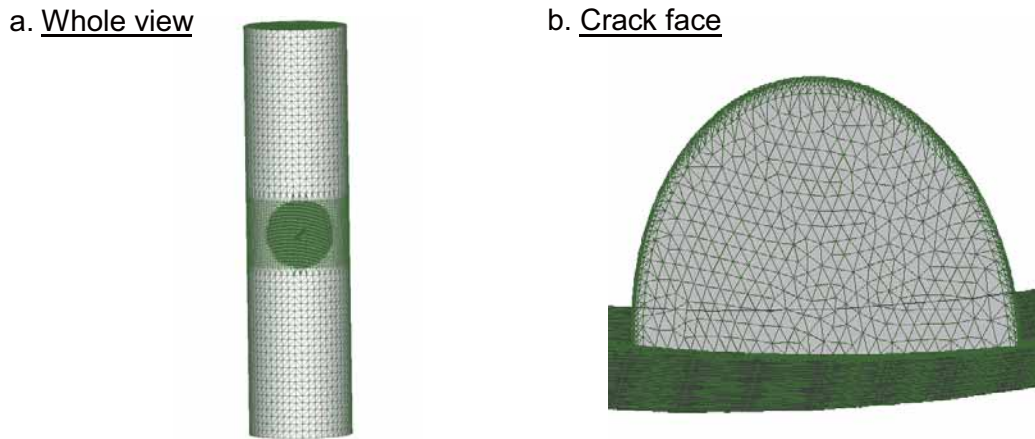


Fig. 2 Finite element mesh for the initial state.

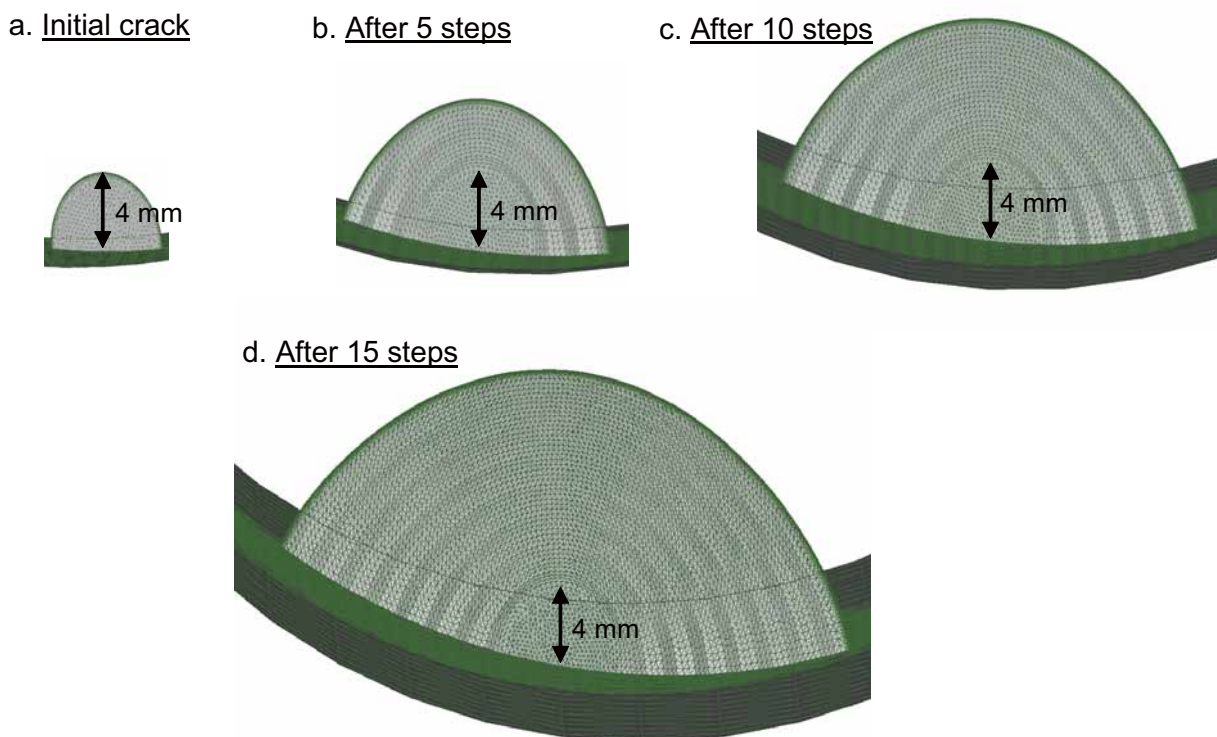


Fig. 3 Evolutions of crack face of the problem of circular bar subject to torsion.

subdomains, computational loads among subdomains should be evenly distributed. Although the domain decomposition process with METIS produces the relatively flat distribution of subdomain size, there are still some differences in mesh subdivision.

There can be two ways to implement this strategy on HDDM. One is to keep the skyline solver and just insert the subdomain-wise loop inside the skyline solver. In this case, load imbalance may be much larger, because the difference of the skyline band width among subdomains may be bigger than the mesh size itself. The other approach is based on explicit evaluation of the local Schur complement of DDM for each subdomain. In this case, the local Schur complement matrix is a symmetric dense square matrix. Although the computational cost increase

slightly compared with the skyline approach, the latter approach is much simpler and it can obtain better vector performance. In this work, we have chosen the latter, local Schur complement approach.

According to the performance measurement on ES2 of a prototype code, which is a hot-spot of ADVENTURE Solid, about 37 G flops is achieved using single processor. It is near 40% of the peak performance per single processor, 104 G flops. In detail, the hot spot code is basically a matrix vector product for each subdomain. The matrix is a local Schur complement. It is dense and symmetric. The two outer loops are unrolled in 5 by 5. Also, because the matrix is symmetric, the code is tuned to reduce memory access. With the vector length over 500, near optimum performance has already been achieved. If it is 200,

the performance number dropped 20%.

Acknowledgements

This work is performed as a part of the ADVENTURE project and the authors also would like to thank all the members of the ADVENTURE project.

References

- [1] ADVENTURE project, <<http://adventure.sys.t.u-tokyo.ac.jp/>>.
- [2] M. Ogino, R. Shioya, and H. Kanayama, "An inexact balancing preconditioner for large-scale structural analysis", *Journal of Computational Science and Technology*, **2-1**, pp. 150-161, 2008.
- [3] R. Shioya, M. Ogino, and H. Kawai, "An seismic response analysis of a BWR pressure vessel using the next-generation computational solid mechanics simulator", *Annual Report of the Earth Simulator*, **April 2006 – March 2007**, pp. 163-167, 2007.
- [4] M. Ogino, R. Shioya, H. Kawai, and S. Yoshimura, "Seismic response analysis of nuclear pressure vessel model with ADVENTURE system on the Earth Simulator", *Journal of the Earth Simulator*, **2**, pp. 41-54, 2005.
- [5] H. Okada and T. Kamibeppu, A virtual crack closure-integral method (VCCM) for three-dimensional crack problems using linear tetrahedral finite elements, *CMES: Computer Modeling in Engineering & Sciences*. 10, pp. 229-238, 2005.
- [6] H. Okada, H. Kawai, and K. Araki, A virtual crack closure-integral method (VCCM) to compute the energy release rates and stress intensity factors based on quadratic tetrahedral finite elements, *Engng. Fracture Mech.*, Vol. 75, (2008), pp. 4466-4485.

安全・安心な持続可能社会のための 次世代計算破壊力学シミュレータの開発

プロジェクト責任者

塩谷 隆二 東洋大学 総合情報学部

著者

塩谷 隆二 東洋大学 総合情報学部

荻野 正雄 九州大学大学院 工学研究院

河合 浩志 東京大学大学院 工学系研究科

岡田 裕 東京理科大学 理工学部

既に多くの超並列計算機や PC クラスタ上において実績を示している、1 億自由度級の大規模メッシュを用いた人工物や自然物の丸ごと詳細解析を可能とする汎用計算力学システム ADVENTURE をもちいて、実用大規模構造材料・機器の直接破壊シミュレータを ES2 上で開発し、低炭素社会構築のカギを握る小型高圧水素貯蔵タンクの超精密破壊解析や、安全・安心社会の基盤である経年化した社会的インフラストラクチャーの超精密破壊解析を通して本技術の確立を目指すことにより、21 世紀の持続可能社会の構築に寄与することを目的としている。

今年度は保有システムを統合した三次元き裂進展解析システムの構築並びに ES2 への移植を行うことを目指し、試験片レベル（～100 万節点）の三次元完全自動疲労き裂進展解析を行うためのプログラム群を整備し、完全自動疲労き裂進展解析を可能とした。なお、複数き裂問題の試行にも成功した。また、四面体有限要素用三次元 J 積分プログラムについて、領域積分法に基づく四面体有限要素のための実装方法の検討とそのプログラム実装を行い、マップドメッシュモデルでは六面体要素による結果と同等であることを確認した。さらに、並列有限要素法アルゴリズムの ES2 向け改良による線形問題計算の高速化のためのアルゴリズムにより、単一プロセッサにおいてピーク性能比約 30% を達成した。本システムを用いて、16 ノード上でのき裂入り 1,700 万自由度規模簡易モデルの応力解析を実現した。

キーワード : fracture mechanics, crack propagation analysis, finite element method, domain decomposition method, aging structure

Large-scale Simulation for a Terahertz Resonance Superconductor Device

Project Representative

Mikio Iizuka

Research Organization for Information Science and Technology

Authors

Mikio Iizuka

Research Organization for Information Science and Technology

Masashi Tachiki

Tukuba University

Hisashi Nakamura

Research Organization for Information Science and Technology

This study is aiming at designing by large-scale simulations a new nano-scale devices of high temperature superconductor (HTC) that would emit the terahertz wave continuously, for the purpose of developing a new application fields of terahertz waves that have been abandoned so far as the untapped frequency range between photon and radio waves. As a new light source, the continuous and frequency tunable terahertz wave, especially in the range of 1-4 THz, would be applicable to the advanced research fields of material science, bioscience, medical and information technology. Our challenge is set to develop the device to generate the terahertz wave using high temperature superconductor. The mechanism of generating the continuous terahertz waves, its optimum conditions and the frequency control have been revealed so far through the large scale simulation that run on the Earth Simulator with vast computing power.

One of challenges we are tackling is to design a wave guide that lead the terahertz waves generated out of the device to the object for flexible irradiation. In the wave guide the terahertz wave propagates dynamically with varying wavelengths from nanometer to millimeters. Thus, for searching the optimum conditions of design, it is required to perform large and multi-scale simulation on the nonlinear dynamics of terahertz in the three dimensional space of the device and wave guide. In this term, we have developed a two dimensional simulation model for designing the way of emitting the terahertz waves as Josephson plasma out of the device to the outer-space.

Keywords: high-temperature-superconductor, device, generating terahertz waves, stable excitation, Josephson plasma, high performance computational resource, wave guide.

1. Introduction

Terahertz wave has been untapped as electromagnetic wave in the frequency range from 0.3 to 10THz. The range is overlapping the resonance frequencies of the molecules and the low-energy collective and elementary excitations such as carrier scattering, recombination, and transporting etc in substances. Thus, terahertz wave has some potential for being applied to the advanced research field of science and technology such as spectroscopic analyses on dense or soft materials and biomolecules, medical diagnoses and information technology. Especially, the continuous, tunable and intense terahertz waves in the range of 1-4 THz are valuable for applications. But, it would be hard to generate the continuous, tunable and intense terahertz wave with 1-4THz, by conventional method such as quantum cascade laser and photo mixing.

It is therefore our challenge to develop a new device of generating the continuous and frequency-tunable terahertz waves in 1-4 THz for the realization of a new terahertz light source. Therefore, until last year, we have revealed the

mechanism and optimum condition of generating terahertz waves with new device of the high temperature superconductor, proposed in 1994 in Japan, by use of large-scale simulation with huge power of Earth Simulator.

The challenge for realization of the device generating terahertz waves of high temperature superconductor is the development of wave guide method that guides the terahertz waves from device inside to objects.

Themes are as follows as shown in Fig. 1;

- (a) Design of the connection from the inside of device to outer space: configuration, size and material of device, electrode, current source and wave guide for realizing the efficient emission of Josephson plasma without loss of power.
- (b) Design of the wave guide from the surface of device to targets: configuration, dimension and material of wave guide for realizing the efficient propagation of terahertz waves without reflection, decay of power.

It is indispensable to perform the optimum design of the

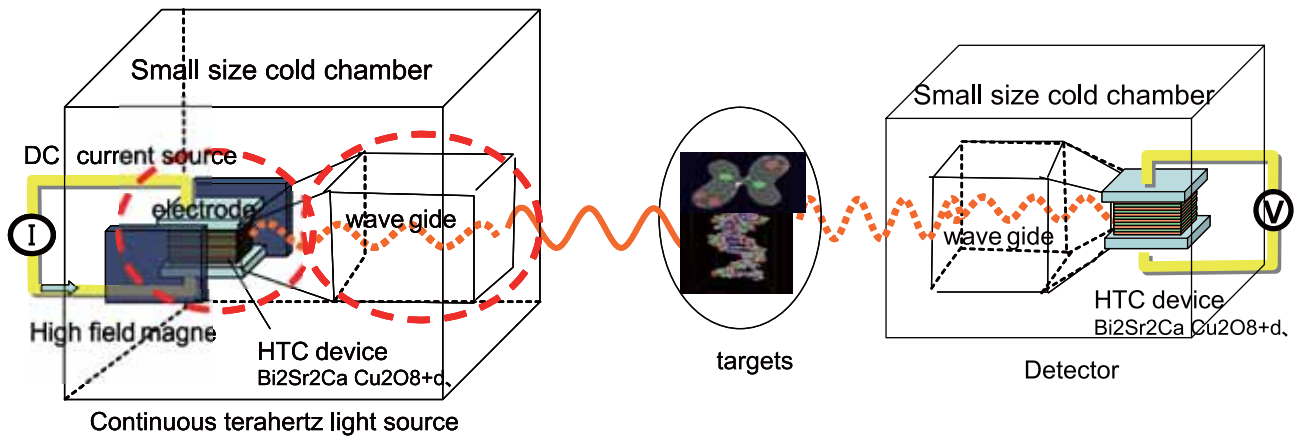


Fig. 1 Schematic diagram of measurement equipment using HTC device and the challenge of development of light source.

terahertz device by large-scale simulation of nonlinear dynamics of terahertz waves in the scale from nano-meter to milii-meter on the HTC device and wave guide system.

Until last year, we performed the basic study by focusing the Josephson plasma excitation inside the device and using quasi 2-dimensional mode of Josephson plasma dynamics for the development of new terahertz light source with HTC device. Hereafter, it is needed to perform the design of the optimum structure of connection between inside and outside of the HTC device and wave guide system from surface of device to targets in this study. Terahertz wave interact with 3-dimensional structure of hetero materials, emit and propagate the space. Therefore, (a) quasi 2-dimensional model must be extended to multi-dimensional model, (b) parallel model of coupling inside and outside of the HTC device must be developed to accurately and efficiently connect the inside and outside of the HTC device and (c) high performance tuning of that simulation code is needed to overcome the increase of calculation volume by multi-dimensional analysis.

In this year, we developed the large-scale 2D simulation model for deign of the method that enables the Josephson plasma to effectively emit as the terahertz waves from inside

of HTC device to outer-space for realization of continuous frequency tunable terahertz source using THC device. And we carried out a simulation of validation calculation.

2. Multi-dimensional model of generation of terahertz waves

2.1 Extension of quasi 2-dimensional model to multi-dimensional mode

Josphson plasma excites when it resonates with the array of fluxons and the most intense vibration of superconducting currents appears in parallel to layers (x-axis) and along layers (z-axis) near the surface of the device. These vibrating current fields on the surface of the device induce the terahertz wave in the outside of the device and then, the terahertz wave propagates to the space.

We have carried out so far the basic study on the HTC device by using a quasi 2-dimensional model neglecting the electric field parallel to the layers, because the electric field is induced by superconducting currents along to the layers (z-axis) generating intense terahertz waves. However, it is required that the vibration of superconducting currents is correctly analyzed on the layers (x-axis) and along layers (z-axis) for simulating the

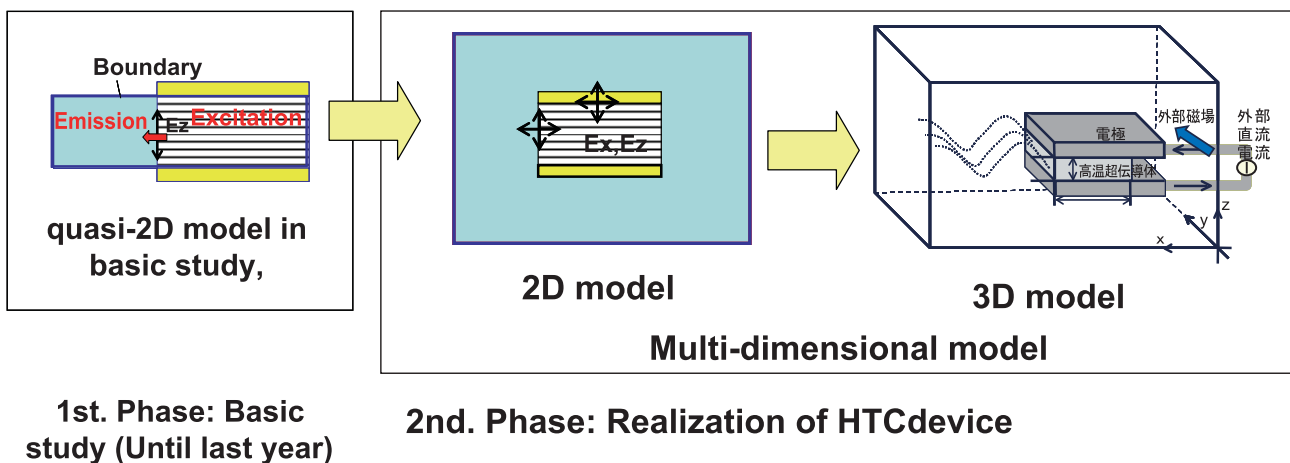


Fig. 2 Development of multi dimensional model

emission of the terahertz waves with a high degree of accuracy. Thus, in this term, the accurate 2-dimensional model of the generation of terahertz waves has been developed by taking the electric field parallel to the layers into consideration, as shown in Fig. 2.

2.2 Parallel model of coupling inside and outside of the HTC device

In this simulation, the equation of intrinsic Josephson plasma and Maxwell's equation of outer-space are solved inside and outside of the HTC device respectively, and the couple of equations are connected at the surface of the device for simulating the terahertz wave generation. The electromagnetic fields of inside /outside of the device are connected through solving the electric-field inside and the magnetic-field outside on the mesh shifted in half mesh as shown in Fig. 3.

Parallel coupling between inside and outside of the HTC device is carried out by partitioning two region each with good load-balance, and combining the electromagnetic field on the surface of the device by communicating between the inside of electric field and the outside of magnetic field. Communication table between IJJ and outer-space domain is automatically generated by the technique of DDM of unstructured grid as shown in Fig. 4.

3. Simulation

A simple simulation was carried out for validation of model as following; the simulation model is shown in Fig. 5.

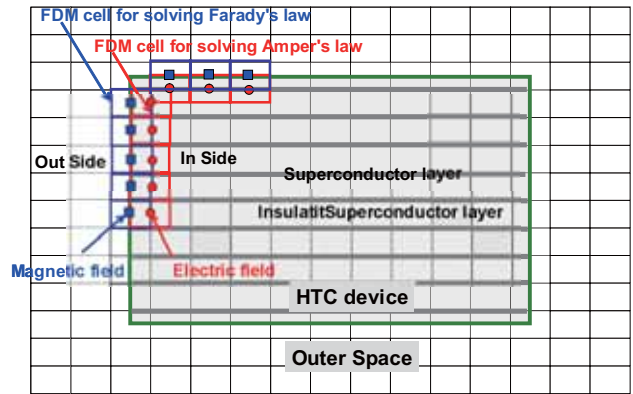


Fig. 3 Computational model of coupling the magnetic field with electric field on the surface of device on FDM cell.

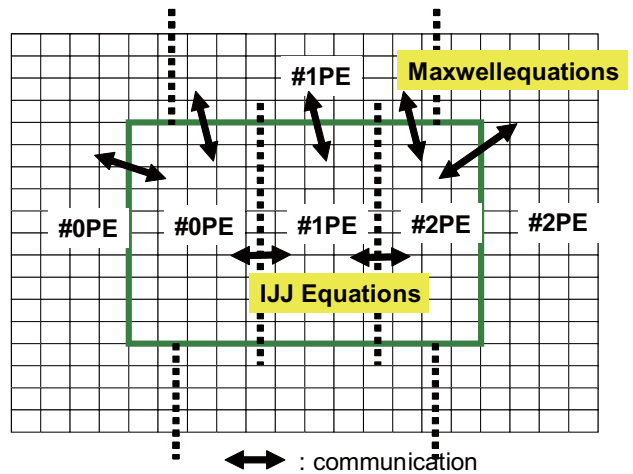


Fig. 4 Parallel model of coupling electromagnetic files inside and outside of the HTC device.

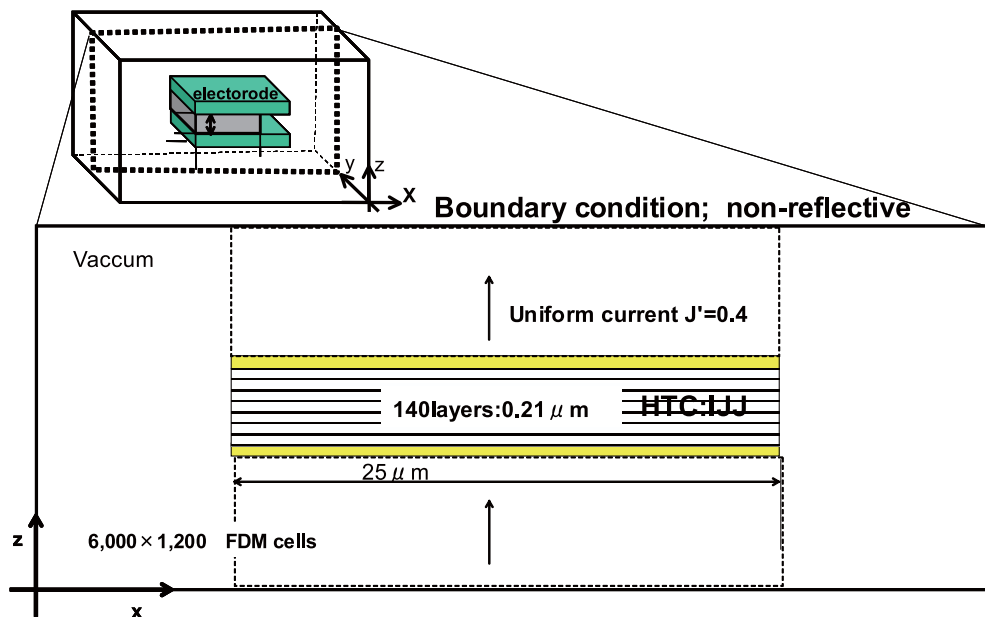


Fig. 5 Schematic diagram of the device generating terahertz waves. $\text{Bi}_2\text{Sr}_2\text{CaCu}_2\text{O}_{8+\delta}$ forms IJJ. The device consists of HTC crystal and electrodes. The green part shows the IJJ sandwiched by electrodes. An external current flows uniformly in the junctions in the direction of the z axis. An external magnetic field is applied to y-direction.

We performed simulations with parameters: (a) Num. of layre:140, (b) Device length :25 μm , (c) Magnetic field penetration depth from the bc and ab surface plane: λ_c, λ_{ab} :150 μm , 0.212 μm , (d) Reduced quasi-particle conductivity along c-axis β : 0.02, (e) External magnetic field: B_y : 0.5T, External DC: $J=0.4$.

Simulation results are shown in Fig. 6 and Fig. 7. Emission of THz waves starts as Josephson plasma starts excitation and the intensity of emission increases as Josephson plasma increases excitation, as shown in Fig.6. Terahertz wave diffuses immediately after the emission from the edge of the device.

The simulation study with the two-dimensional model

has just started. It will be continued toward 3D simulation.

4. Conclusion and future work

In this term, the large-scale 2D simulation model has developed for deigning the effective emission of the Josephson plasma as the terahertz waves from the inside to the outside of HTC device. And validation has been carried out on the simulation models.

In the next phase, we will developed the large-scale 3D simulation model for deigning a terahertz light source that effectively guide the irradiation of terahertz waves from the inside of the HTC device to the object placed in the outer-

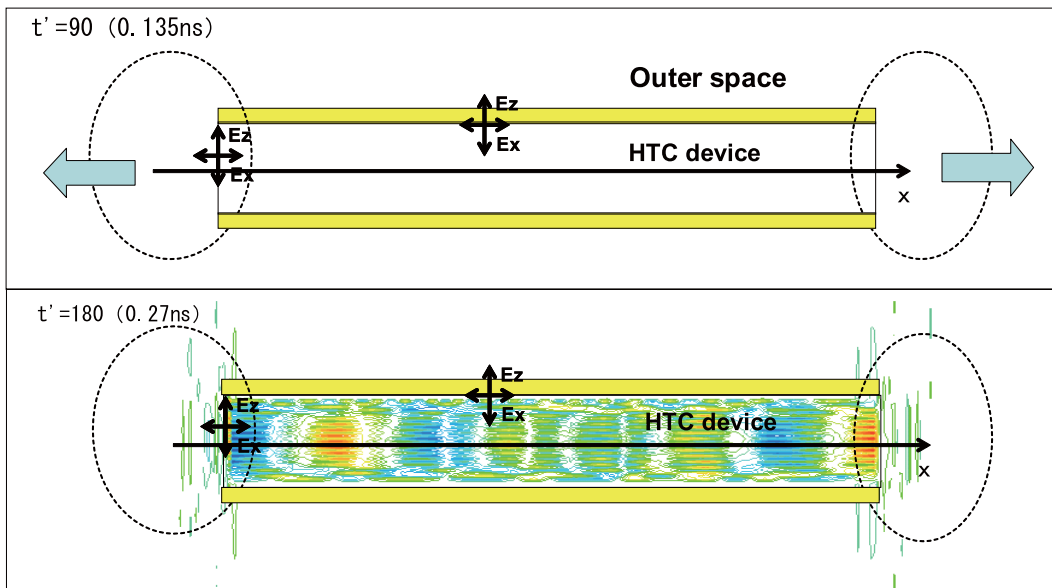


Fig. 6 Contour of Ez'/dt , that is oscillating part of Ez' . Ez' is electric field component propagating to x direction. Time is at 0.135ns and 0.2ns.

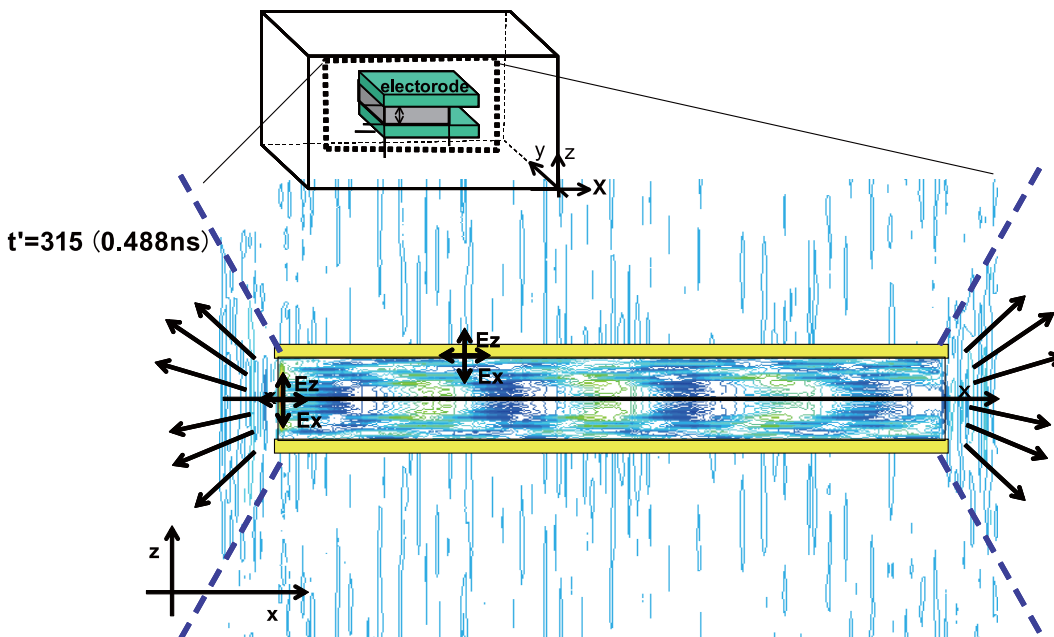


Fig. 7 Contour of Ez'/dt , that is oscillating part of Ez' . Time is at 0.488ns.

space and wave-guide.

The Earth Simulator shows clearly that the large-scale simulation with high performances is an effective methodology for developing new technologies.

References

- [1] M. Tachiki, T. Koyama, and S. Takahashi, Electromagnetic phenomena related to a low frequency plasma in cuprate superconductors, *Phys. Rev. B* 10, 7065 (1994).
- [2] M. Tachiki, T. Koyama, and S. Takahashi, in: G. Deutcher, A. Revcolevshi (Eds.), *Coherent I High Temperature Superconductors*, World Scientific, Singapore, 371 (1996).
- [3] Masashi Tachiki, Mikio Iizuka, Kazuo Minami, Syogo Tejima, and Hisashi Nakamura, Emission of continuous coherent terahertz waves with tunable frequency by intrinsic Josephson junctions, *Phys. Rev. B* 71,134515 (2005).
- [4] M. Iizuka, K. Minami, S. Tejima, M. Tachiki, and H. Nakamura: Large-scale simulation on a high-temperature-superconductor device generating the continuous terahertz wave continuously, *Journal of the Earth Simulator*, Vol 8, Nov. (2007).

テラヘルツ発振超伝導素子に関する大規模シミュレーション

プロジェクト責任者

飯塚 幹夫 高度情報科学技術研究機構

著者

飯塚 幹夫 高度情報科学技術研究機構

立木 昌 筑波大学

中村 寿 高度情報科学技術研究機構

本研究は、電波と光の間の未利用周波数帯域であるテラヘルツ波応用の開拓を目指し、連続波としてテラヘルツ波を発振する高温超伝導素子及びその利用システムを大規模シミュレーションにより設計するものである。

テラヘルツ波は光と電磁波の中間域(0.3 ~ 10THz)の未開拓領域にあり、物質、生体分子の励起振動数(~ 6THz)を含むことから、物性、癌細胞分子の分光分析、細菌・プラスチック爆発物の検出、X線よりも低エネルギーで透過性があるため安全な医療線源、また大容量通信等へ応用が期待される。特に、1 ~ 4THzでの周波数可変で高出力の連続波光源が無いことから、テラヘルツ波の実用化においては、この帯域の連続波の光源開発が課題となっている。そのため、昨年度まで、1994年に日本にて提案された高温超伝導体を使うテラヘルツ生成素子の開発を目的に、連続波テラヘルツ波を発振させる原理、その最適発振条件、さらに周波数制御法を地球シミュレータの計算力を生かした大規模シミュレーションから世界で始めて明らかにした。

さらに、実用化へ向けた克服すべき課題として、素子内で励起されたジョセフソンプラズマをテラヘルツ波として対象物に自在に照射するための導波技術がある。そこでは、素子及び導波システムにおけるナノからミリスケールまでのテラヘルツ波の非線形挙動を3次元空間で扱う大規模マルチスケールシミュレーションで明らかにし、最適設計条件を求めることが必須となる。そのため、今年度は、高温超伝導素子を使った周波数可変の高出力連続波のテラヘルツ光源の実用化へ向けて、素子内部発生ジョセフソンプラズマの外部への効率的放射法を設計するための2次元の大規模シミュレーションモデルを開発した。そしてその検証計算を実施した。これにより、素子端面からのテラヘルツ波放射の詳細な解析が可能となり、テラヘルツ波の反射、減衰を生じない素子と外部空間との接続法の設計が可能となった。また、3Dシミュレーションモデル(外部空間)の準備もできた。

今後は、3次元連続波テラヘルツ波の反射、減衰を考慮した素子・導波管系の大規模シミュレーションを行ない、連続波テラヘルツ波応用の基本となるシステム概要、その設計条件を定量的に明らかにする。また、これらの計算規模はペタスケールであり、そのためのモデル拡張、並列性能向上、演算性能向上へ向けた階層メモリ利用法向上、そのためのアルゴリズムの高度化等を含めた大規模モデルの研究開発も進めていく予定である。本研究は大容量情報伝送やエネルギー伝送の利用研究としての側面も持つことから米、独、中、韓等でも類する研究が盛んに行われており、厳しい競争状況にある。このため、本研究から得られる設計情報は、わが国の学界・産業界に優先的に提示し、日本独自の新しい産業技術の勃興に資する。

キーワード：テラヘルツ発振素子, 超伝導体, 大規模シミュレーション

Direct Numerical Simulations of Fundamental Turbulent Flows with the World's Largest Number of Grid-points and Application to Modeling of Engineering Turbulent Flows

Project Representative

Yukio Kaneda Graduate School of Engineering, Nagoya University

Authors

Yukio Kaneda Graduate School of Engineering, Nagoya University

Takashi Ishihara Graduate School of Engineering, Nagoya University

Kaoru Iwamoto Mechanical Systems Engineering, Tokyo University of Agriculture and Technology

Tetsuro Tamura Interdisciplinary Graduate School of Science and Engineering, Tokyo Institute of Technology

Yasuo Kawaguchi Department of Mechanical Engineering, Tokyo University of Science

We performed high-resolution direct numerical simulations (DNSs) of canonical turbulent flows on the Earth Simulator 2. They include (i) turbulent channel flow, (ii) turbulent boundary layer with zero pressure gradient, and (iii) turbulent thermal boundary layer on a rough wall. The DNSs provide invaluable data for the studies of (i) the small-scale statistics in the log-law layer of turbulent channel flow, (ii) small-scale statistics and related vortex dynamics in turbulent boundary layer, and (iii) turbulent heat transfer in turbulent thermal boundary layer on a rough wall, respectively. We also performed (i) a detailed analysis of the results of Large Eddy Simulation of turbulent boundary layer over an area around Tokyo railroad station to study effects of actual shape of urban roughness on turbulence statistics of atmospheric boundary layer, and (ii) a preliminary analysis of the flow in non-Newtonian surfactant solution between parallel plates equipped with successive ribs.

Keywords: High-resolution DNS, incompressible turbulence, turbulent channel flow, turbulent boundary layer, turbulent thermal boundary layer, rough wall, LES, urban turbulent boundary layer, non-Newtonian fluid, drag reduction

1. Large-scale spectral direct numerical simulation (DNS) of canonical turbulence

1.1 High resolution DNS of turbulent channel flow

Turbulent channel flow (TCF) is one of the most canonical wall-bounded turbulent flows, and there have been therefore extensive studies on TCF by DNS. High-resolution DNS of TCF may provide us not only with detailed practical data for modeling of wall-bounded turbulence but also with detailed fundamental data to explore universality in the small-scale statistics of high-Reynolds-number wall-bounded turbulence.

In the present study, we optimized our DNS code of TCF on the Earth Simulator 2 (ES2), achieved the sustained performance of 5.9Tflops (11.3% of the peak performance) in DNS of TCF on $1024 \times 1536 \times 1024$ grid points using 64 nodes of ES2, and attained $R_\tau = 2560$, where R_τ is the Reynolds number based on friction velocity and 2560 is the world's largest R_τ so far achieved in DNS of TCF. The analysis of the DNS data shows that one-dimensional longitudinal energy spectrum obtained in the log-law layer is consistent with the prediction of

Kolmogorov's theory (K41), but shows also that local isotropy, which is a key hypothesis in K41, does not necessarily hold.

1.2 Large-scale and high-resolution DNS of turbulent boundary layer

Spatially-developing turbulent boundary layer (TBL) over solid boundary is another representative phenomena observed in a wide class of flows in science and technology. Although extensive studies, especially those by large-scale DNSs [1, 2, 3], have been therefore made on TBL, much still remains unknown.

In the present study, we first examined the applicability of the so-called fringe method proposed by Spalart et al. [4], on the basis of DNS of TBL under various flow conditions. We then studied the statistics and related vortical structures of high Reynolds number TBL by a large-scale and high-resolution DNS on ES2 by using the fringe method.

In the method, Spalart et al. [4] introduced a region called fringe region in the computational domain, where the growth of the TBL is artificially suppressed so that one may apply

the Fourier spectral methods not only in the spanwise (y -) but also the streamwise (x -) directions. In the wall-normal (z -) direction, a method based on Jacobi polynomial expansion is used after an appropriate variable transformation. Their numerical method is, therefore, spectral accurate. However, the influence of the introduction of the fringe region on the flow is not known a priori. In order to assess the applicability of the method to a large-scale DNS, we first examined the method by several preliminary DNSs in which the DNS results at the same Reynolds number under different flow conditions are compared. Among the observations by the DNSs are the following:

- (i) Various statistics such as the shape factor, the friction coefficients, and the root-mean-square of velocity fluctuations in a region approximately $300\theta_0$ downstream from the fringe region are insensitive to the conditions in the fringe region, and are consistent with the experimental results so far reported at the similar Reynolds numbers. Here θ_0 is the momentum thickness at the exit of the fringe region.
- (ii) Grid spacing in the streamwise direction should be less than 10 wall units in order to appropriately resolve the fluctuations of the gradients of pressure in the TBL.

On the basis of these observations, we have developed a parallel DNS code of TBL on the ES2, and also determined appropriate parameters to be used in the DNS of TBL. We achieved 6.2Tflops (48% of the peak performance) in the DNS of TBL on $4608 \times 512 \times 768$ grid points using 16 nodes of the ES2, and attained the Reynolds number $R_\theta = 835 \sim 2443$ outside the fringe region. Here R_θ is the Reynolds number based on the momentum thickness. The number of grid points is the world's largest in DNS of TBL so far performed on the basis of the spectral method.

Among the observations by the analysis and

visualization of the TBL flow fields are the following:

- (i) Three-dimensional visualization of iso-surface of vorticity normalized by the mean and standard deviation of vorticity well demonstrates the existence of packets of coherent hairpin-like vortices, the idea of which was proposed by Adrian et al. [5] on the basis of their two-dimensional experimental data. Here the "mean" refers a time average over z (spanwise)- direction for given x and y . (See Fig. 1)
- (ii) Nested hierarchy of the packets of coherent hairpin vortices is observed in the TBL flow field at $R_\theta \sim 2000$.
- (iii) A short log-law-like region is observed in the TBL of flow field at $R_\theta \sim 2000$.
- (iv) It is suggested that in the log-law-like region of TBL, coalescence of the same-signed cane-type neighbor vortices is one of the typical mechanisms of the growth of the packets of hairpin-like vortices.

2. DNS of turbulent thermal boundary layer on a rough wall

Turbulent thermal boundary layer on rough plate is an important problem in fundamental turbulent heat transfer research, practical engineering applications and environmental processes. DNS of turbulent thermal boundary layer on rough wall has been only rarely performed compared with that of other wall-bounded turbulence such as turbulent channel flow.

In this study, we performed DNS of the turbulent thermal boundary layer on a rough plate with zero pressure gradient. Several turbulent thermal boundary layers with the different Prandtl numbers, such as $Pr = 0.71$ and 2, were simultaneously simulated. In the DNSs of spatially developing boundary layers on a rough wall, we provided a driver section with a flat wall and an analysis section with a rough wall as shown in Fig. 2.

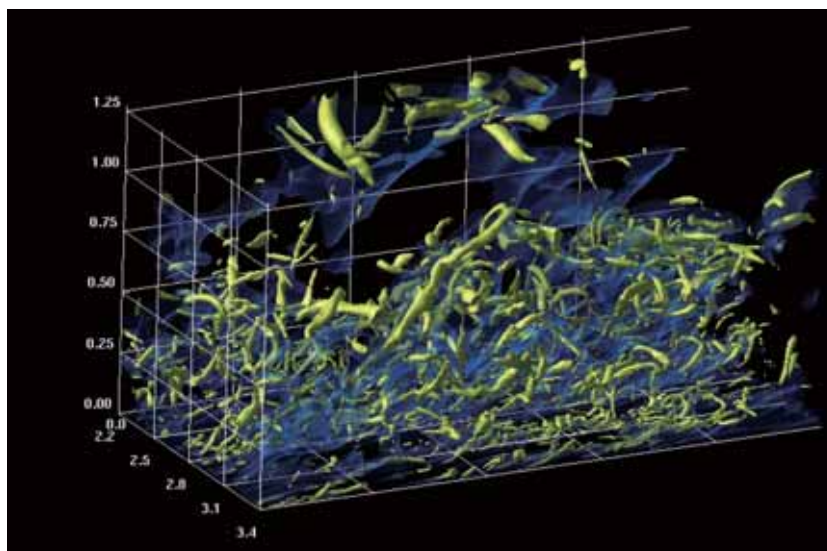


Fig. 1 Iso-surface of normalized vorticity (yellow) and low-speed zone (blue) obtained by the DNS of TBL at $R_\theta \sim 2000$.

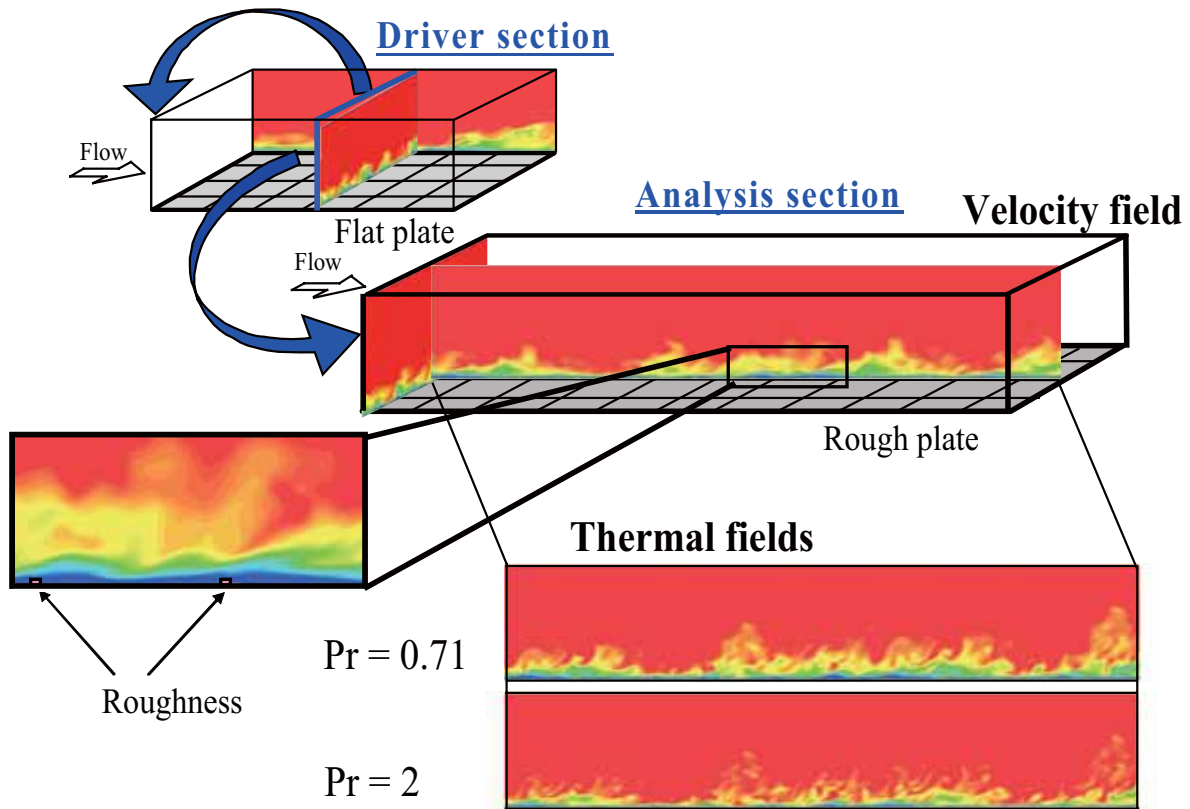


Fig. 2 Computational domains for turbulent thermal boundary layer on a rough plate.

Turbulent inflow conditions for the driver section were generated by rescaling the turbulent boundary layer at some distance downstream of the inflow and by reintroducing the recycled mean profile and fluctuation field. This technique follows those of Kong *et al.* [6] and Lund *et al.* [7]. Turbulent inflow conditions for the analysis section, on the other hand, were generated by exactly copying a turbulent field of the driver section. The parallel and vectorization efficiencies are 98.43% and 99.50%, respectively.

3. High resolution LES study on urban roughness effects on turbulence statistics of atmospheric boundary layer

Turbulent boundary layer over actual shape of urban-city was studied using large eddy simulation (LES)[8]. The area around Tokyo Railroad Station at the center of Tokyo was selected as the computation domain which has Marunouchi area in the west and Yaesu area in the east (Fig. 3). Currently the Marunouchi area has changed its aspect where many tall buildings are built year by year, while the Yaesu area is occupied by low-rise and

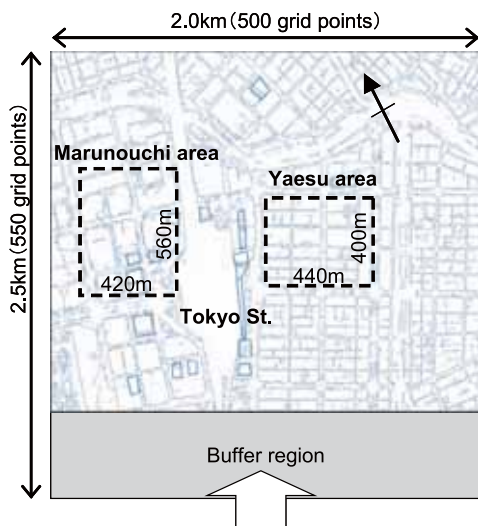


Fig. 3 Computational region.

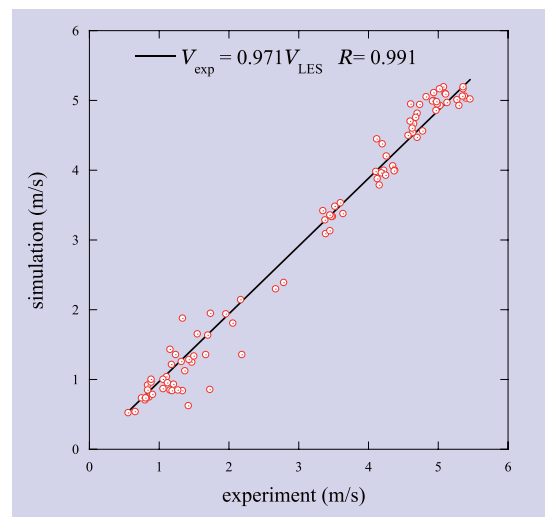


Fig. 4 Mean velocity correlation between experiment and LES.

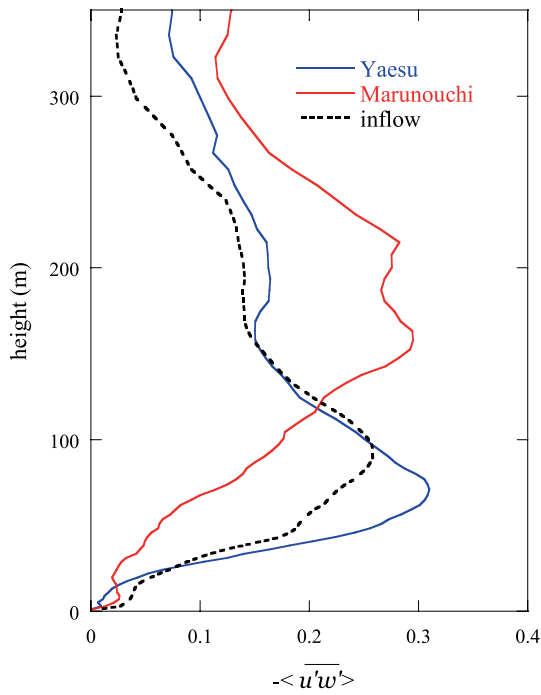


Fig. 5 Reynolds shear stress profiles.

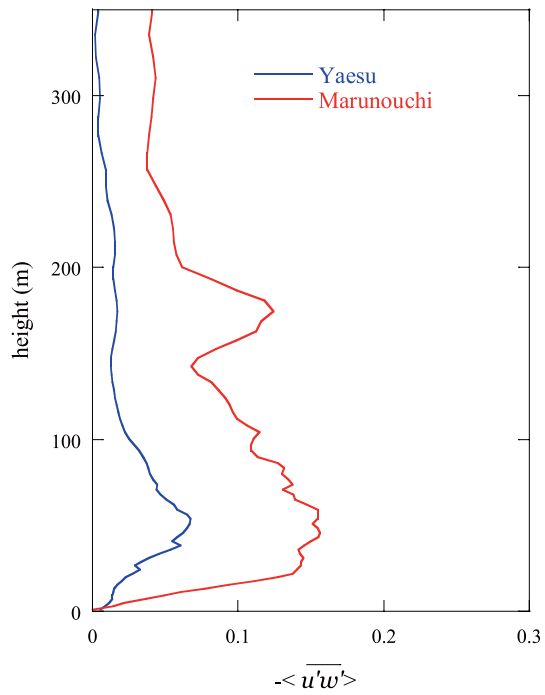


Fig. 6 Dispersive shear stress profiles.

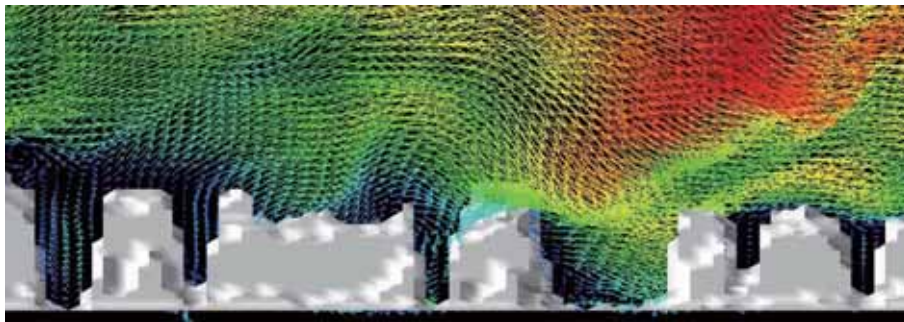


Fig. 7 Sweep-like event blow out the circulation flow in the street canyon.

middle-rise buildings. The computational region has horizontally 2.5 km length in streamwise direction and 2 km width in transverse direction. The horizontal mesh size is 4 m in the both directions and the height of the lowest mesh is around 1m. The total grid number is more than 3×10^7 . The oncoming turbulent inflow was generated using the quasi-periodic method[9]. The Reynolds number based on the free stream velocity and the boundary layer thickness is 93,000. The buildings are modeled using immersed boundary method.

Through this research we obtained the following results.

- (i) The mean wind speed profiles of the simulations and experiments were compared at each measurement point. They agree well with each other (Fig. 4).
- (ii) The effect of roughness was examined in the Marunouchi area and the Yaesu area. The Reynolds shear stress increases where there is strong shear approximately at the building height in the mean velocity profile (Fig. 5).
- (iii) The dispersive shear stress is small compared to the spatially averaged Reynolds shear stress at the locations

above the maximum height of each region, although it is comparable at the locations below the maximum height. The heights of the peaks are higher compared to those of past studies on uniform roughness. The results suggest that in order to predict the spatially averaged time-mean velocity it is necessary to construct a model of dispersive shear stress profile (Fig. 6).

- (iv) The sweep-like flow events occur intermittently and they strongly influence the streamwise velocities in the street canopy parallel to the wind direction. Unexpected high wind gust is recognized. The sweep-like flow events also occur in the broad orthogonal street and blow out the circulation flows formed there (Fig. 7).

4. DNS of the turbulence in non-Newtonian surfactant solution

It is known that a small amount of surfactant additives modifies significantly the turbulence in water through its Rheological characteristics. One of the most attractive points

from the view point of application is that turbulent drag coefficient in pipe is reduced to 30% compared with water flow at the same flow rate. The amount of surfactant necessary for this reduction is order of 0.1%. The large benefit of this reduction in energy conservation in water circulation system is obvious. However, because the drag reduction mechanism is still not clear, optimization of surfactant, flow system and heat exchanger, which is sometimes necessary component of water circulating system, is neither clear. Extensive investigations to find the missing links between the chemicals, Rheology, turbulence and real components through the large scale numerical analysis are wanted.

The purpose of this sub-project is to contribute to the energy conservation experiments with surfactant additives in the real-scale air-conditioning systems in buildings through the DNS analysis. The analysis will be performed for the turbulence in non-Newtonian surfactant solution between parallel plates and also between parallel plates equipped with successive ribs. The result will be used for elucidating the drag reduction mechanism and estimation of heat transfer in heat exchangers.

In FY 2009, modification of DNS code for parallel computing was made. It contains installation of successive solid ribs in the channel. Preliminary analysis of the flow has been made. The results were presented in the symposium but the most important results will be achieved after large-scale simulations on ES2 with changing the Reynolds number, Weissenberg number, rib geometry etc. systematically.

References

- [1] M.P.Simens, J.Jimenez, S.Hoyas and Y.Mizuno, A high-resolution code for turbulent boundary layer, *J.Comput. Phys.*, 228 (2009), pp.4218-4231.
- [2] P.Schlatter, R.Orlu, Q.Li, G.Brethouwer, J.H.M.Fransson, A.V.Johansson, P.H.Alfredsson and D.S.Henningson, Turbulent boundary layers up to $Re_{\mu}=2500$ studied through simulation and experiment, *Phys.Fluids*, 21 (2009), 051702.
- [3] A.Ferrante and S.E.Elghobashi, A robust method for generating inflow conditions for direct simulations of spatially-developing turbulent boundary layers, *J.Comput. Phys.*, 198 (2004), pp.372-387.
- [4] P.R.Spalart and J.H.Watmuff, Experimental and numerical study of a turbulent boundary layer with pressure gradients, *J.Fluid Mech.*, 249 (1993), pp.337-371.
- [5] B.J.Adrian, C.D.Meinhart and C.D.Tomkins, Vortex organization in the outer region of the turbulent boundary layer, *J.Fluid Mech.*, 422 (2000), pp.1-54.
- [6] H. Kong, H. Choi, and J. S. Lee, Direct numerical simulation of turbulent thermal boundary layers, *Phys. Fluids*, 12, (2000), 2666.
- [7] T. S. Lund, X. Wu, and K. D. Squires, Generation of turbulent inflow data for spatially-developing boundary layer simulations, *J. Comput. Phys.*, 140 (2), (1998), 233-258.
- [8] K. Nozawa, M. Ohashi, T. Tamura and Y. Okuda, LES study on urban roughness effects on turbulence statistics of atmospheric boundary layer, *Proc. 5th EACWE*, (2009), pp. 237-240.
- [9] K. Nozawa and T. Tamura, Large eddy simulation of the flow around a low-rise building in a rough-wall turbulent boundary layer, *J. Wind Eng. Ind. Aerodyn.*, 90, (2002), 1151-1162.

乱流の世界最大規模直接数値計算とモデリングによる応用計算

プロジェクト責任者

金田 行雄 名古屋大学 大学院工学研究科

著者

金田 行雄 名古屋大学 大学院工学研究科

石原 卓 名古屋大学 大学院工学研究科

岩本 薫 東京農工大学 工学府

田村 哲郎 東京工業大学 大学院総合理工学研究科

川口 靖夫 東京理科大学 理工学部

地球シミュレータ (ES2) を用いて、乱流の規範的 (カノニカル) な問題の大規模直接数値計算 (DNS) を実施した。具体的には (i) スペクトル法を用いた、世界最大レイノルズ数の平行二平板間乱流 DNS、(ii) 乱流境界層のスペクトル法における世界最大自由度 DNS である。また、(iii) プラントル数の異なる複数の場の同時計算が可能な、粗面上の乱流熱境界層 DNS のコード開発と最適化を実施した。これらの DNS は各々、(i) 高レイノルズ数平行二平板間乱流の対数領域の小スケールにおける普遍的統計法則、(ii) 乱流境界層の小スケールにおける統計法則と関連する渦動力学、及び (iii) 粗面上の乱流熱境界層における熱 (スカラー) 輸送の統計を調べるための貴重なデータを提供するものである。また、応用計算として、ES2 上で実施した、東京駅周辺の領域の地表被覆状態を再現した乱流境界層のラージエディシミュレーションの結果を詳細に解析し、実験結果との一致を確認したほか、抵抗低減メカニズムを調べるため、界面活性剤溶液の境界にリブ構造のある平行平板間乱流の DNS コードを開発し、予備的解析を行った。

キーワード: 大規模直接数値計算, 非圧縮性乱, 平行二平板間乱流, 乱流境界層, 乱流熱境界層, 粗面, 都市型大気乱流境界層, 界面活性剤, 抵抗低減

A Large-scale Genomics and Proteomics Analyses Conducted by the Earth Simulator

Project Representative

Toshimichi Ikemura Nagahama Institute of Bio-Science and Technology

Authors

Takashi Abe Nagahama Institute of Bio-Science and Technology

Toshimichi Ikemura Nagahama Institute of Bio-Science and Technology

Since the development of next-generation DNA sequencers, complete genome sequences of more than 2,000 species have been determined and metagenomic analyses covering a large number of novel species in various environments have become common (Genomes Online Database, <http://www.genomesonline.org/>). Microorganisms in diverse environments should contain an abundance of novel genes, and therefore, intense research activities are underway using samples obtained from a wide variety of environments, such as seawater and soil, and human intestines. The present BLSOM is an unsupervised algorithm that can separate most genomic sequence fragments based only on the similarity of oligonucleotide frequencies. It can separate sequences on a species basis with no additional information other than the oligonucleotide frequencies. Unlike the conventional phylogenetic estimation methods based on sequence homology searches, the BLSOM requires neither orthologous sequence set nor sequence alignment, and therefore, this method is most suitable for phylogenetic estimation for novel gene sequences. It can be used to visualize an environmental microbial community on a plane and to accurately compare it between different environments.

Keywords: batch learning SOM, oligopeptide frequency, protein function, bioinformatics

1. Introduction

Large-scale metagenomic analyses using recently released next-generation sequencers have actively been underway. The number of fragmental sequences obtained and registered in the International Nucleotide Sequence Databases (INSD) has soared above 17 million. For most of these genomic sequence fragments, however, it is difficult to estimate the phylogeny of organisms from which individual fragmental sequences are derived or to determine the novelty of such sequences. Most metagenomic sequences registered in the databases have limited utility because of lack of the phylogenetic information and the functional annotation; this situation has arisen because orthologous sequence sets, which cover a broad phylogenetic range and are required for the creation of reliable phylogenetic trees through sequence homology searches, are unavailable for novel gene sequences. A method for estimating the phylogeny and gene function that is based on principles totally different from sequence homology searches is urgently needed. We previously modified the SOM developed by Kohonen's group for genome informatics on the basis of batch-learning SOM (BLSOM), which makes the learning process and resulting map independent of the order of data input [1-2]. The BLSOM thus developed could recognize phylotype-specific characteristics of oligonucleotide frequencies in a wide range of genomes and permitted clustering (self-organization) of genomic

fragments according to phlotypes with neither the orthologous sequence set nor the troublesome and mistakable process of sequence alignment. Furthermore, the BLSOM was suitable for actualizing high-performance parallel-computing with the high-performance supercomputer "the Earth Simulator", and permitted clustering (self-organization) of almost all genomic sequences available in the International DNA Databanks on a single map [3-5]. By focusing on the frequencies of oligonucleotides (e.g., tetranucleotides), the BLSOM has allowed highly accurate classification (self-organization) of most genomic sequence fragments on a species basis without providing species-related information during BLSOM computation. The present unsupervised and alignment-free clustering method is thought to be the most suitable one for phylogenetic estimation for sequences from novel unknown organisms [3, 6-7] and for comparative genome analyses [8-9].

We employed BLSOM for analyses of environmental genomic fragments in joint research with experimental research groups analyzing various environmental and clinical samples [6-7]. This report introduces a strategy how to efficiently explore the genomic sequences from novel unknown microorganisms, including viral genomes, by utilizing numerous metagenomic sequences and how to determine the diversity and novelty of genomes in environmental microbial communities.

2. Methods

Nucleotide sequences were obtained from DDBJ (DNA Databank of Japan, <http://www.ddbj.nig.ac.jp/anoftp-e.html>). We modified the conventional SOM for genome informatics on the basis of batch-learning SOM (BLSOM) to make the learning process and resulting map independent of the order of data input [1-2]. The initial weight vectors were defined by PCA instead of random values on the basis of the finding that PCA can efficiently classify gene sequences into groups of known biological categories.

3. Results

3.1 Phylogenetic estimation for environmental DNA sequences and microbial community comparison

More than 17 million genomic sequence fragments obtained from various environments through metagenomic analysis have been registered in the International Nucleotide Sequence Databases. A major portion of them is novel but has a limited utility because of lack of phylogenetic and functional annotation. The phylogeny estimation of genomic sequence fragments of novel microorganisms, based on the BLSOM, requires in advance the characterization of oligonucleotide frequency of all species-known microorganisms currently available. Therefore, a large-scale BLSOM covering all known prokaryotic sequences, including those of viruses, mitochondria, chloroplasts, and plasmids was first constructed (Prokaryotes

or Eukaryotes in Fig. 1). On the BLSOM, numerous sequence fragments derived from an environmental sample were mapped; i.e., the similarity of the oligonucleotide frequency in fragmental sequences from environmental samples with that of sequences from species-known genomes was examined. The 210 thousand sequences with a fragment size of 1 kb or more, which were collected from the Sargasso Sea near Bermuda [10], were thus mapped. This mapping of the sequence fragments obtained from an environmental sample can estimate proportions of species present in the sample. Approximately 70% of sequences from the Sargasso Sea were mapped to the prokaryotic territories, while the rest was mapped to the eukaryotic, viral or organelle territories.

To identify the detailed phylogenies of the environmental sequences thus mapped to the prokaryotic territories, a BLSOM analyzing 5-kb genomic sequence fragments derived from 2,389 known prokaryotes, which have been compiled in the International Nucleotide Sequence Databases, was created with tetranucleotide frequencies (Phylum-BLSOM in Fig. 2). For the 5-kb genomic sequences from the 2,813 species-known prokaryotes used to create this BLSOM, their separation into 28 phylogenetic groups was examined, revealing that 85% of the sequences separated according to their phylotypes. The reason why 100% separation was not achieved is thought to be mainly because of horizontal gene transfer between the genomes of different microbial species [2-3].

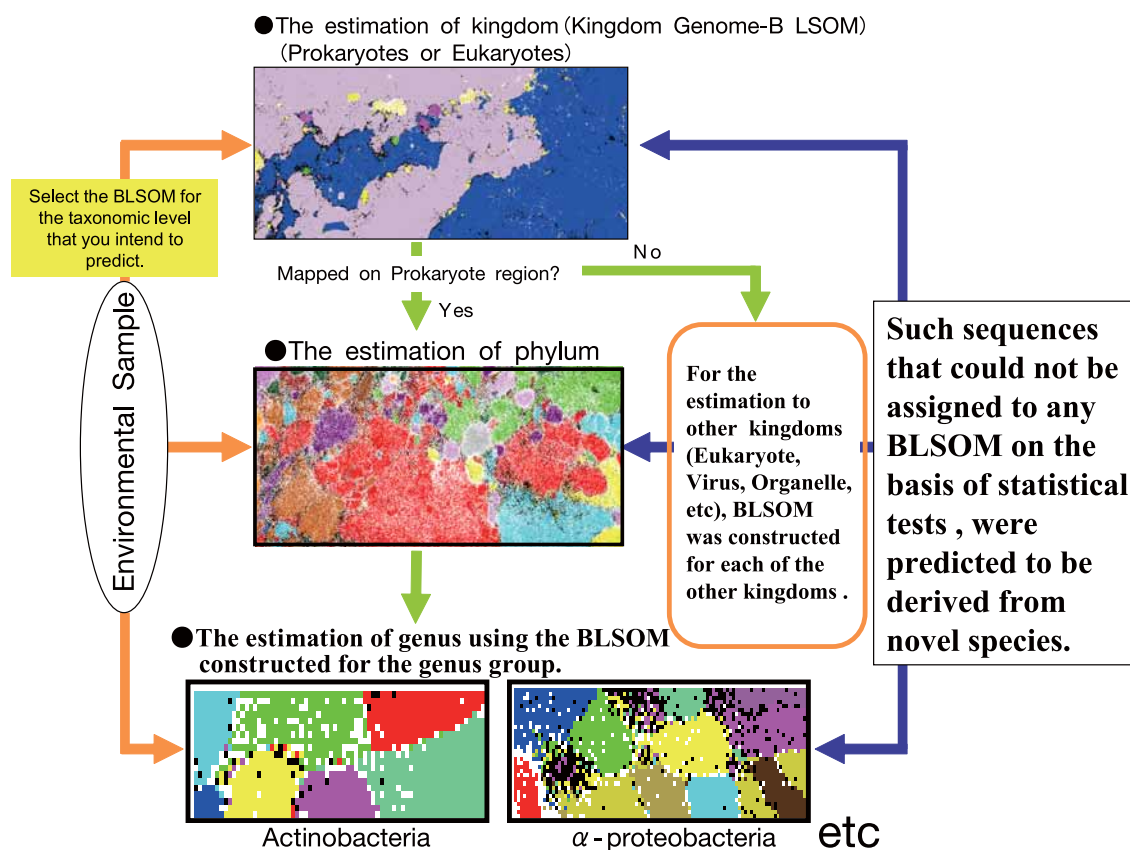


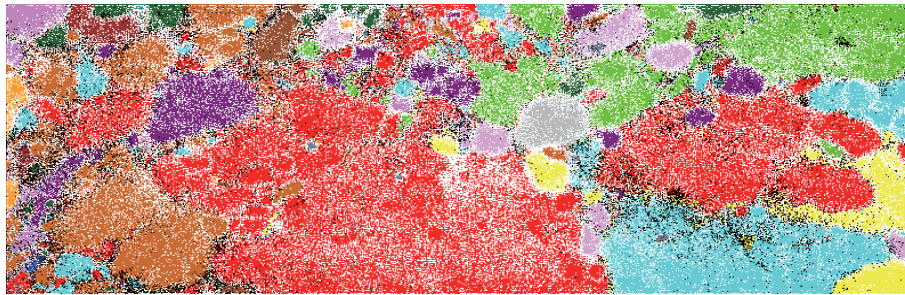
Fig. 1 The workflow of phylogenetic estimation using Genome-BLSOMs.

The 140 thousand metagenomic sequences from the Sargasso Sea that were mapped in advance to the prokaryotic territories (Fig. 1) were remapped on the BLSOM for the detailed prokaryotic phylotype assignment. They broadly spread across the BLSOM, demonstrating that the sequences belonged to a wide range of phylogenies (Fig. 2B). Interestingly, there were areas on the map where metagenomic sequences were densely mapped, which should indicate dominant species/genera. In sum, the estimation of prokaryotic phylogenetic groups could provide phylogenetic information for almost half of sequence fragments from the Sargasso Sea (Fig. 2C). The procedure above can be used to establish the phylogenetic distribution of microbial communities living in any subject environments, e.g.,

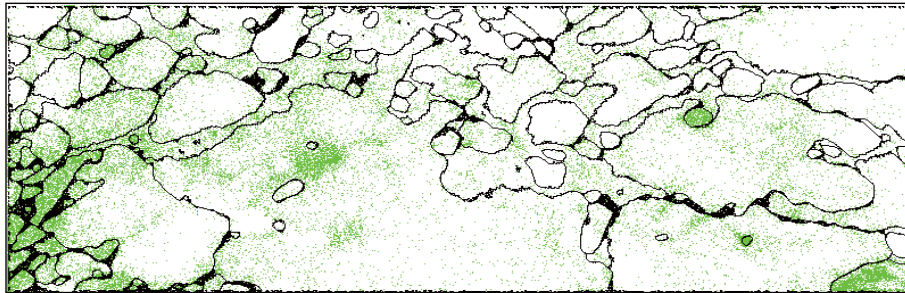
floras.

Further detailed phylogenetic estimation at the genus or species level becomes possible, through successive remapping the subject sequences on a BLSOM created with the sequences from known genomes of each phylogenetic group such as one family. Such systematic and detailed phylogenetic estimation in the stepwise manner from the domains of organisms (e.g., eukaryotes and prokaryotes), through the phylogenetic groups to the genus or species level, was explained in Fig. 1. This procedure can also determine the novelty of environmental sequences at various phylogenetic levels, allowing the efficient detection of sequences with high novelty.

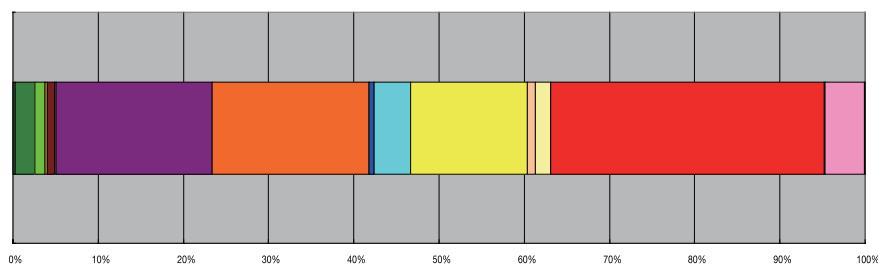
(A) Phylum-BLSOM, DegeTetra, Window 5-kb.



(B) Sargasso sequence longer than 1-kb mapped



(C) Microbial distribution of Sargasso sequence predicted by BLSOM



Nodes that include sequences from plural species are indicated in black, those that contain no genomic sequences are indicated in white, and those containing sequences from a single species are indicated in color as follows: Acidobacteria (■), Actinobacteria (■), Alphaproteobacteria (■), Aquificae (■), Bacteroidetes (■), Betaproteobacteria (■), Chlamydiae (■), Chlorobi (■), Cenibacterium (■), Chloroflexi (■), Crenarchaeota (■), Cyanobacteria (■), Deinococcus-Thermus (■), Deltaproteobacteria (■), Dictyoglomi (■), Epsilonproteobacteria (■), Euryarchaeota (■), Fibrobacteres (■), Firmicutes (■), Fusobacteria (■), Gammaproteobacteria (■), Nanoarchaeota (■), Nitrospirae (■), Planctomycetes (■), Spirochaetales (■), Thermodesulfobacteriales (■), Thermotogales (■), Verrucomicrobiae (■)

Fig. 2 Phylogenetic classification of sequences from an environmental sample. (A) DegeTetra-BLSOM of 5-kb sequences derived from species-known 2,813 prokaryotes. (B) Sargasso sequences that were classified into prokaryotic territories in Fig. 1 were mapped on the 5-kb DegeTetra-BLSOM constructed with the sequences only from the species-known 2,813 prokaryotes. (C) Microbial distribution of Sargasso sequences predicted by BLSOM.

3.2 Visualization of all virus genome sequences on one plane

Currently, metagenomic analyses focusing on an abundance of viruses in seawater have been reported [11]. Since virus genomes contain no rDNA, conventional methods of phylogenetic estimation based on rRNA sequence cannot be used, and therefore, a new method is urgently required. To test the clustering power of BLSOM for wide varieties of virus sequences, we first analyzed tri- and tetranucleotide frequencies in sequences of 43,828 virus genomes, which have been compiled by GIB-V (Genome Information Broker for Viruses, <http://gib-v.genes.nig.ac.jp/>) in DDBJ (DNA Databank of Japan). BLSOM was constructed with tri- and tetranucleotide frequencies (Tri- and Tetra-BLSOM) in all 0.5- and 1-kb fragment sequences derived from virus genomes (Fig. 3A and 3B, respectively). Then, lattice points that contained sequences from a single phylogenetic family are indicated in color, and those that included sequences from more than one family are indicated in black. A major portion of the BLSOMs was colored, showing a major portion of the fragmented sequences to be separated (self-organized) according to phylotype. The level of the phylotype-specific clustering was slightly higher for Tetra-BLSOM than for Tri-BLSOM, and the level for the 1-kb sequences was higher than that of the 0.5-kb fragment sequences. It should be pointed out that no information of virus phylotype was given during the BLSOM calculation; i.e., unsupervised self-organization.

3.3 BLSOM for prediction of protein function

For almost half of protein-gene candidates predicted from novel genomes newly sequenced, protein functions cannot be estimated through sequence homology searches. To complement the homology searches, the establishment of a protein function estimation method based on totally different principles is important. We have applied BLSOM to protein studies by analyzing oligopeptide frequencies and found the separation (self-organization) of proteins according to their functions [12]. This shows that the BLSOM can be used for a protein function estimation that does not rely on sequence homology searches, providing a novel, valuable method to find scientifically or industrially important protein genes that have not been found by sequence homology searches. Large-scale BLSOMs, which analyse vast quantities of genomic sequences and protein sequences, can facilitate the efficient extraction of useful information that supports development in a broad range of life sciences and industrial fields.

4. Conclusion and Perspective

We established a method of phylogenetic prediction for individual genomic fragments obtained by metagenomic analysis, by using BLSOM of oligonucleotide frequencies. The publication of large-scale BLSOM constructed with ES, which can separate all genomic sequences currently available on a plane, will provide a foundation of novel and large-scale genomic information useful for a broad range of life sciences, such as medical and pharmaceutical sciences, and related industrial fields. The mapping of newly obtained sequences

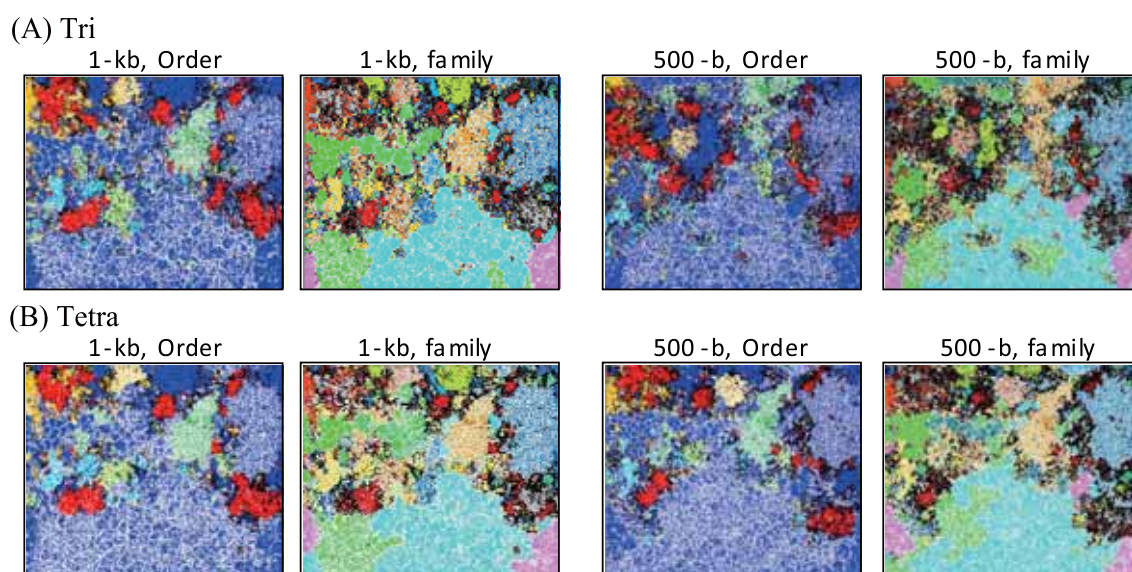


Fig. 3 BLSOMs for non-overlapping 1-kb and 500 bp sequences of all virus genomes. (A) Tri-BLSOMs. (B) Tetra-BLSOMs.

Lattice points that include sequences from plural species are indicated in black, those that contain no genomic sequences are indicated in white, and those containing sequences from a single species are indicated with difference in levels of blackness and with letters as follows: Order: Caudovirales (■), Herpesvirales (■), Mononegavirales (■), Nidovirales (■), Nidovirales (■), Orderunclassified (■). Family: Coronaviridae (■), Siphoviridae (■), Hepadnaviridae (■), Flaviviridae (■), Poxviridae (■), Retroviridae (■), Orthomyxoviridae (■).

on the large-scale BLSOM can be performed using a PC-level computer; our group has created a PC software program for the BLSOM mapping.

We introduced also the BLSOM method for predicting functions of proteins obtained by genome analyses. For function-unknown proteins for which the consistency of the predicted function is observed by BLSOMs with the frequencies of di-, tri-, and tetrapeptides, their predicted functions are thought to be reliable. Use of the high-performance supercomputer ES is essential for these large-scale BLSOM analyses. The data obtained by ES are unique datasets in genomics and proteomics fields and provide a valuable guideline for research groups including those in industry to study functions of novel genes with scientific and industrial usefulness.

Acknowledgements

This work was supported by Grant-in-Aid for Scientific Research (C, 20510194) and for Young Scientists (B, 20700273) from the Ministry of Education, Culture, Sports, Science and Technology of Japan. The present computation was done with the Earth Simulator of Japan Agency for Marine-Earth Science and Technology.

References

- [1] S. Kanaya, M. Kinouchi, T. Abe, Y. Kudo, Y. Yamada, T. Nishi, H. Mori, and T. Ikemura, "Analysis of codon usage diversity of bacterial genes with a self-organizing map (SOM): characterization of horizontally transferred genes with emphasis on the *E. coli* O157 genome", *Gene* vol. 276, pp.89-99, 2001.
- [2] T. Abe, S. Kanaya, M. Kinouchi, Y. Ichiba, T. Kozuki, and T. Ikemura, "Informatics for unveiling hidden genome signatures", *Genome Res.*, vol. 13, pp. 693-702, 2003.
- [3] T. Abe, H. Sugawara, M. Kinouchi, S. Kanaya, and T. Ikemura, "Novel phylogenetic studies of genomic sequence fragments derived from uncultured microbe mixtures in environmental and clinical samples", *DNA Res.*, vol. 12, pp. 281-290, 2005.
- [4] T. Abe, H. Sugawara, S. Kanaya, and T. Ikemura, "Sequences from almost all prokaryotic, eukaryotic, and viral genomes available could be classified according to genomes on a large-scale Self-Organizing Map constructed with the Earth Simulator", *Journal of the Earth Simulator*, vol. 6, pp.17-23, 2006.
- [5] T. Abe, H. Sugawara, S. Kanaya, and T. Ikemura, "A novel bioinformatics tool for phylogenetic classification of genomic sequence fragments derived from mixed genomes of environmental uncultured microbes", *Polar Bioscience*, vol. 20, pp. 103-112, 2006.
- [6] T. Uchiyama, T. Abe, T. Ikemura, and K. Watanabe, "Substrate-induced gene-expression screening of environmental metagenome libraries for isolation of catabolic genes", *Nature Biotech.*, vol. 23, pp. 88-93, 2005.
- [7] H. Hayashi, T. Abe, M. Sakamoto, H. Ohara, T. Ikemura, K. Sakka, and Y. Benno, "Direct cloning of genes encoding novel xylanases from human gut", *Can. J. Microbiol.*, vol. 51, pp. 251-259, 2005.
- [8] T. Kosaka, S. Kato, T. Shimoyama, S. Ishii, T. Abe, and K. Watanabe, "The genome of *Pelotomaculum thermopropionicum* reveals niche-associated evolution in anaerobic microbiota", *Genome Res.*, 18, pp. 442-448, 2008.
- [9] K. Yasui, M. Tabata, S. Yamada, T. Abe, T. Ikemura, R. Osawa, and T. Suzuki, "Intra-Species Diversity between Seven *Bifidobacterium adolescentis* Strains Identified by Genome-Wide Tiling Array Analysis", *Biosci. Biotechnol. Biochem.*, vol 73, pp. 1422-1424, 2009.
- [10] J. C. Venter, K. Remington, J. F. Heidelberg et al., "Environmental genome shotgun sequencing of the Sargasso Sea", *Science*, vol. 304, pp. 66-74, 2004.
- [11] R. A. Edwards, and F. Rohwer, "Viral metagenomics", *Nature Rev. Microbiol.*, vol 3, pp. 504-510, 2005.
- [12] T. Abe, H. Uehara, S. Kanaya, and T. Ikemura, "A novel bioinformatics strategy for function prediction of poorly-characterized protein genes obtained from metagenome analyses", *DNA Res.*, vol. 16, pp. 469-477, 2009.

地球シミュレータで可能になる大規模なゲノミクスと プロテオミクス研究

プロジェクト責任者

池村 淑道 長浜バイオ大学 バイオサイエンス学部

著者

阿部 貴志 長浜バイオ大学 バイオサイエンス学部

池村 淑道 長浜バイオ大学 バイオサイエンス学部

生命の設計図・シナリオであるゲノムは ATGC の 4 種類の塩基からなり、特徴はその配列長が極めて長いことにある。最近では「次世代シーケンサー」と呼ばれる DNA 配列解読のための革命的とも言われる新実験技術・装置類が登場し、既に 2000 を超える生物種のゲノム配列が解読されており、配列情報のデータベースへの蓄積は爆発的な増加を見せている。ゲノム解読技術の発展は、「メタゲノム解析」と呼ばれる新実験技術を生み、全地球レベルでの生物生態系の把握を目標にした大規模解析も可能になってきた。「メタゲノム解析」とは、環境中に生息する生物群集に由来する、多種類のゲノムの混合物を対象にしたゲノム配列解読である。自然環境で生息する 99% 以上の微生物類は実験室での培養が困難であり、通常の実験的な研究がなされておらず、膨大なゲノム資源が未開拓・未利用に残されてきた。この難培養性微生物類のゲノムは新規な遺伝子を豊富に保有すると考えられ、産業的・医学的にも注目を集めている。環境問題における重要性も明らかとなり、多様な環境由来の混合ゲノム試料を対象にした「大規模メタゲノム解析」が普及しつつある。既に、大量なゲノム断片配列が公的データベースに収録されているが、新規性の高い配列類であることから参照配列がなく「どの系統の生物種に由来するのか」や「どのような機能を有するのか」を、配列相同性検索のような従来法で正確に推定することは不可能である。生物系統やタンパク質機能についての情報なしに、利用価値が低いままに、配列だけがデータベースに収録されている。

我々のグループの場合は、超大量のゲノム配列が解読される時代の到来を予測し、その状況に適した情報解析法を開発してきた。既に特許化した BLSOM（一括学習型自己組織化マップ）は、大量ゲノム情報からの知識発見において、当初予想を遥かに超える優れた能力を持つことが判明した。高度な並列化にも適しており、地球シミュレータを使用して、大規模ゲノム解析を行っている。オリゴヌクレオチド頻度に着目した BLSOM は、メタゲノム解析で得られる大量な断片ゲノム配列について、その由来する生物系統の推定を可能にし、オリゴペプチド頻度に着目した BLSOM は各断片配列にコードされるタンパク質遺伝子の機能推定を可能にした。

キーワード: 自己組織化マップ, 環境微生物, オリゴヌクレオチド頻度, オリゴペプチド頻度, 生物系統推定,
タンパク質機能推定

First-principles Calculation on the Diffusion of Hydrogen along a Screw Dislocation Core in BCC Iron

Project Representative

Hideo Kaburaki

Japan Atomic Energy Agency

Authors

Mitsuhiro Itakura^{*1}, Hideo Kaburaki^{*1}, Masatake Yamaguchi^{*1}, Tomoko Kadoyoshi^{*1},
Atsushi Hiratsuka^{*1}, Kenji Higuchi^{*1}, Shigenobu Ogata^{*2} and Hajime Kimizuka^{*2}

*1 Japan Atomic Energy Agency

*2 Osaka University

The new boundary condition for a single screw dislocation core in BCC iron has been devised to calculate the diffusion of hydrogen using the first principles calculation. It is found that the core structure of a screw dislocation changes drastically by extension due to the presence of high density hydrogen atoms in the core region. Also, we searched the diffusion path of a hydrogen atom from the surrounding trapping lattice site to the core of a screw dislocation, and found that there is the large energy barrier of 0.25eV. We conclude that the diffusion of hydrogen atoms along the core of a screw dislocation is very unlikely to occur in BCC iron.

Keywords: first-principles calculation, screw dislocation, BCC iron, hydrogen atom, diffusion.

1. INTRODUCTION

Hydrogen in metals is known to cause a significant change in mechanical properties of solids, in particular for example, embrittlement [1]. Hydrogen in pure iron materials diffuses easily between neighboring lattice t-sites [2]. The presence of dislocations influences significantly the behavior of hydrogen in metals, because dislocations are the strong trapping sites for hydrogen atoms [3]. It is also believed that diffusion of hydrogen is increased through the core region of dislocations. The understanding of the mechanism of hydrogen embrittlement in metals, which is still elusive at present, depends crucially on the resolution of these processes. However, it is generally difficult to predict experimentally and numerically the interaction of hydrogen atoms with defects in metals, let alone the core structures of a dislocation, in particular, for BCC iron [3, 4, 5]. The difficulty arises from the inadequacy of the dependable empirical potential [6] for use in molecular dynamics simulations, where dynamics of more than a million atoms can be tracked. The first principles calculation based on the density functional theory is the most reliable method for predicting the total energy of the system consisting of a mixture of different atoms. This method is particularly required for the accurate calculation of iron materials and the core region of a dislocation where the arrangement of atoms is largely disordered. However, this method is restricted to clarify the static properties for the system of less than nearly one hundred atoms. Therefore, for the

problem of the interaction of a dislocation core with a hydrogen atom, a lot of effort should be put into the improvement of the boundary condition.

In this paper, we apply the first principles method to the diffusion of hydrogen along the core of a screw dislocation in iron. We also employed the molecular dynamics method with the newly developed Fe-H empirical EAM (embedded atom model) potential [6] to predict the general behavior of the system and to evaluate the differences from the first principles results. A new boundary condition for a single dislocation core has been developed to incorporate at least two unit layers of atoms along the dislocation core for the diffusion of hydrogen. Also, we searched the possible diffusion path from the nearby lattice site into the core and estimated the energy barrier of that path.

2. COMPUTATIONAL METHOD

We have employed the VASP (Vienna *ab-initio* simulation package) code with Projector Augmented Wave (PAW) method [7-9] for the electronic structure calculations and the atomic structure relaxations by force minimizations. The generalized gradient approximation by Perdew, Burke, and Ernzerhof (PBE) is used [10]. All calculations are performed in spin-polarized state. The cutoff energy for the plane wave basis set is 280 eV for Fe systems. The Monkhorst Pack k-point mesh is 1x1x8 for the unit cell as shown in Fig. 1 (b). The Methfessel-Paxton

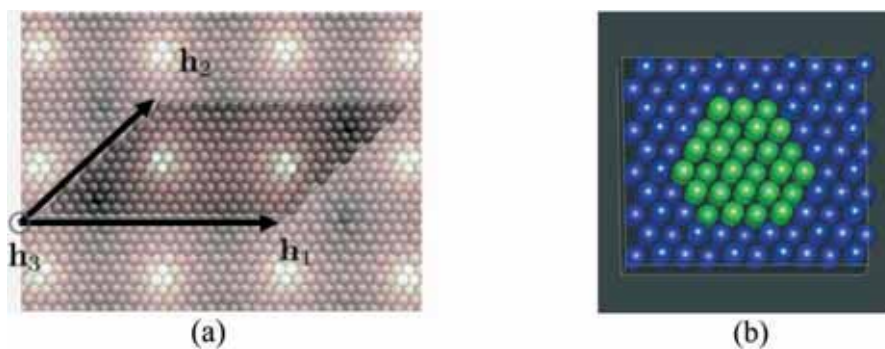


Fig. 1 A system for calculating the core of a screw dislocation.

- (a) The previous system containing a pair of dislocations with one unit layer of atoms.
- (b) The present system containing a single dislocation with two unit layers of atoms.

smearing method with 0.1-eV width is used.

The calculation system is changed from the previous dislocation-dipole arrangement [3,4,5] (Fig. 1(a)) to the single-dislocation arrangement (Fig. 1(b)), for the prediction of diffusion of hydrogen along the dislocation. The previous 231-atom system contains a pair of screw dislocations with the periodic boundary condition and the one unit layer of atoms along the dislocation core. On the other hand, the present 200-atom system contains only one screw dislocation with the surrounding atoms displaced and fixed according to the displacement solution of the elasticity equation for a single screw dislocation. This system contains the two unit layers of the BCC iron crystal along the dislocation core. Although the previous system has the advantage of

canceling the strain field of a dislocation at the boundary, the single dislocation arrangement is employed to enlarge the system along the dislocation with nearly the same number of atoms. The results of the atomic structure relaxation reveal that the atoms on the outer edge are exerted by the artificial forces induced by the mismatch of atomic configurations at the boundaries. However, these artificial forces are shown to decrease on the next line of atoms down to $0.1\text{eV}/\text{\AA}$, so that the boundary effects on the core region are small even with the present size of the system.

3. RESULTS AND DISCUSSION

The effect of the new boundary condition is checked by relaxing the system with a single screw dislocation without

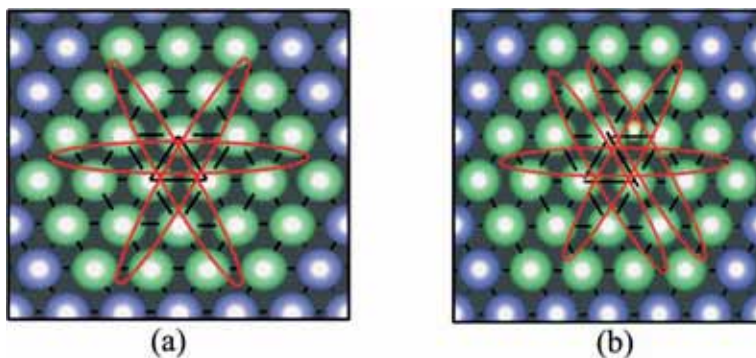


Fig. 2 The relaxed core structure of a screw dislocation without (a) and with one hydrogen atom (b).

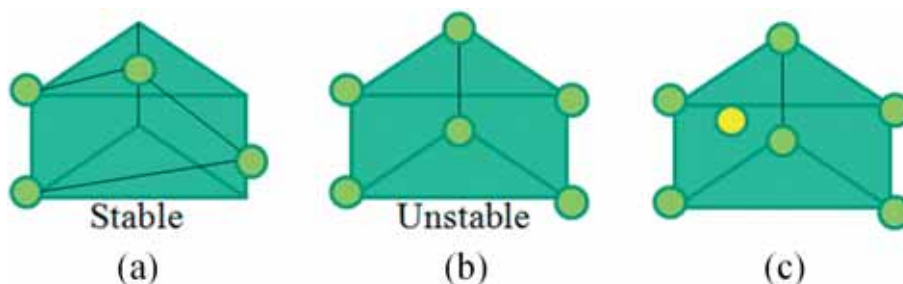
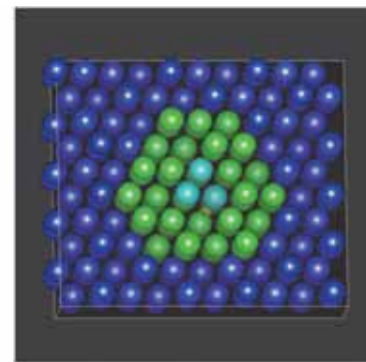


Fig. 3 Atomic configurations of one unit layer for the core region of a screw dislocation.

- (a) Stable core structure for a perfect screw dislocation.
- (b) Unstable structure corresponding to the structure (a).
- (c) The unstable structure is realized when one hydrogen atom is present in the core.

hydrogen. The result shows that the core structure is a symmetric non-degenerate 6-fold structure which is similar to the one obtained in the previous dislocation-dipole arrangement [5]. Next, one hydrogen atom is placed in the core region. It is shown in Fig. 2(b) that the core of a screw dislocation is extended due to the presence of one hydrogen in the system. The atomic configuration of the core of a screw dislocation is shown in Fig. 3(a). The atoms are spirally displaced with one-third of the unit length along the vertical dislocation line. When the hydrogen atom is placed in the core region, the unstable configuration (Fig. 3(b)) is shown to be realized corresponding to the extended structure of Fig. 2(b). This structure is realized because a hydrogen atom prefers an extended space compensating for the high energy unstable iron configuration. It should be emphasized that this result corresponds to the high hydrogen density limit due to the periodic boundary condition in the direction of the dislocation line. Molecular dynamics method is employed to estimate the number of unit layers along the dislocation line, which is required for one hydrogen atom to be isolated. With the system consisting of more than ten unit layers of atoms along the dislocation line, it is found that the dislocation is not extended or the extension is localized to form a kink near the hydrogen atom. The first principles calculation for this system size is intractable at present. However, using the system consisting of the two unit layers, we found in Fig. 4 that, if we fix the z-displacements of three core atoms on the upper and lower boundary surface, the extension of the dislocation core can be prevented to realize the low density limit of hydrogen. The binding energy of hydrogen in the core region is evaluated using the first principles (DFT) calculation and the molecular dynamics method (EAM) as a function of the number of hydrogen atoms per unit layer (Fig. 5). It is seen that the molecular dynamics results overestimate the binding energy systematically compared with the first principles results. However, the trends are found to be very similar. Finally, a

diffusion path of one hydrogen atom from the surrounding trapping lattice site into the core of a screw dislocation is searched firstly by the molecular dynamics method (Fig. 6). When the diffusion path is found, the first principles method is employed to evaluate quantitatively the energy barrier along this path. As shown in Fig. 6, it is found that there is a large energy barrier of 0.25eV from the trapping lattice site into the core of a screw dislocation. Once a hydrogen atom is in the core, the energy barrier along the dislocation core is approximately 0.04eV. However, this in-core state is found to be unstable and the temperature of 50K is sufficient for a hydrogen atom to be easily emitted back to the lattice site. Therefore, it is concluded that the diffusion inside the core region of a screw dislocation in BCC iron is unlikely to occur.



Z \odot

Fig. 4 The boundary condition to realize the low hydrogen density limit by preventing the extension of the core. (The dislocation line is in the z-direction.)

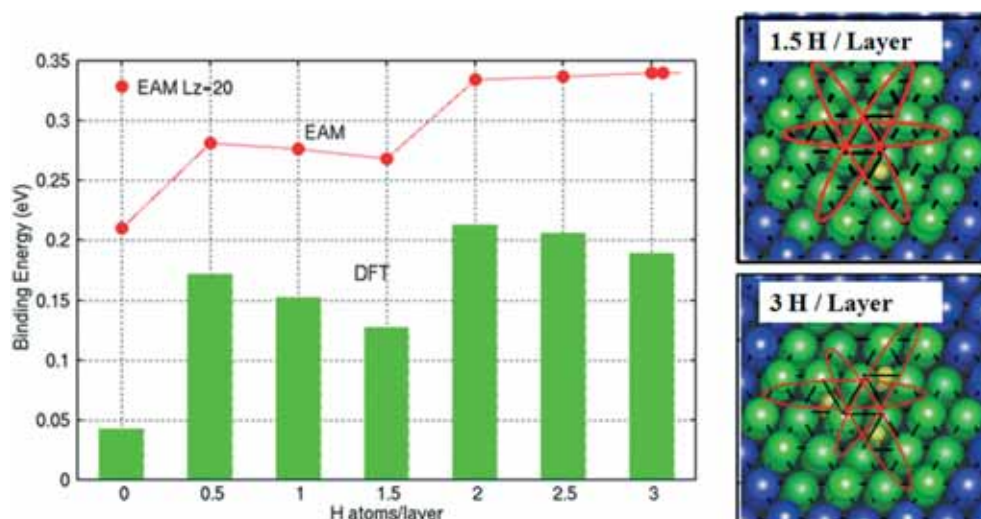


Fig. 5 The binding energy of hydrogen as a function of the number of hydrogen atoms per unit layer.

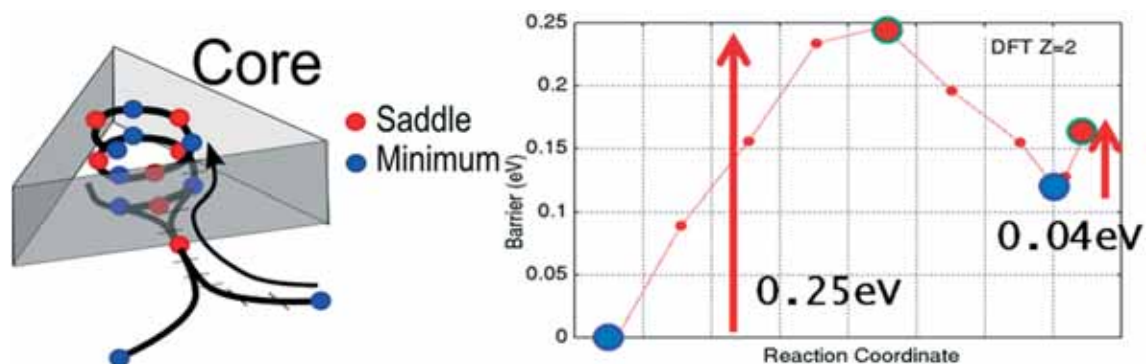


Fig. 6 A diffusion path and its energy landscape from the trapping lattice site to the core of a screw dislocation.

References

- [1] C.J.McMahon Jr., Eng.Frac.Mech. 68,773-788(2001).
- [2] D.E.Jiang and E.A.Carter, Phys.Rev.B70, 064102(2004).
- [3] M.Itakura, H.Kaburaki, M.Yamaguchi, T.Kadoyoshi, F.Shimizu, A.Hiratsuka, S.Ogata, H.Kimizuka, Annual Report of the Earth Simulator Center (Apr.2008-Sept.2008), 213(2008).
- [4] F.Shimizu, S.Ogata, H.Kimizuka, T.Kano, J.Li, and H.Kaburaki, Journ.Earth Simulator, Vol.7, 17-21 (2007).
- [5] F.Shimizu,S.Ogata,M.Yamaguchi,T.Kano,H.Kimizuka,M.Itakura,H.Kaburaki, Annual Report of the Earth Simulator Center, p.235-239 (April 2006-March 2007).
- [6] A.Ramasubramaniam, M.Itakura, E.A.Carter, Phys.Rev. B79, 174101(2009).
- [7] G. Kresse and J. Hafner, Phys. Rev. B47(1993)558.
- [8] G. Kresse and J. Furthmuller, Phys. Rev. B54 (1996)11169.
- [9] G. Kresse and D. Joubert, Phys. Rev. B59(1999)1758.
- [10] J.P. Perdew, K. Burke, and M. Ernzerhof, Phys. Rev. Lett. 77(1996)3865.

第一原理計算による BCC 鉄中らせん転位芯への水素拡散経路

プロジェクト責任者

蕪木 英雄 日本原子力研究開発機構

著者

板倉 充洋^{*1}, 蕪木 英雄^{*1}, 山口 正剛^{*1}, 門吉 朋子^{*1}, 平塚 篤^{*1}, 樋口 健二^{*1},
尾方 成信^{*2}, 君塚 肇^{*2}

*1 日本原子力研究開発機構

*2 大阪大学

第一原理計算により BCC 鉄中の一本のらせん転位芯への水素の拡散経路を調べるために新しい境界条件を提案した。この境界条件を用いて転位芯に水素を一個入れると転位芯は大きく変化して拡張することが分かった。更に転位周囲の水素の捕獲格子サイトから転位芯への拡散経路を見出し、この経路には 0.25eV の大きなエネルギー障壁があることが明らかになった。この結果 BCC 鉄中の転位芯に沿った水素の拡散は起こりにくいことが明らかになった。

キーワード: 第一原理計算, らせん転位, BCC 鉄, 水素原子, 拡散経路

Numerical Simulation of Turbulent Sodium Flows in Subchannels of an LMFBR Fuel Subassembly

Project Representative

Hisashi Ninokata

Research Laboratory for Nuclear Reactors, Tokyo Institute of Technology

Authors

Elia Merzari

Research Laboratory for Nuclear Reactors, Tokyo Institute of Technology

Hisashi Ninokata

Research Laboratory for Nuclear Reactors, Tokyo Institute of Technology

Isothermal and non-isothermal LES (Large Eddy Simulation) has been carried out to fully reproduce the characteristics of the flow field in eccentric annular channels, and rod bundles. The numerical approach is based upon boundary fitted coordinates and a fractional step algorithm; a dynamic Sub Grid Scale (SGS) model suited for this numerical environment has been implemented and tested for both isothermal and buoyancy driven flows inside annular channels with different eccentricities. The agreement with experiment and DNS/LES results has been found good in both isothermal and buoyancy driven flows in annulus channels. Instantaneous flow field presented large scale coherent structures in the streamwise direction at low Reynolds numbers, while these are absent or less dominant at higher Reynolds, thus reproducing successfully the global pulsation phenomena in tight lattice rod bundles of LMFBRs.

Keywords: LES, Eccentric channel, Advanced Nuclear Systems, Tight Lattice, Global Pulsation

1. Introduction

In this work extensive calculations have been carried out for the eccentric annulus channel flows as a simplified geometry in connection to the turbulent flows in tight lattice nuclear fuel pin subassemblies. As a first step the LES results have been verified *a priori* and *a posteriori* in annular channels against DNS data and experimental data to ensure the consistency of the formulation. Then LES has been extensively applied to several eccentric annular channel configurations and confirmed the presence of large-scale coherent structures near the narrow gap. There, the influences of the anisotropic turbulence structure and eddy migration behaviors in the non-uniform flow channels have been investigated in detail. As a last step the methodology has been extended to rod-bundles, where the same oscillations have been observed.

2. Methodology

In previous research several DNS computations have been performed for the concentric and eccentric channels. The data collected has been used to evaluate different SGS model in order to develop an effective LES methodology in boundary fitted coordinates. Several other models have been tested, among which the dynamic mixed model, the self-similarity model and another variant of the dynamic model [3]. Figure 1 shows an example of a *a priori* test. The dynamic model and its variant performed fairly well from the point of view of a *a priori* and a

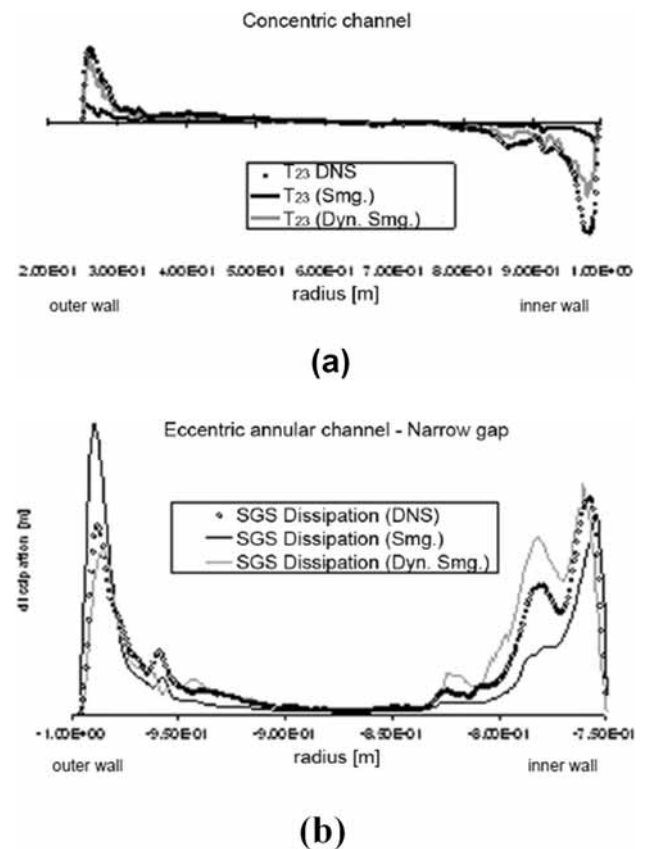


Fig. 1 A priori test for concentric and eccentric channels. Direct comparison for the stresses (a) and comparison for the SGS dissipation (b).

a posteriori tests. They may be considered the ideal choice for the simulation of the flow in annular channels and rod-bundles.

The algorithm used to solve the Navier-Stokes equations coupled with the energy equation is based on the Fractional Step Algorithm on a partially non-staggered grid [4]. The equations have been discretized through a second order consistent scheme [5] and time advancement has been carried out through an Adams-Bashfort scheme. The Poisson equation for the pressure gauge has been solved with either:

1. An FFT solver (since periodic boundary conditions have been employed in the streamwise direction) for eccentric channels; or
2. A multiblock solver [6] for the rod bundles.

The multiblock solver uses non-overlapping domain decompositions. The domain is divided into a set of non overlapping structured grids. The algorithms employed by the solver are the Conjugatete Gradient Squared CGS and Bi-Conjugate Gradient [7]. A two-level preconditioning (block-level and upper level) has been adopted [8]. Alternatively, for large scale calculations a geometric multi-grid preconditioning has also been implemented.

3. Results for eccentric channels

An extensive LES computational campaign has been performed for the eccentric channel at various Reynolds

numbers and the eccentricity to investigate the characteristics of the flow in eccentric channels. Some of the cases run are reported in Table 1 for different values of the geometric parameters D_h (hydraulic diameter), $\alpha = D_{in}/D_{out}$ and $e = d/(D_{out} - D_{in})$ where D_{in} and D_{out} are the inner and outer diameters and d is the distance between the axis of the two cylinders. The computation of some of the cases took a considerable amount of time since all scales of turbulence above the inertial range need to be simulated, the DNS case used to validate the LES model a priori required almost 0.2 billion meshes.

The results of the simulations A, C and D have been validated for available DNS and experimental data [9, 10, 11]. Important aspects of the flow field in concentric and eccentric annuli have been confirmed and reproduced through the present methodology [12]. In particular, the effect of transverse curvature on the inner wall, as well as the effect of eccentricity on the wall shear stress, has been successfully simulated.

From previous works it appears that the transition to turbulence in geometry such as the eccentric annuli [12] is accompanied by the formation of a street of counter-rotating vortices in the region near the narrow gap. These coherent structures persist at low Reynolds numbers but they progressively become less dominant, at least for an eccentricity equal to 0.5, as the Reynolds number increases.

Contemporarily, in the narrow gap the local profile of the

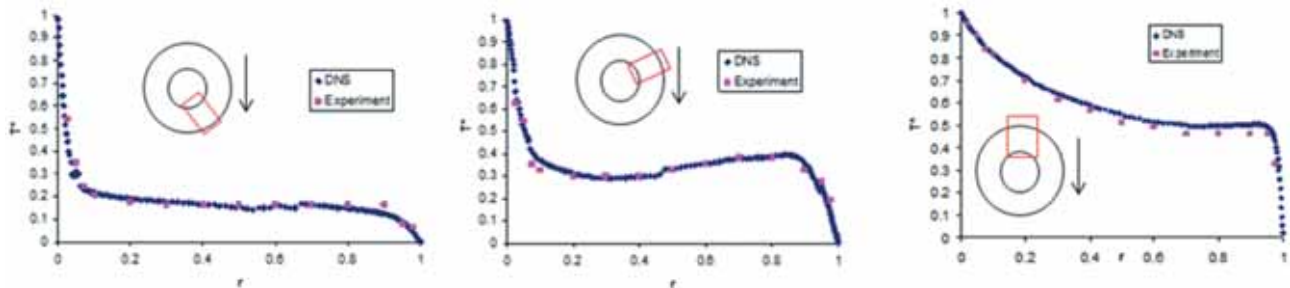


Fig. 2 Radial temperature distributions at different angle positions in the concentric annulus: comparisons of DNS and experiment.

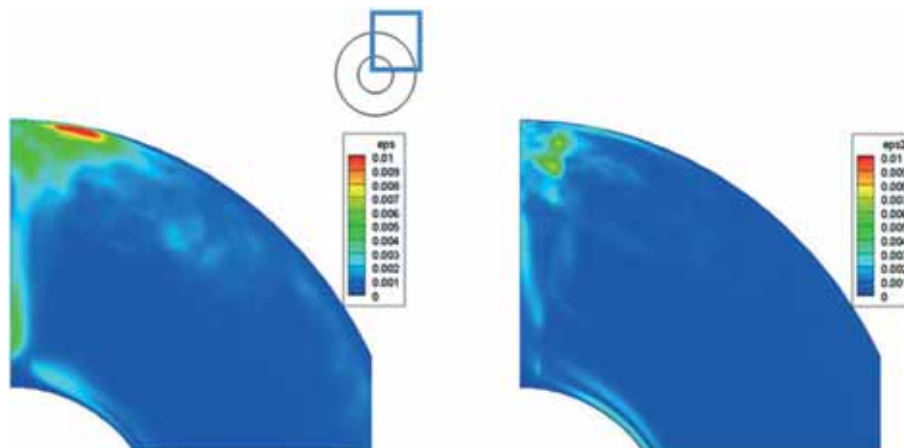


Fig. 3 SGS dissipation: DNS filtered (left) and Dynamic Smagorinsky (right).

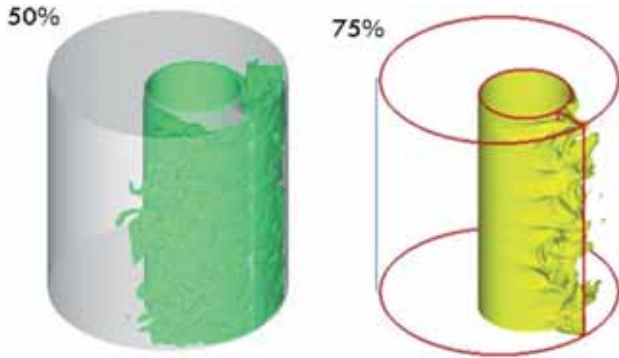


Fig. 4 Normalized temperature ($T^* = (T - T_{out}) / (T_{out} - T_{in})$) contours in an eccentric channel: $T^* = 0.5$ (left) and $T^* = 0.75$ (right).

streamwise velocity evolves from a purely laminar solution to a solution characterized by the presence of turbulence production near walls. The shear stress in the narrow gap region evolves from an almost laminar condition for a Reynolds number equal to 3,200 to an increasingly turbulent solution [12].

At low Reynolds number and eccentricity equal to 0.5 the relative dominance of the coherent structures is associated with a strong anisotropy in the narrow gap (turbulence has a local two-component pattern), while at higher Reynolds numbers a nearly isotropic condition is recovered far from the walls. At higher eccentricity ($e = 0.95$) the coherent structures are absent in the narrow gap region, accounting for a strong viscous damping effect in the case of almost touching channels. When Reynolds averaging is performing over the flow field, secondary vortices are observed in the cross section.

For non-isothermal flows of $Pr = 0.71$ and $Ra = 2,160,000$, in a concentric annulus channel with $D_{in}/D_{out} = 0.6$, the mesh sizes are chosen to be of the order of the Kolmogorov length scale. A total of 32 million meshes are employed to calculate velocity and temperature distributions inside the annulus. Figure 2 shows comparisons of time-averaged and normalized temperature distributions at different angles to demonstrate good agreement with experiment. In the SGS modeling of the energy equation, filtering introduces a source term which could be approximated by the additional variables to be proportional to the temperature gradient with the turbulent viscosity given by the SGS model and turbulent Prandtl number. Figure 3 compares the time average over 5 time steps ($= 0.0025s$) of

the DNS filtered dissipation with the LES with Dynamic Smagorinsky. Total number of meshes in the LES is about one million (1/30 of the DNS case). The agreement is found less satisfactory but still acceptable in the sense that the distributions are similar. This indicates the Smagorinsky model fails if no damping is employed. However the averaged stresses τ_{12} are found remarkably in good agreement between LES and DNS. We have also examined the alignment between the SGS source term introduced and the temperature gradient. There we find that the alignment is not particularly good, especially in the plume region where the stresses are more irregular. Figure 4 shows snapshots of temperature contours in the case where the narrow gap is on the upper side. It is shown the plume hits the upper wall resulting in high value of variance near the outer wall and stronger temperature fluctuations are generated even near the bottom of the outer wall. Assessment of the SGS modeling is still on-going and more computational results are being examined for eccentric annulus channels.

4. Results for rod bundles of LMFBRs

As a preliminary work we have performed the large eddy simulation of the flow in two-subchannels connected by a narrow gap for an infinite triangular lattice rod bundles, typical of fuel subassembly of sodium-cooled LMFBRs, with periodic boundary conditions in the cross section and in the streamwise direction. Figure 5 (a) streamlines and (b) contour plot for the cross flow velocity are a result of LES for a low Reynolds number turbulent flow ($Re = 5,500$) in a tight lattice rod bundle with $P/D = 1.05$ where P is the pin pitch and D is the rod diameter. The rectangles in (b) represent the regions where coherent structures can be clearly identified. The values are normalized by the 0.1 times the bulk velocity in the axial direction. The vector plot of the horizontal flow components shows a vortex positioned near the gap driving the cross flow between the two subchannels, thus mimicking the same phenomenon described previously for eccentric channels and other related geometries ([2]). The cross velocity has a sinusoidal behavior (Fig. 6) that is consistent with the principal mode of turbulence. This oscillatory behavior is called global flow pulsation and has been successfully reproduced by LES.

Table 1 LES and DNS cases.

	e	α	p/D	Re	Grid $N_\zeta - N_\eta - N_\xi$	L/D	Meshes	Time [wks]	CPUs
Case A	0.5	0.5	–	3200	256-64-256	4π	4×10^6	8	8
Case B	0.5	0.5	–	26600	768-300-768	2π	0.18×10^9	52	128
Case C	0.5	0.5	–	27100	512-300-512	2π	7.8×10^7	24	128
Case D	0.95	0.5	–	8700	256-64-128	2π	2×10^6	8	8
Case E	–	–	1.05	6800	(12 ξ) 72-42-256	4π	0.9×10^7	16	32
Case F	–	–	1.05	20200	(12 ξ) 152-99-512	4π	9.2×10^7	24	128

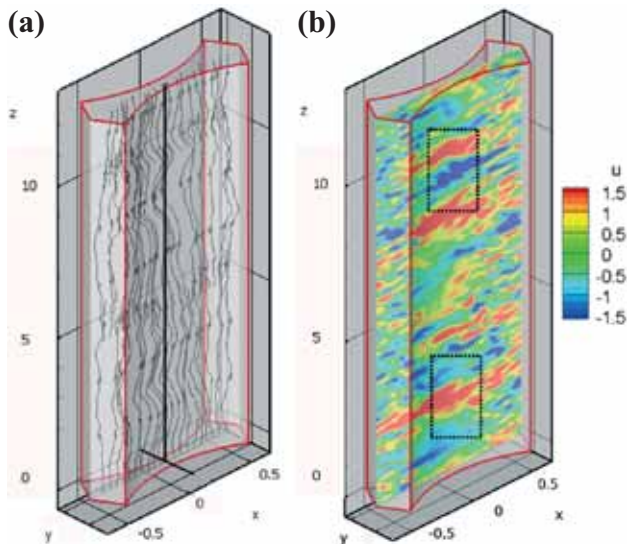


Fig. 5 (a) Streamlines (b) Contour plot for the instantaneous cross flow velocity in an infinite triangular lattice rod bundle $P/D=1.05$, $Re=5,500$.

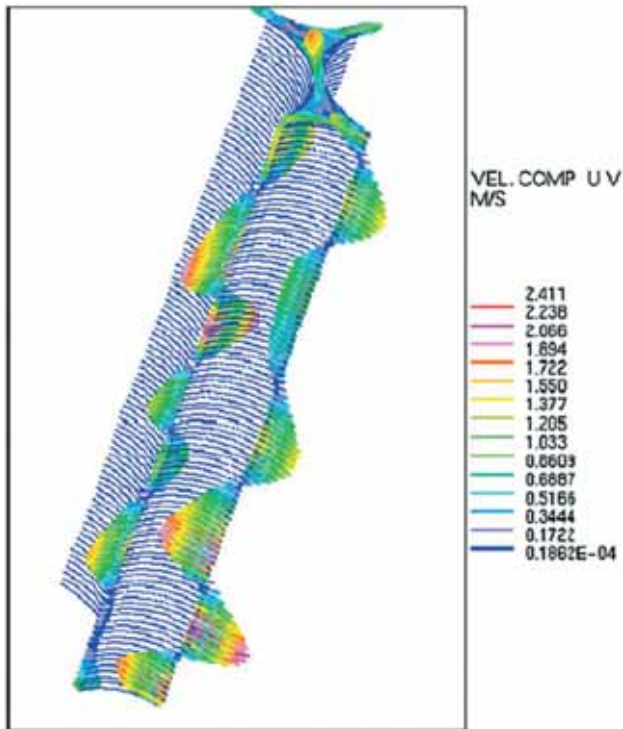


Fig. 6 Flow oscillation between subchannels and cross flow velocity components.

5. Conclusions

A LES code has been developed on the boundary fitted coordinates, with multi-block domain decomposition and a Dynamic SGS model for the isothermal and non-isothermal flows in complex geometries, suitable for the simulation of fuel bundles and annular channels. When applied to rod bundles, the code has reproduced successfully the turbulent flow features, i.e., presence of secondary flows and the global flow pulsations common to both in annular channels and in tight lattice rod-bundles.

References

- [1] S.A. Jordan., "A Large Eddy simulation methodology in generalized curvilinear coordinates", *Journal of Computational Physics*, **Vol. 148**, pp. 322-340 (1999).
- [2] S.A. Jordan., "Dynamic Subgrid-Scale Modeling for Large-Eddy Simulations in Complex Topologies", *Journal of Fluids Engineering*, **Vol. 123**, 3, pp. 619-627 (2001).
- [3] E. Merzari and H. Ninokata., "Test of LES SGS models for the flow in annular channels", *Proceedings of ICAPP 2007*, Nice, France, 13-18 May 2007.
- [4] Y. Zang, R.L. Street, J.R. Koseff, "A non-staggered grid, fractional step method for time-dependent incompressible Navier-Stokes equations in curvilinear coordinates", *Journal of Computational Physics*, **Vol. 114**, p. 1 (1994).
- [5] T. Suzuki and N. Kawamura., "Consistency of Finite – Difference Scheme in Direct Simulation of Turbulence", *Trans. JSME*, **Vol. 60**, pp. 578 (1994). (in Japanese).
- [6] T.F. Chan and T.P. Mathew, "Domain Decomposition Algorithms", *Acta Numerica*, pp. 61-143 (1994).
- [7] D.R. Fokkema, G.L. Sleijpen, and H.A. Van der Vorst, "Generalized Conjugate Gradient Square", *Journal of Computational and Applied Mathematics* (1996).
- [8] S.H. Lee, P. Jenny, and H.A. Tchelepi, "A finite-volume method with hexahedral multiblock grids for modeling flows in porous media", *Computational Geo-science*, **Vol. 6**, pp. 353-379 (2002).
- [9] N.V. Nikitin., "Direct Numerical Simulation of turbulent flows in eccentric pipes", *Computational Mathematics and Mathematical Physics*, **Vol. 46**, pp. 509-526 (2006).
- [10] J.M. Nouri, H. Umur, and J.H. Whitelaw., "Flow of Newtonian and non-Newtonian fluids in concentric and eccentric annuli", *Journal of Fluid Mechanics*, **vol. 253**, pp. 617-64, (1993).
- [11] S.Y. Chung, G.H. Rhee, and H. Sung, "Direct numerical simulation of turbulent concentric annular pipe flow Part 1: Flow field", *International Journal of Heat and Fluid Flow*, **vol. 23**, pp. 426-440, (2002).
- [12] E. Merzari and H. Ninokata, "Anisotropy and Coherent Structures for the flow in Annular Channels", *Flow, Turbulence and Combustion*, DOI: 10.1007/s10494-008-9170-2 (2009).

高速増殖炉燃料集合体サブチャンネル内ナトリウム冷却材の乱流シミュレーション

プロジェクト責任者

二ノ方 寿 東京工業大学 原子炉工学研究所

著者

Elia Merzari 東京工業大学 原子炉工学研究所

二ノ方 寿 東京工業大学 原子炉工学研究所

本研究の目的は、流路チャンネルが複雑で実験計測上取得困難な詳細な流速分布、乱流特性などを高い信頼性の裏づけをもった直接乱流シミュレーション (DNS) および大渦シミュレーション (LES) によって提供し、現象の解明を実施するとともに現象の機構論的なモデル化を行って高速増殖炉などの集合体設計および原子炉安全性評価に必要な乱流熱流動データベースの構築に資するとともに工学的な応用に有効に活用することである。

複雑形状流路の典型である高速炉または低減速型軽水炉炉心における稠密格子配列型燃料集合体サブチャンネル内の乱流構造の Re 数依存性や配列格子のピッチ対燃料直径比に対する依存性は現象論的に極めて複雑である。その現象解明を行うには計算科学的手法が唯一の手段と考えられる。稠密格子燃料集合体内サブチャンネル内の乱流は、燃料要素間隔が狭いために壁の影響を強く受け、非等方性が強い。一般的に燃料集合体内の乱流は、 P/D の減少および Re 数が低くなると燃料間隙部近傍でその非均質性が増すとともに、局所的な乱流 - 層流遷移領域を含み、流れそのものが不安定となることが予測される。

本稿は、境界適合型座標系上の LES を用いた二重円環流路内流路において浮力が卓越する自然循環支配の流れ場に対する SGS モデルの検討と、DNS との比較においてモデルの妥当性を評価するとともに偏心二重円環流路内に生じる複雑な流れ場の解析の報告である。高速増殖炉の稠密格子燃料集合体内流路における乱流挙動との類似性に着目して実施した二重円環流路内乱流の解析結果に基づき、これまでに得られている直接乱流シミュレーション結果および実験データと比較して十分な精度で一致していることの確認を行うとともに、流路形状の非一様性から生じる二次流れによって輸送される乱流渦の動的な挙動と主流方向における大局的な流れとの相互作用、これらの流路形状と Re 数依存性の解明に関する報告である。とくに低 Re 数条件下では、燃料集合体内の燃料と燃料との間の狭隘ギャップ部における層流と乱流の遷移現象、軸方向スパンに見た大局的な乱流場におけるコヒーレントな振動モードを示すグローバルパルセーション現象を同定することができた。

キーワード: LES, 偏心二重円環流路, 新型原子炉, 稠密格子, グローバルパルセーション

Analysis of Mutation Mechanisms of Influenza Virus Based on the Fragment Molecular Orbital Method

Project Representative

Shigenori Tanaka

Graduate School of System Informatics, Kobe University

Authors

Shigenori Tanaka

Graduate School of System Informatics, Kobe University

Yuji Mochizuki

Department of Chemistry, Rikkyo University

Kaori Fukuzawa

Mizuho Information and Research Institute, Inc.

Katsumi Yamashita

NEC Soft, Ltd.

Tatsuya Nakano

National Institute of Health Sciences

On the basis of the fragment molecular orbital (FMO) method, we performed the FMO-MP2 and FMO-MP3 electronic-state calculations on the Earth Simulator (ES2) for a protein complex consisting of HA (hemagglutinin) trimer and two Fab fragments and a complex of NA (neuraminidase) and oseltamivir inhibitor of influenza virus. The FMO-MP2/6-31G jobs were completed in 0.8 hours for the HA monomer and in 4.3 hours for the HA trimer with 128 nodes (1024 VPUs) of ES2. Comparison of these timings illuminates the low scaling nature of the present FMO calculations. In addition, the increase rate of computational cost by MP3 compared to MP2 is significantly low. In particular, the FMO-MP3 calculation for the HA trimer, which might be the world's largest target system (36160 atoms) for correlated all-electron calculations to date, was completed in only 5.8 hours with 128 nodes. In the case of NA-oseltamivir, a favorable performance of FMO-MP3 calculation was obtained as well. Thus, a realistic applicability of FMO-MP3 calculations to large-scale proteins has been demonstrated with the ES2 system. Molecular interaction analyses based on the FMO results were then carried out for the prediction of probable mutations in influenza proteins associated with the escape from antibody pressure and the resistance against drugs.

Keywords: FMO (fragment molecular orbital) method, MP (Moeller-Plesset) perturbation theory, influenza virus, HA (hemagglutinin), NA (neuraminidase)

1. Introduction

Influenza is one of the most important infectious diseases of humans. Recent concerns about the avian and swine influenza viruses highlight its threat and the need to understand its evolutionary dynamics. The influenza virus has a remarkable ability to escape host defense mechanisms by altering its binding characters through changes of amino acid residues in the pertinent proteins. This property is referred to as antigenic drift and has been thought to result from the accumulation of a series of amino acid changes in antigenically important regions of proteins. In addition, the viral resistance against some drugs is associated with analogous mutation properties as well. It is thus essential to elucidate the molecular mechanisms by which viruses alter their ligand binding characters in order to find an efficient way to suppress the pandemics and epidemics of influenza.

There are two types of well-known proteins on the surface of influenza virus. One is hemagglutinin (HA) associated with the infection into host cells. Another is neuraminidase (NA)

involved in the escape from infected cells. To investigate the interactions between these proteins and their binding partners at the molecular level, we need to resort to some theoretical methods in computational chemistry. Considering the accuracy in molecular simulations, ab initio quantum-chemical approaches would be most dependable for the computational analysis on molecular interactions, whereas these kinds of simulations would demand huge amount of computer resources for biomolecular systems. Here, we employ the fragment molecular orbital (FMO) method [1], which has been developed for efficient and accurate ab initio calculations for biomolecules, for the detailed analysis of molecular interactions in HA and NA systems. In this context, we pay attention to the inclusion of electron correlation effects in terms of Moeller-Plesset (MP) type perturbative treatments in order to appropriately describe the weak interactions such as dispersion forces between hydrophobic residues.

In 2008, we performed [2] the FMO-MP2/6-31G calculation for an antigen-antibody system consisting of the HA monomer

and the Fab fragment (14086 atoms, 921 residues and 78390 AOs), where a total of 4096 vector processors (VPUs) of the Earth Simulator (ES) were utilized to complete the job within an hour. Later, the calculation with the extended 6-31G* basis set (121314 AOs) was carried out on cluster computers, and some specific residues associated with probable mutations were successfully identified through the IFIE (inter-fragment interaction energy) analysis, thus providing a method to predict the forthcoming mutations in HA [3].

Although the second-order MP2 calculations have become feasible even for large proteins in conjunction with the FMO scheme, there has been a potential demand for correlated methods better than MP2. The third-order MP (MP3) theory can be a straightforward option by the perturbative inclusion of electron pair-pair interactions. Here, we employ a parallelized integral-direct implementation of FMO-MP3 scheme in ABINIT-MPX software. The OpenMP shared-memory parallelization is also introduced for the intra-fragment calculations of monomers and dimers at the lower level processing. The Earth Simulator, which was renewed in 2009 as ES2, was used as a massively parallel-vector computational platform, in which some technical points for the vectorization were addressed [4].

Table 1 Timing data for HA monomer, HA trimer and NA systems. The timing shown here is the turn-around job time in hours. Each node with eight VPUs was assigned to the intra-fragment calculations with OpenMP. The 64 node jobs were processed during the usual production run hours, whereas the 128 node jobs were performed under a dedicated usage with special permission. The 6-31G basis set was used throughout, except for the cases of HA monomer and NA with the asterisk (*) meaning the use of the 6-31G* basis set.

(System) Calc. level	Nodes	Time (hour)	Rel. ^a	Acc. ^b	TFLOPS
(HA monomer)					
FMO-MP2	64	1.7			0.97
FMO-MP3	64	2.7	1.6		2.27
FMO-MP2*	64	4.4			1.19
FMO-MP3*	64	8.7	2.0		3.02
FMO-MP2	128	0.8		2.1	2.06
FMO-MP3	128	1.3	1.6	2.1	4.67
(HA trimer)					
FMO-MP2	64	9.4			0.83
FMO-MP3	64	11.9	1.3		1.66
FMO-MP2	128	4.3		2.2	1.83
FMO-MP3	128	5.8	1.3	2.1	3.44
(NA)					
FMO-MP3	64	1.0			3.04
FMO-MP3*	64	4.4			3.09

^aCost factor of MP3 job relative to MP2 job.

^bAcceleration due to the increase of VPUs from 512 to 1024.

2. Results

In the present study, we performed [4] the FMO-MP2 and FMO-MP3 calculations with the 6-31G or 6-31G* basis set for a complex consisting of HA trimer and two Fab fragments (2351 residues and 201276 AOs; PDB-ID: 1KEN) and a complex of NA and oseltamivir ligand (386 residues; PDB-ID: 2HU4) on the ES2. The modeling of the complex structures was performed with the aid of MOE software, in which the addition and structural optimization of hydrogen atoms were carried out. Table 1 compiles the timing data of benchmark calculations of HA and NA systems by using 64 nodes (total 512 VPUs) and 128 nodes (1024 VPUs) of ES2. The FMO-MP2 jobs were processed in 0.8 hours (48.3 minutes) for the HA monomer and in 4.3 hours (260.6 minutes) for the HA trimer with 128 nodes. Comparison of these timings illuminates the low scaling nature of the present FMO calculations. The acceleration from 64 to 128 nodes was slightly over 2, presumably due to the difference in background conditions. Nevertheless, a value close to 2 was expected because of an inherent parallelism of the FMO calculations. It is remarkable that the increase rate of computational cost by MP3 compared to MP2 is quite low. In particular, the FMO-MP3 calculation for the HA trimer, which might be the world's largest target system (36160 atoms) for correlated all-electron calculations to date, was completed in only 5.8 hours with 128 nodes. In the case of NA-oseltamivir, a favorable performance of FMO-MP3 calculation was obtained as well. As a whole, a realistic applicability of FMO-MP3 calculations to large-scale proteins has just been demonstrated with the ES2 system, while further improvements in the ABINIT-MPX code would still be required for better efficiency.

Figure 1 (a) shows the structure of HA trimer complexed with two Fab fragments. From the top view (b) of Fig. 1, it is observed that a hollow structure is formed by the bundled monomers (labeled with roman numbers and colors) and

Table 2 IFIE results (in units of kcal/mol) for pairs of monomeric domains in HA trimer complex obtained by the Hartree-Fock (HF), MP2 and MP3 level FMO calculations with the 6-31G basis set.

	HF	MP2	MP3
HA(I)-HA(II)	-1022.4	-1280.3	-1237.1
HA(II)-HA(III)	-981.7	-1245.7	-1200.7
HA(I)-HA(III)	-1189.0	-1469.9	-1421.3
Fab(I)-HA(I)	-288.8	-367.0	-352.8
Fab(I)-HA(II)	177.5	155.6	158.7
Fab(I)-HA(III)	134.3	134.2	134.3
Fab(II)-HA(I)	137.0	137.0	137.0
Fab(II)-HA(II)	-292.7	-380.5	-363.7
Fab(II)-HA(III)	170.8	157.0	159.5
Fab(I)-Fab(II)	210.8	197.8	199.6
HA(sum)-Fab(sum)	38.1	-163.6	-127.0

also that the Fab fragment is situated in contact with plural monomers. Figure 2 then illustrates the results of IFIEs calculated at the FMO-MP3/6-31G level for the complex consisting of the HA trimer and two Fab fragments. The interactions between the yellow domain and each colored residue are depicted in the figures, where the red and blue correspond to the attractive and repulsive interactions, respectively. On the basis of the evaluated interactions with the Fab fragment antibody, as shown in Fig. 2 (a) and (b), it would be possible [3] to enumerate those residues (identified with deep-red) in HA that have a high probability of forthcoming mutations to escape from antibody pressure. This information about the probable mutations in HA would, in turn, facilitate the development of effective vaccines against influenza viruses. Figure 2 (c) represents the IFIEs between the HA monomer (II) and other amino acid residues in the complex. Such analyses should be useful for the comprehensive understanding of the specific roles played by various domains in the complex. For instance, we can discuss the inter-domain interactions by partially summing up the IFIE values. Table 2 then shows the interaction energies between various monomeric domains (see Fig. 1). Interestingly, there are clear differences among the Hartree-Fock (HF), MP2 and MP3 values for the pairs of attractively contacted domains,

e.g. HA(I)–HA(II), being in contrast to the cases of repulsive pair. Pitonak et al. [5] pointed out that the MP3 correction could reduce the tendency of over stabilization at the MP2 level, and the numerical results in Table 2 are consistent with this indication. It is noteworthy that the inter-domain interactions break the symmetries and also that the attractive and repulsive interactions are balanced in a delicate way in the antigen-antibody complex. More detailed analyses concerning the biochemical functions based on interaction patterns have to be carried out for the HA trimer system.

The IFIE analysis between each residue of NA and the oseltamivir inhibitor was also performed [4] with the FMO-MP3/6-31G* calculation. The results are visualized in Fig. 3. The energetically stabilized residues would play key roles in recognizing oseltamivir, and therefore mutations at these residues could reduce the binding affinity. Such mutations have potential to yield the emergence of oseltamivir-resistant viruses. In contrast, the rational drug design to alter repulsive (blue) interactions to attractive (red) interactions could make up better inhibitors with high binding affinities, which would be more effective against the drug-resistant viruses. Figure 4 illustrates a set of attractive interactions between oseltamivir and surrounding residues in the pharmacophore. These stabilizations

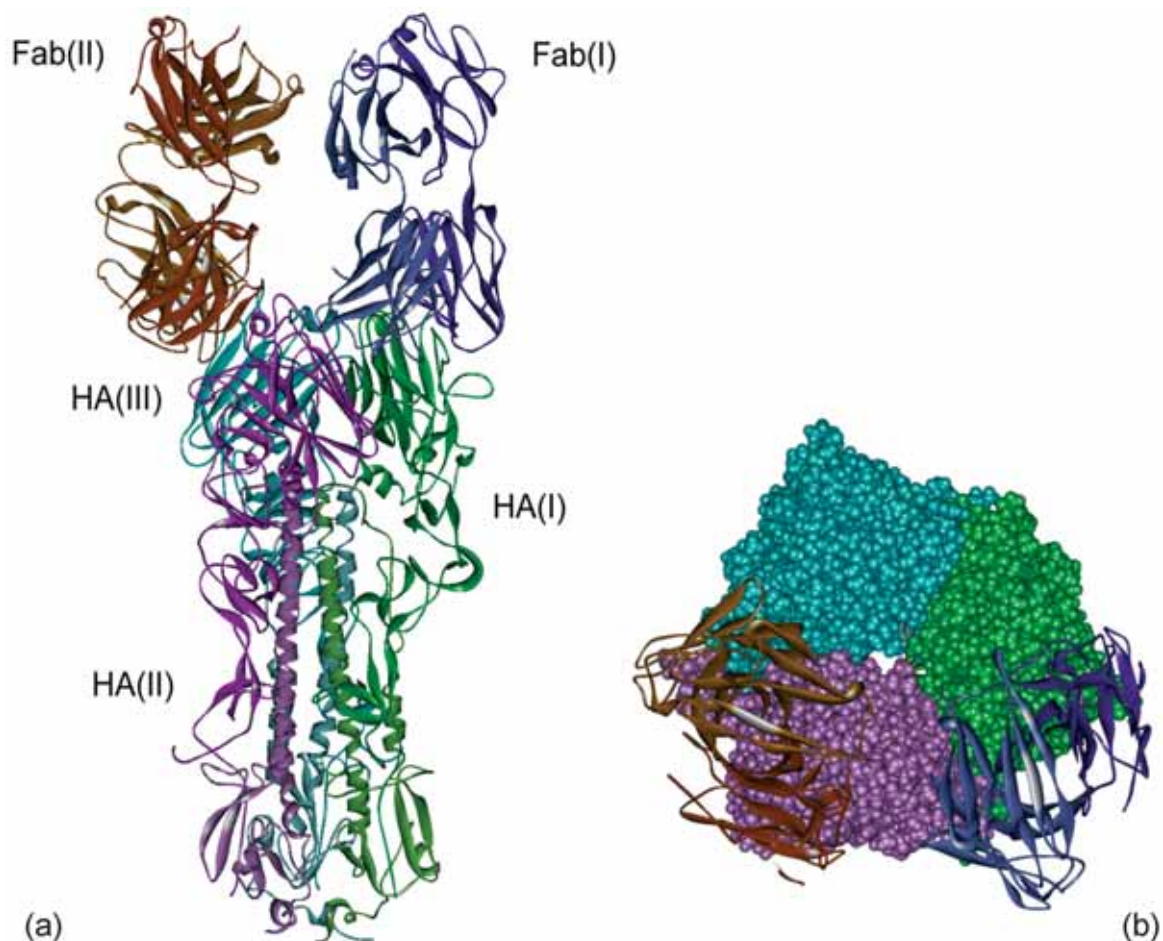


Fig. 1 Graphic representations of the influenza HA trimer with two Fab fragments: (a) side view, (b) top view. Each monomeric domain is identified with roman numbers and colors.

could be characterized by the electrostatic and hydrogen-bond interactions with Glu119, Asp151, Arg152, Arg292, Arg371 and Tyr347. These theoretical analyses could be helpful in revealing the oseltamivir-resistant mechanism and also in developing the effective inhibitors.

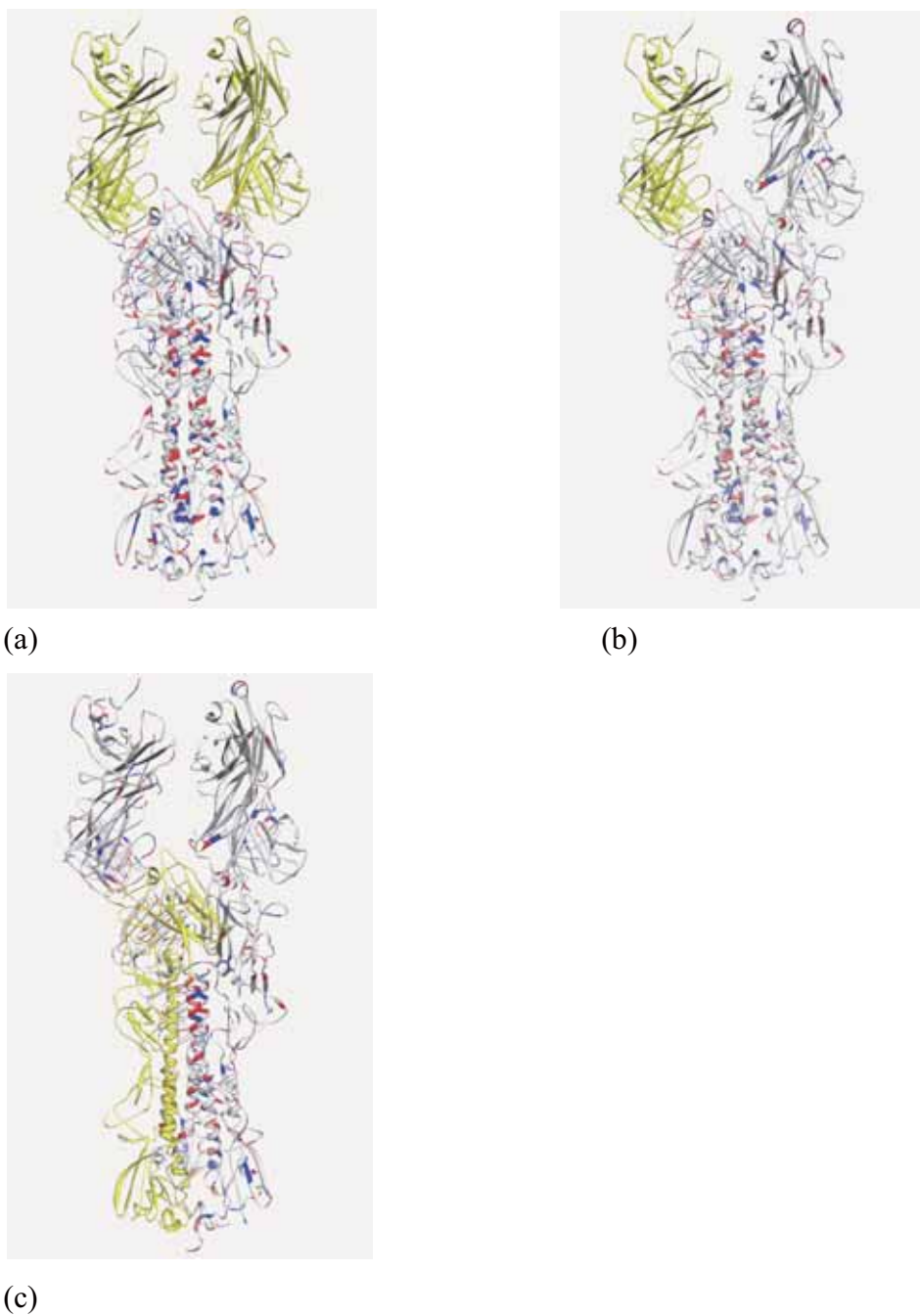


Fig. 2 Visualized IFIE results calculated at the FMO-MP3/6-31G level for the influenza HA trimer with two Fab fragments, by gathering all residues in yellow domains: (a) Fab (I)-fragment and Fab (II)-fragment, (b) Fab (II)-fragment, (c) HA (II)-monomer. Red and blue for residues refer to the interaction energies of stabilization (negative) and destabilization (positive), respectively.

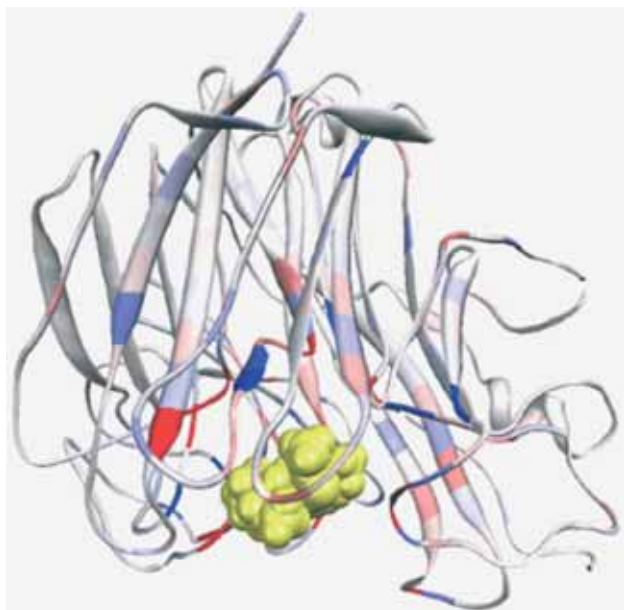


Fig. 3 Visualized IFIE results calculated at the FMO-MP3/6-31G* level for the influenza NA monomer with oseltamivir (yellow). Red and blue for residues refer to the interaction energies of stabilization (negative) and destabilization (positive), respectively.

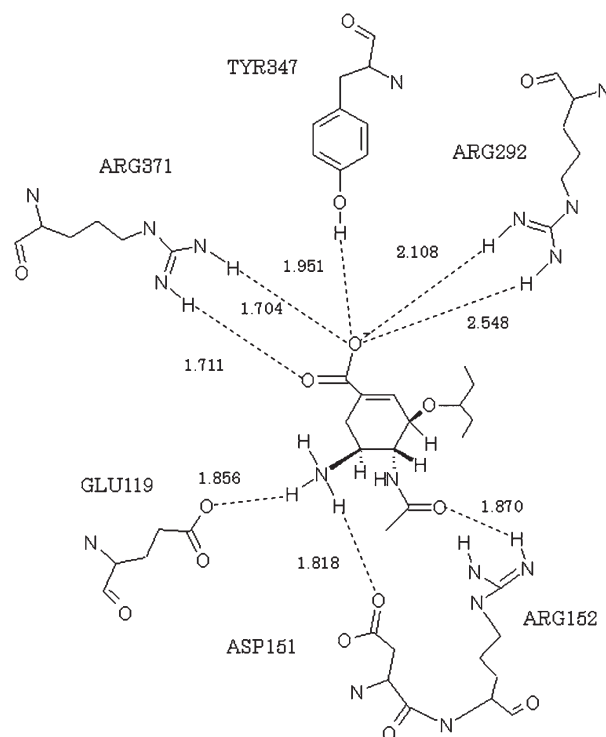


Fig. 4 Hydrogen bond network surrounding oseltamivir in pharmacophore of the influenza NA monomer.

Acknowledgement

This work was supported by the CREST project of the Japan Science and Technology Agency (JST) and by the CISS project at the Institute of Industrial Science (IIS) of the University of Tokyo.

References

- [1] D.G. Fedorov and K. Kitaura, ed., *The Fragment Molecular Orbital Method: Practical Applications to Large Molecular Systems*, CRC Press, Boca Raton, 2009.
- [2] Y. Mochizuki, K. Yamashita, T. Murase, T. Nakano, K. Fukuzawa, K. Takematsu, H. Watanabe, and S. Tanaka, *Chem. Phys. Lett.* 457, pp.396-403, 2008.
- [3] K. Takematsu, K. Fukuzawa, K. Omagari, S. Nakajima, K. Nakajima, Y. Mochizuki, T. Nakano, H. Watanabe, and S. Tanaka, *J. Phys. Chem. B* 113, pp.4991-4994, 2009.
- [4] Y. Mochizuki, K. Yamashita, K. Fukuzawa, K. Takematsu, H. Watanabe, N. Taguchi, Y. Okiyama, M. Tsuboi, T. Nakano, and S. Tanaka, *Chem. Phys. Lett.* 493, pp.346-352, 2010.
- [5] M. Pitonak, P. Neogrady, J. Cerny, S. Grimme, and P. Hobza, *Chem. Phys. Chem.* 10, pp.282-289, 2009.

フラグメント分子軌道法によるインフルエンザウイルスの変異機構の解析

プロジェクト責任者

田中 成典 神戸大学 大学院システム情報学研究科

著者

田中 成典 神戸大学 大学院システム情報学研究科

望月 祐志 立教大学 理学部化学科

福澤 薫 みずほ情報総研 サイエンスソリューション部

山下 勝美 NEC ソフト ニューソリューション事業部

中野 達也 国立医薬品食品衛生研究所 医薬安全科学部

フラグメント分子軌道 (Fragment Molecular Orbital; FMO) 法に基づき、インフルエンザウイルスの表面タンパク質に対する FMO-MP2 および FMO-MP3 計算を地球シミュレータ (ES2) を用いて行った。計算の対象としたのは、ヘマグルチニン (HA) 三量体と Fab 抗体二量体の複合体 (2351 残基、36160 原子) ならびにノイラミニダーゼ (NA) とタミフル分子の複合体 (386 残基) である。HA 単量体および三量体系に対して、電子相関を 2 次の Moeller-Plesset 摂動法で考慮した FMO-MP2/6-31G 計算は、ES2 の 128 ノード (1024 VPU) を用いて、それぞれ 0.8 時間および 4.3 時間で完了した。このことは、本 FMO 計算がサイズ増加に対して良好なスケーリング関係を有することを示している。また、MP2 計算に対する 3 次の MP3 計算の相対的なコスト増加も極めて低く、例えば HA 三量体系に対する FMO-MP3/6-31G 計算は ES2 の 128 ノードを用いてわずか 5.8 時間で終了した。NA タミフル系に対しても、同様に FMO-MP3 計算を 6-31G および 6-31G* 基底関数を用いて実行し、それぞれ 1.0 および 4.4 時間で完了した。このように、これらの計算を通じて、大規模タンパク質系に対する FMO-MP3 計算が ES2 上で効率的に実行可能であることが示された。また、これらの FMO 計算の結果を用いて系に含まれるフラグメント間の相互作用解析を行い、HA タンパク質や NA タンパク質内のアミノ酸が抗体や薬剤による阻害から逃れるためにどのように変異を起こすのかのメカニズムを理論的に考察した。これらの解析手法はインフルエンザウイルスの将来の変異予測や薬剤開発にも役立てることができる。

キーワード: フラグメント分子軌道法, メラー・プレセット摂動法, インフルエンザウイルス, ヘマグルチニン, ノイラミニダーゼ

Chapter 3

■ Visualization ■

Studies of Large-Scale Data Visualization, GPGPU Application and Visual Data Mining

Project Representative

Fumiaki Araki

Earth Simulator Center, Japan Agency for Marine-Earth Science and Technology

Authors

Fumiaki Araki^{*1}, Shintaro Kawahara^{*1}, Nobuaki Ohno^{*1} and Daisuke Matsuoka^{*1}

*1 Earth Simulator Center, Japan Agency for Marine-Earth Science and Technology

Research and development for visualization technologies carried out by Advanced Visualization and Perception Research Group of the Earth Simulator Center in the fiscal year 2009 is reported. In terms of in-situ visualization, speeding up and vectorization of several pre-processing parts of a visualization program containing software-rendering algorithms is considered and examined. A ray-skip algorithm with octree-structured bounding volumes is implemented into pre-processing parts of the visualization program to accelerate ray-casting calculations. In terms of an application of GPGPU, implementation methods of GPGPU technology to a virtual reality visualization program, especially for an isosurface reconstruction algorithm, are examined. It is confirmed that the processing time including drawing was greatly shortened in comparison with CPU implementation. Implementations of it to each process of CAVELib program and memory managements are also discussed. In terms of visual data mining, our developed methods can classify magnetic field lines automatically into three types based on the difference between their topologies and detect the number of loop times. 3D distribution of magnetic field lines' topology and its separatrix surfaces are visualized by using this automatic classification method. Brief overviews of the survey for recent researches and developments in terms of large-scale data visualization are reported. Current progress of VFIVE development is also reported.

Keywords: large-scale data visualization, vectorization, GPGPU, virtual reality visualization, visual data mining

1. Introduction

Computer technology is quickly advancing and has become able to process more tremendously than before. Typical sizes of datasets produced by high-resolution simulations on recent supercomputers are enlarged from terabytes to petabytes. It would be a serious problem if scientists could not get any knowledge from the data because its size is too much to analyze it. To avoid this situation, it is important to develop fully-powerful and useful tools to visualize such the massive data at high speed and extract hidden information effectively. We are focusing on the problems on visualizing large-scale datasets and proceeding to study the visualization methodology and develop various useful tools.

In the fiscal year 2009, we have tried following six themes; vectorization of visualization algorithm, application of the general purpose computing on graphics processing units (GPGPU) with virtual reality visualization, visual data mining approach, a survey for large scale data visualization, and VFIVE development. For the first theme, one of the solutions to visualize massive data produced by a large-scale simulation is to execute the visualizing process at the same computational environment to do the simulation. In the case that the environment is a supercomputer system with vector

processors like as the Earth Simulator, it is important to vectorize the visualization algorithm, in addition to parallelize it. We explore the possibility to do it in this section. For the second theme, GPGPU has nowadays become used for various areas that need to execute massive calculations. We think that applying GPGPU technology with speeding up visualization processes is important for interactive visualization methods, and especially our virtual reality (VR) visualization method, which has to keep both immediate response and interactivity to gain highly immersive sense. This is denoted in Section 3. For the third theme, we introduce an application example with our visual data mining approach to an analysis for the data of a space plasma simulation in Section 4. Magnetic field lines reproduced from that dataset are classified automatically on the basis of a few topologically different types. In Section 5, as the fourth theme, we describe brief overviews of our investigations of recent researches and developments in terms of large-scale data visualization, in order to take a comprehensive view of this research area and find clues toward to the next-generation visualization paradigm. In Section 6, progress of our virtual reality software VFIVE is reported. The last section is devoted to summery.

2. Vectorization of visualization algorithm

In the fiscal year 2009, we prepared a visualization program for software-rendering and vectorized the pre-processing parts of it. This program is implemented with both of isosurface and volume rendering functions based on the ray-casting algorithm for scalar computers without GPU. This program is also equipped with pre-processing parts to accelerate those ray-casting calculations. Each of these pre-processes acts as following; (1) to generate bounding volumes, (2) to memorize the empty regions of a target volume data to an octree data, and (3) to do ray-skip at each empty region based on this octree data, as shown in Fig. 1. Computation time for the ray-casting is greatly reduced through these pre-processing. Another pre-processing is also equipped into this visualization program. That is for derivation of gradient vectors of the target volume data which are used as the normal vectors to shade both of isosurface and volume rendered objects. Vectorization is applied with all of the pre-processing parts of this visualization program. We confirmed that computation time is successfully reduced by the vectorization on vector type computers. We are planning to vectorize the main part of this program, the ray-casting algorithm, of this software.

3. Application of GPGPU with virtual reality visualization

We tried to apply the general purpose computing on graphics processing units (GPGPU) [1] technology to the visualization using a virtual reality (VR) system. In the fiscal year 2009, we examined implementation methods of this technology to a visualization program for BRAVE [2], which is a CAVE system [3] of the Earth Simulator Center, and evaluated whether the GPGPU technology was effective for the acceleration of the program. Using high-speed calculation functions of GPGPU, we aimed to keep interactivity of visualization programs for VR system and enable to visualize a much larger volume of data

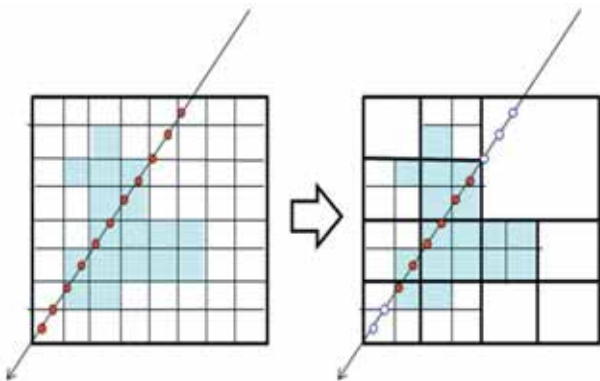


Fig. 1 Concept of bounding volume. When volume rendering is carried out by ray casting method, the time for calculation is greatly reduced by setting bounding volumes distinguishing from empty regions and non-empty regions in data and making ray skip the empty regions.

than before.

Specifically, we implemented the isosurface reconstruction algorithm that was written in GPU code to the visualization program for VR system and evaluated the performance. We developed the prototype program using CAVELib [4] as API for VR system, CUDA [5] as the GPGPU programming language, and OpenGL as 3-D CG API. As the isosurface reconstruction algorithm written in GPU code, we improved and used a sample code included in CUDA SDK. This sample code used Marching Cubes method as an isosurface reconstruction algorithm. In the performance assessment described later, we compared this implementation with VFIVE [2, 6, 7], because same algorithm (Marching Cubes) is also implemented to the isosurfacing function of VFIVE.

Fig. 2 is the hardware configuration of graphics workstation generating stereoscopic images to screens of BRAVE. Four graphics cards (NVIDIA Quadro FX 5600) are connected to graphics workstation (SGI Asterism: 8CPU/16Cores, 128GB Memory) with PCI-Express. Each graphics card is connected to the projector of BRAVE, and renders stereoscopic images. Fig. 3 is program behavior written by CAVELib. Processes executed in each thread are divided broadly into three parts: the initialization part, the calculation part and the rendering part. At the start of the program, four threads are launched corresponding to each screen of BRAVE. Then, calculation and rendering process are executed repeatedly until the program termination.

When we applied the GPGPU technology to the program with

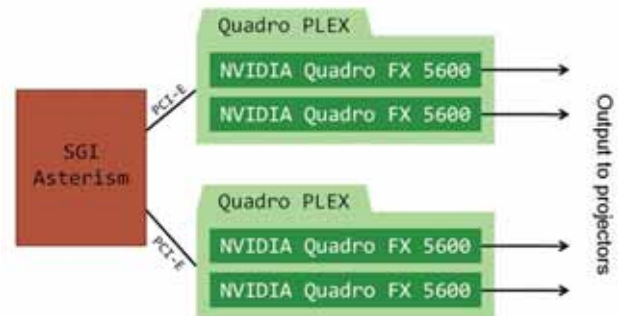


Fig. 2 The hardware configuration of graphics workstation of BRAVE.

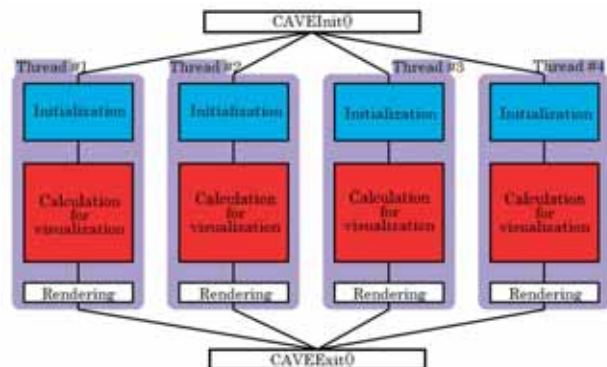


Fig. 3 The Processing flow of CAVELib program.

CAVELib, initialization process of GPU devices was added to the initialization part of each thread in Fig. 3. In the calculation part of each thread, CPU-based visualization algorithm was replaced to GPU-based one. In the case with implementation by CPU code, vertex and normal data, which were generated as execution results of visualization algorithm, are stored on main memory managed by CPU. These data must transfer to GPU memory, when the rendering process is executed. In this case, the data transfer time can become significant problem. In the case with implementation by GPU code, vertex and normal data are calculated and stored on GPU memory. These data can be used directly to render, and speeding up of the rendering process can also be expected.

Fig. 4 shows a snapshot of executing the prototype program implemented GPU-based isosurface reconstruction algorithm, and Fig. 5 shows benchmark results. As a result, it was confirmed that the processing time including drawing was greatly shortened in comparison with CPU implementation. Therefore, the effectiveness of the application of the GPGPU technology to the visualization program for the VR system was suggested. In addition to the implementation method described in this report, we are also trying to implement and evaluating the method using multi-GPU, and these methods can expect

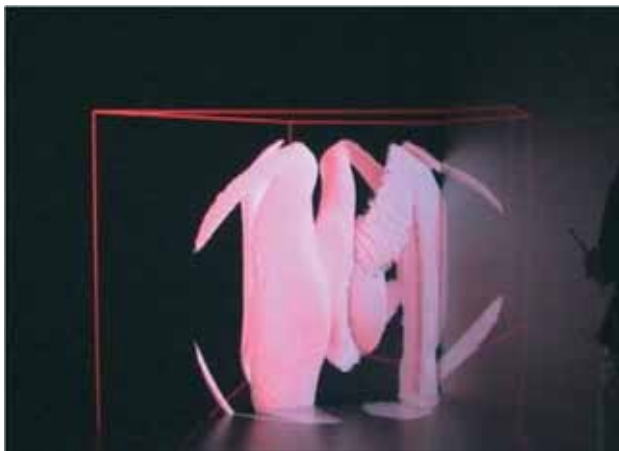


Fig. 4 A snapshot of executing the prototype program implemented GPU-based isosurface reconstruction algorithm.

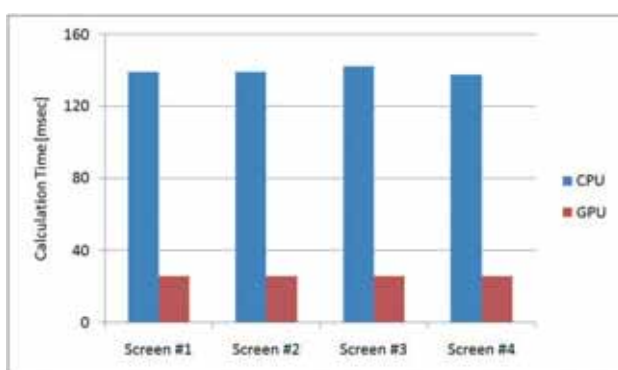


Fig. 5 Comparison of calculation time between CPU and GPU (datasize: 128x128x128).

applying to other visualization software.

4. Visual data mining

We developed visual data mining methods to analyze automatically large amounts of time-varying volume dataset [8]. In this study, we applied these methods to space plasma simulation data. In the field of solar terrestrial physics, it is known that the magnetic reconnection (interaction between the interplanetary magnetic field and the geomagnetic field) has a crucial role in the magnetospheric convection. The automatically classification method, which extracts magnetic field lines' topology from a highly temporal- and spatial-resolution dataset, has developed in order to understand a time-dependent change of complex magnetic field lines called magnetic flux rope. In this study, nine types of magnetic field lines are defined based on magnetic topology and the number of loop times. First, the magnetic field lines were visualized and projected onto x-y and x-z planes as shown in the lower right-hand of Fig. 6. Next, topological type of each magnetic field line is distinguished between the following three types; 'open (Sun to Earth)', 'closed (Earth to Earth)' or 'detached (Sun to Sun)', automatically by using eight scanning lines from central point located on the core field line. The number of loop times is also detected at the same time. Here, when the magnetic field line is helical, three or more intersecting points are detected on each scanning line in the x-z plane. When it is quasi-helical, one or two points are detected. When there is no flux rope, intersecting point is only one or not detected. Finally, we scan intersecting points along core field line of magnetic flux rope (drawn by dashed line as shown in Fig. 6) in the x-y plane, and classified the magnetic field line's topology as well as the x-z plane. By using 2D projected image processing, 3D time-dependent change of magnetic field line's topology of magnetic flux ropes are obtained.

By using the automatic classification method as mentioned above, a 3D distribution of magnetic field lines' topology and its separatrix surfaces are visualized. 3D distribution of magnetic field line's topology can be visualized as the 3D separatrix surfaces specified as boundary surfaces between 'open' and

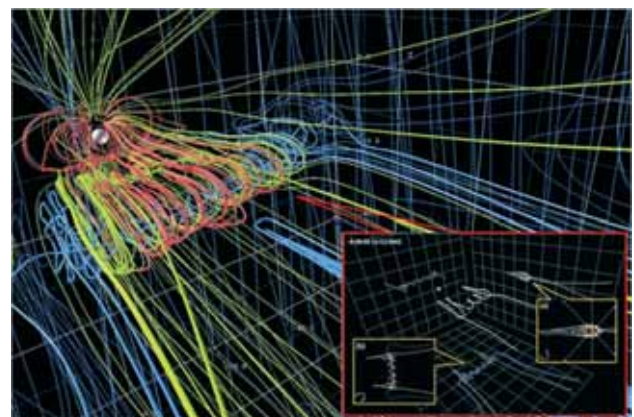


Fig. 6 Visual data mining of magnetic field line's topology.

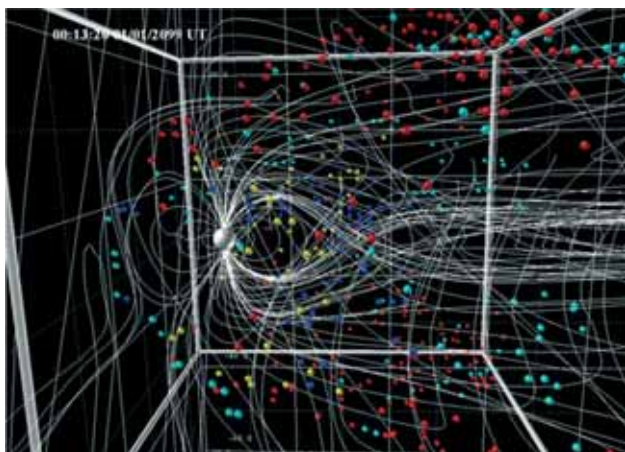


Fig. 7 Extraction of magnetic reconnection region.

'detached' field line bundles. In comparison with time-dependent change of the 3D separatrix surfaces, the magnetic reconnection region was automatically extracted as shown in Fig. 7. Red spheres represent the points at which topological type of magnetic field lines changes from 'detached' to 'open'. As the same way, blue, yellow and light-blue ones represent the points to change 'closed' to 'open', 'closed' to 'detached', and 'open' to 'detached', respectively.

5. Survey of large-scale data visualization

We investigated the studies of all sorts and sources about large-scale visualization. In this section, we introduce only the result of this survey research.

5.1 Parallel visualization

Visualization of massive datasets produced by large-scale numerical simulations takes lots of time. One solution to visualize large-scale dataset efficiently is parallelization of visualization pipeline such as filtering, mapping and rendering process. Filtering is the process to select data portion to be visualized. Data compressions (delta encoding, quantization or wavelet compression) and data structuralizing (octree, k-d tree) are known as effective filtering techniques to a handle large-scale volume dataset. Time-Space Partitioning (TSP) tree, enhanced TSP tree and wavelet TSP tree have also been developed for time-varying datasets. Volume rendering is the useful method to display a 2D projection of a 3D discretely sampled dataset. In order to handle large-scale volume dataset, many researchers have focused on its efficient algorithms. Volume rendering algorithms are roughly classified into the geometry processing and the rasterization. To achieve efficient parallel volume rendering, the sorting algorithms (sort-first, sort-middle and sort-last) during the geometry processing, the image compositing methods (direct send and binary swap) during the rasterization and other optimization techniques have been developed.

5.2 Visualization of time-varying dataset

In this case, data I/O processing occurs continuously and periodically each time step. As the efficient I/O techniques for time-varying visualization, pre-fetching, parallel I/O and parallel pipeline (temporal and spatial parallelism) are widely used on parallel computing system. In particular, parallel pipeline is widely used as effective method that can remove the I/O bottlenecks and minimize the interframe delay.

5.3 Remote visualization

The most serious bottleneck is the transferring large amounts of dataset from data storage to user's desktop machine. The method to solve this bottleneck is remote visualization that use network environment. The concepts of remote visualization are removal the bottleneck of data transferring process and utilization the available resource. Remote visualization methods are classified into several types based on server/client model and data flow model. We also investigate distributed visualization by using grid environment and collaborative visualization.

5.4 Other recent works

With the recent development of GPU, general purpose computing on GPU (GPGPU) is utilized in the visualization as well as the numerical simulation. Moreover, utilization of a GPU cluster in which each node is equipped with a GPU also reported to handle more large-scale dataset. We also investigated large-scale data visualization via GPU cluster as hybrid (tightly and loosely coupled) system and its future prospects.

6. VFIVE development

We have been developing an interactive visualization software VFIVE [2, 6, 8] for CAVE systems [3]. VFIVE has various visualization methods and its user interface is designed especially for CAVE systems unlike many of other visualization software for CAVE systems, which were designed for PCs or graphics workstations with 2D monitors. As a result of our vigorous developments, VFIVE became a powerful tool for interactive visualization.

The source code of the basic version of VFIVE has been opened on the AVPRG web site [9]. This version is executable on single systems with UNIX / Linux. Currently, VFIVE is being proceeded to tune for the PC cluster-based CAVE system with MS-Windows, which is widely installed in many laboratories of universities and research institutes in Japan.

In the fiscal year 2009, we added an animation function to handle time-developing data as shown in Fig. 8, to the original VFIVE. This extension enables users to perform 4D visualization in CAVE systems. This version is also available to download on our web site [9].

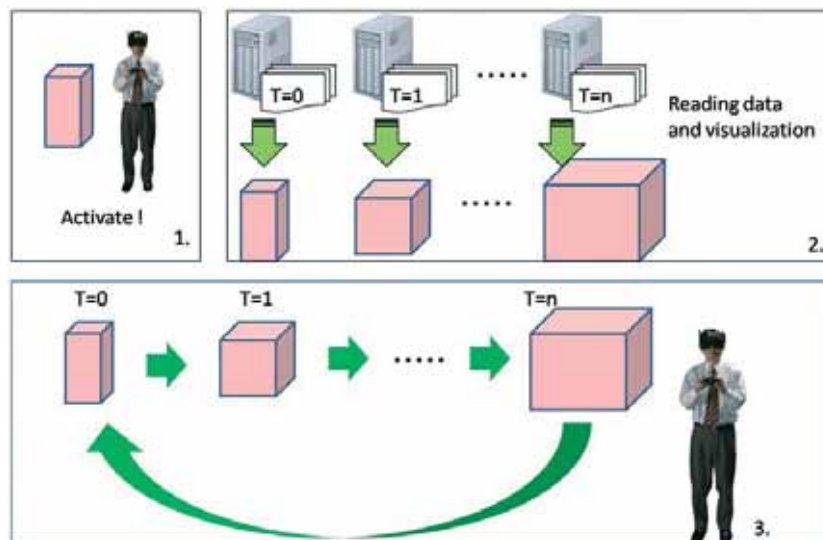


Fig. 8 VFIVE's animation function. (1) a user activate the animation function. (2) VFIVE reads data, visualizes data and saves visualized objects such as isosurface as OpenGL's display list. VFIVE does this process at all the time step. (3) VFIVE shows the saved visualized objects one after another.

7. Summery

Speeding up and vectorization of several pre-processing parts of a visualization program containing software-rendering algorithms was considered and examined. A ray-skip algorithm by octree-structured bounding volumes was equipped with pre-processing parts to accelerate ray-casting calculations. We confirmed that vectorization is effective to all of pre-processing parts and the computation time was successfully reduced by the vectorization on vector type computers.

Implementation methods of GPGPU technology to a virtual reality visualization program, especially for an isosurface reconstruction algorithm, were examined. Applications of GPGPU technology to each process of CAVELib program and memory managements were discussed. It was confirmed that the processing time including drawing was greatly shortened in comparison with CPU implementation. This result suggests that the application of GPGPU technology to the visualization program for the VR system is effective.

Visual data mining methods to analyze automatically large amounts of time-varying volume dataset of a space plasma simulation were developed and examined. These methods can classify magnetic field lines automatically into three types based on the difference between their topologies and detect the number of loop times. 3D distribution of magnetic field lines' topology and its separatrix surfaces were visualized by using this automatic classification method.

Brief overviews of the survey of recent researches and developments for large-scale data visualization were reported. The results fell roughly into four categories; parallel visualization, Visualization of time-varying dataset, Remote visualization and other recent works.

Current progress of VFIVE development was reported. The

version for PC cluster-based CAVE system with MS-Windows is being tuned, which is widely installed in many laboratories of universities and research institutes in Japan. Extended version of VFIVE to handle time-developing data was opened on the AVPRG web site.

References

- [1] D. Luebke, M. Harris, N. Govindaraju, A. Lefohn, M. Houston, J. Owens, M. Segal, M. Papakipos, and I. Buck, "GPGPU: general-purpose computation on graphics hardware", Proc. of 2006 ACM/IEEE Conference on Supercomputing, Tampa, Florida, USA, Nov., 2006.
- [2] F. Araki, H. Uehara, N. Ohno, S. Kawahara, M. Furuichi, and A. Kageyama, "Visualizations of Large-scale Data Generated by the Earth Simulator", J. Earth Sim., Vol. 6, pp.25-34, 2006.
- [3] C. Cruz-Neira, D. J. Sandin, and T. A. DeFanti, "Surroundscreen projection-based virtual reality: The design and implementation of the CAVE", Proc. of the Computer Graphics International Conference, pp.135-142, 1993.
- [4] CAVELib, URL: <http://www.mechdyne.com/integratedSolutions/software/products/CAVELib/CAVELCA.htm>
- [5] CUDA, http://www.nvidia.com/object/cuda_home.html
- [6] A. Kageyama, Y. Tamura, and T. Sato, "Visualization of Vector Field by Virtual Reality", Progress Theor. Phys. Suppl., Vol.138, pp.665-673, 2000.
- [7] N. Ohno and A. Kageyama, "Scientific visualization of geophysical simulation data by the CAVE VR system with volume rendering", Physics of The Earth and Planetary Interiors, Vol. 163, Issues 1-4, pp.305-311, Computational

Challenges in the Earth Sciences, 2007.

- [8] D. Matsuoka, K. T. Murata, S. Fujita, T. Tanaka, K. Yamamoto, and N. Ohno, "3D Visualization and Visual Data Mining", Journal of the National Institute of Information and Communications Technology, Special Issue on Space Weather (in press).
- [9] VFIVE : Virtual Reality Visualization Software for CAVE System, <http://www.jamstec.go.jp/esc/research/Perseption/vfive.en.html>

大規模データ可視化, GPGPU およびビジュアルデータマイニングの研究

プロジェクト責任者

荒木 文明 海洋研究開発機構 地球シミュレータセンター

著者

荒木 文明^{*1}, 川原慎太郎^{*1}, 大野 暢亮^{*1}, 松岡 大祐^{*1}

^{*1} 海洋研究開発機構 地球シミュレータセンター

地球シミュレータセンター高度計算表現法研究グループで 2009 年度に実施した可視化に関する研究開発について報告する。シミュレーションと同一環境において実施する可視化手法の研究については、ソフトウェアレンダリング可視化プログラムを開発し、その中のいくつかのプリプロセスについての高速化とベクトル化を考察する。レイキャスティング計算の高速化のために、八分木で構造化されたバウンディングボリュームを用いて空領域で処理をスキップさせるアルゴリズムを提案し、可視化プログラムのプリプロセス部分への実装を行う。GPGPU 応用については、バーチャルリアリティ可視化プログラム、特に等値面再構成アルゴリズムへの GPGPU 技術の実装方法を考察し、実験および評価を実施する。このとき、描画を含む処理時間が CPU 実装の時に比べて大幅に短縮されることが確認される。他、GPU 実装に関して CAVELib に基づくプログラムの各処理との関係を議論する。データマイニングに関しては、磁力線をそのトポロジ的構造に基づいて 3 種類に分類する方法を開発する。また、この分類手法を用いて磁力線トポロジーの 3 次元分布と磁気セパトリック面が可視化される。近年の大規模可視化研究の調査については、その概略を報告する。また VFIVE 開発に関する現在の取り組みについても報告する。

キーワード: 大規模データ可視化, ベクトル化, GPGPU, バーチャルリアリティ可視化, ビジュアルデータマイニング

Published by

The Earth Simulator Center, Japan Agency for Marine-Earth Science and Technology

3173-25 Showa-machi, Kanazawa-ku, Yokohama, 236-0001 JAPAN

Tel: +81-45-778-5861 Fax: +81-45-778-5491

<http://www.jamstec.go.jp/esc/>

First edition: October 1, 2010

© The Earth SimulatorCenter

Reproduction or distribution of the contents of this publication without permission is strictly prohibited.